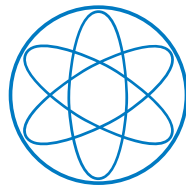


FAKULTÄT FÜR PHYSIK

Study of the hyperon-nucleon interaction via femtoscopy
in elementary systems with HADES and ALICE

Oliver Werner Arnold



DER TECHNISCHEN UNIVERSITÄT MÜNCHEN
FACHBEREICH: DENSE AND STRANGE HADRONIC MATTER (E62)

2017



FAKULTÄT FÜR PHYSIK

DER TECHNISCHEN UNIVERSITÄT MÜNCHEN

FACHBEREICH: DENSE AND STRANGE HADRONIC MATTER
(E62)

Study of the hyperon-nucleon interaction via femtoscopy
in elementary systems with HADES and ALICE

Oliver Werner Arnold

Vollständiger Abdruck der von der Fakultät für Physik der Technischen Universität
München zur Erlangung des akademischen Grades eines

Doktors der Naturwissenschaften (Dr. rer. nat.)

genehmigten Dissertation.

Vorsitzender:

apl. Prof. Dr. Norbert Kaiser

Prüfer der Dissertation:

1. Prof. Dr. Laura Fabbietti

2. Prof. Dr. Lothar Oberauer

3. Prof. Dr. Marcus Bleicher

Die Dissertation wurde am 17.07.2017 bei der Technischen Universität München
eingereicht und durch die Fakultät für Physik am 02.08.2017 angenommen.

Zusammenfassung

Diese Arbeit beschäftigt sich mit der Untersuchung der Wechselwirkung zwischen Λ Hyperonen und Protonen. Das Verständnis dieser Wechselwirkung ist elementar zur Beschreibung verschiedener physikalischer Systeme z.B. von Neutronensternen. Der Zusammenhang zwischen der Wechselwirkung von Hadronen und Eigenschaften des Neutronensterns wird in der Einleitung näher erläutert. Die Methode, die zur Untersuchung der Wechselwirkung von Protonen und Λ Hyperonen verwendet wurde ist Femtoscopy. Femtoscopy basiert auf der Messung von Teilchenpaaren bei kleinen Relativimpulsen. Dadurch ist es experimentell möglich eine Zweiteilchen-Korrelationsfunktion zu bilden. Dies wird in dieser Thesis zu Beginn näher erläutert. Durch verschiedene Annahmen kann die experimentell bestimmte Zweiteilchen-Korrelationsfunktion mit einem mathematischen Formalismus verglichen werden, der die Wechselwirkung der Hadronpaare in Form von Streulängen und effektiven Radien beinhaltet. Somit können verschiedene Vorhersagen von Theorien oder Modellen mit den gemessenen Daten getestet werden. In dieser Arbeit wurden vor allem neueste Rechnungen einer chiralen effektiven Feldtheorie berücksichtigt. Im ersten Teil dieser Thesis wurde eine Studie der Zweiteilchen-Korrelationsfunktion mit Proton-Proton und Proton- Λ Paaren am HADES Experiment durchgeführt. Diese Paare wurden in Reaktionen von $p+Nb$ bei einer kinetischen Protonenergie von 3.5 GeV produziert. Zu Beginn wurden alle experimentellen Korrelationsfunktionen für verschiedene Detektoreffekte korrigiert, wobei der Effekt der endlichen Impulsauflösung von HADES und des sog. “Track mergings” die signifikantesten Einflüsse darstellten. Durch Vergleich der experimentellen Daten mit Modellrechnungen konnte die Quellgröße des Systems für Proton-Proton Paare bestimmt werden. Zusammen mit UrQMD Simulationen war es möglich die Quellgröße für Proton- Λ Paare im Modell zu fixieren. Dies ermöglichte eine Reduktion des freien Quellgröße Parameters. Dadurch basiert die theoretische Korrelationsfunktion nur auf Parametern der Wechselwirkung. Es zeigt sich, dass die Proton- Λ Korrelationsfunktion sensitiv auf den Wert der Streuparameter reagiert. Um dies zu sehen wurden die “leading order” (LO) und “next-to-leading-order” (NLO) Parameter getestet, die sich in der Vorhersage des totalen Wirkungsquerschnitts für kleine Impulse des Λ Hyperons stark unterscheiden. Die vorhandene Paarstatistik war allerdings nicht ausreichend um eine Separation zwischen beiden Parametersets vorzunehmen.

Im zweiten Teil dieser Arbeit wurde die Analyse für Kollisionen von Protonen bei einer

Schwerpunktsenergie von 7 TeV wiederholt. Die Kollisionen wurden am Large Hadron Collider durchgeführt und die Daten durch das ALICE Experiment aufgezeichnet. In dieser Analyse wurde die Quellgröße durch einen simultanen Fit der Proton-Proton und Proton- Λ Korrelationfunktionen bestimmt. Dabei wurde für die Wechselwirkung des Proton- Λ Paares die NLO Parametrisierung verwendet. Nach Beendigung des Fits wurde die LO Parametrisierung angenommen und mit dem Fitresultat für NLO verglichen um einen möglichen Unterschied zu untersuchen. Auch hier zeigte sich, dass die Korrelationsfunktion sensitiv auf den Wert der Streuparameter reagiert. Allerdings reichte auch in diesem Fall die vorhandene Paarstatistik nicht aus um eine definitive Unterscheidung vorzunehmen.

Preface

In this thesis the interaction of Λ Hyperons with protons is studied. This interaction is important to understand various physical systems e.g. the behavior of neutron stars. The connection of the hadron interaction and properties of neutron stars is discussed in more details in the introduction of the thesis. The method with which the interaction is investigated is femtoscopy. It is based on the measurement of pairs at small relative momenta. This allows to establish a two-particle correlation function. This is discussed in more details at the beginning of the thesis. Making different approximations allows to compare the experimental correlation function with one based on a mathematical framework, which includes the interaction parameter of the particle pair. This allows to test and compare different predictions from theories or models. In this thesis recent calculations of a chiral effective field theory is tested. In the first part of the thesis a study of a two-particle correlation function of proton-proton and proton- Λ pairs at the HADES experiment is performed. These pairs were produced in reaction of p+Nb, where the proton had a kinetic energy of 3.5 GeV. At the beginning, all experimental correlation functions were corrected for various detector effects. Here the finite momentum resolution of HADES and the effect of “track merging” played the most significant role. A comparison of the proton-proton correlation function with a model calculation allowed the extraction of the source size of the system. This allowed together with help of UrQMD simulations to fix the source size of proton- Λ . This reduced the free source size parameter of proton- Λ and the theoretical correlation function depends then only on the parameters of the interaction. It showed up that the theoretical correlation function is sensitive to the values of the interaction parameter. To see this the parameter sets of “leading-order” (LO) and “next-to-leading-order” (NLO) were tested. These two expansions differ quite significantly in the predictions of the total cross section for small Λ momenta. The collected pair statistics was not sufficient to distinguish between both predictions.

In the second part of the thesis the analysis was repeated in a collision system of protons at a center of mass energy of 7 TeV. The collisions were recorded by the ALICE experiment. In this analysis the source size parameter was determined by a simultaneous fit of the proton-proton and proton- Λ correlation function. For the interaction of proton- Λ pairs the NLO parameter set was chosen. After the fit was performed the LO parameters were plugged in to the theoretical correlation function to explore possible differences. It showed up, that the correlation function is sensitive to the values of the scattering pa-

parameter. However, also there the collected pair statistics was not sufficient to draw a definite conclusion.

Contents

| | | |
|----------|---|-----------|
| 1 | Introduction | 1 |
| 1.1 | Neutron stars, equation of state, gravitational waves | 6 |
| 1.2 | Hyperon-Nucleon interaction | 12 |
| 1.3 | Motivation for this work | 16 |
| 2 | Basics of Femtoscopy | 17 |
| 2.0.1 | Mathematical framework | 17 |
| 2.0.2 | The source function | 19 |
| 2.0.3 | Typical correlation functions | 22 |
| 2.0.4 | Coulomb interaction | 24 |
| 2.0.5 | Strong interaction and the Lednicky model | 25 |
| 2.0.6 | Resonance decays, energy conservation | 33 |
| 2.0.7 | Inelastic scattering | 34 |
| 2.0.8 | Combinations of correlation sources | 34 |
| 2.0.9 | Correlation function and bound states | 34 |
| 2.0.10 | Construction of experimental correlation function | 36 |
| 2.0.11 | The out-side-long reference frame | 36 |
| 2.0.12 | Pair statistics | 38 |

Part I PART I

| | | |
|----------|---|-----------|
| 3 | The HADES detector at SIS18 | 43 |
| 3.0.13 | The target | 44 |
| 3.0.14 | The RICH detector | 45 |
| 3.0.15 | The Multi-Wire-Drift Chambers | 46 |
| 3.0.16 | The Magnet | 47 |
| 3.0.17 | The Time-of-flight detectors | 48 |
| 3.0.18 | The Forward Wall | 48 |
| 3.0.19 | Trigger in the p+Nb run | 49 |
| 3.0.20 | Analyzed files | 49 |

| | | |
|----------|---|-----------|
| 3.1 | Particle identification | 50 |
| 4 | Data analysis | 53 |
| 4.0.1 | Protons and Lambda hyperons track selection | 54 |
| 4.1 | Correlation functions | 54 |
| 4.2 | Corrections | 57 |
| 4.2.1 | Two track cuts | 57 |
| 4.2.2 | Long range correlations | 61 |
| 4.2.3 | Momentum Resolution | 63 |
| 4.2.4 | Purity and residual Correlations | 66 |
| 4.3 | Comparison to transport model predictions | 69 |
| 4.4 | Experimental results | 73 |
| 4.4.1 | Source size extraction | 73 |
| 4.4.2 | Test of scattering parameter | 75 |

Part II PART II

| | | |
|----------|---|-----------|
| 5 | The ALICE detector at the LHC | 85 |
| 5.0.3 | The Inner Tracking System - ITS | 86 |
| 5.0.4 | The Time-Projection Chamber - TPC | 87 |
| 5.0.5 | The Time-Of-Flight detector - TOF | 89 |
| 6 | Data analysis | 91 |
| 6.1 | Event selection | 92 |
| 6.2 | Track selection | 92 |
| 6.2.1 | Proton candidates | 92 |
| 6.2.2 | V0 candidates | 95 |
| 6.3 | Correlation functions | 99 |
| 6.3.1 | Baryon-Antibaryon correlations | 100 |
| 6.3.2 | Baryon-Baryon correlations | 104 |
| 6.4 | Linear decomposition of correlation functions | 105 |
| 6.4.1 | Decomposition of the proton-proton correlation function | 116 |
| 6.4.2 | Decomposition of the proton-Lambda correlation function | 118 |
| 6.4.3 | Decomposition of the Lambda-Lambda correlation function | 121 |
| 6.5 | Corrections | 123 |
| 6.5.1 | Residual Correlations | 123 |
| 6.5.2 | Finite momentum resolution | 127 |
| 6.5.3 | Pair selection criteria | 130 |
| 6.5.4 | Non-femtoscopic background | 132 |
| 6.6 | Systematic uncertainties | 132 |

| | | |
|----------|--|------------|
| 6.7 | Experimental results | 133 |
| 6.7.1 | The Lambda-Lambda correlation function and the relation to bound states | 137 |
| 6.7.2 | EPOS predictions for the source function | 140 |
| 7 | Outlook | 145 |
| 7.1 | Imaging - Fixing the source | 145 |
| 7.2 | Femtoscscopy in two spatial dimensions | 147 |

Part III Appendix

| | | |
|----------|--|------------|
| A | Solution of the Schrodinger Equation | 151 |
| B | Probability density function for two-particle correlation functions | 155 |
| C | How to obtain projections in out-side-long coordinate system | 157 |

1

Introduction

Our current knowledge of the fundamental interactions between all observed particles is incorporated in the Standard model of particle physics. This model is based on the symmetry group $G_{\text{SM}} = SU(3)_C \times SU(2)_L \times U(1)_Y$, where $SU(2)_L \times U(1)_Y$ corresponds to the electroweak sector of the standard model governing weak and electromagnetic interactions e.g. the binding of electrons on atomic nuclei. The standard model was experimentally completed with the finding of the Higgs boson at the Large Hadron Collider (LHC) [Aad+12; Cha+12], which is responsible for the generation of mass for the fundamental constituents of the standard model[Hig64]. The $SU(3)_C$ color symmetry is the symmetry of quantum chromodynamics (QCD), the theory of strong interactions. Since the symmetry is of non-Abelian nature QCD is very rich in phenomena and a research field by itself. QCD is constructed on the basis of fermion fields, the quarks and bosonic mediators of the strong force, the gluons. Gluons appear automatically in the theory if a local gauge principle is required. The Lagrangian of QCD reads:

$$\mathcal{L} = \bar{\psi}(i\gamma_\mu D^\mu - m)\psi - \frac{1}{4}G_{\mu\nu a}G^{\mu\nu a}, \quad (1.1)$$

where ψ are the fermionic quark fields and $G_{\mu\nu a}$ is the tensor including the gluon fields. The quarks are distinguished by their flavor, u=up, d=down, s=strange for the light quarks. They come in three colors $N_C = 3$ since they transform in the fundamental representation of $SU(3)_C$. The mass term m is the bare mass of the quarks. The indices a are introduced by the color symmetry. Contrary to quantum electrodynamics (QED), where only one photon is present the theory includes $N_C^2 - 1 = 8$ gauge boson fields due to the additional quantum number “color” and they transform under the adjoint repre-

sensation of the symmetry group. The derivative D_μ is a covariant derivative and must include the gluon fields due to the locality of the symmetry. This Lagrangian is consistent with principles of renormalizability, but theoretically an additional term would be allowed $\sim \tilde{G}_{\mu\nu a} G^{\mu\nu a}$, where one gluon tensor is contracted with the Levi-Civita symbol $\epsilon_{\mu\nu\rho\sigma}$. Such a term violates the combination of charge (C) and parity (P) CP symmetry. It is fully allowed by all principles but seems not to be realized in nature and the smallness of this term is an open question. Especially, because the electroweak force does violate CP symmetry. Contrary to QED, which is an Abelian theory, the gluon fields A_μ^a include self-couplings:

$$G_{\mu\nu}^a = \partial_\mu A_\nu^a - \partial_\nu A_\mu^a + g f^{abc} A_{\mu b} A_{\nu c}, \quad (1.2)$$

mediated by the term $g f^{abc} A_{\mu b} A_{\nu c}$, where g is the flavor independent coupling constant and f^{abc} is the structure constant of $SU(3)_C$. Thus gluons can interact among themselves because they carry the gauge symmetry charge ‘‘color’’ and this has strong implications on the resulting physics observables. This is very contrary to QED. In Eq. (1.1) one deals with massless gauge bosons, thus a static local potential would look Coulomb like $\sim 1/r$ at small quark separations. The energy for breaking up a quark pair would be finite in this case. However, quarks and gluons were never observed isolated in any experiment. Something must prevent this and here the gluon self-interaction comes into play. A hint is deduced at large momenta transfers or short distances in a perturbative expansion of the quantized Eq. (1.1). Higher order corrections lead to a running of the coupling constant $\alpha(Q) \equiv g(Q)^2/(4\pi)$. At large momenta the coupling between quarks becomes small and for lower momenta it increases. This is a reflection of the non-Abelian nature of the underlying symmetry of QCD. This prediction was confronted with many experimental measurements displayed in Fig. (1.1) [Bet07]. It is said that QCD is *asymptotically free*, which means at large momenta or short distances quarks and gluons are effectively free and a perturbative treatment of Eq. (1.1) is possible. Since the coupling constant increases for smaller momenta Q quarks are *confined* into hadrons. These hadrons are colorless and transform as singlet under $SU(3)_C$. Basically two classes of hadrons can be distinguished, baryons, which are hadrons with three quarks inside and mesons containing a quark anti-quark pair. However, any quark configuration which is color neutral is allowed and experimental searches for hadrons containing four or more quarks are ongoing [Aai+15; Aba+16]. The establishment of *confinement* as a rigor mathematical proof is still an unsolved issue. It is a millenium problem awarded \$1 million dollar for its solution (together with the proof that the theory has a mass gap $\Delta > 0$ and ‘‘chiral symmetry breaking’’) ¹ by the Clay Mathematics Institute. Due to ‘‘dimensional transmutation’’ the dimensionless running coupling constant is connected with a dimensionful mass scale Λ_{QCD} , an intrinsic scale of the theory. This mass scale sets the scale for the

¹<http://www.claymath.org/millennium-problems/yang%E2%80%93mills-and-mass-gap>

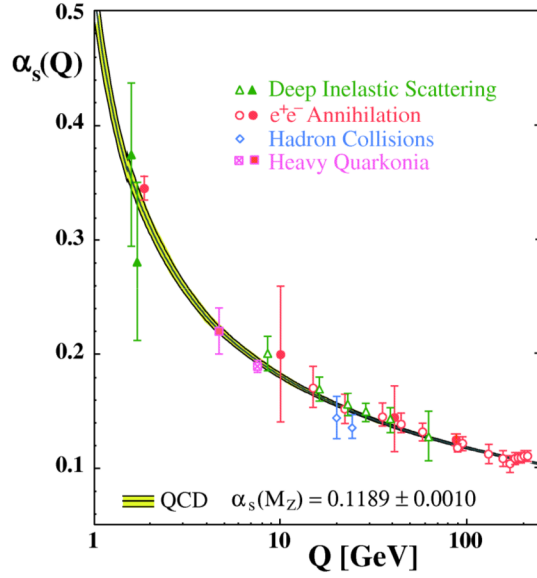


Figure 1.1: Running coupling from QCD compared to measurements. Taken from [Bet07].

validness of perturbative techniques. It is of the order of $\Lambda_{QCD} \sim 200$ MeV, which is the size of hadrons $\Lambda_{QCD}^{-1} \sim 1$ fm. For smaller momentum transfers, where a perturbative treatment of QCD is not applicable anymore one has to rely on effective theories or models. This is actually the scale of nuclear physics. In such theories the fundamental degrees of freedom, quarks and gluons, are integrated out into hadrons. The force carrier between baryons is then mediated by mesons. If the masses in Eq. (1.1) vanish then the Lagrangian is invariant under the chiral transformation $SU(3)_L \times SU(3)_R$, where L, R stand for left and right handedness of the fields (for three light quark flavors u,d,s). The left and right handed part of the fields can be projected out with the operator $P_{R/L} = \frac{1}{2}(1 \pm \gamma_5)$. This symmetry is also adopted for the low energy limit in the effective theories. According to Weinberg's proposal, one has to write down a Lagrangian which is fully consistent with all symmetry principles of QCD [Wei79] for the construction of effective theories. Chiral symmetry is broken spontaneously and explicitly. Explicitly, because the quarks have a finite mass. The spontaneous breakdown of the symmetry leads to the appearance of Goldstone bosons, which are identified with pions, kaons and the eta meson. Ideally, they would be massless by breaking a global symmetry according to Goldstone's theorem. The explicit symmetry breaking of QCD makes the Goldstone boson massive. The consequence of the spontaneous breakdown of chiral symmetry to the groundstate of QCD explains the mass of baryons. The mass term in Eq. (1.1) is for the bare mass of the quarks and of the order of 5-10 MeV due to the coupling to the Higgs field. But baryons containing quarks have masses of the order

of 1 GeV. If the chiral symmetry is broken the quarks propagate through a chiral condensate. This leads to quarks dressed by their interactions leading to an increase in mass which explains the mass of baryons. Since pions are approximate Goldstone bosons a large mass gap between them and other hadrons exists e.g. to the mass of the ρ meson. This separation of scales suggests an expansion in the two scales Q/Λ_χ where $Q \sim m_\pi$ and $\Lambda_\chi \sim m_\rho$ [ME11], where Λ_χ is the chiral-symmetry breaking scale. Another approach to solve Eq. (1.1) in the strongly coupled regime is a numerical treatment of the Lagrangian on a discrete (Euclidean) space-time lattice. This is the approach of lattice QCD. The grid is chosen with a finite spacing a . Observables calculated on this lattice are in the end extrapolated to the continuum by requiring $a \rightarrow 0$. An example of the outcome of such a calculation is shown in Fig. 1.2 [Lus03]. It displays the spectroscopy of hadrons from a lattice QCD calculation as black points and the experimental measurement as horizontal lines. They agree quite well. To summarize, at large momentum transfer QCD is a perturbative theory in terms of the strong coupling constant α_S , the relevant degrees of freedoms are quarks and gluons. For low energy, quarks and gluons are confined to hadrons. Thanks to a separation of scales QCD is in this energy regime an expansion in soft modes, set by the pion scale $Q \sim m_\pi$ over hard modes Λ_χ , a scale where the chiral symmetry breaks down.

QCD is also explored in its thermodynamical properties. Basically two phase transi-

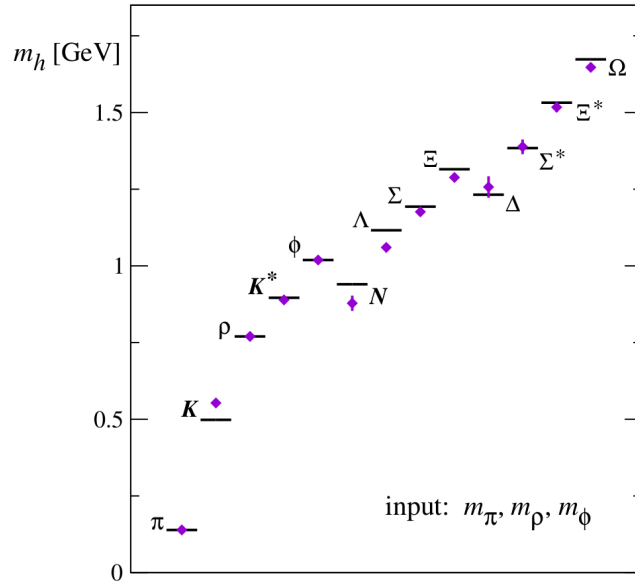


Figure 1.2: Comparison of predictions from lattice QCD (points) to experimental results (horizontal lines). Taken from [Lus03].

tions immediately catch the eye. Firstly, since QCD is an asymptotically free theory for large energies Q a phase separation between hadrons and free quarks and gluons seems

more than natural. Secondly, a feature of QCD at low energies is the spontaneously broken QCD vacuum, which leads to the generation of non-perturbative quark masses. Thus, if the system is heated up the quarks turn more and more into bare quarks and the symmetry is restored. The breakup into quarks and gluons happens around the intrinsic energy scale of QCD Λ_{QCD} . Thermodynamically, the system is governed by the matter equation of state (EoS). The EoS interrelates thermodynamic variables, which describe the system in the equilibrium state. To describe QCD matter the phases are explored in terms of the temperature T and chemical potential μ_B . The phase diagram of QCD matter is displayed in Fig. 1.3.

The phase diagram is explored experimentally by colliding two heavy ions at large energies. Facilities where experiments of this kind are conducted are the Large Hadron Collider (LHC) and the Relativistic Heavy Ion Collider (RHIC). The paradigm of such collisions is, that due to the high energy the nucleons inside the nuclei are melting into deconfined quarks and gluons during the collision and a quark gluon plasma state is formed. This state cools down and hadronizes. The final hadron spectra are studied e.g. for anisotropies in the azimuthal angle to constrain properties of the QGP like its viscosity. RHIC with its beam energy scan is also searching for the critical point in the phase diagram e.g. by indications of strong fluctuations of proton yields. Because of

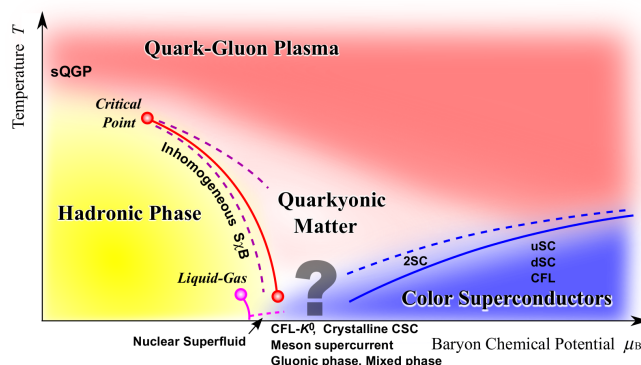


Figure 1.3: Phase diagram of QCD in terms of the temperature T and chemical potential μ_B . Taken from [FH11].

the non-Abelian nature of QCD, the phase diagram is quite rich in structures. For small chemical potentials $\mu_B \rightarrow 0$ and large temperatures $T \gg \Lambda_{QCD}$ quarks and gluons are deconfined. Keeping μ_B fixed and decreasing the temperature one ends in the hadron gas phase by a continuous cross over. The cross over temperature is of the order of $T_C = 170$ MeV. This result was actually obtained by lattice-QCD simulations, which uses as microscopic description the true QCD Lagrangian. Unfortunately, lattice-QCD suffers from a sign problem for finite chemical potentials and is for this reason hard to apply for finite baryon densities. Otherwise the whole phase diagram could be calculated by first principles. One has to rely on effective model calculations for the other regions.

At finite chemical potentials and temperatures the quark gluon and hadronic phase are separated by a phase boundary, which is of first order. The phase boundary is concluded with a critical point. At very large μ_B and moderate to low temperatures the quarks can be correlated in Cooper pairs. This actually leads to a superconducting phase of quarks in quark matter.

1.1 Neutron stars, equation of state, gravitational waves

In Fig. 1.3 the phase diagram of QCD matter is shown. Neutron stars are very heavy and compact objects and the temperature in the interior is rather low. This locates them on a very different area of the QCD phase diagram compared to heavy-ion experiments of LHC and RHIC and new insights into matter properties can be gained by studying this objects. Recently, very heavy neutron stars were observed, PSR J0348+0432 and PSR J1614–2230 [Dem+10; Ant+13], which have masses around twice the solar mass M_\odot . This actually sets very strict limits on the Equation of state for the neutron star matter and appears a challenge for nuclear physics to describe such heavy stars. First of all, it is interesting how the EoS is connected with the mass of the star. A relation of this kind was established by Tolman, Oppenheimer and Volkoff (TOV) [OV39; Tol39]. The TOV equation is derived for an isotropic matter distribution in hydrostatic equilibrium. The hydrostatic equilibrium ensures that the configuration is constant in time. This means that the matter inside the star counter balances its tendency to gravitationally collapse. The TOV equation reads:

$$\frac{dp}{dr} = -\frac{G\epsilon(r)m(r)}{c^2 r^2} \left(1 + \frac{p(r)}{\epsilon(r)}\right) \left(1 + \frac{4\pi r^3 p(r)}{m(r)c^2}\right) \left(1 - \frac{2Gm(r)}{c^2 r}\right)^{-1}, \quad (1.3)$$

where $p(r)$ is the pressure, $\epsilon(r)$ the energy density and $m(r)$ the mass:

$$\frac{dm}{dr} = 4\pi r^2 \epsilon(r). \quad (1.4)$$

A relativistic treatment of gravity is necessary because neutron stars are rather small objects. The Schwarzschild radius for a two solar mass object is:

$$r = \frac{2GM}{c^2} \approx 6 \text{ km}. \quad (1.5)$$

The neutron star radii are of the order of 10 km, so rather close to the Schwarzschild radius and close to a black hole configuration. Thus Newtonian mechanics is not a good approximation anymore. The coupled equations are solved by the input of the EoS $p(\epsilon)$. An example would be a polytropic equation of state, where the energy density is directly connected to the pressure:

$$p = K\epsilon^\gamma. \quad (1.6)$$

Such an EoS would be realized e.g. for pure neutron matter. The maximal reachable mass is around $M \approx 0.7M_\odot$ in this case. Thus, the Fermi pressure alone is able to counterbalance significantly the gravitational force. However, to reach a star mass of around two solar masses one can see the importance of interactions. An integration of the TOV equation with a polytropic EoS of Eq. (1.6) is performed to visualize the influence of the EoS to the neutron star properties. To do this the polytropic EoS is initialized with three different values of the constant K . The larger the K value becomes, the stronger the internal pressure grows with density. For the calculations an index $\gamma = 5/3$ is chosen, which is e.g. realized in a non-relativistic electron gas (without electromagnetic interactions). The geometrized unit system $G = c = 1$ is used for the calculation. In this units e.g. the mass of the sun is measured in km $M_\odot = 1.48$ km. To perform the calculations a form of the energy density of the neutron star matter is needed, which is deduced from the thermodynamic relation ($dQ = 0$):

$$dU = -pdV \rightarrow d\left(\frac{\epsilon}{\rho}\right) = -pd\left(\frac{1}{\rho}\right) \rightarrow \epsilon = \left(\frac{p}{K}\right)^{1/\gamma} + \frac{p}{\gamma - 1}, \quad (1.7)$$

where the integration constant was set to one (and the EoS (1.6) used). With the known energy density the mass of the star can be calculated. The calculation stops until the pressure turns negative because then gravity wins and the star collapses. This defines the maximum mass M and radius R of the star. In Fig. 1.4 the maximum mass versus the neutron star radius is shown. Also properties of the star in terms of the central ($r \rightarrow 0$) density ρ_c or pressure p_c are displayed (which are anyway connected via the EoS). One can see the expected behavior. The largest value of K produces the stiffest EoS (blue lines). This also means that the star can withstand longer the gravitational pressure until it collapses and more heavy stars can be described. The maximal masses of the stars is reached for central ($r \rightarrow 0$) densities around $\approx (1-2)\rho_0$ for this EoS. Also the energy density for the stiffest EoS is shown for the case of the largest mass configuration, which is around $2.7M_\odot$. It is largest in the centre of the star and decreases with increasing radius. This was an exercise to show how the EoS influences neutron star properties. This makes the neutron star an astrophysical laboratory for testing nuclear models. A possibility would be e.g. that the constant K is linked to some microscopic model and if K from this model is too small then the EoS is too soft to produce a two solar mass neutron star. This makes it highly unlikely that this model describes the interior of neutron stars. In the example of Eq. (1.6) the red EoS would be ruled out by the measurement. In general a microscopic model with all relevant degrees of freedom and interactions is constructed e.g. on the basis of mean field models [WCS12] or chiral effective field theories [Krü+13]. From this model the EoS is deduced and put to the TOV equation to get the mass radius relation of the star. Usually pure nucleonic models are able to describe heavy stars [HW14]. A EoS must have a pressure larger $p > 150 \frac{\text{MeV}}{\text{fm}^3}$ at around five times nuclear saturation density [HW14]. A problem appears mostly whenever hyperons are included in the models. The reason is that in such

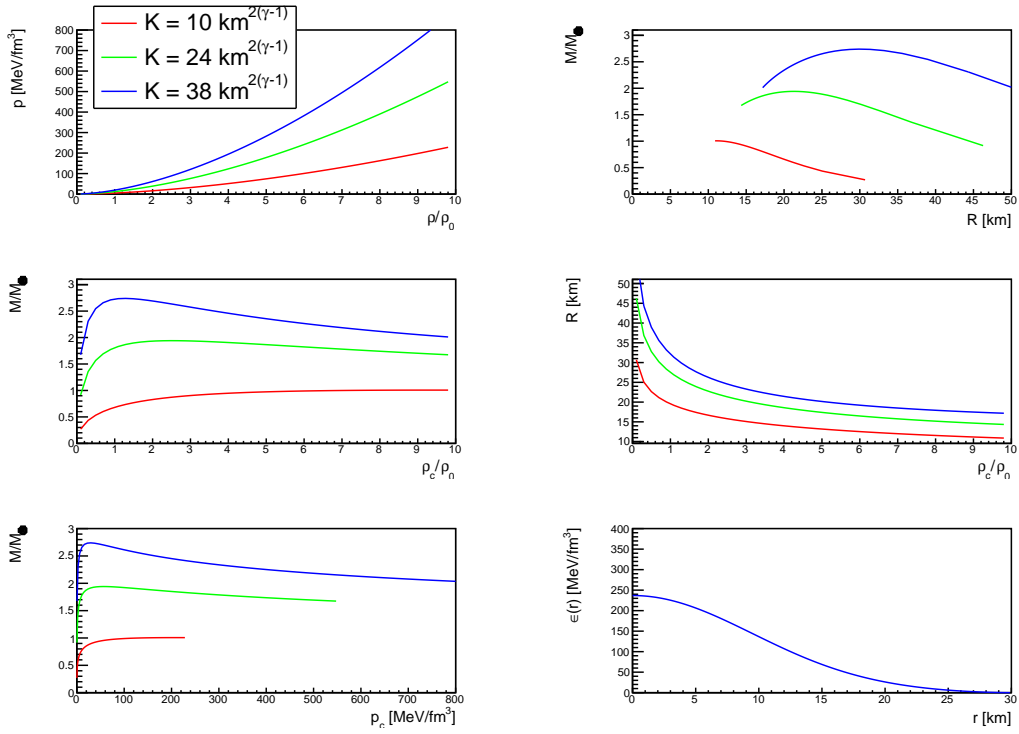


Figure 1.4: Neutron star properties for the EoS of Eq. (1.6) with $\gamma = 5/3$. The energy density $\epsilon(r)$ is calculated for the stiffest version of the EoS and the largest reachable neutron star mass.

models it is rather likely that at a certain threshold density hyperons are produced. This is achieved via decays of nucleons at the fermi surface and a new fermi sea is filled with hyperons. Thus the degrees of freedom are reshuffled via an exchange of fast nucleons to more heavy and slower hyperons. Without taking interactions into account the system cannot react in the same way to an external force like in the pure nucleonic case. Usually the EoS softens. The softening of the EoS is in most cases so strong that the two solar mass barrier cannot be reached anymore. This remains a puzzling situation that whenever hyperons are produced the EoS is too soft to describe heavy stars. Many attempts are made to overcome this puzzle or deliver other explanations of the star core [Cha+13]. Some of them are now discussed. A promising candidate to get stiffer EoS is the inclusion of three body forces among hyperons and nucleons. This was concluded by a Quantum Monte Carlo simulation [Lon+15]. In this calculation a two-body ΛN and a three body ΛNN are included additionally to two- and three-body forces among the nucleons. Two versions of ΛNN three-body forces were tested which were constrained to hypernuclei data and gave very similar results there. The outcome of the mass radius relation for this model is shown in Fig. 1.5. If one takes only two-body interactions into

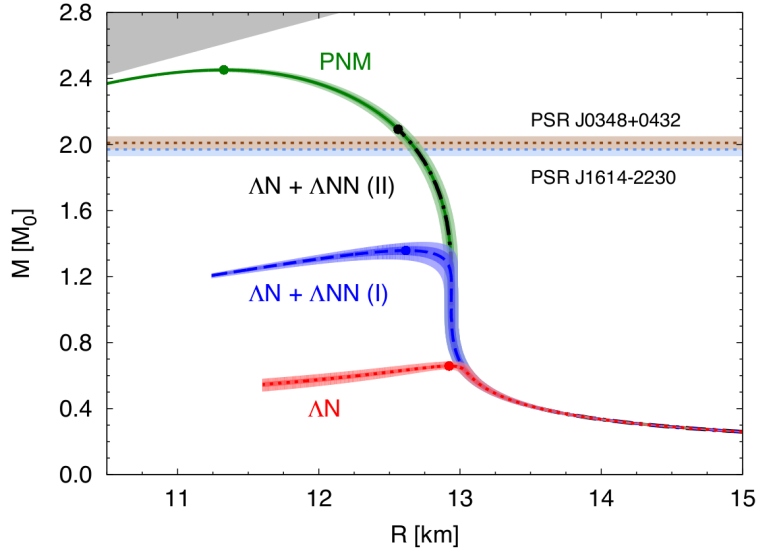


Figure 1.5: Results of a mass radius relation calculated on the basis of a Quantum Monte Carlo simulation [Lon+15]. The red curve shows only the inclusion of two-body forces whereas the other two curves include two different versions of three-body ΛNN interactions.

account then the EoS softens so strong that the maximal mass is of the order of $0.5M_{\odot}$. The inclusion of three body forces ΛNN stiffens the EoS and shifts the appearance of hyperons to larger densities. The two versions of the three-body force give significantly different results. For the blue curve hyperons appear at around 0.3fm^{-3} and the EoS is stiffer compared to the pure two-body case but not stiff enough to describe the two heavy stars. For the other version of the three-body force no hyperons appear for densities up to 0.56fm^{-3} . This configuration follows the line of pure nucleonic matter and is able to cross the threshold set by the measurements. Thus a solution of the hyperon puzzle might be that the three-body ΛNN force is so repulsive that hyperons don't appear in the density regime of neutron stars.

Another interesting approach comes from chiral effective field theory (EFT) and the study of the density dependence of the two-body ΛN force [Hai+17]. For this they use a G-matrix ansatz where they get out the single-particle Λ potential $U_{\Lambda}(p_{\Lambda}, \rho)$ at next-to-leading order expansion. The next-to-leading order result describes already quite accurately the $\Lambda/\Sigma p$ scattering [Hai+13]. The results of this calculation are shown in Fig. 1.6. The green band is the result of a NLO calculation and the red band includes also effects from a density dependent three-body ΛNN force. It is interesting to observe that around $(1.5-2.5)\rho_0$ the two-body interaction turns repulsive. As an implication such an outcome would shift the appearance of hyperons to larger densities. The reason behind this repulsion is understood by looking at the phaseshift of the Λp 3S_1 state and its cou-

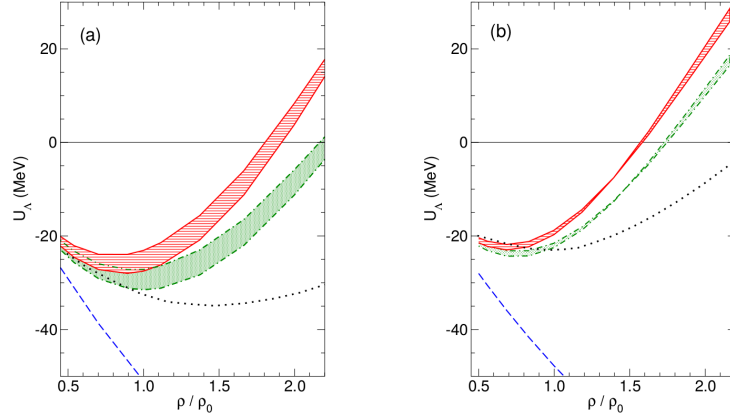


Figure 1.6: Single-particle potential $U_\Lambda(p_\Lambda = 0, \rho)$ for (a) nuclear matter and (b) neutron matter. The dashed dotted curve (green band) shows the result from NLO calculations and the red band includes also effects from a density dependent three-body ΛNN force. Taken from [Hai+17].

pling to the ΣN channel. This phase shift is shown on the left in Fig. 1.7 for three different models which all include couplings to the ΣN channel. All models show different influences of this channel coupling. In the right plot the coupling is switched off. One can see that then the NLO result turns more repulsive which suggests that the attraction in the full calculation comes from the coupling to the ΣN channel. From hypernuclei measurements it is argued that the coupling to ΣN is suppressed. This means that the more repulsive NLO phaseshifts on the right govern the interaction in a nuclear medium. For this reason the interaction turns repulsive at moderate densities. If this is true then it is important to include also such couplings in the calculations of neutron star masses. This might be also a reason why calculations which don't include such a coupling like the model based on Quantum Monte Carlo simulation discussed above might fail to reproduce large masses and have to introduce three body forces. Unfortunately, no phaseshift data is available to constrain the coupling to the ΣN channel. A question which remains is if other hyperons can take over the role of the Λ . Usually, the single-particle potentials define the ordering of the hyperon appearance in a dense system. Thus, the hyperons with the deepest potentials are produced first. If the Λ potential is repulsive at moderate densities potentials the one for Ξ might be still attractive such that they are produced instead of the Λ . The puzzle is still far away of being solved, but many new ideas in the “baryonic sector” might point to its solution.

Another idea is to leave the pure baryonic case and allow for the appearance of deconfined quarks and gluons in the interior of neutron stars. Such a matter configuration can usually cope with large star masses but has also problems of its own, which have to be overcome [Cha+13]. This option will not be discussed further. Another possibility is to

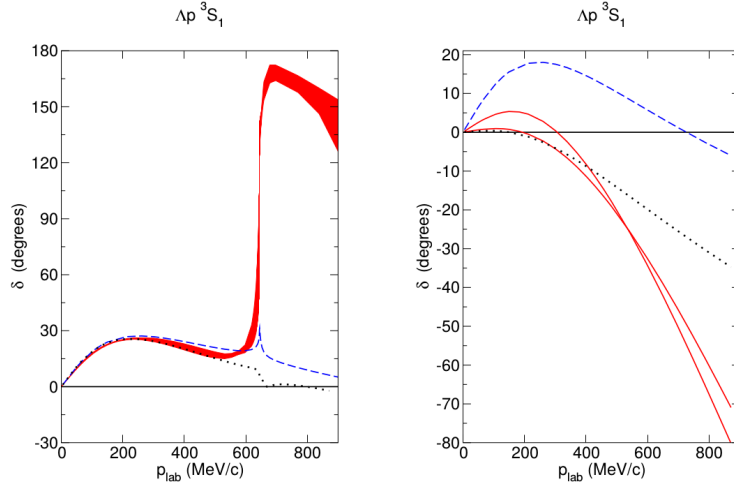


Figure 1.7: Phaseshift of the $\Lambda p \ ^3S_1$ state for the NLO model as well as Jülich '04 (blue dashed) and NSC97f (black dashed). Taken from [Hai+17].

relate both concepts since both of them have some complementarities. Hadronic matter compositions can describe quite compact stars but fail to produce large masses, whereas quark stars can produce large masses [DLP14]. According to the authors a star might accrete matter from a companion and hyperons form in the inner core of the star. If then droplets of strange quark matter builds up in the interior they might “decay” into a quark star because their gravitational mass is lower and thus energetically favored.

Whatever the solution of the hyperon puzzle might be new methods could help to constrain the parameter space further. A new epoch of understanding the evolution of the universe started recently with the finding of gravitational waves. According to Einsteins theory of general relativity a certain mass configuration e.g. two rotating stars can lead to distortions of the space-time which propagate at the speed of light and can be detected on earth. Recently, such gravitational waves were successfully measured by the LIGO Collaboration [Abb+16]. These waves stem from two spiraling black holes, which merged to one supermassive black hole and around $3M_{\odot}$ were radiated into gravitational waves. The question that arises is if there is a chance that the waveform or frequency of the gravitational wave can tell us something about the EoS of neutron stars if a binary neutron star system merges to on hypermassive neutron star. This question is adressed by simulations [Sek+11; Rad+16]. While neutron stars merge gravitational waves are emitted and the effects of different EoS on the gravitational waves are studied. According to [Sek+11] the frequency of gravitational waves for stars with a hyperon core increases (by around 20%) compared to stars with pure nucleonic cores. A different simulation suggested that gravitational waves from a merger with a hyperonic core have larger amplitudes [Rad+16] and the frequency is very similar for both possibilities. So there is

still some tension in the understanding and additional work needed. But the good news is that a difference seems to be present.

1.2 Hyperon-Nucleon interaction

The low energy data of the Λp scattering in vacuum comes from CERN Saclay 81-cm hydrogen bubble chamber experiments carried out in 1968 [Ale+68; Sec+68]. A K^-p system at rest was created with a beam of negative kaons to study reactions where the produced Λ scattered elastically on a proton. Following reactions were taken into account for the production of Λ which might scatter elastically on a proton:

$$\begin{aligned}
 i) & K^- + p \rightarrow \Lambda + \pi^0 \\
 ii) & K^- + p \rightarrow \Sigma^0 + \pi^0, \Sigma^0 \rightarrow \Lambda + \gamma \\
 iii) & K^- + p \rightarrow \Sigma^- + \pi^+, \Sigma^- + p \rightarrow \Lambda + n \\
 iv) & K^- + p \rightarrow \Sigma^- + \pi^+, \Sigma^- + p \rightarrow \Sigma^0 + n, \Sigma^0 \rightarrow \Lambda + \gamma
 \end{aligned}
 \tag{1.8}$$

The reaction ii) is the primary source of Λ (70%) [Sec+68]. This reaction delivers Λ in a momentum range between 90 to 250 MeV. For scattering processes closer to the production threshold reaction iv) is responsible for. It delivers Λ with momenta between 0 to 130 MeV. The photographs were scanned for different hypotheses. Fig. 1.8 shows a film which contains an elastic scattering event of Λp . The event fulfills two hypotheses: Λ originates at point B and decays at C. Λ originates at A and scatters at B. One can see on the film also the proton recoil. Around 100k Λ were measured and only 336 of them fulfilled the elastic scattering hypothesis and were processed further in a weighting procedure. From this data the total cross section was determined in six momentum intervals between 120 and 330 MeV [Sec+68]. In [Ale+68] as similar number of events was available for final analysis. Also there the total cross section was extracted in a very similar interval of 120 and 320 MeV in six intervals. In both analyses the scattering angle was rather isotropic in the considered energy range which suggests that the scattering is dominated by the S-wave contribution. These analyses resulted basically in twelve experimental data points in a momentum range ≈ 100 MeV away from the threshold. In another analysis which was performed around 1971 another 11 experimental data points at larger momenta between 300 and 1500 MeV were added to the total elastic cross section [Kad+71]. These data points are basically available to constrain models. Since there is data missing for $p_\Lambda \rightarrow 0$ the low energy scattering parameter cannot be precisely determined [GHM16]. There is also no phaseshift analysis possible, which would constrain the interaction quite significantly like in the NN case. A recent calculation on the basis of a chiral effective field theory expansion is displayed in Fig. 1.9 together with the measurements from the bubble chamber experiments. One can see that the leading

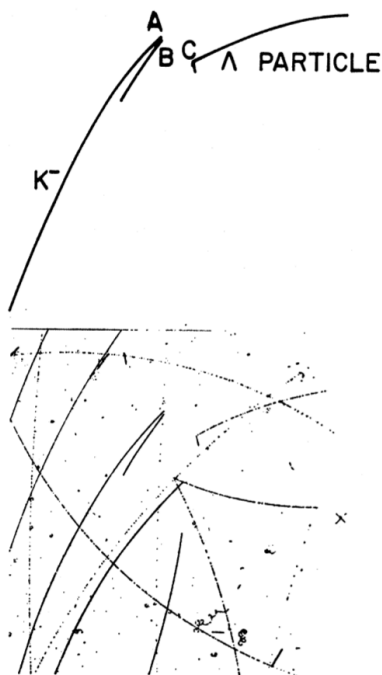


Figure 1.8: A film containing an elastic Λp scattering event. Taken from [Sec+68].

order (green band) expansion fails to reproduce data points in the region 300-800 MeV whereas the NLO expansion (red band) is in better agreement. Also for small momenta the LO expansion scratches only the lower boundary of the error bars. This lower cross section is naturally also reflected in different values for the scattering lengths [Hai+13]. Fig. 1.10 displays the phaseshift in the 1S_0 state from the same theoretical framework. The striking difference between LO and NLO phaseshifts is the much earlier turning of the phaseshift to a repulsive interaction around 600 MeV whereas the LO phaseshift is still positive. For the 3S_1 both calculations are much more in agreement for momenta up to 600 MeV. Thus, this repulsion in the 1S_0 state might be responsible for the smaller total cross section of the NLO prediction and is for this reason more in agreement with the data which seems to favor this repulsion. As explained above the more important phaseshift is the 3S_1 state because of the ΣN mixing. Any information in this direction would push the solution of the hyperon puzzle but phaseshifts for this baryon pair is experimentally hard to access. There are also some data points on the ΣN interaction but overall the experimental knowledge about the interaction strengths in the hyperon sector is quite scarce.

To describe the ΛN interaction in terms of Feynman diagrams one can start with considering the isospin of the involved constituents. The Λ is represented by an isospin singlet state $I = 0$. This means that the ΛN pair is represented in the isospin $I_{\Lambda N} = 1/2$ isospin state. This rules out the possibility that they interchange only one pion due to

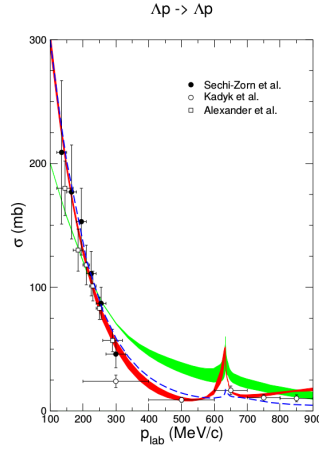


Figure 1.9: A comparison of the measurement of the elastic Λp cross section to calculations from an chiral effective field theory prediction. The green band is for the leading order expansion whereas the red band represents the next-to-leading-order expansion. Taken from [Hai+13].

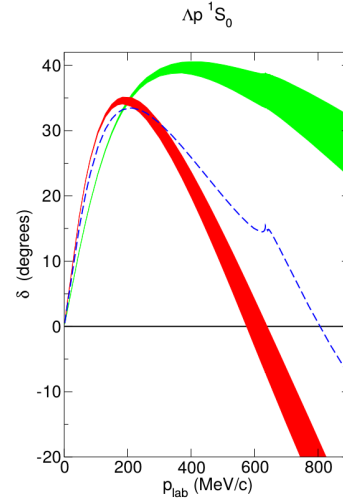


Figure 1.10: Phaseshift calculations from the effective field theory. No data points are available for elastic Λp scattering. Taken from [Hai+13].

the conservation of isospin in strong interactions. For the lowest order interaction involving pions already two pions must be exchanged. Quite interestingly, also a three body force ΛNN involves two pions, so one can speculate that the strength of the two and three body force is of similar order. To describe the interaction with only one meson exchange kaons are needed. Since they are more heavy than pions they might become relevant at shorter distances. The relevant Feynman diagrams for the interaction are displayed in Fig. 1.11. To model the interaction with a local interaction potential the

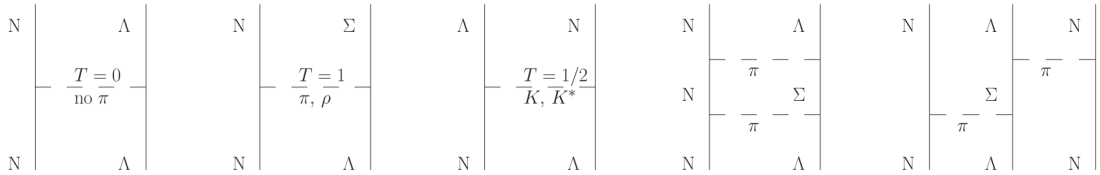


Figure 1.11: Feynman diagrams to describe the ΛN interaction. Taken from [GHM16].

following terms are considered [GHM16]:

$$V_{\Lambda N}(r) = V_0(r) + V_\sigma(r) \mathbf{s}_N \cdot \mathbf{s}_\Lambda + V_\Lambda(r) \mathbf{l}_{N\Lambda} \cdot \mathbf{s}_\Lambda + V_N(r) \mathbf{l}_{N\Lambda} \cdot \mathbf{s}_N + V_T(r) S_{12}, \quad (1.9)$$

where V_0 includes the central spin averaged part of the interaction, V_σ the spin-spin coupling which leads to different interaction strength in the singlet and triplet state, and the other terms are responsible for spin-orbit couplings. The last term models a tensor force. A realization of such a potential is the ‘‘Usmani’’ potential [BU88]. The form used to calculate correlation functions includes only the spin averaged and spin-spin part. It corresponds to the diagram of the two-pion exchange in Fig. 1.11:

$$V_{\Lambda N}(r) = V_{2\pi} = V_C - (\bar{V} - \frac{1}{4}\boldsymbol{\sigma}_\Lambda \cdot \boldsymbol{\sigma}_N)T_\pi^2, \quad (1.10)$$

where V_C is parametrized by a Woods-Saxon potential including a hard-core repulsion for small distances and T_π is the one-pion exchange tensor potential [BU88]. Since it is used in femtoscopy it is interesting to explore its properties in terms of phaseshifts. This is achieved by the solution of the Schrödinger equation with the potential above. The result is displayed in Fig. 1.12. The phaseshifts in Fig. 1.12 reflect the typical behaviour

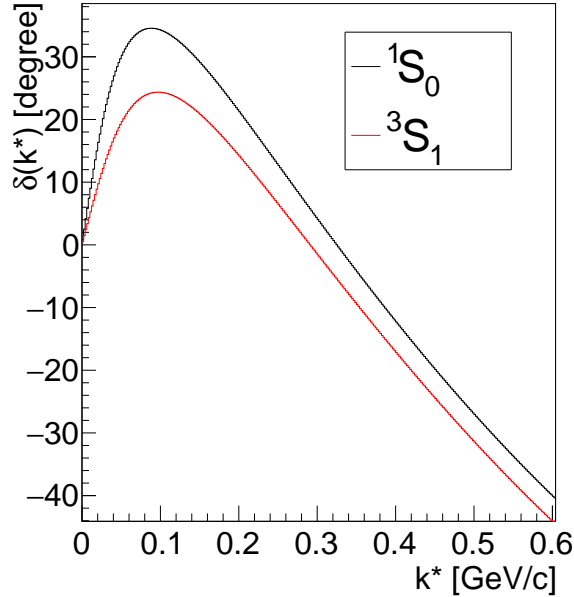


Figure 1.12: Phaseshift of Usmani potential of the form given in Eq. (1.10)

of the ΛN interaction. First of all the interaction in the s-wave channel is attractive at small momentum differences (which corresponds to small Λ laboratory momenta) and is weaker in the spin-triplet state compared to the spin-singlet configuration. The 3S_1 phaseshift does not contain any couplings to ΣN in Eq. (1.10). Thus it is less complex

than e.g. the phaseshift from NLO predictions displayed in Fig. 1.7. The phaseshifts turn negative where the resolution $\lambda \sim 1/k^*$ is large enough to resolve the hard-core repulsion present in this potential. It is also interesting to compare the strength of the ΛN to the NN interaction. The NN scattering length in the 1S_0 state are $a_{nn} = (-18.7 \pm 0.6)$ fm, $a_{pp} = (-17.1 \pm 0.2)$ fm (Coulomb corrected) and $a_{np} = (-23.715 \pm 0.015)$ fm [Pae14]. The scattering length for the Usmani potential in Eq. 1.10 for the singlet state is $a_{\Lambda p} = -2.66$ fm [WP99]. There is roughly a factor seven between these values. Thus, the interaction of ΛN is much weaker and does not support a ΛN bound state.

1.3 Motivation for this work

As we have seen, the Λp interaction is important to understand several physical systems. A hot topic is to find a way towards the solution of the hyperon puzzle in neutron stars. In the Section above it was shown how the experimental data for the ΛN interaction were collected with bubble chamber experiments at CERN. On the one hand side the data on the total cross section is rather scarce. On the other side, due to the fact that negative kaons and protons are studied at rest in these experiments the Λp momenta start roughly 100 MeV above the mass threshold. For this reason this project was started to explore possibilities to investigate Λp final state interactions with the femtoscopy technique. How femtoscopy exactly works will be explained later in this thesis. The advantage of femtoscopy is that it focuses on Λp pairs, which are very small in momenta. This is actually a complementary technique to scattering experiments. The goal is to study within this thesis how much statistics is needed to constrain the interaction at low momenta and to develop new techniques that may help to study also hyperon-nucleon interactions of other kinds like Ξp .

2

Basics of Femtoscopy

The pre-femtoscopy era was started in astronomy by measuring the (angular) size of stars by Hanbury Brown and R. Q. Twiss, who constructed a two-particle correlator using the principles of intensity interferometry. Their aim was to investigate possible correlations between photons emitted from an astronomical object [BT56; HT56]. In particle physics the method was independently established by Goldhaber *et al.* [Gol+60], which studied the production of pions in antiproton-proton reactions and had to introduce a symmetrization of the multiparticle wave function to describe the observed spectra. This (anti)symmetrization of the total wave function is a basic principle of quantum mechanics and influences particles which are located closely in phase-space. But not only quantum statistics influences the final spectra, also final state interactions can play a role e.g. if the particles are charged or if they are hadrons undergoing strong interactions. Femtoscopy normally focuses on the investigation of the size of the region the particles are emitted from, which happens on the Femtometer scale (10^{-15} m). Such studies help to understand the system properties in collisions of heavy-ions e.g. the collective behavior of the produced hadrons due to the underlying physics. But since femtoscopy is also based on final state interactions one can use the method to study strong final state interactions of pairs where not much is known about the interaction and scattering experiments are difficult to realize.

2.0.1 Mathematical framework

The two-particle correlation function is defined as a ratio of a coincidence yield $N(\mathbf{p}_1, \mathbf{p}_2)$, which describes the probability of finding a particle with a certain momentum \mathbf{p}_2 under

the condition that a second particle with momentum \mathbf{p}_1 was already emitted. This yield is compared to the product of the single-particle probabilities of finding such particles in an event separately [HJ99]:

$$C(\mathbf{p}_1, \mathbf{p}_2) = \frac{N(\mathbf{p}_1, \mathbf{p}_2)}{N(\mathbf{p}_1)N(\mathbf{p}_2)} = \frac{E_1 E_2 dN / (d^3 p_1 d^3 p_2)}{(E_1 dN / d^3 p_1)(E_2 dN / d^3 p_2)}. \quad (2.1)$$

We have kept the energies E_i in front of the yields to visualize that the equation is a Lorentz scalar thus invariant under transformations. One can see immediately in this equation that in absence of any correlations $N(\mathbf{p}_1, \mathbf{p}_2) = N(\mathbf{p}_1)N(\mathbf{p}_2)$ the correlation function is equal to unity, which serves as a baseline to check if correlations are present. The link of Eq. 2.1 to calculable quantities is described in the pioneering paper of S. Pratt for the case of having pions in the final state by starting from a quantum mechanical description using creation and destruction operators $c^\dagger(\mathbf{p})$, $c(\mathbf{p})$ acting on a vacuum state [Pra84]. A generalized equation valid for any pair reads [Lis+05]:

$$C(P, q) = \frac{\int d^4 x_a d^4 x_b s(p_a, x_a) s(p_b, x_b) |\psi(q, r^*)|^2}{\int d^4 x_a s(p_a, x_a) \int d^4 x_b s(p_b, x_b)}, \quad (2.2)$$

where $P = p_a + p_b$ denotes the total and q the relative 4-momentum of the pair. A short remark on the relative momentum of the pair. Our argumentations are based on [Lis+05] and here the relative momentum is defined as:

$$q^\mu = \frac{(p_a - p_b)^\mu}{2} - \frac{(p_a - p_b) \cdot P}{2P^2} P^\mu. \quad (2.3)$$

In this Equation the “reduced” relative momentum is used this means it is multiplied with $1/2$. The above Equation is equivalent to the momentum $k = k^* = \frac{1}{2} |\mathbf{p}_a^* - \mathbf{p}_b^*|$, where $\mathbf{p}_a^* + \mathbf{p}_b^* = 0$. Throughout this thesis we present all results in this “reduced” momentum basis. The functions $s(p_i, x_i)$, $i = 1, 2$ in Eq. (2.2) can be identified as single-particle emission functions containing the probability of emitting a particle with momentum $p_i = (E_i, \mathbf{p}_i)$ at the space-time point $x_i = (t_i, \mathbf{x}_i)$, $i = 1, 2$. The function $\psi(q, r^*)$ coincides at this stage with the Bethe-Salpeter amplitude [Led09], which depends explicitly on time. Eq. 2.2 can be further simplified by using the equal-time approximation, which states that particles are emitted simultaneously in the pair rest frame $t_1^* - t_2^* = 0$ (PRF: $\mathbf{P} = 0$) [Led09] valid if $|t^*| < m_{1,2} r^{*2}$ ¹. With this assumption the Bethe-Salpeter amplitude reduces to the stationary two-particle wave function $\psi(q, r^*) \rightarrow \psi(\mathbf{q}, \mathbf{r}^*)$ and any time integration does not act on $\psi(\mathbf{q}, \mathbf{r}^*)$ anymore. Other approximations used in femtoscopy are described in [Lis+05; Led09]. Using this approximations one gets:

$$C(\mathbf{P}, \mathbf{q}) = \int d^3 r^* |\psi(\mathbf{q}, \mathbf{r}^*)|^2 \int dt^* \mathcal{S}_{\mathbf{P}}(r^*), \quad (2.4)$$

¹For theoretical equations we denote variables evaluated in the PRF with an asterisk.

where the function $\mathcal{S}_{\mathbf{P}}(r^*)$ contains the distribution of the relative distances in the PRF. Introducing properly normalized single-particle emission functions $\tilde{s}(x_i, p_i), i = 1, 2$ one can write the two-particle emission function in Eq. (2.4) as:

$$\mathcal{S}_{\mathbf{P}}(r^*) = \int d^4x_a d^4x_b \tilde{s}(x_a, \bar{p}_a) \tilde{s}(x_b, \bar{p}_b) \delta(r^* - x_a + x_b). \quad (2.5)$$

In a statistical language $\mathcal{S}_{\mathbf{P}}(r^*)$ is a probability density function (p.d.f.) of the random variable $r^* = x_a - x_b$. It is constructed out of the single-particle p.d.f. $\tilde{s}(x_i, \bar{p}_i)$, which contain the individual production information of the particles and the delta-function accomplishes the transformation to the new p.d.f.. In Eq. (2.5) the momenta $\bar{p}_i = m_i/(m_1 + m_2)P$ are used, coming from the smoothness approximation, which says that femtoscopy takes place around the total momentum P and the difference between using \bar{p}_i instead of p_1, p_2 is negligible. The final source function containing the probability of emitting a pair with a certain separation \mathbf{r}^* is simply given by using the time integrated 4D emission function:

$$S_{\mathbf{P}}(\mathbf{r}^*) = \int dt^* \mathcal{S}_{\mathbf{P}}(r^*). \quad (2.6)$$

The source function in Eq. 2.6 contains the information how probable it is to emit a certain pair with a spatial difference \mathbf{r}^* . Since it corresponds to a probability, it is normalized to unity:

$$\int d^3r^* S_{\mathbf{P}}(\mathbf{r}^*) = 1. \quad (2.7)$$

The final equation used in femtoscopy is derived by plugging Eq. (2.6) into Eq. (2.4):

$$C(\mathbf{P}, \mathbf{q}) = \int d^3r^* |\psi(\mathbf{q}, \mathbf{r}^*)|^2 S_{\mathbf{P}}(\mathbf{r}^*). \quad (2.8)$$

One can see in Eq. (2.8) that basically two ingredients are needed to calculate the correlation function, the source function and the wave function. If the interaction is well understood e.g. in case of charged particles then the wave function is well known too and one can study in detail the source function. Since these two ingredients play an important role we will explore them further.

2.0.2 The source function

A basic ingredient of (2.8) is the source function. We will show how one can construct it using assumptions about the single-particle emitters. Assuming no explicit time and momentum dependence of the single-particle emitters and a spatial distribution following a Gaussian profile with width r_0 , one obtains for the single particle emitters:

$$s(x_a, \bar{p}_a) = \delta(t^*) \exp\left(-\frac{x^{*2} + y^{*2} + z^{*2}}{2r_0^2}\right). \quad (2.9)$$

This single-particle emitters have to be transformed to the relative distance variable \mathbf{r}^* :

$$\begin{aligned} S(\mathbf{r}^*) &\sim \int d^3x^* s(\mathbf{r}^* - \mathbf{x}^*) s(\mathbf{x}^*) = \int d^3x^* \exp\left(-\frac{(\mathbf{r}^* - \mathbf{x}^*)^2}{2r_0^2}\right) \exp\left(-\frac{\mathbf{x}^{*2}}{2r_0^2}\right) \\ &= \prod_{i=1}^3 \int dx_i^* \exp\left(-\frac{(\mathbf{r}_i^* - \mathbf{x}_i^*)^2}{2r_0^2}\right) \exp\left(-\frac{\mathbf{x}_i^{*2}}{2r_0^2}\right) = \prod_{i=1}^3 \sqrt{\pi} r_0 \exp\left(-\frac{\mathbf{r}_i^{*2}}{4r_0^2}\right). \end{aligned} \quad (2.10)$$

The normalization for the source function is given by:

$$\left(\int d^3x^* \exp\left(-\frac{\mathbf{r}_i^{*2}}{2r_0^2}\right) \right)^2 = (\sqrt{2\pi} r_0)^6. \quad (2.11)$$

This leads finally to the Gaussian two-particle source function very often used in femtoscopy:

$$S_G(\mathbf{r}^*) = \frac{\exp\left(-\frac{\mathbf{r}^{*2}}{4r_0^2}\right)}{(4\pi r_0^2)^{3/2}}. \quad (2.12)$$

By using Eq. (2.12) one measures basically the width r_0 of the single-particle emitters, which is the width of the production probability of the individual Gaussians. We have assumed that the width of the production probability is the same for both particles (i.e. the particles are identical). But one could also assume different width e.g. in case of non-identical particle pairs having different freeze-out conditions. This can be easily accomplished by making the substitution $r_0 \rightarrow (r_{0,1} + r_{0,2})/2$ in Eq. (2.12), where the width $r_{0,i}$ describes the width of particle i . We will use the Gaussian profile for analyzing the experimental data with one width parameter.

One could also analyze the data with a different assumption about the single-particle emission function. To explore this further we assume that the single-particle emission function has a Cauchy form and no correlations are present for the individual spatial dimensions. Then the single particle emission function reads:

$$s(x_a, \bar{p}_a) = \delta(t^*) \prod_{i=1}^3 \frac{1}{x_i^{*2} + (\frac{r_0}{2})^2}. \quad (2.13)$$

Repeating the same calculations as for the Gaussian source delivers for the the Cauchy-type single-particle emitter:

$$S_C(\mathbf{r}^*) = \left(\frac{r_0}{\pi}\right)^3 \prod_{i=1}^3 \frac{1}{x_i^{*2} + r_0^2}. \quad (2.14)$$

In Eq. (2.14) it is seen that the convolution of two Cauchy functions is again a Cauchy function, for every spatial coordinate in the PRF a separate function. Already at this stage the observation is that a different assumption about the form of the single-particle emitter can lead to completely different results, not only in how one treats the width of the emitters also in the emission process of the pairs itself. To explore the difference between a Gaussian and a Cauchy source further we analyze the source functions not in cartesian but in spherical coordinates. Since we are using functions of random variables we can use the transformation law for functions of random variables, which states that starting from n random variables $\mathbf{x} = (x_1, \dots, x_n)$ the function of new variables $a_i(\mathbf{x})$ is given by [Cow98]:

$$g(a_1, \dots, a_n) = f(x_1, \dots, x_n) |J|, \quad (2.15)$$

where $|J|$ is the absolute value of the Jacobian determinant. The Jacobian determinant for spherical coordinates is just $|J| = r^{*2} \sin(\Theta)$. This means the source function is in general given in spherical coordinates by:

$$S(r^*, \Theta, \varphi) = r^{*2} \sin(\Theta) S(r_x^*(r^*, \Theta, \varphi), r_y^*(r^*, \Theta, \varphi), r_z^*(r^*, \Theta, \varphi)). \quad (2.16)$$

Using this approach one gets for the two different source functions mentioned above:

$$\begin{aligned} S(r^*, \Theta, \varphi)_G &= r^{*2} \sin(\Theta) \frac{\exp\left(-\frac{r^{*2}}{4r_0^2}\right)}{(4\pi r_0^2)^{3/2}}, \\ S(r^*, \Theta, \varphi)_C &= \left(\frac{r_0}{\pi}\right)^3 \frac{r^{*2} \sin(\Theta)}{(r^* \sin(\Theta) \cos(\varphi))^2 + r_0^2} \frac{1}{(r^* \sin(\Theta) \sin(\varphi))^2 + r_0^2} \frac{1}{(r^* \cos(\Theta))^2 + r_0^2}. \end{aligned} \quad (2.17)$$

The transformed source functions in Eq. (2.17) are still three dimensional objects depending now on two angles and the radial distance between the pairs. To investigate the properties further it is useful to build the marginal p.d.f. by integrating out two of the three variables. For the Gaussian case this is straightforward, for the Cauchy source this is analytically challenging. For this reason we could either perform the integration numerically or do a small Monte Carlo simulation. We checked both methods and present the Monte Carlo study. We simulated single-particle random variables distributed according to a Gaussian and a Cauchy profile both having a width of $r_0 = 1.5$ fm and calculated the relative distance and the corresponding angles for both choices. The results are displayed in Fig. 2.1. One can see in Fig. 2.1 that the choice of the single-particle emitters has a highly non-trivial influence on the emission of pairs, the most dramatic difference is seen in the angle projections. The Gaussian φ distribution is completely flat whereas the Cauchy one predicts certain peaks. The same is true in the Θ projection, where the Gaussian distribution follows the $\sin(\Theta)$ curve coming from the Jacobian

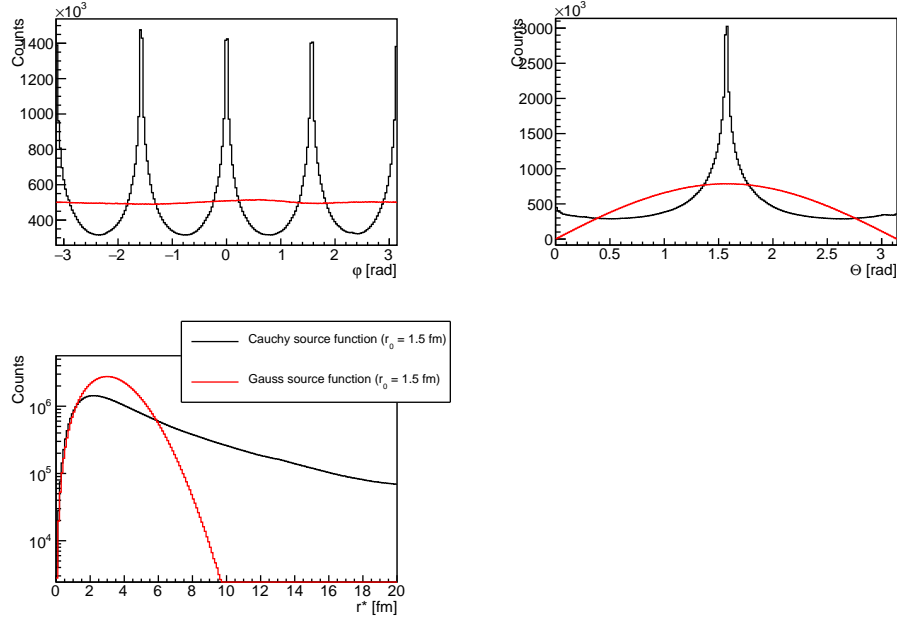


Figure 2.1: Projections of the source functions on r^* , Θ and φ . The red distribution corresponds to a Gaussian and the black to a Cauchy source choice. See text for more details.

whereas the Cauchy curve shows a clustering of pairs around $\pi/2$. In the radial difference the pairs of a Cauchy source are much wider distributed. Such a different choice of source functions would also result in a difference in the correlation function because the Cauchy source emits particles in certain preferred directions. Thus it is not only the radial direction which is affected by a different choice of single-particle emitters, the whole source function behaves differently. Which kind of source is finally realized has to be checked with experimental data. We calculated for the two different source choices a Bose-Einstein correlation function (introduced in next subsection) as would be the case for identical pion pairs. The result is displayed in Fig. 2.2. For comparison we calculated also the correlation function if one neglect the angle correlations of the cauchy source. One can see that the correlation function looks quite different for the same source size.

2.0.3 Typical correlation functions

In this section all possible femtoscopic sources of correlations and their implications on the correlation function are discussed. Eq. (2.8) represents the main femtoscopy equation and also our starting point. Since we have also seen in Eq. (2.7) that the source function is normalized to unity, we can rewrite Eq. (2.8) by subtracting from the corre-

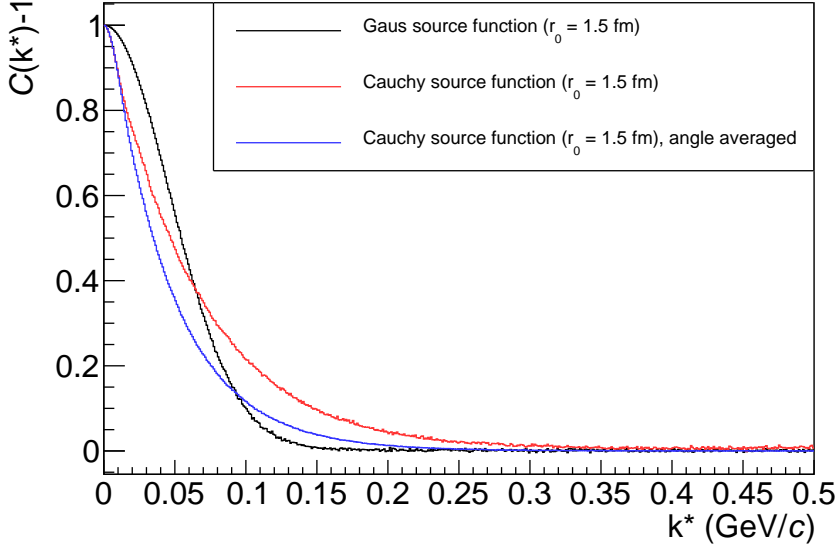


Figure 2.2: Bose-Einstein correlation function for a source size of $r_0=1.5$ fm calculated for single-particle emitters having a Gaussian and Cauchy shape. The influence on the correlation function is significant. For comparison also the correlation function obtained neglecting the typical angular behavior included in a Cauchy source function is displayed.

lation function the flat baseline:

$$R(\mathbf{P}, \mathbf{q}) = C(\mathbf{P}, \mathbf{q}) - 1 = \int d^3r^* (|\psi(\mathbf{q}, \mathbf{r}^*)|^2 - 1) S_{\mathbf{P}}(\mathbf{r}^*) = \int d^3r^* K(\mathbf{q}, \mathbf{r}^*) S_{\mathbf{P}}(\mathbf{r}^*), \quad (2.18)$$

where $R(\mathbf{P}, \mathbf{q})$ is just the correlation signal. Assuming that the source function shows no additional angle dependence (like for a Gaussian source) one can write:

$$R(\mathbf{P}, \mathbf{q}) = \int dr^* K(q, r^*) S_{\mathbf{P}}(\mathbf{r}^*). \quad (2.19)$$

and $K(q, r^*) = 2\pi r^{*2} \int_{-1}^1 d \cos(\Theta) (|\psi(\mathbf{q}, \mathbf{r}^*)|^2 - 1)$ can be interpreted as integral kernel. The specific representation of the kernel depends on the pair interaction. The femtoscopy Eq. (2.19) reads like an operator equation, where a specific kernel is acting on the source function. For a given momentum \mathbf{q} it takes all possible \mathbf{r}^* pairs and maps them onto a $R(\mathbf{q})$ value. If the kernel would have an inverse one would have an access

to the source function directly without making any assumption on the functional form. We don't want to go into detail, examples of this technique of source imaging can be found in [BD98; BD01].

Quantum statistics

A basic correlation signal which is widely used to study the source properties is based on quantum statistics. If one has identical particles in a pair the total wave function must be (anti)symmetrized depending if the particles are fermions or bosons. For two identical bosons described by a plane wave the kernel reads:

$$K(q, r^*) = 2\pi r^* \frac{\sin(2qr^*)}{q}. \quad (2.20)$$

For this case the kernel has the form that Eq. (2.18) acts as a Fourier transform of the source function. The width of the source function σ_{r^*} is then inversely related to the width of the measured correlation signal $\sigma_r^* \sim \sigma_q^{-1}$. Fig 2.3 shows the kernel for two identical bosons and Fig 2.4 the resulting correlation function for two different source sizes.

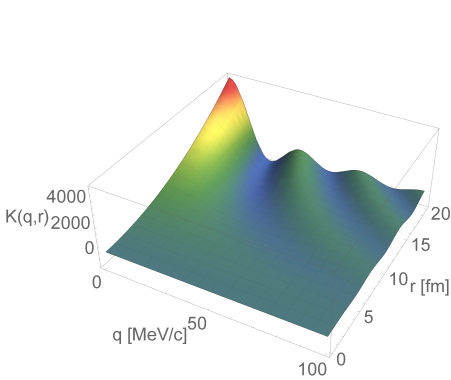


Figure 2.3: Kernel for two identical bosons.

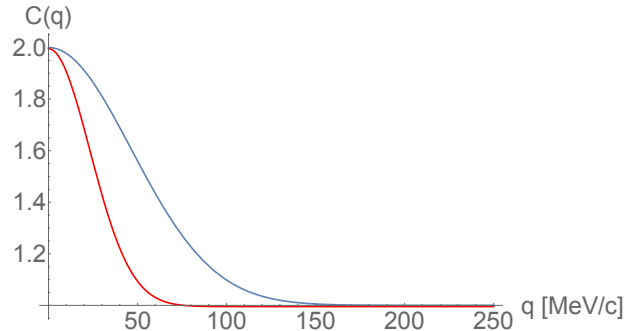


Figure 2.4: Correlation function for two identical bosons. The blue line is the quantum statistics correlation function for a Gaussian source size of $r_0 = 1.5$ fm and the red one for a source size of $r_0 = 3$ fm.

2.0.4 Coulomb interaction

The asymptotic form $r^* \rightarrow \infty$ of the wave function for the Coulomb potential can be derived [Lis+05; MM09; HJ99]. Since the static Coulomb potential decays like r^{*-1}

even at infinity the potential strength cannot be neglected. The kernel in this case reads:

$$K(q, r^*) = 2\pi r^{*2} \int_{-1}^1 d \cos(\Theta) G(\mathbf{q}) \left(\left| {}_1F_1\left(-i\frac{\eta}{q}; 1; iqr^*(1 - \cos(\Theta))\right) \right|^2 - 1 \right), \quad (2.21)$$

where $G(\mathbf{q})$ is the Gamov factor which is the probability of finding a pair at zero spatial separation $|\psi(\mathbf{r}^* \rightarrow 0)|^2$, ${}_1F_1(a; b; z)$ is a hypergeometric function defined via a series expansion and η is the Bohr radius ($\eta_\pi = 388 \text{ fm}^{-1}$ for pions) [MM09]. Fig 2.5 shows the kernel for two identical charged pions (neglecting quantum statistics) and Fig 2.6 the resulting correlation function for two different source sizes. Also only the Gamov factor is plotted for comparison to demonstrate that this factor dominates the Coulomb correlation function.

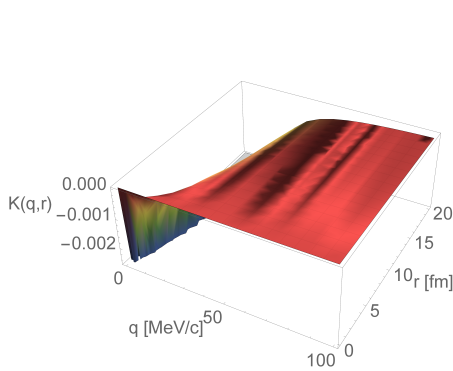


Figure 2.5: Kernel of the Coulomb interaction.

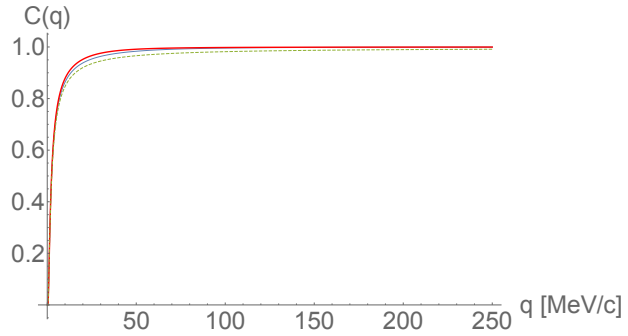


Figure 2.6: Coulomb correlation function. The green dashed line shows just the Gamov factor. The blue line is the Coulomb correlation function for a Gaussian source size of $r_0 = 1.5 \text{ fm}$ and the red one for a source size of $r_0 = 3 \text{ fm}$.

2.0.5 Strong interaction and the Lednicky model

Since we are mostly interested in the study of strong final state interactions we will spend some effort to explain how a model is constructed with which such correlations are modeled. For non-identical uncharged particles the asymptotic solution of the wave function for the scattering problem can be written as [Daw78]:

$$\psi(\mathbf{q}, \mathbf{r}^*) = \exp(-i\mathbf{q} \cdot \mathbf{r}^*) + \phi(q, r^*), \quad (2.22)$$

where we have adopted the convention in femtoscopy $\mathbf{q} \rightarrow -\mathbf{q}$ (which is related to time reversal). The total wave function of the scattering problem can thus be divided

in a plane wave and a scattered wave ϕ . In a scattering experiment one would measure only the scattered part of the wave function with a detector in the asymptotic region, which is related to the cross section $d\sigma = |r^*\phi(q, r^*)|^2 d\Omega$. However, in femtoscopy one measures not only the scattered part of the wave function but the absolute square of it. This means also interference effects between the plane and the scattered part of the wave function play a role. A derivation of a model for strong interactions for a source function with a finite lifetime was first done by Lednický and Lyuboshits [LL82]. We will show the steps starting from a Gaussian source of the form given in Eq. (2.12). First the scattered wave can be written in the asymptotic region as an outgoing spherical wave modified by the scattering amplitude:

$$\phi(q, r^*) = f(\Theta) \frac{\exp(iqr^*)}{r^*}, \quad (2.23)$$

where $f(\Theta)$ is the scattering amplitude containing all the information about the interaction. It can be written as [LL79]:

$$f(\Theta) = (q \cot(\delta(q)) - iq)^{-1} \approx \left(f_0^{-1} + \frac{1}{2} d_0 q^2 - iq \right)^{-1}, \quad (2.24)$$

where $\delta(q)$ is the phaseshift between an undistorted and a scattered wave. Additionally, we have adopted the effective range expansion, valid for momenta q around the production threshold of the pair. The effective range expansion introduces two new parameters, the scattering length $f_0 = \lim_{q \rightarrow 0} f(\Theta)$ and the effective range of the potential d_0 . We have used the sign convention in femtoscopy that an attractive potential leads to a positive scattering length $f_0 > 0$. The square of the total wave function leads basically to three contributions:

$$|\psi(\mathbf{q}, \mathbf{r}^*)|^2 = |\exp(-i\mathbf{q} \cdot \mathbf{r}^*) + \phi(q, r^*)|^2 = \underbrace{1}_{\text{plane wave}} + \underbrace{|\phi(q, r^*)|^2}_{\text{scattered wave}} + \underbrace{2\Re(\exp(-i\mathbf{q} \cdot \mathbf{r}^*)\phi(q, r^*)^*)}_{\text{interference}} \quad (2.25)$$

Contrary to a scattering experiment, where one counts the number of interactions and is thus sensitive to the scattered wave one needs in femtoscopy the full wave function. This leads to the kernel:

$$K(q, r^*) = 4\pi r^* \left(2\Re\phi(q, r^*) \frac{\sin(qr^*)}{q} + r^* |\phi(q, r^*)|^2 \right), \quad (2.26)$$

where the real part of the scattered wave function is:

$$\Re\phi(q, r^*) = \frac{1}{r^*} (\Re f(\Theta) \cos(qr^*) - \Im f(\Theta) \sin(qr^*)). \quad (2.27)$$

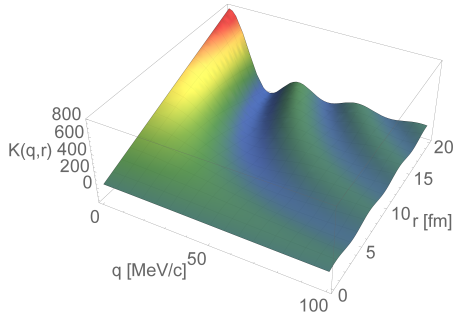


Figure 2.7: Kernel of the strong interaction.

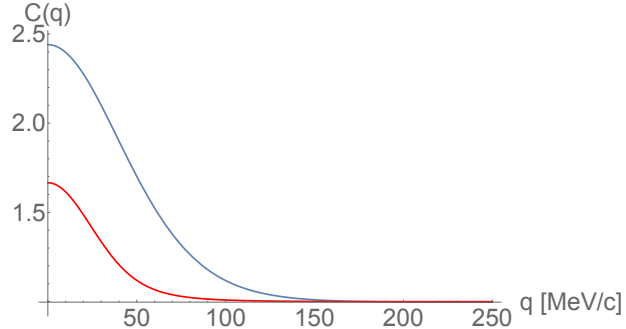


Figure 2.8: Strong interaction correlation function. The blue line is the strong interaction correlation function for a Gaussian source size of $r_0 = 1.5$ fm and the red one for a source size of $r_0 = 3$ fm. They were calculated using $f_0 = 1.5$ fm, $d_0 = 2$ fm.

Fig 2.7 shows the kernel for the strong interaction and Fig 2.8 the resulting correlation function ($f_0 = 1.5$ fm, $d_0 = 2$ fm).

To obtain the Lednicky model the averaging over the kernel has to be performed with a source function. The non-trivial averaging with the Gaussian source function of Eq. (2.12) appears for the interference terms between the scattered and the plane wave:

$$\begin{aligned}
8\pi\Re f(\Theta) \int_0^\infty dr^* \frac{\cos(qr^*) \sin(qr^*) \exp(-r^{*2}/4r_0^2)}{q (4\pi r_0^2)^{3/2}} &\equiv 2 \frac{\Re f(\Theta)}{\sqrt{\pi} r_0} F_1(2qr_0), \\
8\pi\Im f(\Theta) \int_0^\infty dr^* \frac{\sin^2(qr^*) \exp(-r^{*2}/4r_0^2)}{q (4\pi r_0^2)^{3/2}} &\equiv \frac{\Im f(\Theta)}{r_0} F_2(2qr_0),
\end{aligned} \tag{2.28}$$

where the functions $F_1(z) = D_+(z)/z$ and $F_2(z) = (1 - \exp(-z^2))/z$ are introduced and $D_+(z) = \exp(-z^2) \int_0^z dt \exp(t^2)$ is the Dawson function. To perform the integration the incoming plane wave was aligned with the z-component of \mathbf{r}^* . Two aspects have to be discussed before writing down the full model. First, for a pair of fermions the interactions usually depend on the total spin state of the pair. For this reason two interaction kernels are introduced weighted by a factor ρ_S ($S = 0, 1$). For an unpolarized emission of the pair the factor is $\rho_0 = 1/4$, $\rho_1 = 3/4$. The second aspect deals with the form of the wave function in Eq. (2.22) and will be discussed now in more details. Usually in a scattering experiment one measures the pairs with a detector in the asymptotic region $r^* \rightarrow \infty$ and thus is only sensitive to properties of the wave function in its asymptotic form. The asymptotic form of a scattering wave function deviates from the free one just by a shift in phase δ_l . In femtoscopy one integrates the square of the wave function over

a source function according to Eq. (2.8). Thus pairs are also produced in a spatial range, where the short range nuclear interaction potential is non-zero $V(r^*) \neq 0$. In this region the wave function deviates strongly from its asymptotic form. This has an influence on the correlation function as will be discussed. We can define an angle average source function which contains also the Jacobian determinant as:

$$\bar{S}(r^*) = 4\pi r^{*2} S(\mathbf{r}^*), \quad (2.29)$$

where it was assumed that the source function does not include any angle dependence. The wave function square is weighted with this source function. In Fig. 2.9 this function is displayed for a Gaussian source function having a size of $r_0 = 1.5$ fm together with a typical nuclear short range potential. The two shaded areas show that a fraction of pairs is produced within the range of the nuclear potential. In this region the asymptotic form of the wave function breaks down. When the breakdown exactly happens depends on the energy of the pair $E = \frac{\hbar^2 q^2}{2\mu}$. The “first part” of the Lednicky model is calculated with

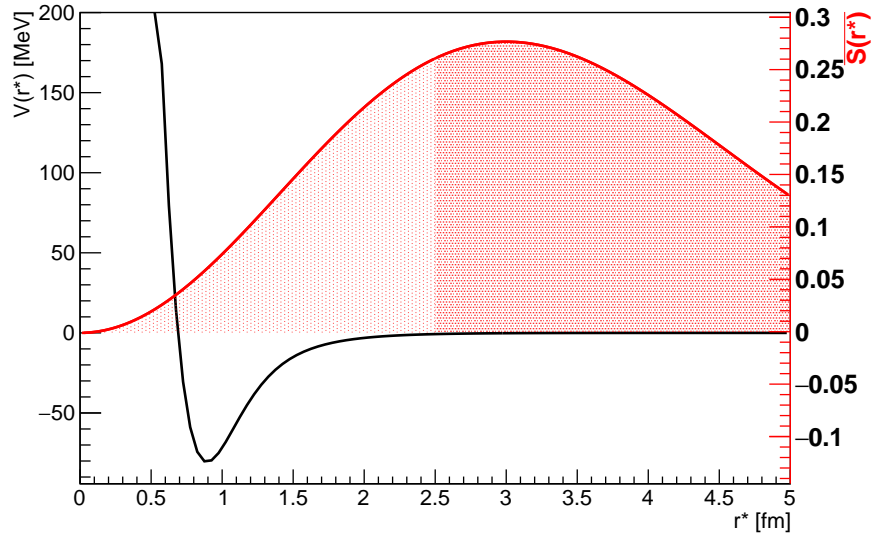


Figure 2.9: The black function represents a typical short range nuclear potential and the red function corresponds to a pair distribution according to Eq. (2.29) for $r_0 = 1.5$ fm. A fraction of pairs is produced within the range of the potential and the rest in a region where it vanishes. This plot demonstrates that at some point the assumption of the asymptotic form of the wave function breaks down if the potential strength becomes non-negligible.

the assumption that the form of the wave function is applicable everywhere, also within

the range of the nuclear potential. This can be explicitly seen in Eq. (2.28) where the integration starts at zero. To correct for this effect, a subtraction has to be performed, otherwise one would overestimate the correlation function since the amplitude of the pair wave function within the nuclear potential is smaller than unity. Lednicky introduced in his model a term, which takes exactly this correction into account. It has the form [LL82]:

$$\Delta C(q) = 4\pi S(r^* = 0) |f(q)|^2 \frac{d}{dq^2} f(q)^{-1} = \frac{d_0 |f(q)|^2}{4\sqrt{\pi} r_0^3}, \quad (2.30)$$

where d_0 is the effective range of the interaction. A sketch of the derivation of this term can be also found in [BGJ90]. It is actually based on arguments of the effective range theory which was developed by H. Bethe [Bet49]. The correction term is evaluated at zero pair separation $S(r^* = 0)$ and depends on the details of the interaction via d_0 . This formula is also only an approximation to the problem and might break down for small source sizes. The whole Lednicky model is then the sum of the correlation function with the asymptotic form of the wave function and the correction term for pairs which are produced within the range of the interaction:

$$C(q)_{\text{Lednicky}} = C(q)_{\text{asymptotic wave function}} - \Delta C(q). \quad (2.31)$$

The total Lednicky model including the correction term reads [LL82]:

$$C(q) = 1 + \sum_S \rho_S \left| \frac{f(\Theta)^S}{r_0} \right|^2 \left(1 - \frac{d_0^S}{2\sqrt{\pi} r_0} \right) + \frac{2\Re(f(\Theta)^S)}{\sqrt{\pi} r_0} F_1(2qr_0) - \frac{\Im(f(\Theta)^S)}{r_0} F_2(2qr_0). \quad (2.32)$$

This model is valid for non-identical pairs without Coulomb interaction. If a dominant fraction of pairs is produced within the range of the interaction potential then at some point one could be also sensitive to the detailed structure of the interaction potential itself. This possibility was investigated theoretically in [Gmi+86] for $p-p$ pairs. An experimental study of this kind for $p-p$ pairs produced in $e+A$ collisions was performed in [Sta+04]. A dependency on the chosen interaction potential showed up for a RMS value of the Gaussian source size of $r_{\text{rms}} < 2$ fm ($r_0 = r_{\text{rms}}/\sqrt{3}$). The source size of pp collisions might be larger than in a $e+A$ system. Since a dependence on the chosen potential or better said the effect of the smallness of the source was never studied for $p-\Lambda$ pairs, an exploratory investigation is performed here. A short comment why the correlation function could depend on the chosen potential. The spatial resolution of the pair is given by the wavelength $\lambda \sim q^{-1}$. Any structure smaller than this wavelength cannot be resolved. This means that if the wavelength is small enough, details of the potential become visible. Since $q \rightarrow 0$ in femtoscopy, the wavelength is quite large and the effective range expansion of the scattering amplitude becomes possible.

In an usual scattering experiment at $q \rightarrow 0$ one would never have enough resolution to observe details of the underlying short-range interaction, because of the just mentioned arguments. This means that the exact functional form of the potentials is unimportant as long as they predict the same scattering parameters. In femtoscopy the situation is a bit different. The effective range expansion is used because of $q \rightarrow 0$, but if many pairs are produced at small separations (small source size), a sensitivity on the potential could be visible due to the fact that the wave function deviates strongly from the asymptotic form. For small sources more weight is given exactly to these deviations. This is the advantage compared to scattering experiments. In a scattering experiment one would need energies > 250 MeV to observe e.g. the onset of the hard-core potential in the 1S_0 state for nucleon pairs, where the phaseshift turns negative [WSS95].

The first approach to study effects of small sources is based on the finite size of the emitted hadrons. It was shown in theoretical studies e.g. [WFH99] that it makes no difference if the emitted particles are emitted as plane waves or wave packages. The final radius is then just a measure of the size of the source and the size of the wave packages, which is indistinguishable in an experimental measurement. Thus the finite size of hadrons itself described as wave packages plays actually no role. But it might be that the finite size has an influence on the emission of pairs. This is discussed e.g. in [BFZ15] and a similar line of thought is applied for p - Λ . The two hadrons can at some point overlap. It is then hard to speak of two distinct hadrons anymore. This influences the source function since it is usually described as a convolution of two independent particle emitters $s(x_a), s(x_b)$. The independence might break down if the emitters are close to each other. To take this into account a new function $D(x_a - x_b)$ is introduced, which suppresses the emission of pairs at some point thus depends only on the relative distance of the two emitters. One has to perform the substitution:

$$s(x_a)s(x_b)\delta(r - x_a + x_b) \rightarrow s(x_a)s(x_b)D(x_a - x_b)\delta(r - x_a + x_b). \quad (2.33)$$

The functional form of $D(x_a - x_b)$ is chosen to be a Gaussian form:

$$D(x_a - x_b) = 1 - \exp(-(x_a - x_b)^2/4R^2), \quad (2.34)$$

where the parameter R is a length scale at which finite size effects of the hadrons may play a role and the independent emission breaks down. The new normalized source function reads:

$$S(r^*)_{\text{small}} = \frac{1}{8\pi^{3/2}} \frac{1}{r_0^3 - \sigma^3} D(r^*) \exp(-r^{*2}/4r_0^2), \quad (2.35)$$

where a combined length scale was introduced: $\sigma = (R^{-2} + r_0^{-2})^{-1/2}$. Since deviations should show up at small R , a Taylor expansion might lead to more insights into the problem. If doing so one gets as result to first order in R around zero:

$$S(r^*)_{\text{small}} \approx S(r^*)_{\text{Gauss}} D(r^*), \quad (2.36)$$

where $S(r^*)_{\text{Gauss}}$ is the “standard” Gaussian source function. Since the function $D(r^*)$ is also parametrized with a Gaussian form one can solve the integrals for the correlation function analytically. Additionally, because of the form of Eq. (2.34) and (2.36) one can see immediately that the new correlation function results in the Lednicky model and an additional term due to the overlap of the two hadrons:

$$C(q)_{\text{small}} = C(q)_{\text{Lednicky}} - C(q)_{\text{overlap}} . \quad (2.37)$$

By defining a parameter $\xi \equiv \sigma^3/r_0^3 \in [0, 1]$, which measures the “smallness” of a system. The overlap term has the form of the Lednicky Equation since the new source function is again Gaussian. The same calculation steps as shown above are applied and the result for the overlap correlation function in Eq. (2.37) reads:

$$C(q)_{\text{overlap}} = \xi \left(1 + \frac{1}{2} \left| \frac{f(q)}{\sigma} \right|^2 + \frac{2\Re f(q)}{\sqrt{\pi}\sigma} F_1(2q\sigma) - \frac{\Im f(q)}{\sigma} F_2(2q\sigma) \right) . \quad (2.38)$$

In principle one is able to quantify the effect of a small source at this stage. However, there are basically two remarks which have to be made. First of all, the usual correction term in Eq. (2.30) is evaluated at $S(r^* = 0)$. But at $r^* = 0$ there are no pairs produced anymore with the new source parametrization of Eq. (2.36). Thus, this correction term of Eq. (2.30) is zero. Instead the source function is now taking over this job by suppressing the production of pairs at low distances and thus suppresses the correlation strength as can be seen in Eq. (2.37). One can say that the correction for pairs inside the range of the nuclear potential is reshuffled. Either one neglects the finite size of the hadrons and corrects for the form of the wave function with Eq. (2.30) or one takes always the asymptotic form of the wave function and suppresses the emission of pairs at small separations and gets a new correction term with Eq. (2.38). The size of the corrections is very similar. A completely consistent model would include a suppression of the production of pairs at low separations and a correction for the non-asymptotic form of the wave function in a consistent way. For this reason another path was chosen to quantify the effect of the smallness of a source.

The second approach to study effects of small sources is based on a comparison of the correlation function when the wave function is calculated with the Schrödinger Equation and the Lednicky model. Lets have a look again on Eq. (2.8). In this equation the wave function serves as a weight for the produced pairs. If it is calculated with the Schrödinger equation including a realistic interaction potential, then the wave function includes automatically a suppression for pairs at small separations e.g. if the potential includes a hard-core repulsion. How the Schrödinger equation is solved is explained in Appendix A. For this study the Usmani potential is used [BU88], which predicts parameters for the scattering length and effective range in the two spin configurations and are taken from [WP99]. The values are reproduced by the code used for this analysis. They are plugged

in to the Lednicky model to describe the strong interaction. The two correlation functions are compared in Fig. 2.10 for a source radius of $r_0 = 3$ fm and in Fig. 2.11 for a source size value of 1.5 fm. One can see that the Lednicky model is still doing a good

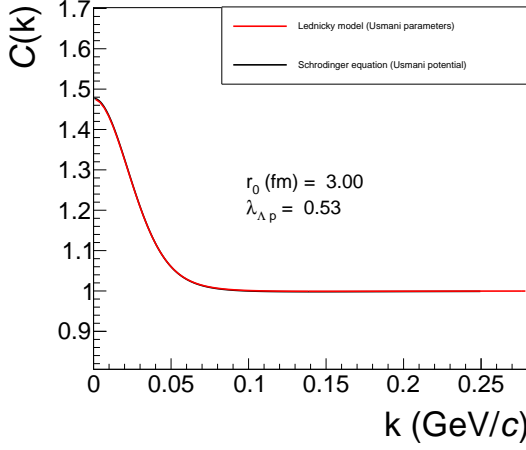


Figure 2.10: Comparison of the Lednicky model and the full solution of the Schrodinger Equation for a source radius of $r_0 = 3$ fm.

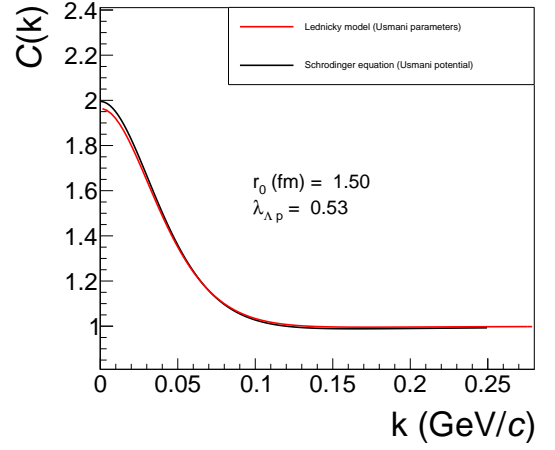


Figure 2.11: Comparison of the Lednicky model and the full solution of the Schrodinger Equation for a source radius of $r_0 = 1.5$ fm.

job for small source radii which are expected in pp collisions. For this reason there is no need to implement further corrections and it is used in the fitting procedure.

A final word on a possible connection of the correlation function and the total cross section. The correlation function depends on the scattering amplitude and this amplitude is connected to the cross section. Is it possible to transform from the “correlation basis” to the “cross section basis”? To answer this question we have a look on the relation of the scattering amplitude and the cross section. The absolute square of the scattering amplitude and its imaginary part (via the optical theorem) are directly connected to the cross section (we are only interested in s-wave scattering):

$$\begin{aligned}\sigma(q) &= 4\pi|f(\Theta)|^2 \\ \sigma(q) &= \frac{4\pi}{q} \Im(f(\Theta = 0)) .\end{aligned}\tag{2.39}$$

The problem is the real part of the scattering amplitude, which has no direct interpretation, but if the imaginary and absolute square are fixed a relation to the real part shows up:

$$|f(q)|^2 = (\Re f(q))^2 + (\Im f(q))^2, \rightarrow \Re f(q) = \pm \sqrt{|f(q)|^2 - (\Im f(q))^2} .\tag{2.40}$$

With this equation one can rewrite the Lednicky model in the cross section basis:

$$C(q)-1 = \sigma(q) \left(\frac{1}{8\pi r_0} - \frac{q}{4\pi r_0} F_2(2qr_0) \right) \pm \frac{2}{\sqrt{\pi r_0}} \sqrt{\frac{\sigma(q)}{4\pi} \left(1 - \frac{q^2}{4\pi} \sigma(q) \right)} F_1(2qr_0), \quad (2.41)$$

where $\sigma(q)$ is the total cross section close to the threshold. The correction term for pairs within the range of the nuclear potential was not taken into account and also not different spin states. The equation shows that there might be a decent chance to transform the measured correlation function points to the cross section basis and enhance the number of data points in the hyperon sector.

2.0.6 Resonance decays, energy conservation

The extreme case that a pair stems from a resonance decay imprints a strong correlation on the pair. This can be seen by looking at a pair of identical particles. For this pair the invariant relative momentum is given by:

$$q = \sqrt{-(p_1 - p_2)_\mu (p_1 - p_2)^\mu}. \quad (2.42)$$

But the particles are correlated by the mother of the resonance too:

$$P_R = p_1 + p_2, \quad (2.43)$$

where P_R is the resonance momentum. Using both equations delivers for the invariant relative momentum:

$$q = \sqrt{m_R^2 - 4m_{1,2}^2}, \quad (2.44)$$

where m_R is the mass of the resonance and $m_{1,2}$ the mass of particle 1,2. This means that q is fixed by all the masses involved. If one would measure e.g. $\pi^+\pi^-$ correlations the correlation function would show various peaks due to resonances decaying in such pairs. The case of two particles stemming from a resonance decay is an example of a very special case of energy conservation. Thus energy conservation can in general introduce additional correlations not related to femtoscopy. They are mostly showing up for small systems where not much particles are produced per event and a hint for such an effect is a non-flat baseline. A detailed study of energy conservation effects is given in [CL08], where also a method is presented how to model non-flat baselines.

2.0.7 Inelastic scattering

After a pair is emitted from a source it can undergo strong final state interactions. This can be of elastic nature enhancing or suppressing certain states depending on if the interaction is attractive or repulsive. But the pair can also undergo inelastic scattering which leads to losses of pairs. An example is an emission of an Baryon-Antibaryon pair which has total baryon number zero in the entrance channel. Thus the exit channel has also to have total baryon number zero. This is easily achieved with oppositely charged (or neutral) mesons in the final state having a lower lying pair mass (and fulfilling an allowed isospin transition from the entrance to the exit channel):

$$B\bar{B}' \rightarrow M^+M'^- . \quad (2.45)$$

Such pairs undergoing inelastic scattering (often referred to as annihilation in femtoscopy) are not reaching the detector, thus the correlation function is suppressed. The inelastic scattering can be described theoretically by allowing the scattering length being a complex quantity and the imaginary part describes the loss of pairs and the real part the elastic transitions of the scattering process.

2.0.8 Combinations of correlation sources

The correlation signals above were discussed individually. There is also the possibility that a pair of particles includes all three effects at the same time. A prominent example is given by proton-proton correlations, where the antisymmetrization and Coulomb repulsion lead to a suppression of the correlation signal below unity and the attractive strong interaction induces a bump structure at around 20 MeV/c. This can be related to the Bohr radius of protons which is for protons $\eta = 57.5$ fm. The peak position is located at $q \approx 2\pi/\eta \approx 21$ MeV/c [LL82]. The influence of quantum statistics would be that the correlation function approaches $C(q \rightarrow 0) = 0.5$. Coulomb repulsion leads to an additional suppression such that $C(q \rightarrow 0) \rightarrow 0$. This means that two charged particles are never in the same state not even at infinity due to the long-range behavior of Coulomb. The proton-proton correlation function was firstly calculated by Koonin [Koo77]. Combining all three sources was done in this case in a numerical way by the solution of the Schrodinger equation including the Reid soft-core potential [Day81; Rei68]. An example plot of proton-proton correlation functions is shown in Fig. 2.12 for source sizes of $r_0 = 1.5$ fm and $r_0 = 3$ fm.

2.0.9 Correlation function and bound states

Since the correlation function is sensitive to scattering parameter at $q \rightarrow 0$ one could in principle also study effects of bound states on the correlation function. A bound state would show up as a pole in the scattering amplitude in Eq. (2.24). Introducing a new

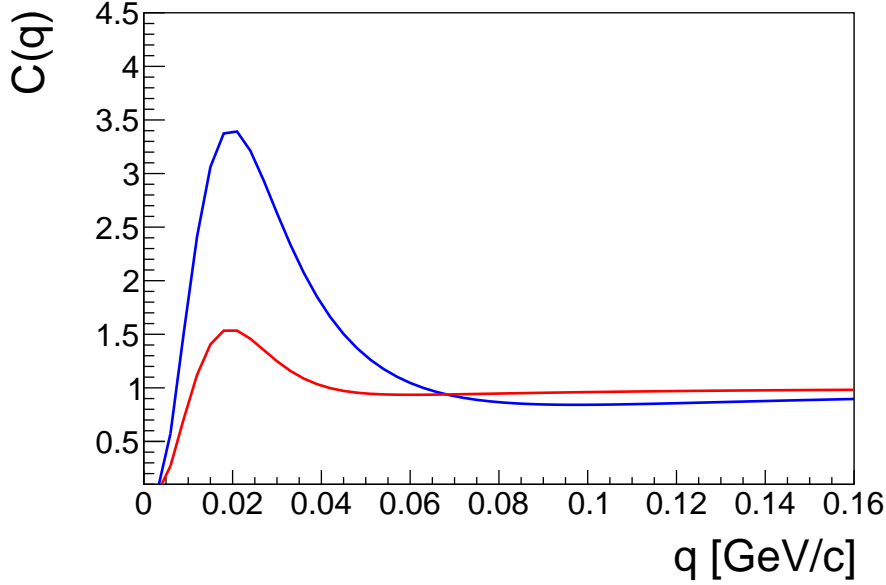


Figure 2.12: Two example plots of proton-proton correlation functions for source sizes of $r_0 = 1.5$ fm (blue) and $r_0 = 3$ fm (red). The proton-proton correlation function includes Fermi-Dirac statistics and Coulomb repulsion, which lead to a suppression of the correlation signal below unity for $q \approx 0$ as well as strong interaction which shows up as a bump structure at $q \approx 20$ MeV/c.

momentum scale $\kappa = -iq$ the bound state would lie on the positive imaginary axis $\kappa > 0$. Using the effective range expansion the condition for a pole in the scattering amplitude reads (where we set for the moment $f_0 = -a$ to have a better comparison to literature values):

$$\kappa^2 - \frac{2}{d_0}\kappa + \frac{2}{d_0 a} = 0. \quad (2.46)$$

This equation has two solutions, where we omit the one with (+) which would describe a virtual state [LL79]. The bound state lies just below the energy continuum [LL79]:

$$\kappa = \frac{1}{d_0} \left(1 - \sqrt{1 - \frac{2d_0}{a}} \right), d_0 > 0. \quad (2.47)$$

The binding energy of the bound state is given by:

$$E_B = \left| \frac{\hbar^2 q^2}{2\mu} \right| = \frac{\hbar^2 \kappa^2}{2\mu}, \quad (2.48)$$

where μ is the reduced mass. If the scattering problem would be totally governed by the scattering length $|a| \gg |d_0|$ then κ would be dominated by the scattering length only $\kappa \approx a^{-1}$. One can see from this relation for a bound state ($\kappa > 0$) one needs a positive scattering length a and the binding energy is then completely determined by it:

$$E_B = \frac{\hbar^2}{2\mu} \frac{1}{a} \quad (2.49)$$

This would be the case e.g. in the ultracold atoms regime [BDZ08] but for nuclear physics $a \sim d_0$, thus d_0 is not negligible.

2.0.10 Construction of experimental correlation function

Up to now we discussed the theoretical framework of femtoscopy. The correlation function can be measured also experimentally. Looking at Eq. (2.1) the correlation function is a comparison of a coincidence and an uncorrelated yield. The correlated yield is extracted by pairing the particles of interest in the same event. The uncorrelated yield is extracted by using the technique of event mixing, where the particles of interest from different events are paired which was for the first time proposed in [Kop74]. Such a pairing is free of femtosopic effects. The pairing was done as a function of the relative momentum of the pairs in the PRF:

$$C(k^*) = \mathcal{N} \frac{N_{same}(k^*)}{N_{mixed}(k^*)}, \quad (2.50)$$

where $k^* = \frac{1}{2} |\mathbf{p}_1^* - \mathbf{p}_2^*|$ with $\mathbf{p}_1^* + \mathbf{p}_2^* = 0$ ¹. Since the mixed event sample is not limited by statistics one mixes enough pairs (around ten times more) such that the statistical error of Eq. (2.50) is governed by the same event distribution only. For this reason a normalization factor \mathcal{N} is introduced to normalize the correlation function to unity in a region where no femtosopic signal is present. Strictly speaking, Eq. (2.50) does not fully reproduce the theoretical definition of Eq. (2.1) since the theoretical equation is valid for a single event. Since the experimental correlation cannot be measured in a single event an event average is build and one might neglect with this procedure some source function fluctuations. This is briefly mentioned in [PSH13] but not further explored.

2.0.11 The out-side-long reference frame

The correlation function is sensitive on pairs which are emitted very homogeneously from the source, which means the kinematics of the emitted particles is very similar.

¹We started femtoscopy with the interest of p - Λ correlations, which was for the first time proposed from theoretical side in [WP99]. Since the relative momentum is named k in this publication we adopted this labeling for the HADES analysis. Later on in the ALICE analysis we switched to the more common labeling of k^* instead of k for the relative momentum.

Such pairs have very low relative momenta in the PRF $k < \approx 150 \text{ MeV}/c$ and depending on the particle production multiplicity the statistics can be quite scarce in this region. However, if the production multiplicity is large e.g. for pions then there exists the possibility to perform a 3D analysis in the longitudinally-comoving-system (LCMS), which rests along the beam direction $\mathbf{P}_z = 0$. The relative momentum vector is then decom-

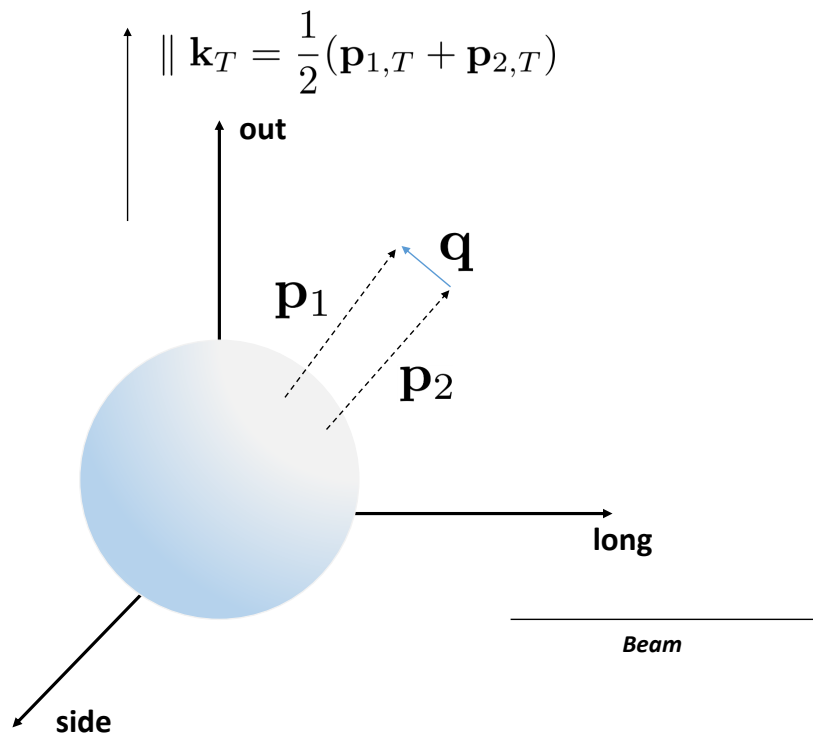


Figure 2.13: Definition of the longitudinally-comoving-system. The “long” component is aligned with the beam direction, “out” is parallel to the pair transverse momentum and “side” perpendicular to the other two directions.

posed in its out-side-long (o-s-l) direction, where the “long” component points along the beam direction, “out” is parallel to the total transverse momentum of the pair and “side” perpendicular two the other two. A sketch of the system is shown in Fig. 2.13 showing a source which emits a pair of particles. A nice description how to obtain the values of

any 4-Vector V in the LCMS is given in [Lis+05]:

$$\begin{aligned} V_{out} &= \frac{P_x V_x + P_y V_y}{P_T}, \\ V_{side} &= \frac{P_x V_y - P_y V_x}{P_T}, \\ V_{long} &= \frac{P_0 V_z - P_z V_0}{M_T}, \end{aligned} \tag{2.51}$$

where P_T is the total transverse momentum and M_T the total transverse mass of the pair. To boost into the PRF one has to boost along the transverse momentum \mathbf{k}_T direction of the pair, which modifies the “out” component of the 4-Vector. A discussion about the radii in the LCMS and their physics interpretation can be also found in [Lis+05].

2.0.12 Pair statistics

It is interesting how the initial lab momenta of the particles influences the statistics at low relative momenta where the correlation function is sensitive to. To study this we simulate 10^6 events containing one proton pair per event with Gaussian momenta for the protons for all momentum components. We defined the femtoscopy region as $k^* < 150 \text{ MeV}/c$. A result of how many protons are contained in this region as a function of the Gaussian proton momentum width is given in Fig. 2.14. One can see the expected trend that for particles which are on the average faster one produces less pairs ending up in the femtoscopy region since its harder to find such low-relative momentum pairs and the open available phase-space which can be populated is larger. The curve is highly non-linear. To have a high statistics data sample one has to perform the femtoscopy study where the average particle momentum is quite small. Additionally, there are many other effects which play a role e.g. the pair multiplicity, acceptance, efficiency and so on.

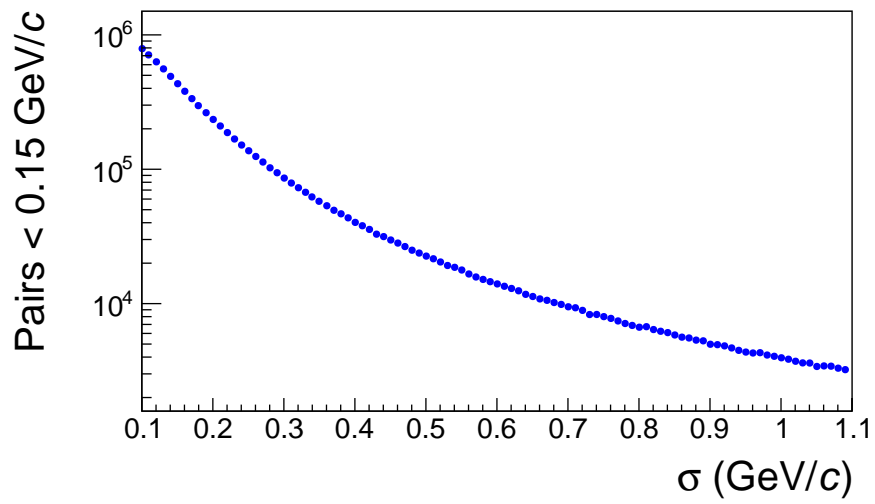


Figure 2.14: Number of proton pairs in the femtoscopy region $k^* < 150$ MeV/c as a function of the Gaussian momentum production width of the protons. The pair statistics in the femtoscopy range is highly non-linear.

Part I

PART I

3

The HADES detector at SIS18

The study of strong interactions delivers insight into the hadron-hadron interactions. Such interactions are described by effective models and theories and a keypoint is the understanding of the link between the fundamental chiral symmetry and the hadron properties. Chiral symmetry is broken spontaneously and explicitly due to the finite quark masses. However, if hadrons are embedded in a strongly interacting environment their mass is linked to this symmetry. At large temperatures and moderate densities this symmetry is expected to be partially restored. To have a strong influence of the medium on the embedded hadrons it is useful to study hadrons which have a short lifetime. This ensures that they have a larger probability to decay inside the medium. The light vector mesons ω , ρ and ϕ provide such properties. They also have the advantage that they can undergo electromagnetic decays into pairs of dileptons e^+e^- , which are not affected by strong interactions and deliver the information of the embedded mother particle undistorted towards the detector [Aga+09].

The High Acceptance Di-Electron Spectrometer (HADES) was designed to measure such rare decays in fixed target reactions. It is located in Darmstadt, Germany, at the GSI Helmholtzzentrum für Schwerionenforschung. The HADES heavy-ion program is focused on beam energies of 1-2 AGeV achieved with the heavy-ion synchrotron Schwer-Ionen Synchrotron (SIS18). At these energies the compression duration of colliding nuclei in heavy-ion reactions is comparable to the lifetime of light vector mesons. SIS18 delivers the beam for the experiments with energies between 1-2 A GeV for heavy-ions and up to 4.5 GeV for protons. Secondary pion beams with momenta up to 2 GeV/c are also available at this facility. An expanded view of the HADES detector is shown in Figure 3.1. It consists of six identical sectors defined by the superconducting coils ar-

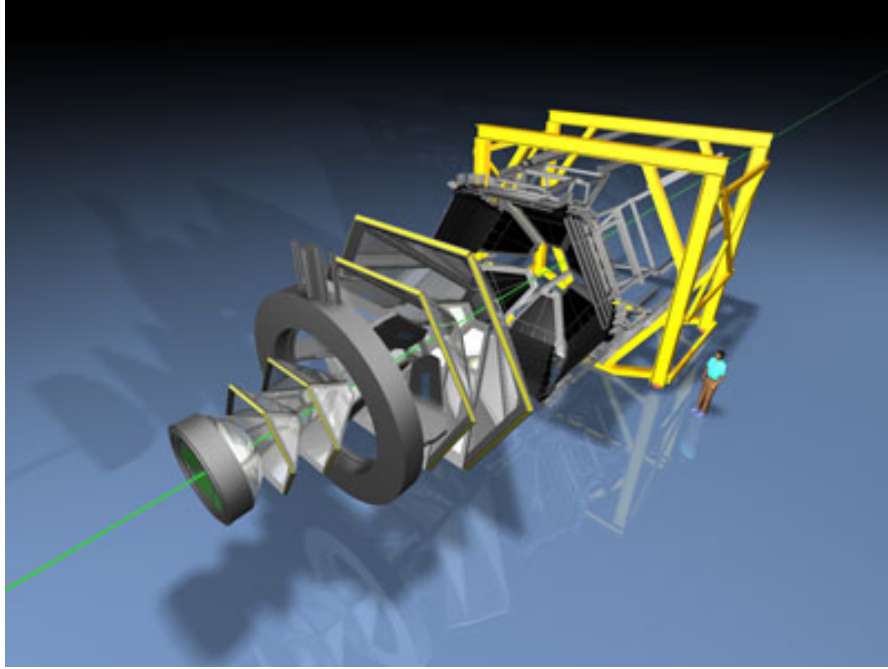


Figure 3.1: Setup of the HADES detector. The green line indicates the beam.

ranged symmetrically around the beam axis and optimized for dielectron measurements. It covers around 85% of the azimuthal angle and the Θ range is from 15° to 85° . This corresponds to a pseudo-rapidity range of $\eta \in [0.1, 2]$, where the pseudo-rapidity is defined as:

$$\eta = -\ln \left(\tan\left(\frac{\Theta}{2}\right) \right). \quad (3.1)$$

Figure 3.2 illustrates the schematic layout of the detector system and all the important detector parts. In the next Sections the most important parts of the detector are explained. Since an analysis of the p+Nb reaction is presented in this thesis also some older components are described. In 2009 HADES underwent an upgrade with an interchange of some parts of the detector due to the upgrade on the hardware side.

3.0.13 The target

The fixed target is located in front of the RICH detector. Elementary reactions are studied with a liquid hydrogen target, whereas for heavy-ion collisions or $\pi/p+A$ reactions a segmented solid state target was used. The start detector delivers the starting time of the reaction. Unfortunately, in the p+Nb run no start detector was participating in the data collection. Thus no direct time-of-flight measurement was accessible which could contribute to the particle identification information.

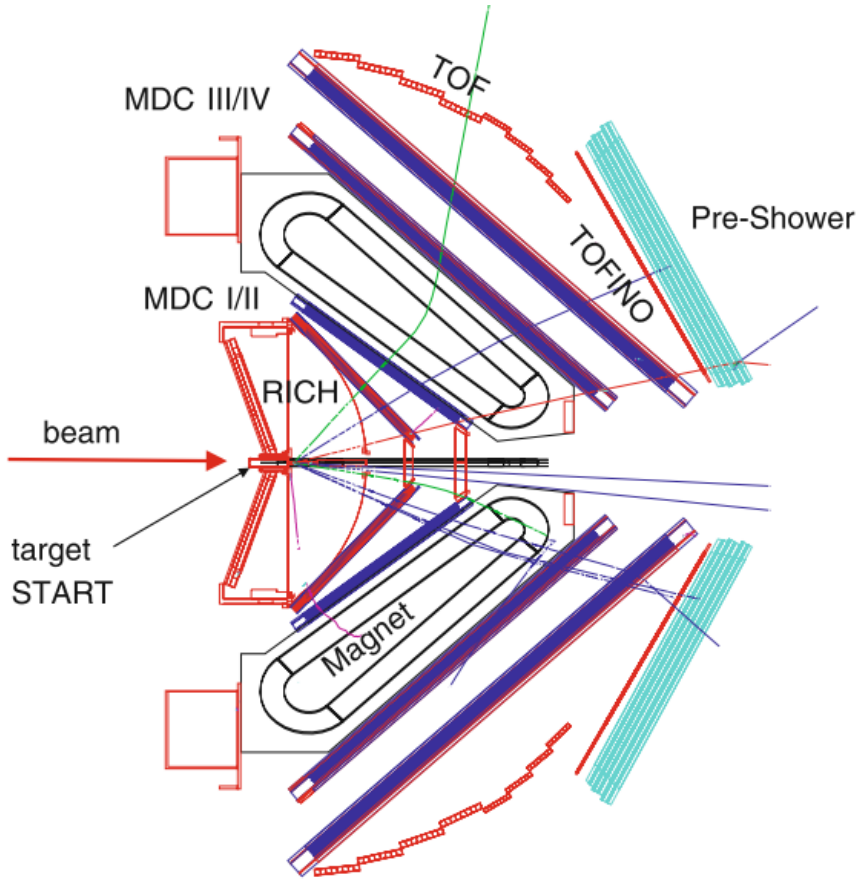


Figure 3.2: Side view of the HADES detector system and its detector components.

3.0.14 The RICH detector

For rare decays of vector mesons into dilepton pairs a good particle identification for the decay products is necessary to clean the sample from hadron contamination. For this purpose a Ring Imaging Cherenko (RICH) detector is used to identify electrons and positrons in the momentum range $0.1 \text{ GeV}/c < p < 1.5 \text{ GeV}/c$. The detector contains as radiator gas perfluorobutane (C_4F_{10}). This gas has a threshold for emitting Cherenkov light of $\gamma_{\text{thresh}} = 18$. Because of this large threshold the RICH detector is hadron blind in the SIS18 energy regime since mainly electrons or positrons pass this kinematic barrier. The produced Cherenkov light is reflected by a spherical symmetric low mass carbon shell mirror and hits finally the photosensitive CsI cathodes of six Multi-Wire Proportional Chambers (MWPC). The light is then finally focused to rings because of the detector geometry in a way that the ring radius stays nearly constant. The information of the ring position together with the reconstructed particle track is used to identify electrons and positrons. A schematic layout of the RICH detector is shown in Figure

3.3.

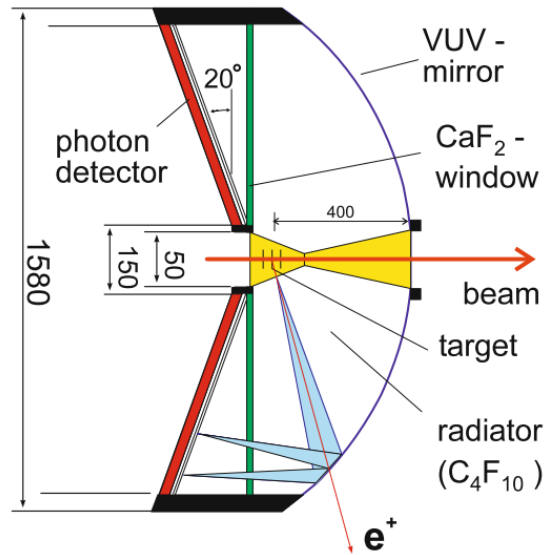


Figure 3.3: Schematic layout of the RICH detector. The Cherenkov light of the positron is reflected at the mirror and focused to a ring on the readout pads.

3.0.15 The Multi-Wire-Drift Chambers

The HADES program aims to measure in-medium modifications of particles. To achieve this goal a good momentum reconstruction together with a sufficient spatial resolution of the tracked particles and large detector acceptance is needed. Therefore, 24 trapezoidal planar *Multewire Drift Chambers* MDC are placed symmetrically around the beam axis in six identical sectors. Each sector contains four tracking planes (I-IV), two planes in front (I-II) of the magnet and two behind (III-IV). This is illustrated in Figure 3.2. The space between the planes II-III defines the active area of the chambers, where charged particles are deflected thanks to the magnetic field. Each of the 24 MDCs are divided into six anode wire frames (about 1100 tungsten wires per frame) oriented in six different angles ($\pm 0^\circ$, $\pm 20^\circ$, $\pm 40^\circ$) as displayed in Figure 3.4. This setup enlarges the spatial resolution in polar direction. The MDC chambers are flushed with a counting gas. A charged particle traversing the gas is ionizing it along the particle trajectory which forms clusters. The produced electrons in the gas are accelerated towards the wires due to an active electric field. The amount of electrons gets multiplied during the acceleration stage by the avalanche effect. Finally, the cloud of electrons reaches the MDC wires and introduces an electric signal, which is read out.

With this principle hit positions in the MDC layers (I-IV) are determined. The hit points in MDC I and II are grouped together to an inner track segment and from MDC III and

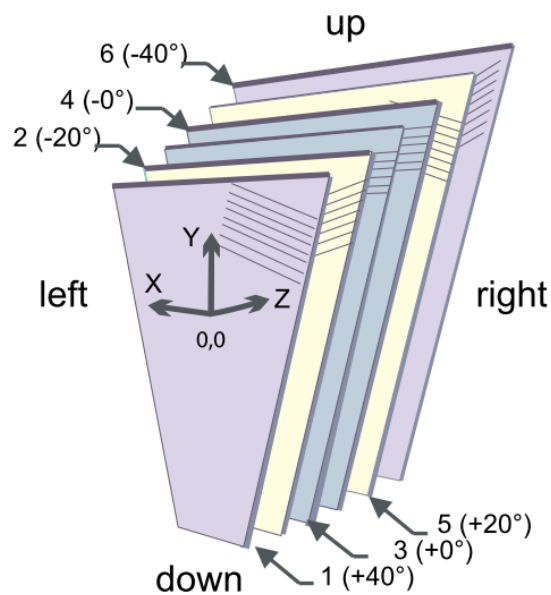


Figure 3.4: Schematic view of the drift chambers oriented at $\pm 0^\circ$, $\pm 20^\circ$, $\pm 40^\circ$.

IV to an outer one. The points in the inner and outer segment are connected with the assumption of straight tracks, because they are in an almost free magnetic field region. In the active area the particles are deflected and the momentum is determined solving its equation of motion in the field region in a recursive way with the Runge-Kutta method. The hit points are therefore used as initial conditions.

3.0.16 The Magnet

A charged particle entering a magnetic field region is deflected according to the Lorentz force, whereas the total momentum stays constant. By measuring the deflection one is able to obtain the momentum of the particle. To make use of this principle, the HADES detector contains six superconducting magnets placed around the beam axis among the drift chambers. The magnets create a strong inhomogeneous toroidal magnetic field with strengths ranging from $B = 0.9$ T up to $B = 3.6$ T at the sector edge. The magnet was built in such a way that the target region and the active volume of the RICH detector is free of any magnetic field to not influence the particle reactions and identification of electrons and positrons.

3.0.17 The Time-of-flight detectors

The three time of flight detectors are part of the Multiplicity Electron Trigger Array (META) system. Particles traversing the META system give an additional hit point which is used for the tracking of the particles. The detector subsystems are in detail:

- TOF detector

The TOF detector covers a polar acceptance of $44^\circ < \Theta < 88^\circ$ and follows the azimuthal six-fold symmetry of the whole HADES setup. Each one of the six detectors consists of eight modules, and each module is subdivided into eight scintillator rods. A charged particle induces a photon emission in the scintillators measured with Photo-Multiplier-Tubes PMT's, which deliver the arrival time and also a signal height. The signal height is related to an energy loss, which can be used for particle identification. The time resolution of the TOF detector was obtained by using dileptons from C+C reactions and is of the order $\sigma_{\text{TOF}} \approx 150$ ps. The TOF detector is also capable of delivering a specific energy loss signal dE/dx which is used for particle identification.

- TOFINO

The TOFINO detector has a polar acceptance of $18^\circ < \Theta < 45^\circ$. It is a low granularity system divided into six sectors, each containing four scintillator paddles with a trapezoidal form. The lower granularity increases the probability of double hits. Its time resolution is worse than those of the TOF of about $\sigma_{\text{TOFINO}} \approx 420$ ps. As the TOF detector, also TOFINO provides a specific energy loss signal dE/dx .

- Pre-Shower

The Pre-Shower is located just behind the TOFINO detector. It is used for dilepton identification and based on the fact that electrons and positrons induce an electromagnetic shower in the converter material made out of lead.

- Resisitive Plate Chambers (RPC)

To achieve better time resolutions of about $\sigma_{\text{RPC}} \approx 100$ ps, which leads to an improved particle identification and to be able to work at SIS intensities of $2 \cdot 10^7$ Hz, the new RPC wall ESTRELA (Electrically Shielded Timing RPC Ensemble for Low Angles) was developed and exchanged for the TOFINO detector [Gil+07] in an upgrade which started in 2009. It covers the low polar angle acceptance region $18^\circ < \Theta < 45^\circ$ with 2π azimuthal coverage.

3.0.18 The Forward Wall

HADES started in 2007 to investigate proton deuteron reactions. A characteristic feature of these reactions is that spectator nucleons move in forward direction at small polar angles. The HADES spectrometer covers polar angles from $15^\circ < \Theta < 85^\circ$, not able to register these spectators. For this purpose, a forward wall scintillator hodoscope was built. It consists of about 300 scintillating cells having a thickness of 2.54 cm each and

are read out by photomultipliers [Lap+09]. It was placed 7 m downstream the target and covers a polar acceptance of $0.33^\circ < \Theta < 7.17^\circ$.

3.0.19 Trigger in the p+Nb run

As already mentioned, the HADES detector aims for detecting rare e^+e^- pairs stemming from decays of light vector mesons. To suppress hadronic channels and enhance final states containing dileptons, an event filtering procedure (trigger system) is included in the setup. It also helps to avoid overloading of the data acquisition system and of the front-end electronics. The trigger system consists of two different trigger conditions:

- *LVL1 Trigger* :

The TOF and TOFINO detectors (building the META system) determine the multiplicity M of an event. The first level trigger (LVL1) rejects events that do not exceed a predefined multiplicity condition. In the p+Nb run a M3 trigger was used registering only events with at least three hits in the META system.

- *LVL2 Trigger* :

The second level trigger (LVL2) is meant to enhance the lepton fraction in the data. During a run, data samples recorded by the corresponding detector parts are evaluated by Image Processing Units (IPU) for possible lepton signatures like RICH-rings. The Matching Unit (MU) connected to all IPUs correlates the signatures and provides a trigger decision (e.g. at least one ring is needed to give a positive trigger decision).

- *Downscaled Events*

In this thesis hadronic reactions are analyzed thus the the LVL2 trigger decision is not considered. To not introduce any trigger bias into the data sample a downscaling of the minimum bias events was introduced. In the data acquisition process the LVL2 trigger gives a positive signal if there is a sign for a leptonic event. Only events with a positively LVL1 and LVL2 decisions are recorded except for a fixed fraction of events independent of the second level trigger decision. These events are called downscaled events. The amount of LVL1 events recorded without paying attention to the LVL2 trigger output is fixed by the downscaling factor DS . In the p+Nb run DS was set to three which means that every third event was written to tape. Downscaled events become denoted by a DS1 flag which can afterwards be used to distinguish them from other events in the hadron analysis.

3.0.20 Analyzed files

The reconstructed signals of the tracked particles are stored in DST files, which are used for the physics analysis. If e.g. some tracking procedures are updated new DSTs are produced for the analysis. In the p+Nb analysis filtered microDSTs are analyzed. They

were filtered for all relevant quantities like momenta, track quality parameters and the track sorter ¹ was run already through the files. The track sorter selects the best track hypothesis in case many track hypothesis would fit through given hitpoints.

3.1 Particle identification

The MDCs provide besides the momentum determination also the information of the energy loss of a particle. This quantity helps to determine the PID of charged hadrons. The principle of energy loss is that a charged particle which crosses a medium scatters inelastically with electrons that are bound in atoms in the medium. This scattering process causes an energy loss of the traversing particle. At each collision process n the particle loses the energy $E_n - E_0$ and it collides with a rate (per unit length) of $N\sigma$ where σ is the cross section. This motivates the following ansatz for the energy loss [Sak94]:

$$\frac{dE}{dx} = N \sum_n (E_n - E_0) \int \frac{d\sigma}{d\Omega} dq. \quad (3.2)$$

A full relativistic treatment was given by Bethe and Bloch in the famous Bethe-Bloch formula [Bet30]:

$$-\left\langle \frac{dE}{dx} \right\rangle = 4\pi N_A r_e^2 m_e c^2 z^2 \frac{Z}{A} \frac{1}{\beta^2} \left[\ln \left(\frac{2m_e c^2 \beta^2 \gamma^2 T_{max}}{I^2} \right) - \beta^2 - \frac{\delta}{2} \right]. \quad (3.3)$$

The factors in detail are:

- z : charge of the incident particle
- Z, A : atomic and mass number of the traversed medium
- m_e : rest mass of the electron
- r_e : Bohr electron radius
- N_A : Avogadro number
- I : mean excitation potential of the material
- δ : density correction
- T_{max} : maximum kinetic energy which can be transferred

Eq. (3.3) depends on the charge ($z \cdot e$) and on the momentum ($p/m = \gamma\beta$) of the particles. With the dependence of the momentum on the mass different curves for different particle species are expected. This allows to separate between the different hadron species if the

¹<http://web-docs.gsi.de/%7Ehalo/docs/hydra/classDocumentation/hydra-8.21/out/HPidTrackSorter.html>

mass is different. In this analysis the energy loss of the MDC is always used. Additionally, for $p - p$ correlations also the specific energy loss of TOF and TOFINO is used for particle identification. To minimize the loss of statistics in the anyway scarce statistics p - Λ sample only the MDC is employed for PID for this pair. The specific energy loss distributions for the three detectors as a function of the momentum of the tracks are shown in Fig. 3.5. The black dashed lines show the used selection regions for protons and negative pions.

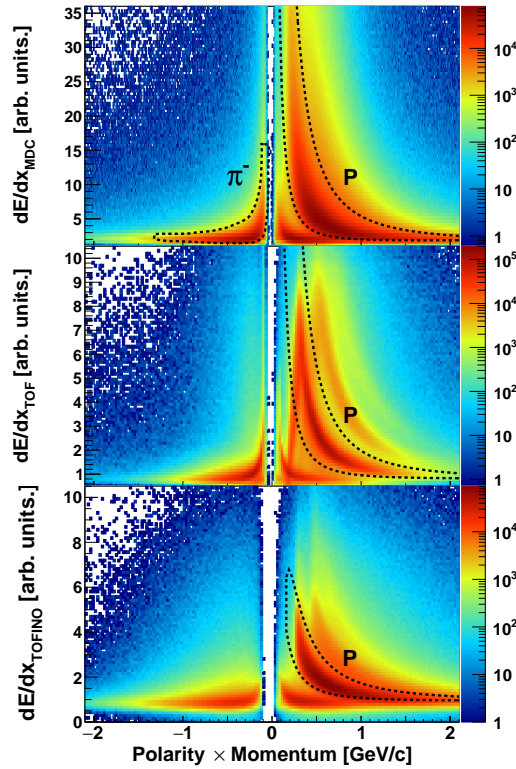


Figure 3.5: Specific energy loss distributions for MDC, TOF and TOFINO as a function of the particles momentum. One can clearly see the different bands corresponding to different particle species.

4

Data analysis

In this chapter the femtoscopic analysis in the p+ Nb system is presented. The experiment was performed in September 2008 with beams from the SIS18 located at GSI. Protons with a kinetic energy of $T_p = 3.5$ GeV were incident on a 12-fold segmented niobium target. Such a target configuration was chosen because it is a good compromise between maximizing the number of in medium decays of ρ and ω mesons and keeping the γ conversion probability low since the main aim of the experiment was to study virtual photons stemming from the ω and ρ mesons produced in cold nuclear matter. The target was also used in other experiments e.g. in JLAB. Details of the run are listed in Tab. 4.1 and taken from [Lor12; Web11]:

| | |
|---------------------------|--------------------------------|
| Beam energy | 3.5 GeV |
| Average intensity | $2 \times 10^6 \text{ s}^{-1}$ |
| Target | ${}_{41}^{93}\text{Nb}$ |
| Target diameter | $d = 2.5 \text{ mm}$ |
| Number of segments | 12 |
| Distance between segments | $\Delta z = 4.5 \text{ mm}$ |
| Thickness of segment | $t = 0.45 \text{ mm}$ |
| Interaction probability | 2.8% |
| Downscaled Events | $3.15 \cdot 10^9$ |

Table 4.1: Overview of the conditions of the p+ Nb reaction.

4.0.1 Protons and Lambda hyperons track selection

All tracks are required to have a good match of the track segment in the outer MDC segment with a META hit point. Protons for the $p - p$ analysis are selected with the energy loss information from the MDC as well as TOF or TOFINO detectors. For the p - Λ pair only the MDC information is used for particle identification to not lose pairs with additional selections. This leads to a slightly worse purity, which will be discussed in Section 4.2.4. The Λ is a neutral strange baryon which decays weakly into pairs of $p\pi^-$ with a branching ratio of $\sim 64\%$ [Oli+14] and a lifetime of about $c\tau = 7.9$ cm in the rest frame of the Λ . This finite lifetime allows to introduce topological cuts to reduce sources of combinatorial background. Four combinatorial cut selections are employed:

- Distance of closest approach between the daughter tracks ($DCA_{p\pi^-}$).
- Distance of closest approach of the daughter tracks to the primary vertex (DCA_p, DCA_{π^-}).
- A cut on the flight distance of the Λ , which is the distance between the primary and decay vertex ($d(|PV - SV|)$).
- A selection on the pointing angle α which is the angle between the vector which points from the primary to the decay vertex and the Λ momentum vector.

A sketch of a Λ decay is presented in Fig. 4.1. The red arrow shows the momentum vector of the Λ which is reconstructed with the daughter tracks. The black arrow shows the vector connecting the primary and secondary vertices. The primary vertex must have a smaller z-component than the decay vertex in a fixed target experiment. This is ensured with the pointing angle selection because large opening angles between the two vectors means that the Λ momentum vector points towards a positive z-direction whereas the vector between the primary and decay vertex points in the opposite direction. The cuts are chosen to maximize the Λ purity defined as $\mathcal{P} = S/(S+B)$ and not losing too much signal. They are found by a variation of values for every topological observable, which are predefined in an array. To reduce the dimension of the parameter space the pointing angle and the distance between the tracks is kept constant. For every combination the invariant mass of $p\pi^-$ is fitted to obtain the signal S and background B . Fig. 4.2 shows tested cut combinations (the z-value corresponds to a specific cut combination) and the corresponding Λ signal and purity. The chosen cut values are indicated as black circles and are listed in Tab. 4.2. In any future study it might be worth to develop an automatic cut finding procedure, where the desired purity and/or fraction of signal loss is given to a function which is then minimized. The corresponding invariant mass plots of $p\pi^-$ for the chosen cut selections are shown in Fig. 4.3, 4.4, 4.5.

4.1 Correlation functions

The correlation function is obtained by comparing the pair statistics in the relative momentum difference k representation from same event to a mixed event sample. The

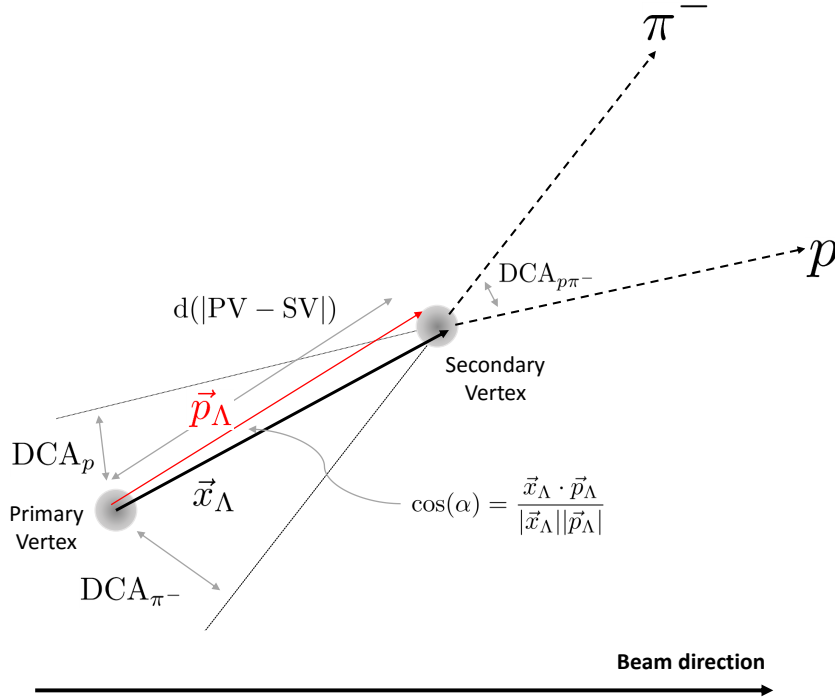


Figure 4.1: Sketch of a Λ decay and the explanation of topological selection criteria.

| Comb. | DCA_p [mm] | DCA_{π^-} [mm] | $d(PV-SV)$ [mm] | $DCA_{p\pi^-}$ [mm] | Pointing angle [rad] | Purity [%] |
|-------|-----------------|-----------------------|----------------------|------------------------|----------------------------|---------------|
| 1 | 7 | 15 | 52 | 10 | 0.1 | 86.1 |
| 2 | 7 | 25 | 57 | 10 | 0.1 | 89.6 |
| 3 | 10 | 28 | 61 | 10 | 0.1 | 92.5 |

Table 4.2: Topological cut selections for the Λ hyperon to reduce combinatorial background. The corresponding purities are also listed.

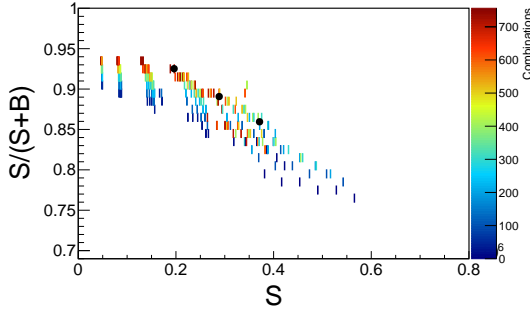


Figure 4.2: Purity as a function of the remaining signal for different topological cut selections. The black circles show the selected cuts.

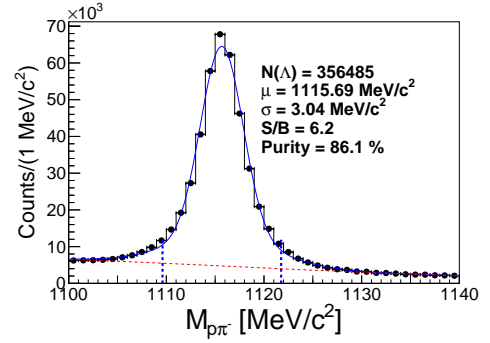


Figure 4.3: $p-\pi^-$ invariant mass spectrum for combination 1 of topological cuts.

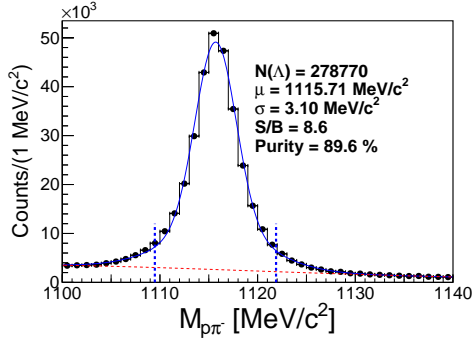


Figure 4.4: $p-\pi^-$ invariant mass spectrum for combination 2 of topological cuts.

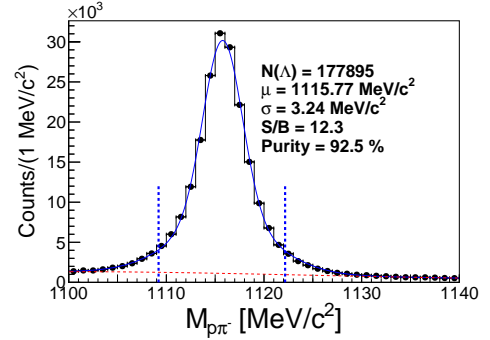


Figure 4.5: $p-\pi^-$ invariant mass spectrum for combination 3 of topological cuts.

z -coordinate of the target is reconstructed in the events and it is required to lie within $-60 \text{ mm} < z < 0 \text{ mm}$, where the target is located. Details about the target are given in Tab. 4.1. For the event mixing the events are grouped in bins of the z -vertex of 6 mm for $p-p$ pairs and 10 mm for $p-\Lambda$. For $p-\Lambda$ in event mixing two primary vertices from the two different events are present. The primary vertex with the tracks from the two events is recalculated to have one common primary vertex. This primary vertex is used to calculate the topological observables. The events are binned in multiplicity M with a width of two tracks below $M < 9$. Events with multiplicity $9 \leq M$ are put into one mixing bin. The multiplicity was evaluated with hit points in the inner Segments, the Shower and the TOF detector.

4.2 Corrections

In this section all the applied corrections are discussed. The major correction is related to cure the sample from track merging. Also the finite momentum resolution of HADES plays a significant role on the correlation functions as will be shown.

4.2.1 Two track cuts

Femtoscopy is based on a measurement of a pair of particles with a small relative momentum. In order for a pair to fulfill this criteria ϕ , θ and p_T must be quite similar and this means that the track trajectories of the particles in the pair are very similar. The detector might have at some point problems to distinguish two distinct tracks due to the finite detector granularity. Then two tracks are merged into one track. One refers to this effect as close track efficiency (CT). This can happen in HADES e.g. if the pair hits the same MDC wire at very similar points. If this merging happens very often then many pairs at low momentum differences are missing. A problem appears when the ratio with the mixed event sample is computed, where all tracks are distinct. Thus the track merging process introduces an artificial correlation where solely the detector is responsible for. The opposite effect can also happen and then one track is reconstructed as two tracks. This can happen in HADES in case of double hits, e.g. that different track hypotheses can describe the recorded hit points. To find the best track candidate is the task of the track sorter on the software side of HADES¹. This is done at the DST level and for the pNb system only microDSTs were accessible for the analysis. The track sorter for the microDSTs production was already run over the DST sample but many non-unique track hypotheses are not sorted out since the track sorter was initialized with rather loose conditions. Such tracks have rather similar momentum and thus a small momentum difference, which leads to fake positive correlations. Certain track quality parameter are stored in the microDSTs. A requirement of a good match indicated by a positive $\chi_{\text{META}}^2 > 0$ of the track segment in the outer MDC and a META hit point helped to get rid of such fake tracks. The more severe problem is introduced by track merging as will be shown. To investigate this effect the differences in the $\Delta\phi$ and $\Delta\Theta$ angles are explored for the $p-p$ pair and the opening angle between the primary and Λ daughter proton for $p-\Lambda$ pairs. To get the proper $\Delta\phi$ observable in the same event distribution one has to perform first a randomization of the tracks before calculating the angle difference. HADES tabulates the tracks according to the six segments, which introduces a bias in the angle difference showing up in an asymmetry in $\Delta\phi$. The mixed event sample is automatically randomized and is perfectly symmetric.

The track merging phenomenon is now explored and it is shown that the HADES track-

¹<http://web-docs.gsi.de/%7Ehalo/docs/hydra/classDocumentation/hydra-8.21/out/HPidTrackSorter.html>

ing is responsible for it. This can be seen in Fig. 4.6. The left plot shows the distribution for $p - p$ pairs generated from UrQMD simulations and filtered through the HADES acceptance, which means after GEANT. The right plot includes also the tracking of the particles through the HADES apparatus. A hole appears in the middle of the right plot. This is a clear sign that the tracking of the particles is responsible for the merging. Merged pairs are rejected by the requirement of a minimal cut on $\Delta\Theta$ and $\Delta\phi$ in

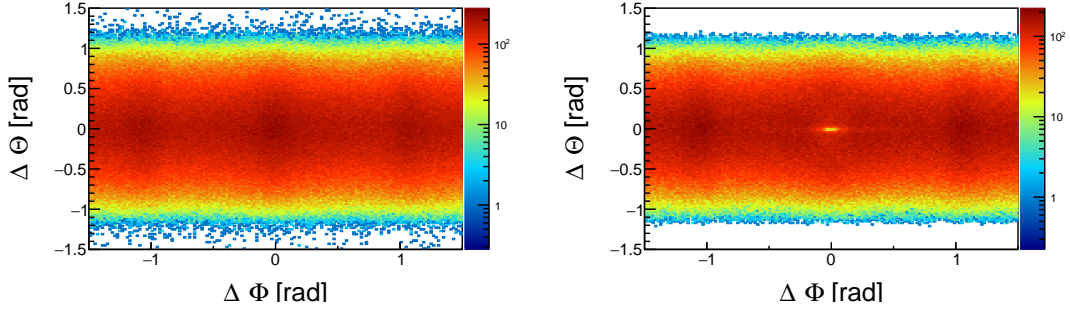


Figure 4.6: Angle correlations of $(\Delta\phi, \Delta\Theta)$ for $p - p$ pairs. The left plot shows $p - p$ pairs after GEANT which filters the pairs for acceptance. The right plot includes also the tracking which introduces a hole in the distribution.

the same event as well as in the mixed event sample. To find proper selection values the effect of rejecting pairs at small angles is investigated with the experimental correlation function for $p - p$ pairs. The experimental correlation function for $p - p$ pairs in $(\Delta\phi, \Delta\Theta)$ is shown in Fig. 4.7. One can see that for $(\Delta\phi, \Delta\Theta) \rightarrow (0, 0)$ the merging is so strong that nearly no pair can be measured by the detector in this region. The region where the merging happens is actually rather broad, which makes it hard to find selection criteria where all the merging is rejected without losing too much or all pairs in the interesting low momentum region. The efficiency to measure pairs which are close together in space depends always on the pair under investigation. To demonstrate this the angle differences are also calculated for pion pairs. This is illustrated in Fig. 4.8, 4.9, 4.10. For identical pion pairs it depends on the charge of the pair, since the acceptance changes with the magnetic field. For unlike-sign pions the efficiency is shifted away from the origin. This is a typical effect for non-identical pairs. The influence of cutting out pairs at small angles is displayed in Fig. 4.11 for $p - p$ pairs. One can clearly see that the experimental correlation function is strongly influenced by the merging of pairs by the HADES detector. The peak position at around 20 MeV/c goes up to larger values when pairs at small angles are rejected and saturates when most pairs from merging are cut out from the sample. As already said it is not directly clear which selection values should be chosen since the merging is rather broad. It is decided that a medium range of $|\Delta\Theta| > 0.05$ rad and $|\Delta\phi| > 0.12$ is a compromise between the rejection of the most

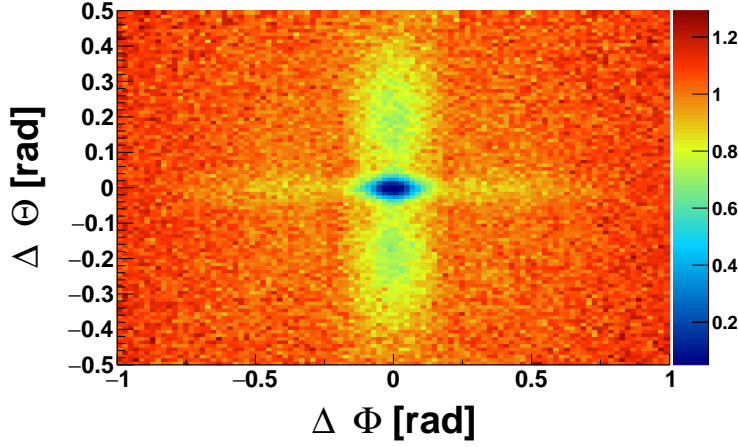


Figure 4.7: Experimental correlation function in $(\Delta\phi, \Delta\Theta)$ for $p-p$ pairs.

severe merging region and keeping enough pairs left for the analysis. The baseline of the correlation function is also not flat. A correction for this is to divide the measured correlation function by a correlation function from UrQMD as will be shown in Section 4.2.2. Since the correlation function from UrQMD will be also influenced by the close track efficiency any residual merging is corrected by this division. A variation of the chosen cut parameters on the final result is taken into account as systematic uncertainty. The effect of the chosen selection interval on the correlation function is displayed in Fig. 4.12 in the one-dimensional relative momentum basis as well as in three-dimensional $q_{o,s,l}$ coordinates. One can see that for all coordinates the rejections of too close pairs improves the correlation functions significantly. Also in simulations the merging effect is observed. To get the correlation function from simulations the UrQMD [Bas+98; Ble+99] transport model is used for $p-p$ pairs and GiBUU [Bus+12] as event generator for $p-\Lambda$. GiBUU allows to tune production cross sections quite easily plus it can be run in perturbative mode [Bus+12], which is faster to compute sufficient statistics. For the production of strange baryons GiBUU relies on calculations of cross sections from the Tsushima resonance model [Tsu+99]. This cross sections were tuned in an experimental K_S^0 analysis [Aga+14b] performed by the HADES collaboration. They are parametrized in the Tsushima model as follows [Tsu+99]:

$$\sigma = a \left(\frac{s}{s_0} - 1 \right)^b \left(\frac{s_0}{s} \right)^c, \quad (4.1)$$

where s and s_0 are the invariant collision and the threshold energy. All channels involving a Λ/Σ^0 in the production are scaled by a factor $100 \times a$. The relevant channels contributing to the Λ production in GiBUU with the corresponding values of scaled cross

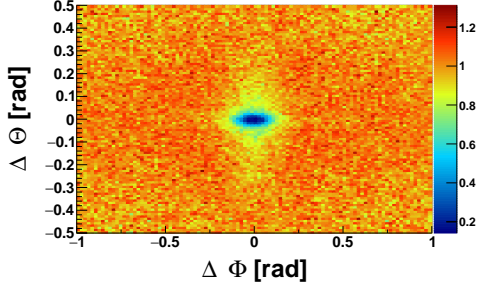


Figure 4.8: Experimental correlation function in $(\Delta\phi, \Delta\Theta)$ for $\pi^- - \pi^-$ pairs.

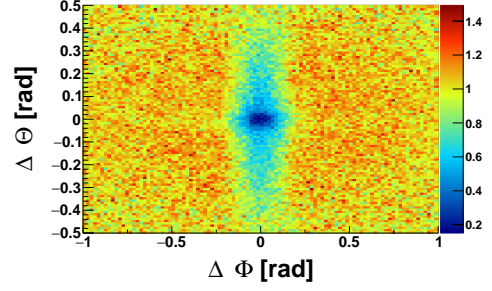


Figure 4.9: Experimental correlation function in $(\Delta\phi, \Delta\Theta)$ for $\pi^+ - \pi^+$ pairs.

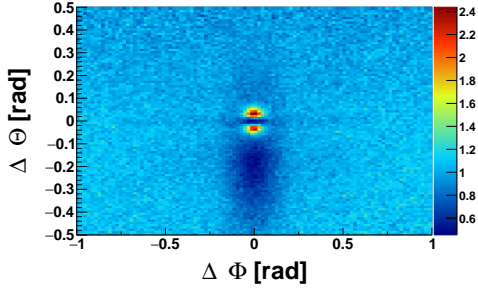


Figure 4.10: Experimental correlation function in $(\Delta\phi, \Delta\Theta)$ for $\pi^- - \pi^+$ pairs..

sections are listed in Tab. 4.3. The two simulation samples from UrQMD and GiBUU are sent through the whole analysis chain including acceptance and tracking efficiency. The correlation functions from simulations are displayed in Fig. 4.13. One can also see in the simulated correlation functions the strong merging effect for the $p - p$ pair. The suppression is so strong that at low k no pair can be measured anymore. For the $p - \Lambda$ pair the merging is not that strong compared to $p - p$. The reason is that the secondary proton is a bit displaced from the Λ direction due to the decay, which softens the merging effect by the detector. This more flat merging signal was also observed in a $p - \Lambda$ femtoscopy analysis in Ar+KCl reactions at $\sqrt{s_{NN}} = 1.76$ GeV [Aga+10] measured by HADES. For $p - p$ the angle selection criteria, which were discussed above are used to reject close pairs. In $p - \Lambda$ a one-dimensional cut is investigated. In the decay $\Lambda \rightarrow p + \pi$ most of the momentum is transferred to the proton. This means that the direction of the proton is strongly correlated with the Λ direction. Thus, the merging appears between the primary and the secondary proton in the $p - \Lambda$ pair. With help of GiBUU simulations one observes that a opening angle between these two protons of $5^\circ = 0.09$ rad is sufficient to get rid of track merging.

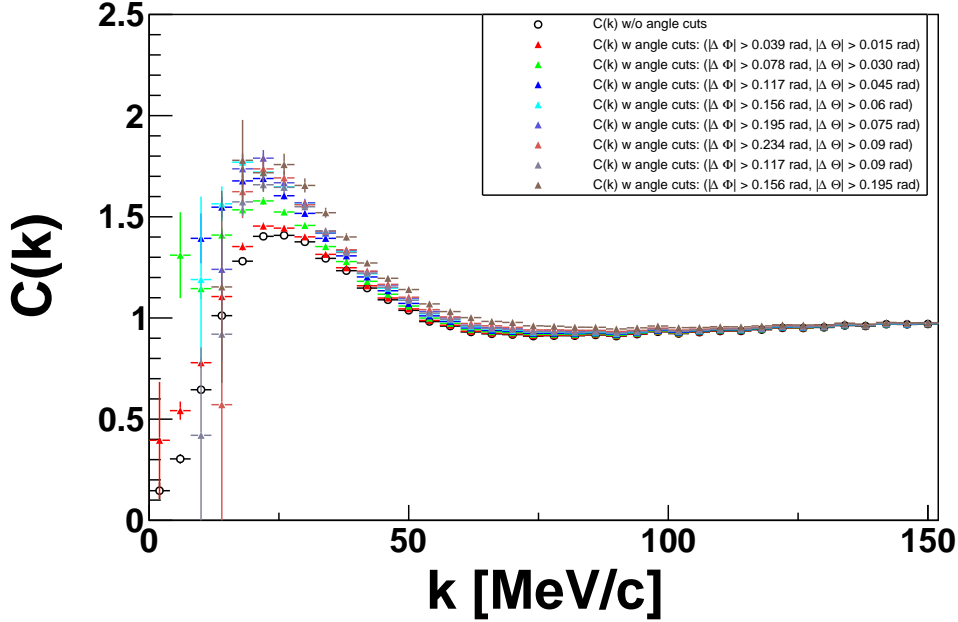


Figure 4.11: Experimental correlation $p - p$ function with different cut selections on $(\Delta\phi, \Delta\Theta)$ to reject close pairs.

4.2.2 Long range correlations

In the best case the experimental correlation function contains only the femtosopic correlations. However, especially in smaller collision systems also other correlations can show up. They are visible via a non-flat baseline at large relative momentum values, where the femtosopic correlations flatten out. The origin of such non-flat structures can be addressed to correlations from energy and momentum conservation at smaller energies or minijets and kinematic conservations at larger energies. In p +Nb reactions one deals with a small collision system, which is reflected in the number of participants of $\langle A_{\text{part}} \rangle = 2.5$ [Aga+14a]. Thus the average multiplicity is also quite low $\langle M \rangle \sim 4$. For this reason it is not surprising that in such a small system event mixing cannot perfectly fulfill the kinematic constraints from energy and momentum conservation. Effects of this kind were investigated in [CL08; Boc11; Cha09]. But even in larger systems the baseline can be not flat due to collective effects like flow, which are also not present in event mixing. However, their influence in heavy-ion collisions is usually much smaller. To correct for such effects several strategies were developed in the femtoscopy field. In the analysis presented here baselines from Monte Carlo simulations are investigated. Since UrQMD and GiBUU were used for two track cuts, they are reused for the investi-

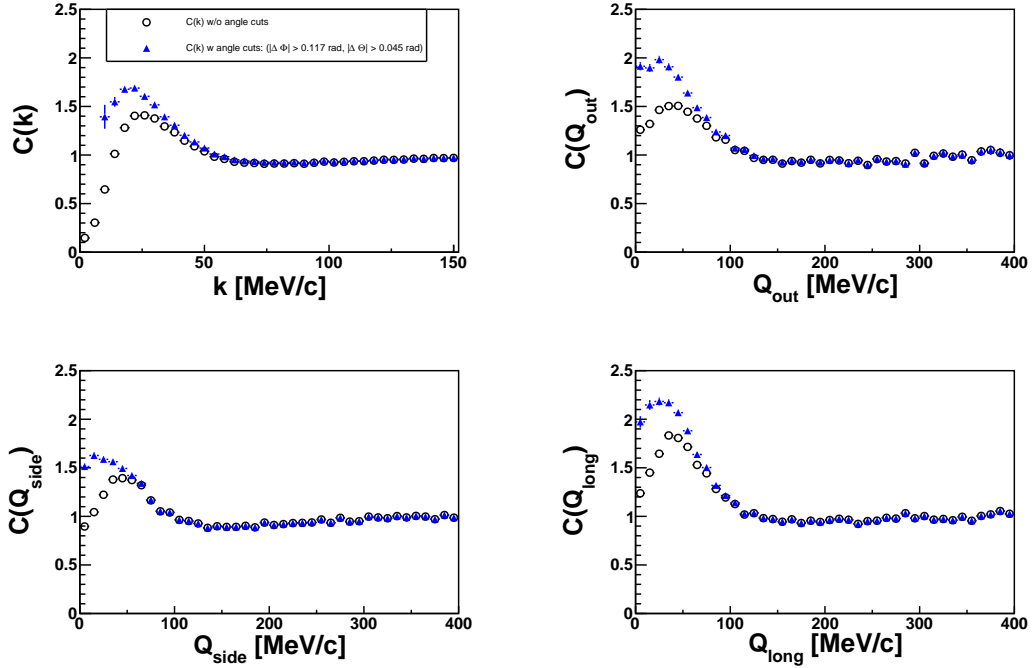


Figure 4.12: Comparison of the $p-p$ correlation function in the k and $q_{o,s,l}$ representation. The reduction of the merging effect is clearly visible.

gation of non-flat baseline structures. Most transport models like UrQMD and GiBUU don't contain femtoscopic effects. Thus any correlations visible from these models can be traced back to correlations from e.g. energy and momentum conservation. This additional correlations are displayed in Fig. 4.14. One can see that for $p-p$ as well as $p-\Lambda$ the baseline is not flat and rises when going to larger relative momenta. This non-flatness could also have an influence on the lower momentum region. For this region a correction procedure is applied. The correlation function corrected for close track efficiency is divided by the correlation function describing the LRC:

$$C_F(k) = \frac{C(k)_{\text{measured}}}{C(k)_{\text{LRC}}}, \quad (4.2)$$

where $C(k)_{\text{measured}}$ is the experimental correlation suffering from LRC and $C(k)_{\text{LRC}}$ is the correlation function which includes only LRC. Two different approaches are chosen to obtain the latter. For the $p-p$ pair the UrQMD correlation function is directly used for $C(k)_{\text{LRC}}$ since the statistics is quite large. This also helps to reject any residual merging effects as discussed in the previous Section. A very similar ansatz to model LRC was exploited in a femtoscopy analysis of identical neutral Kaons measured by ALICE in pp collisions [Abe+06]. To model LRC for the $p-\Lambda$ pair a different path is chosen since the

| Reaction | a [mb] |
|--|----------|
| $pp \rightarrow p\Lambda K^+$ | 187.9 |
| $pn \rightarrow n\Lambda K^+$ | 140.6 |
| $pp \rightarrow p\Sigma^0 K^+$ | 532.1 |
| $pn \rightarrow p\Sigma^0 K^+$ | 131.55 |
| $\Delta^+n \rightarrow \Delta^0\Lambda K^+$ | 31.2 |
| $\Delta^+p \rightarrow \Delta^+\Lambda K^+$ | 291.7 |
| $\Delta^+n \rightarrow \Delta^0\Sigma^0 K^+$ | 111.2 |
| $\Delta^+p \rightarrow \Delta^+\Sigma^0 K^+$ | 1062.0 |

Table 4.3: Channels in GiBUU that are responsible for the Λ production. The corresponding (scaled) cross section factor is displayed.

statistics in these simulations is lower. A polynomial function is sufficient to describe the baseline:

$$C_{\text{LRC}}(k) = 1 + ak + bk^2, \quad (4.3)$$

where a, b are coefficients determined by a fit to the baseline outside of the femtoscopic region in the range $k \in [250, 600]$ MeV/ c to the simulated as well as to the experimental correlation function. This was done to exploit possible effects at low relative momentum between the two baselines. But no significant difference is observed as shown on the bottom of Fig. 4.14. The dashed line represents a fit of Eq. (4.3) to the experimental correlation function whereas the solid line represents a fit to the correlation function from GiBUU.

4.2.3 Momentum Resolution

HADES measures the produced particles with a finite momentum resolution of about 2-6%. At the collision vertex particles are emitted with ideal unsmeared momenta $\mathbf{p}_1, \mathbf{p}_2$. This perfect momenta set the scale for the final state interactions between the particles and the ideal correlation function is based on them $C(\mathbf{p}_1, \mathbf{p}_2) = C(k)$. In the experiment the smeared momenta are used $C(\mathbf{p}'_1, \mathbf{p}'_2) = C(k')$, which deviate from the ideal momenta. To account for this effect a correction factor is introduced [Ada+05]:

$$K(k) \equiv \frac{C(k)_{\text{ideal}}}{C(k')_{\text{smeared}}} = \frac{C(k)_{\text{real}}}{C(k')_{\text{F}}}, \quad (4.4)$$

where the “ideal” correlation function is the one without detector resolution and the “smeared” is affected by momentum resolutions. $C_{\text{F}}(k)$ is the measured correlation function. Thus, to get back the “real” correlation function one has to obtain the ratio

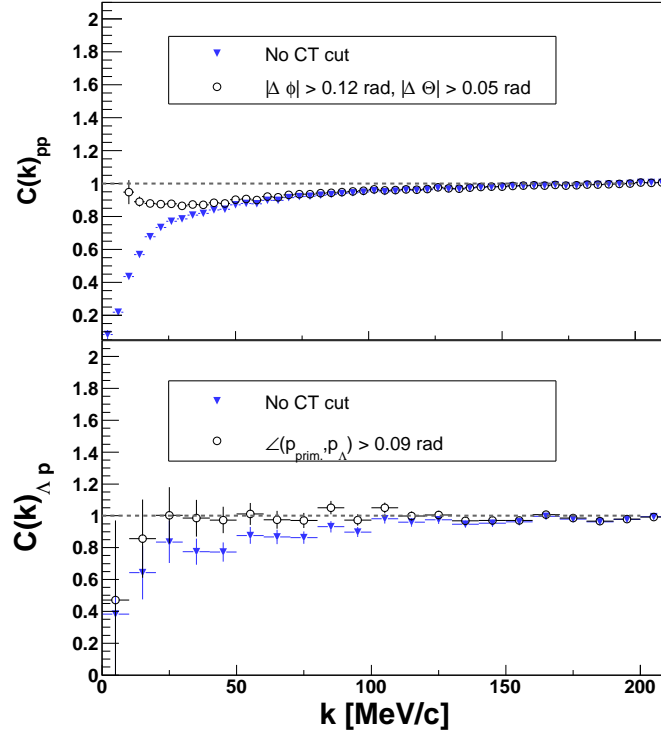


Figure 4.13: Correlation functions for $p - p$ (top) and $p - \Lambda$ (bottom) obtained from UrQMD and GiBUU (see text). One can see that a minimal cut on angles between the particles cures the track merging.

of the “smeared” and “ideal” correlation function. To get this ratio a simulation sample from UrQMD is used. This sample is processed through the whole analysis chain thus includes also the momentum resolution introduced by the track reconstruction. For every track which enters the analysis also the input momentum can be accessed. To not include any other correlations mixed event samples are used. They contain also proper pair statistics following a k^2 distribution. The samples are weighed with a femtoscopic weight which is calculated with the ideal momentum:

$$C(k)_{\text{ideal}} = \frac{B(k, w(k))}{B(k)}, \quad (4.5)$$

where $B(k)$ is a mixed event sample and $w(k)$ the femtoscopic weight. The weights are calculated from CRAB using as input a Gaussian source from a random number generator. Since “ideal” is just a labelling of the momenta in Eq. (4.5) the correlation function is invariant if all momenta are switched to the smeared momenta $k \rightarrow k'$, also for the weight. The momentum resolution comes into play when the weight is calculated with the “ideal” momenta but the smeared momentum is weighted. This is actually what

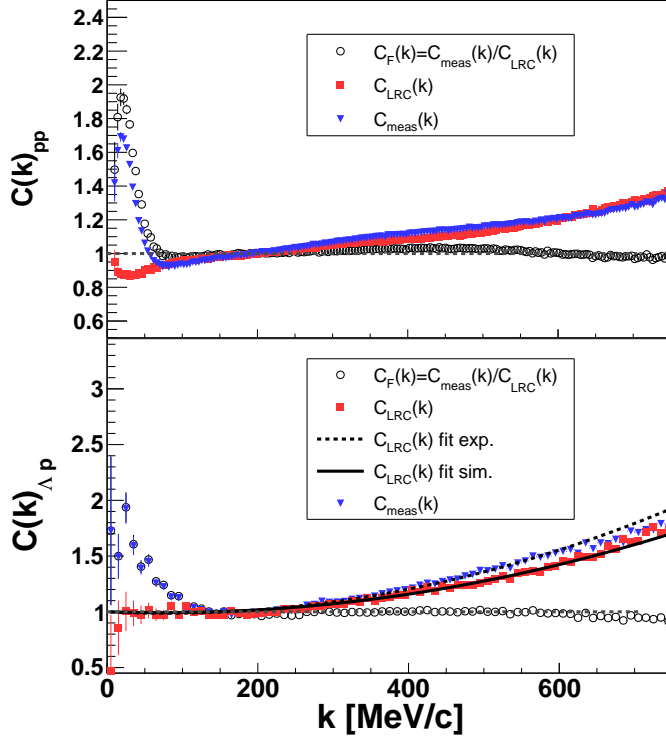


Figure 4.14: Effects of LRC on the correlation function. Top: $p-p$ pairs where UrQMD is used to describe the baseline. Bottom: $p-\Lambda$ pairs where Eq. 4.3 is used to describe LRC. The experimental (dashed) as well as the simulation (solid) correlation function is fitted in $k \in [250, 600]$ MeV/c to check for any differences at low k .

happens in the experiment:

$$C(k)_{\text{smearred}} = \frac{B(k', w(k))}{B(k')} . \quad (4.6)$$

One can think of a histogram where the correct weight enter in the wrong bin of the histogram due to the finite resolution. It has the effect that the correlation function broadens. This is displayed on the right of Fig. 4.16 for $p-p$ pairs. Figure 4.15 shows the resolution matrix for the input and reconstructed momenta differences. They are correlated but a finite width is present, which is the resolution. The effect of the momentum resolution is also evaluated for the $k_{o,s,l}$ representation. This is displayed in Fig. 4.17. Also there a significant influence on the measurement can be observed. The resolution matrix for $p-\Lambda$ is displayed in Fig. 4.18 and the effect of the smearing in Fig. 4.19. The corrected experimental correlation functions $C_{\text{unsmeared}}(k) = C_{\text{real}}(k) = K(k) \times C_F(k)$ for $p-p$ and $p-\Lambda$ are displayed in Fig. 4.20. One can see that the momentum resolution has a sizeable effect for $p-p$ pairs. The restored correlation function is much more peaked

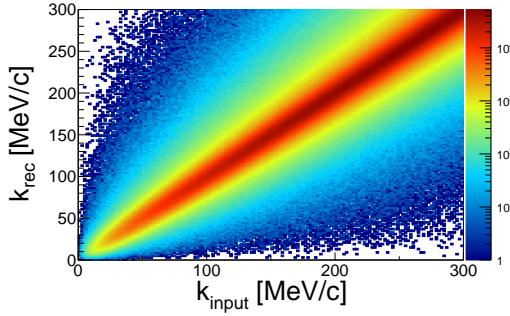


Figure 4.15: Resolution matrix of $p-p$ for the momentum differences k . The x-axis shows the input momenta and the y-axis the reconstructed momenta.

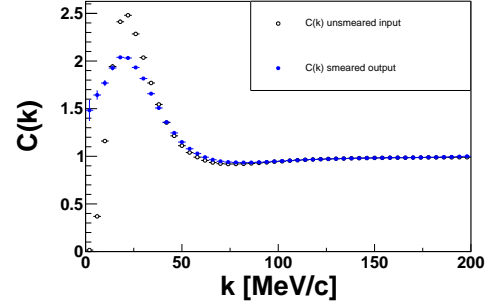


Figure 4.16: Right: Correlation function from simulation for $p-p$. The open circles show the unsmeared correlation function and the blue triangles the effect of the momentum resolution.

and and also less broad. The behavior of the momentum resolution depends clearly on the functional form of the correlation function. The $p-p$ form is in general rather complex, thus a small deviation in the relative momentum Δk leads to a strong change in ΔC . If the unsmeared ideal correlation function $C(k)$ is reconstructed at a slightly different momentum k' the change is strongly pronounced. The $p-\Lambda$ correlation function is a smoother function. The finite resolution has a different effect even when the resolution matrix is very similar. A final word on the method. It uses as input already an assumption about the correlation function. Thus it needs an assumption about the source function and the interaction. The source radii are varied and changes are included in the systematic error. In future it is better to use a model in which the fit function is propagated through the resolution matrix and then compared to the data. For every interaction the resolution is then separately taken into account. However, in the method presented here the ratio of Eq. (4.4) is rather insensitive to any parameter choices.

4.2.4 Purity and residual Correlations

Particles are measured with a finite purity with the detector setup. If the purity is rather large one measures basically only the pairs of interest. The misidentified pairs don't contribute to the correlation signal and just dilutes it. To restore the complete signal and correct for the misidentified pairs a purity correction has to be performed. It is based on the fact that only the femtoscopic signal is diluted, thus one subtracts from the true correlation function the baseline, reweights the femtoscopic signal and adds the baseline to it [Lis+05]. This leads to a diluted correlation function. Mathematically it reads:

$$C(k)_{\text{pur,uncorr}} = \lambda(C(k)_{\text{pur,corr}} - 1) + 1, \quad (4.7)$$

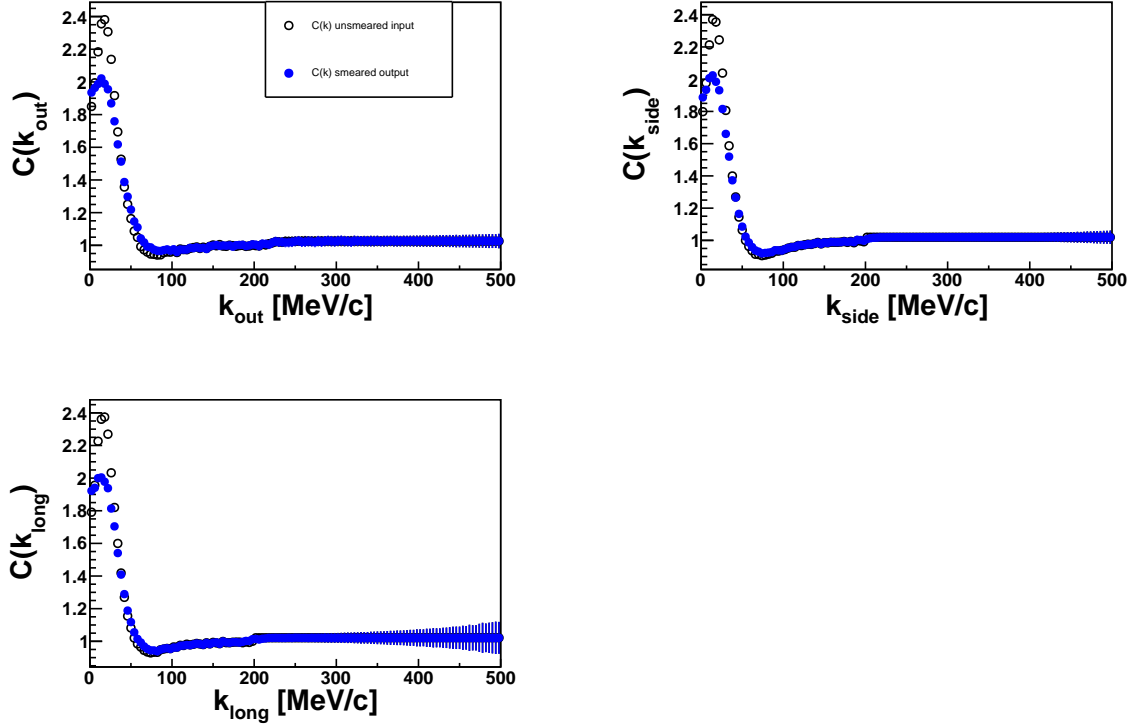


Figure 4.17: Effect of the momentum resolution for $k_{o,s,l}$ projections.

where $C(k)_{\text{pur,uncorr}}$ is the purity uncorrected correlation function like it is measured in the experiment and $C(k)_{\text{pur,corr}}$ is the “true” correlation function for perfect purity. Thus, this equation can be converted for $C(k)_{\text{pur,corr}}$. The exercise which is left is then to determine the parameter λ . It is the product of the pair purity and the fraction of directly produced pairs assumed in many analyses e.g. [Ada+06; Ant+11] and also by analyses developed in HADES [Aga+10; Aga+11]. The pair purity is simply the product of the single-particle purities and the fraction of directly produced pairs is the product of the single-particle fractions:

$$\begin{aligned} \lambda &= \text{Pur}_b \text{Pur}_b, \\ \text{Pur}_i &= \mathcal{P}_i f_i, \end{aligned} \tag{4.8}$$

where \mathcal{P} is the single-particle purity and f is the fraction of directly produced particles in the sample. The single particle purity in case of Λ is directly given by the fit of the invariant mass spectra shown in Tab. 4.2. The proton purity is determined by UrQMD where the tracks entering the analysis via all experimental selections are checked for the

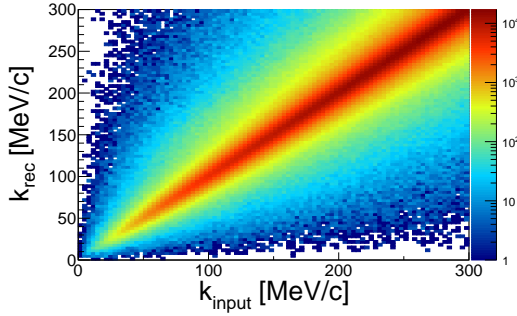


Figure 4.18: Resolution matrix of p - Λ for the momentum differences k . The x-axis shows the input momenta and the y-axis the reconstructed momenta.

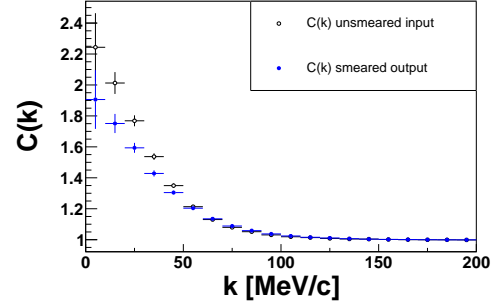


Figure 4.19: Right: Correlation function from simulation for p - Λ . The open circles show the unsmeared correlation function and the blue triangles the effect of the momentum resolution.

correct PID. The protons for the p - Λ pair are only selected with the MDC specific energy loss, which results in a slightly worse purity of about 2%.

The effect of feed-down from higher lying resonances can introduce residual correlations. The weakly decaying resonance transfers its momentum mostly to the daughter baryon and the initial correlation is transformed to the daughter pair. Due to kinematic limitations of the observed reaction it is ruled out that e.g. two protons stem from a Λ decay $\Lambda \rightarrow p_{\Lambda} p_{\Lambda}$. The produced particles are always quite baryon rich since all initial particles consist of baryons. The fraction of protons coming from a Λ decay is estimated with UrQMD to about 0.003. This feed-down can be neglected and all protons are primary protons. The main source of Λ feed-down is coming from Σ^0 . The Σ^0 hyperon decays electromagnetically almost exclusively in a Λ, γ pair already at the primary vertex. There is no chance to distinguish between direct Λ and Λ_{Σ^0} experimentally. The fraction Λ from Σ^0 is determined from a statistical model analysis performed in p+Nb reactions [Aga+16]. It calculates on basis of measured multiplicities thermodynamic quantities. This model predicts the ratio $\Lambda/(\Lambda + \Sigma^0) = 0.82$. A variation of this of 10% is taken into account as systematic uncertainty in the final parameter. Experimentally, the $p - \Sigma^0$ interaction was studied in reactions of $pp \rightarrow pK^+\Sigma^0/\Lambda$ at different excess energies by the COSY-TOF Collaboration [Abd+10]. The cross section for including a Σ^0 was perfectly in agreement with a phasespace parametrization whereas for the description for the Λ channel also final state interactions had to be taken into account. This shows that the $p - \Sigma^0$ interaction seems to be quite weak. For this reason it is not taken into account as residual correlation. The initial correlation is anyway hard to model [Sta+07], because of different isospin configurations of the pair system and couplings to other channels. A summary of the single particle purities and the λ parameter are shown

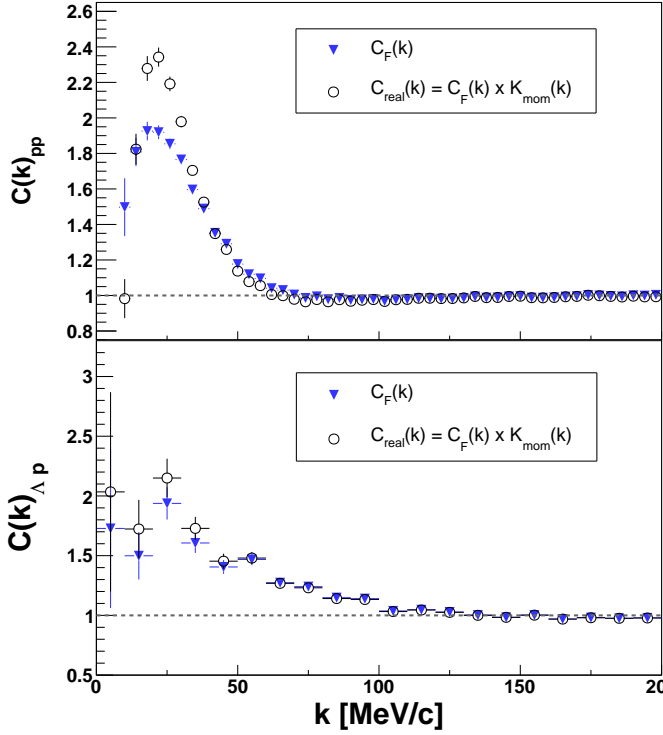


Figure 4.20: Effect of the correction for momentum resolution the measured experimental correlation functions of $p - p$ (top) and $p - \Lambda$ (bottom).

in Tab. 4.4 (combination 1 is the default parameter set of the analysis).

4.3 Comparison to transport model predictions

With femtoscopy the size of the emission region is measured by comparing it to a model, which includes an assumption about the source function. A transport model can provide besides the kinematic information of the particles also the coordinates of the last interaction point. This spatial coordinate is exactly the quantity which enters the calculation of the source function. Thus the source function can be reconstructed from transport

| Particle Pair | Pur _a | Pur _b | λ |
|---------------|--------------------|------------------|-----------|
| $p - p$ | 0.99 | 0.99 | 0.98 |
| $p - \Lambda$ | 0.86 \times 0.82 | 0.97 | 0.68 |

Table 4.4: Purity parameter used to correct the correlation functions for purity.

model simulations and if one trusts the predictions it can be used to constrain the source function used to describe the experimental data. This reduces the number of free parameters in the interpretation of the correlation function and allows to test the scattering parameters that govern the interaction more precisely. Since UrQMD worked already perfectly to describe the LRC as discussed before, it is natural to use it further to constrain the source function. One has to keep in mind that UrQMD is a semi-classical transport model, so it does not include any quantum mechanical treatments of the emitted pairs. For this reason one needs an additional software which is able to compute final state interactions based on the kinematic and spatio-temporal output of the transport model. In this analysis the publicly available Correlation After Burner CRAB [Pra17], is used to compute these final state interactions. It solves the Schrödinger equation numerically to obtain the wave function. The ansatz for the wave function in CRAB is motivated by the asymptotic solution of the radial wavefunction in a partial wave basis, see e.g. [Daw78]:

$$R_l(r) \sim u_l^{(+)}(r) - S_l u_l^{(-)}(r), \quad (4.9)$$

where $u_l^{(\pm)}$ are the incoming and outgoing waves of the scattering process. The outgoing wave is modified by the scattering potential. This information is included in the unitary scattering matrix which contains the phaseshift $S_l = \exp(i2\delta_l)$. At $r \rightarrow \infty$ the functions $u_l^{(\pm)}$ match with plane waves and the only difference to a non scattered wave is the shift in phases of the outgoing wave. The phaseshift and the incoming and outgoing waves are computed by CRAB. The ansatz in Eq. (4.9) is actually questionable for small separations $r \rightarrow 0$ since in this case the phaseshift between the incoming and outgoing wave function might not be sufficient to describe the deviation. At small separations the wave function is inside the strong interaction potential and the phaseshift builds up when the wave function propagates outside of the strong potential. For this reason it is questionable to use it for very small source sizes like pp or even smaller systems and a development of a new model was triggered within this thesis [Mih]. The influence of small sources is discussed in section 2.0.5 where the construction of the Lednicky model is explained.

To test UrQMD a simulation was performed at seven different impact parameter in a range of $b = 1 - 7$ fm to include also the tails of the Nb nucleus. CRAB needs also the information how probable such an event is. For this the probability of having an empty events is used to compute it since in. After a UrQMD simulation was performed the model prints the number of events in which no collision took place. At larger impact parameter it is more likely that the proton misses the nucleus compared to central collisions where more or less in every event a reaction takes place.

UrQMD uses for the scattering of the produced particles parametrizations of cross sections. For the hyperon-nucleon scattering and corresponding resonances it relies on calculations of the additive quark model (AQM) [Gou83]. This parametrization of the cross

section is independent of the energy between the particles. The experimental p - Λ cross section extracted from hyperon-nucleon scattering data shows a rising for lower incoming Λ lab momenta [Ale+68; Sec+68]. Within this work the UrQMD p - Λ scattering parametrization was adapted according to the scattering data. The scattering data is displayed in Fig. 4.21 together with the standard AQM model predictions and two other parametrizations. The two different parametrizations are motivated by a chiral effective field theory calculation at leading order and next-to-leading order [Hai+13] to check for systematic effects on the outcome. Following functions are found to describe the calculated cross sections of [Hai+13] at the two expansions:

$$\sigma(p)_{\text{LO}} = \begin{cases} 247.86 - 0.688p + 49.56410^{-5}p^2 & p < 0.6 \text{ GeV}/c \\ 14.4p^{-0.12} & p > 0.6 \text{ GeV}/c \end{cases} \quad (4.10)$$

$$\sigma(p)_{\text{NLO}} = \begin{cases} 203.56 \exp(-14.47p^2) + 253.88 \exp(-76.19p^2) & p < 0.4 \text{ GeV}/c \\ 14.4p^{-0.12} & p > 0.4 \text{ GeV}/c \end{cases} \quad (4.11)$$

One can see in Fig. 4.21 that the AQM predicts the order of magnitude of the cross section correct but the rising of the cross section at lower Λ momenta is not included. This is only included by the NLO parametrization of Eq. (4.11). The different parametrizations of LO and NLO are tested in the extractions of the freeze-out coordinates. The influence is negligible. For the extraction of freeze-out coordinates kinematic selections are employed. Since the femtoscopic signal is located at small relative momenta only pairs which fulfill $k < 30 \text{ MeV}/c$ are taken into account. The source function depends also on the total momentum. The center of mass of the pair is moving with \mathbf{P} and emits the pairs around this center of mass movement $\mathbf{P} \pm \mathbf{k}$. Pairs with larger $|\mathbf{P}|$ might stem from a different underlying process than particles with lower values. As an example, in heavy-ion collisions pairs with large total momentum might be strongly influenced by flow effects. This actually suggests to also use a gating in $|\mathbf{P}|$ [Led; Bro]. Only pairs which have very similar \mathbf{P} are used to reconstruct the source. For every component a maximal deviation of $100 \text{ MeV}/c$ is allowed. Additionally, the HADES acceptance is taken into account by using only particles which fly in the region $\Theta \in [15^\circ, 85^\circ]$ with a positive z -momentum component $p_z > 0$. The predicted freeze-out coordinates in the out-side-long coordinate system from UrQMD with the discussed selections are shown in Fig. 4.22 for $p-p$ and in Fig. 4.23 for p - Λ . Already at this stage it seems that the width of the p - Λ correlation function is a bit smaller compared to $p-p$. To quantify this the coordinates are transformed into the PRF (indicated by asterisk) also in out-side-long representation. Basically the out-component is affected by the boost. The one-dimensional radius is then defined as the sum of the components:

$$r_{\text{inv}}^* = \sqrt{r_{\text{out}}^{*2} + r_{\text{side}}^{*2} + r_{\text{long}}^{*2}}. \quad (4.12)$$

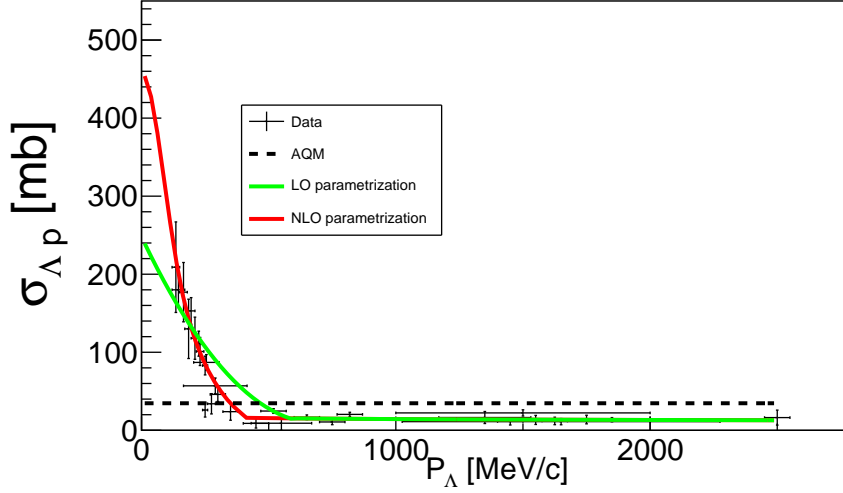


Figure 4.21: Cross section for p - Λ scattering. The AQM is part of the standard UrQMD model. The LO and NLO expansions are motivated by [Hai+13].

This equation gives strictly speaking the projection of the full source function onto the r_{inv}^* component. Usually, one fills a histogram with this variable and divides it by the Jacobian $\sim r^{*2}$ [Sha+15]. In case of a perfect Gaussian source one retrieves the full Gaussian source because it contains no special angular dependence. Actually, the full source information is included in the out-side-long representation. To avoid the weighting with $1/r^{*2}$ the source is investigated directly in the out-side-long basis in the PRF. In [Kis10] it was shown that one can define an average radius by:

$$r_{av}^* = \sqrt{\frac{r_{out}^{*2} + r_{side}^{*2} + r_{long}^{*2}}{3}}, \quad (4.13)$$

which connects the 1D and 3D radii. The goal is to fit the out, side and long projections for p - Λ and p - p pairs of UrQMD separately and extract the width in all three directions. With Eq. (4.13) the average radius for both pairs is then calculated. This can be used to define a scaling between both parameters. Since the p - p radius can be extracted from the experimental measurement one can use the scaling of the radii from UrQMD to fix the p - Λ radius. This allows to investigate solely the scattering parameter.

Since all models use Gaussian descriptions for the source and the distributions look pretty Gaussian from UrQMD, a Gaussian parametrization is used to extract the width

in the region $r_i \in [-10, 10]$ fm:

$$dN/dr_{o,s,l}^* \sim \exp(-r^{*2}/2\sigma_{o,s,l}^{*2}). \quad (4.14)$$

The width of this Equation is related to the radii via $\sigma_{o,s,l} = \sqrt{2}r_{o,s,l}^*$ because a two-particle quantity is described. The fit of the out-side-long projections is shown in Fig. 4.24. The curves for p - Λ in Fig. Fig. 4.24 are scaled to fit on the same histogram due to the lower statistics of this pair. One can see that the width parameter of the projections is a bit smaller for p - Λ . The fits are repeated for the LO parametrization in exactly the same way. The extracted average radii for the NLO case are $r_{av,pp} = 2.15$ fm and $r_{av,p\Lambda} = 1.76$ fm which are compatible with the radii obtained from the fitting. The ratio of the width is finally obtained using Eq.(4.13) to be:

- $RF_{LO} = \frac{r_{av,pp}}{r_{av,p\Lambda}} = 1.179$,
- $RF_{NLO} = \frac{r_{av,pp}}{r_{av,p\Lambda}} = 1.184$.

This ratios are used in the next Section to fix the radius of the p - Λ correlation function via the measurement of the experimental $p-p$ radius $r_{0,pp}$. The source relation is then

$$r_{0,p\Lambda} = \frac{r_{0,pp}}{RF}, \delta r_{0,p\Lambda} = \left| \frac{\delta r_{0,pp}}{RF} \right|. \quad (4.15)$$

In a last step the coordinates are put to CRAB that it calculates the correlation functions with a impact parameter gating discussed above. CRAB allows also to perform a boost into the LCMS, which is then used to calculate projections of the 3D correlation function on the out-side-long axes in this frame. The definition of this frame is shown in section 2.0.11. Exactly the same projection intervals of $k_{o,s,l} < 20$ MeV/c are used for the projections like in the experimental data. The results of the comparison are displayed in Fig. 4.25.

4.4 Experimental results

4.4.1 Source size extraction

First the Gaussian source sizes for both pairs are extracted by comparing it to femto-scopic models. For $p-p$ a model is used, which was developed to describe $p-p$ and nuclear correlations [Kot+99]. It calculates the Schrödinger Equation numerically with the Reid potential. For partial waves $l = 0, 1$ the nuclear modification of partial waves is taken into account. For $l > 1$ only Coulomb waves are summed up. The function is minimized using a χ^2 minimization implemented with TMinuit ¹, which is part of the ROOT framework. The theoretical p - Λ correlation is compared to the Lednicky model of Eq. (2.32). For the Lednicky model an analytic form exists. This allows to use it

in a TF1 χ^2 minimization. Results of the fits are shown in Fig. 4.26. For $p-p$ pairs a source size of $r_{0,pp} = 2.02 \pm 0.01(\text{stat})_{-0.12}^{+0.11}(\text{sys})$ fm is extracted. The systematic errors are obtained by a variation of the two track cuts to reject merging, the correction of the momentum resolution of 20%, a change of the normalization and a change of the interaction potential of the triplet state. All errors are summed up quadratically assuming its independence. The $p-p$ source sizes are also extracted as a function of the total transverse momentum $k_T = \frac{1}{2}|\mathbf{p}_{T,1} - \mathbf{p}_{T,2}|$ in three bins in $k_T \in [175, 750]$ MeV/c. One can see in Fig. 4.27 that the source size drops slightly (on the order of 10%) as a function of the transverse momentum. In heavy-ion collisions such a drop is usually addressed to a collective expansion of the particle emitting system. This induces correlations among spatial and kinematic coordinates. Also for smaller systems a dependence of the source size as a function of the transverse momentum is measured [Nig+16] (and references therein). In ALICE for pp collisions at 7 TeV also a decreasing of the source size with larger transverse for large multiplicity events is observed, for pion as well as kaon pairs [Aam+11; Abe+13; Abe+12]. If this is a sign of any collectivity is still under debate. In this analysis the decrease is not addressed to any collective effect. In the momentum region where the pairs are produced the Nucleon-Nucleon cross section drops as a function of momentum [Oli+14]. Thus rescattering becomes less probable with the nucleons inside the nucleus and the protons freeze-out earlier when going to larger k_T . A very similar interpretation was made in [Sta+04], where $p-p$ correlations from $e(4.46 \text{ GeV})+A$ were measured.

The extracted $p-\Lambda$ source size by fitting the Lednicky model to the experimental correlation function is $r_{0,p\Lambda} = 1.62 \pm 0.02(\text{stat})_{-0.18}^{+0.19}(\text{sys})$ fm. The systematic errors were evaluated by a variation of the correction for momentum resolution, close track rejection, purity correction, normalization of the baseline, the chosen interaction, and the contribution from Σ^0 feed-down. The $p-\Lambda$ source size is smaller compared to the one obtained in $p-p$ correlations. A similar finding is obtained for the Ar+KCl collision system [Aga+10]. It might be that the Λ has a smaller interaction probability with nucleons in this energy regime due to the smaller cross section. A comparison of the elastic $p-\Lambda$ cross section together with the total cross section of $p-p$ and $p-n$ [Oli+14] is shown in Figure 4.28. One can see that indeed the NN cross section is larger compared to $p-\Lambda$.

The extracted source sizes can be compared to other measurements. For the $p-\Lambda$ radius only measurements from A+A collisions are published. The one-dimensional radius for $p-p$ pairs were extracted mainly at SPS energies in p+A reactions by the WA80 and NA44 Collaborations. WA80 measured $p-p$ pairs in p+Au,Ag,Cu,C reactions at 200 AGeV [Awe+95]. NA44 in p+Pb collisions at 450 GeV/c [Bog+99]. Also at Fermilab H2-Ne bubble chamber experiments radii for $p-p$ were extracted in p+Ne reactions [Azi+84]. They are of the order of 2 – 6 fm but because of the old data its hard to evaluate them. The radii measurements of this thesis are compared to results of

¹<https://root.cern.ch/doc/master/classTMinuit.html>

large and medium size nuclei, where the source is of the size of the Nb nucleus. This is shown in Fig. 4.29. One can see in this Figure that the energy gap is rather large between HADES and the other measurements. There might be an energy dependence between the radii but more data would be needed to clarify this.

4.4.2 Test of scattering parameter

To fix the source radius for p - Λ the reduction factors of Section 4.3 are used. The goal is to investigate the sensitivity of the correlation function $C(k)$ to scattering parameters, which are predicted from a chiral effective field theory expansion [Hai+13]. The parameters are taken at a cutoff value of 600 MeV. The scattering length of the two expansions lead to completely different total cross sections, whereas the total cross section of NLO describes the scattering data much better. It is investigated with the correlation function if a similar trend is also there observed. The radius for the p - Λ correlation function is fixed with help of Eq. 4.15. The result of the correlation function with the fixed radius and the two different scattering sets of LO and NLO is presented in Fig. 4.30. The bands are related to the total statistical and systematic uncertainty which enters Eq. 4.15. Before discussing the result a remark on Fig. 4.30. It is based on the Lednicky model which includes a correction term for the wave function in the range of the nuclear potential, which is described by Eq. 2.30. In Fig. 4.30 this correction term was initialized with $1/\pi$ instead of $1/\sqrt{\pi}$. The fully correct Lednicky model is shown in Fig. 4.31.

One can see that the correlation function develops a sensitivity on the chosen scattering parameter and prevails with the correct description of the Lednicky model. The behavior of the cross section is also reflected in the correlation function. However, the statistics is not enough to draw any definite conclusion. An increase of a factor 10 in pairs would lead to a sensitivity that would allow for the discrimination between the results. HADES will be upgraded with a forward detector which increases the acceptance at low angles below $\Theta < 18^\circ$. Additionally, an electromagnetic calorimeter will be installed. This will enable also to reconstruct Σ^0 by the detection of the daughter photon. This opens also the possibility to study the $p - \Sigma^0$ correlation function.

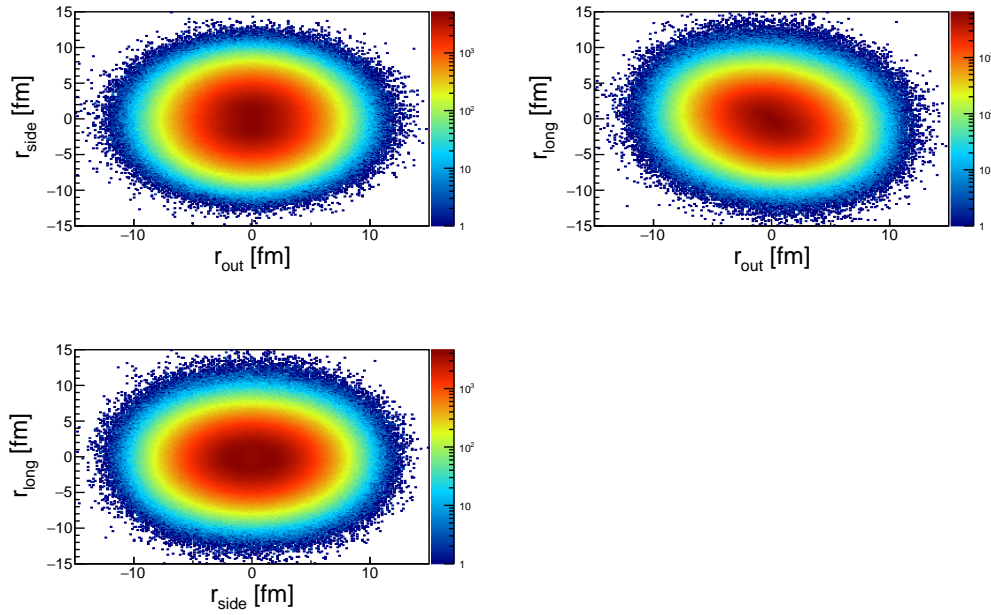


Figure 4.22: Freeze-out coordinates in the out-side-long basis for $p - p$ pairs from UrQMD.

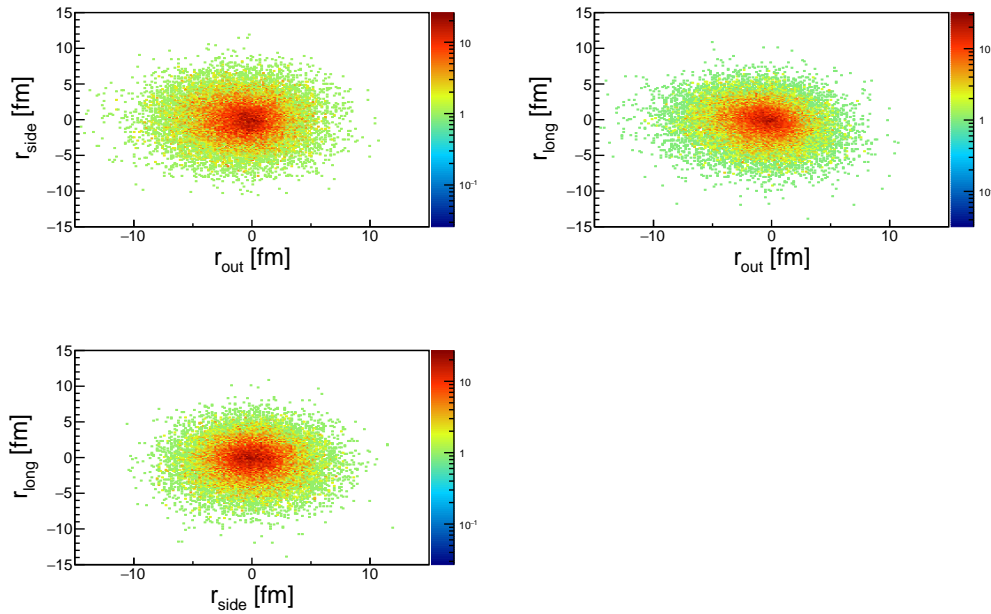


Figure 4.23: Freeze-out coordinates in the out-side-long basis for $p-\Lambda$ pairs from UrQMD.

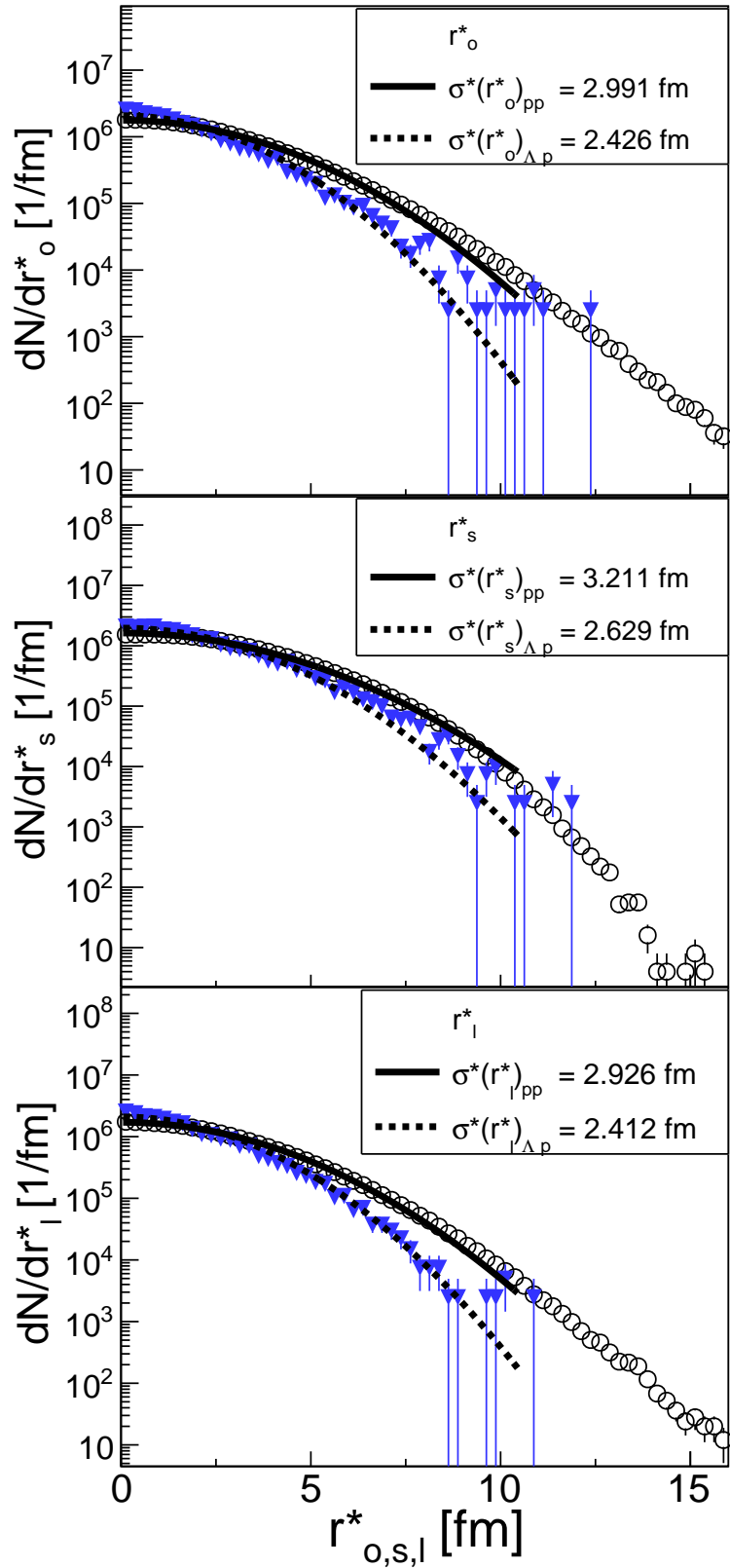


Figure 4.24: The projections in out-side-long direction in the PRF for $p-p$ (open circles) and $p-\Lambda$ (blue triangles) pairs from UrQMD. The $p-\Lambda$ values are scaled to fit on the same plot. The width in every direction is obtained by fitting to it a Gaussian function (solid $p-p$, dashed $p-\Lambda$).

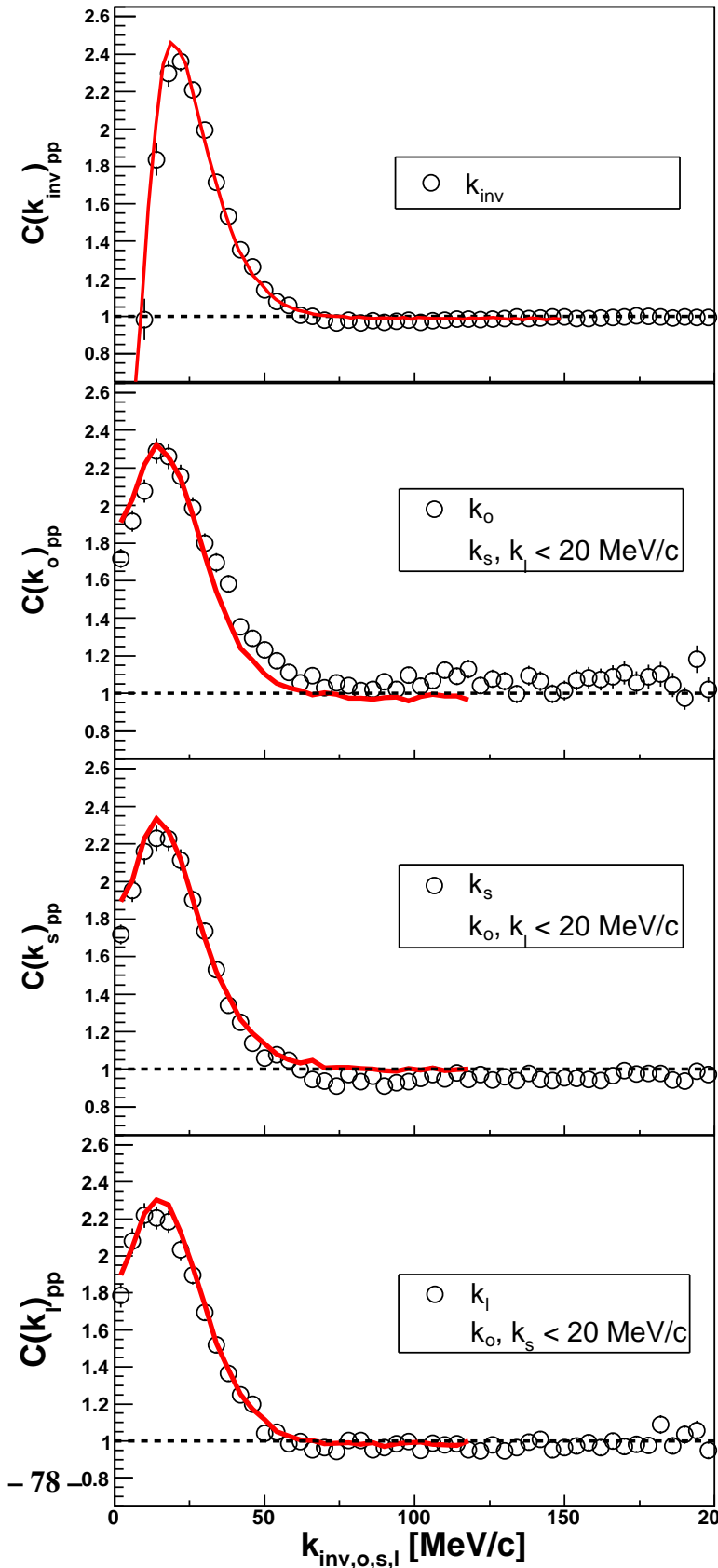


Figure 4.25: Comparison of fully corrected experimental $p - p$ correlations (open circles) to predictions of CRAB (red lines) which use UrQMD as input. The plot at the top is the one-dimensional correlation function. The other three are projections of the 3D correlation function in the LCMS.

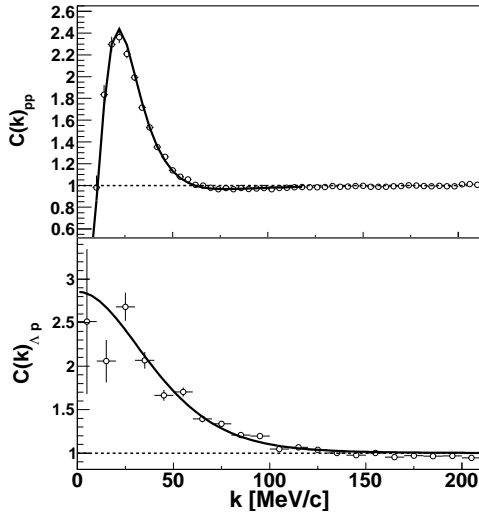


Figure 4.26: Model comparison of the $p-p$ correlation function (top) and $p-\Lambda$ (bottom) to extract the source size.

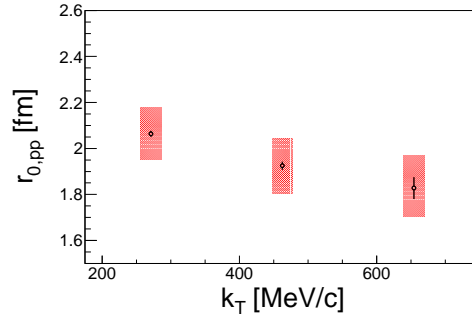


Figure 4.27: The $p-p$ source size as a function of the total transverse momentum k_T .

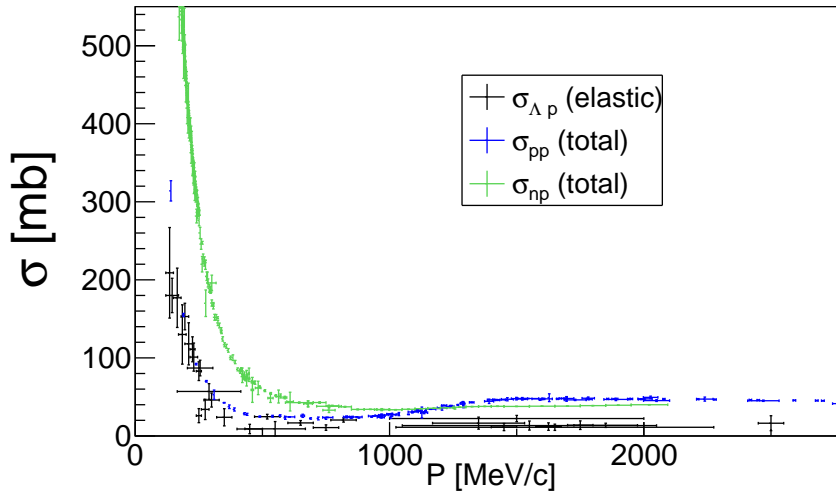


Figure 4.28: Comparison of cross sections of NN scattering and $p-\Lambda$.

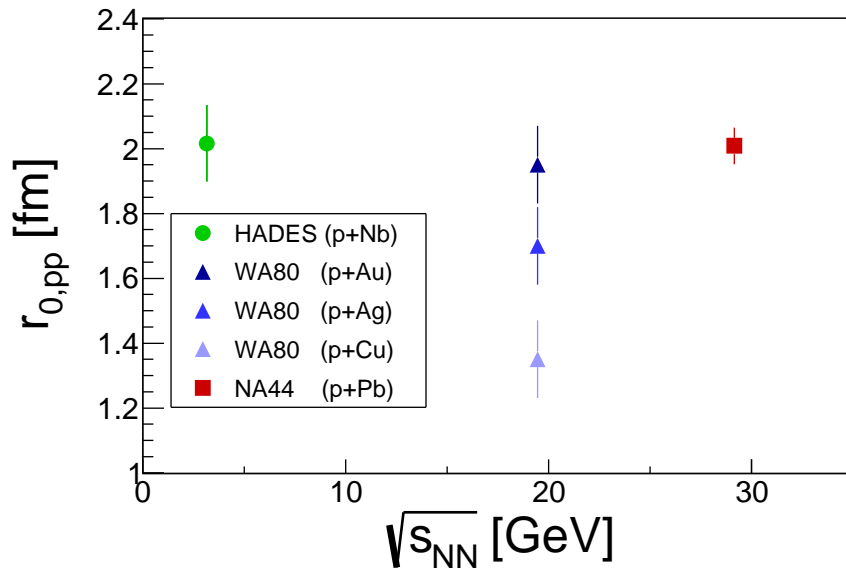


Figure 4.29: Comparison of the extracted source radius to measurements of other radii from p+A collisions.

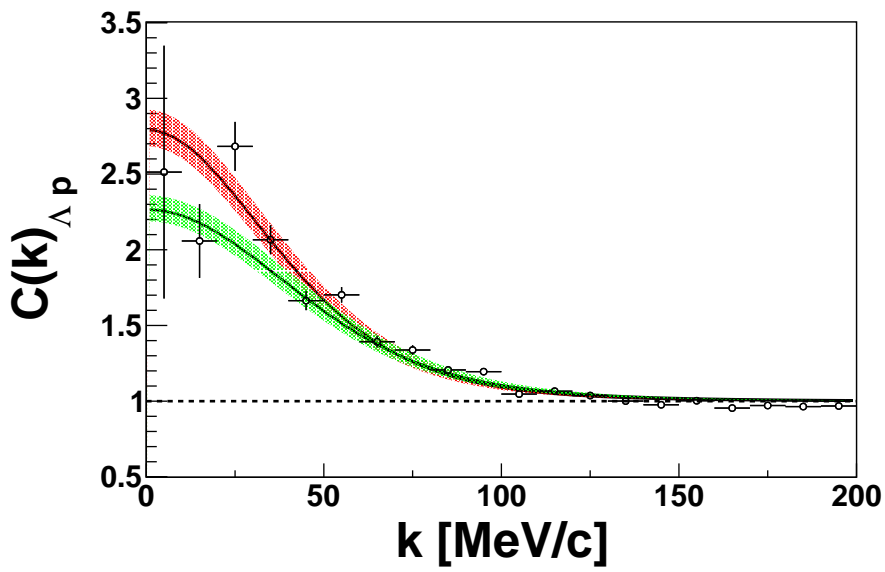


Figure 4.30: Influence of different sets of scattering parameter on the correlation function. The LO and NLO scattering length at a cutoff value of 600 MeV are taken from [Hai+13]. A small bug entered this figure, which is explained in the text.

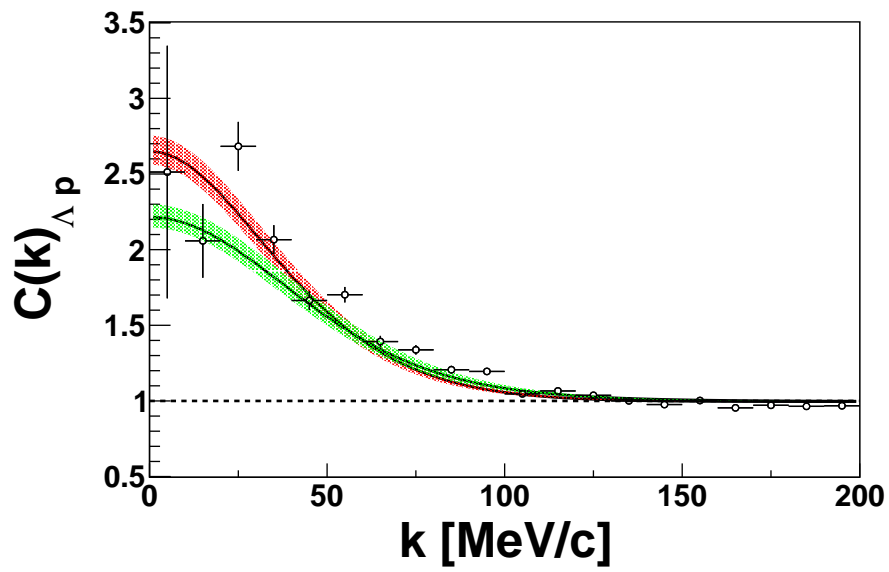


Figure 4.31: Influence of different sets of scattering parameter on the correlation function. The LO and NLO scattering length at a cutoff value of 600 MeV are taken from [Hai+13]. This figure includes the fully correct Lednický model. See text for details.

Part II
PART II

5

The ALICE detector at the LHC

To study the production of heavy particles like the Higgs or predicted supersymmetric particles which are supposed to exist at the TeV scale, a powerful machine is necessary. Also for investigations of matter under extreme conditions created in heavy-ion collisions one has to deposit a lot of energy in a small volume. For this reasons the Large Hadron Collider (LHC) was built. It is a two-ring-superconducting-hadron accelerator which was installed in the existing 26.7 km tunnel that was constructed for the CERN LEP (Large Electron-Positron Collider) machine [EB08].

A Large Ion Collider Experiment (ALICE) is one of the four major experiments (ALICE, ATLAS, CMS, LHCb) operating at the LHC and situated at interaction point IP2. It is optimized for the study of QCD matter created in high-energy heavy-ion collisions, where it is believed that right after the collision hadrons are not the relevant degrees of freedom anymore but deconfined quarks and gluons. General features of ALICE are its high detector granularity, a low transverse momentum threshold $p_T \approx 0.15 \text{ GeV}/c$ and a good capability for particle identification up to $20 \text{ GeV}/c$ [Abe+14b]. The ALICE global reference system is defined as follows: the z axis is aligned with the beam line, the x axis in the LHC plane pointing to the center of the accelerator, and the y axis points upward. The detector setup with its individual components is shown in Fig. 5.1. It consists of a central barrel part, which aims to measure hadrons, electrons, and photons and a forward muon spectrometer [Aam+08]. The central part covers a polar region between $45^\circ < \Theta < 135^\circ$ ($|\eta| < 0.9$) and is embedded in a large solenoid magnet providing a magnetic field of $B = 0.5 \text{ T}$. Here the quantity η is introduced, which is

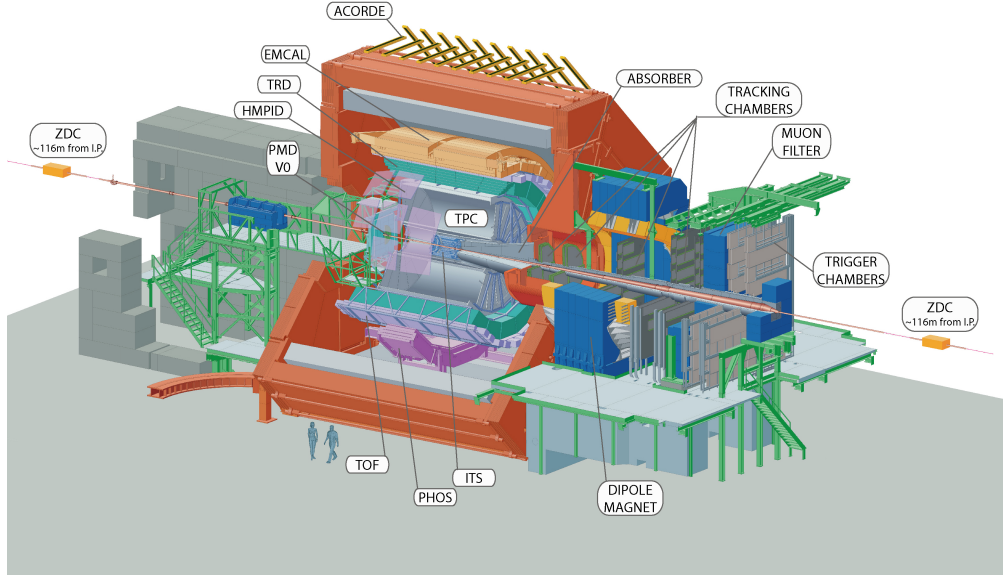


Figure 5.1: The ALICE detector with its individual components [Aam+08].

known as pseudo-rapidity and connected to the polar angle:

$$\eta = -\ln \left(\tan \left(\frac{\Theta}{2} \right) \right) . \quad (5.1)$$

The most inner component of the central barrel is the Inner Tracking System (ITS) consisting of six planes of high-resolution silicon pixel (SPD), drift (SDD), and strip (SSD) detectors. The ITS is surrounded by a cylindrical Time-Projection Chamber (TPC) followed by three particle identification arrays of Time-of-Flight (TOF) arrays, Ring Cherenkov (HMPID) and Transition Radiation (TRD) detectors. These detectors have a full azimuthal coverage. For photon measurements the central barrel is equipped with two electromagnetic calorimeters (PHOS and EMCAL). Additionally to the mentioned detector components ALICE includes several smaller components at smaller polar angles (ZDC, PMD, FMD, T0, V0) installed for global event characterization and triggering. The specific coverages of each detector can be found in [Aam+08]. We will describe the detector parts which played a major role in the analysis.

5.0.3 The Inner Tracking System - ITS

The main task of the Inner Tracking System (ITS) is to provide a precise vertex and track reconstruction. The whole setup has a cylindrical shape and is located around the interaction region covering a pseudo-rapidity region of $|\eta| < 0.9$. It is a silicon tracker

consisting of six layers, with an inner radius starting at 3.9 cm and an outer radius of 43.0 cm [Aam+10]. The two innermost layers contain Silicon Pixel Detectors (SPD), the two intermediate layers Silicon Drift Detectors (SDD), and the two outermost layers are equipped with Silicon Strip Detectors (SSD). Fig. 5.2 shows the structure of the ITS with its six layers. With the ITS an improved angle, momentum, and position resolution

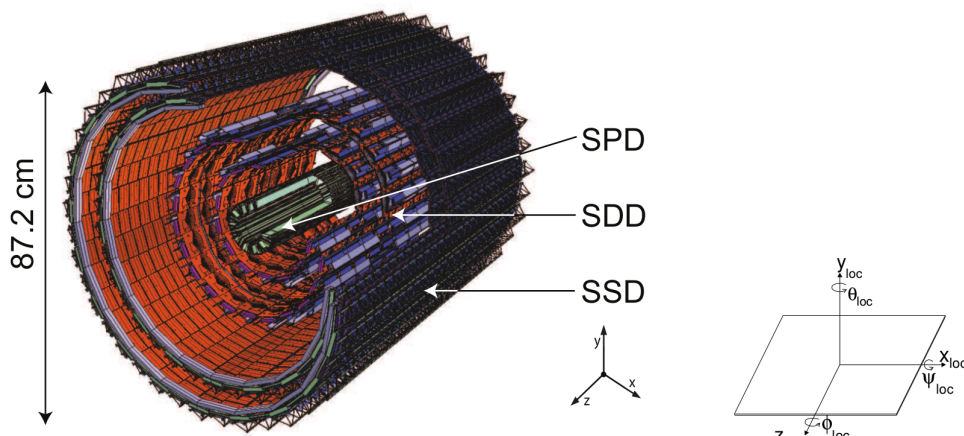


Figure 5.2: The structure of the Inner Tracking System (ITS) with its six layers SPD (two innermost), SDD (two intermediate), SDD (two outermost) [Aam+10].

is achieved for tracks which were reconstructed in the Time-Projection Chamber (TPC). Another achievement is the capability to identify in a precise way secondary vertices from the decay of hyperons and heavy flavored hadrons and to reconstruct the interaction vertex with a resolution better than $100 \mu\text{m}$ [Aam+10]. It also fills the acceptance for e.g. very slow particles which are too slow to reach the TPC and would be otherwise lost.

5.0.4 The Time-Projection Chamber - TPC

The Time-Projection Chamber (TPC) is the main device for charged particle identification and tracking in the central barrel of ALICE [Alm+10]. It consists of a hollow cylinder which surrounds the Inner Tracking System and is aligned with the beams from the LHC. The inner radius of the TPC starts at about 85 cm and the outer radius is about 250 cm. The extent along the beam direction is 500 cm [Alm+10]. It covers the full azimuthal angle and a pseudo-rapidity range of $|\eta| < 0.9$. It was designed to cope with at that time predicted charged particle densities of up to $dN_{\text{ch}}/d\eta = 8000$ for central Pb-Pb collisions at a center-of-mass energy of 5.5 TeV. The detector is filled with a counting gas in the inner part of the cylinder in which an axial electric field is operat-

ing at 400 V/cm. The setup of the electrostatic field is realized in the field cage which defines the uniform field in the gas volume and ensures a smooth transport for the ionization electrons from the point of creation to the endplates. The field cage is shown in Fig. 5.3. The working principle of the TPC is that charged particles which traverse the

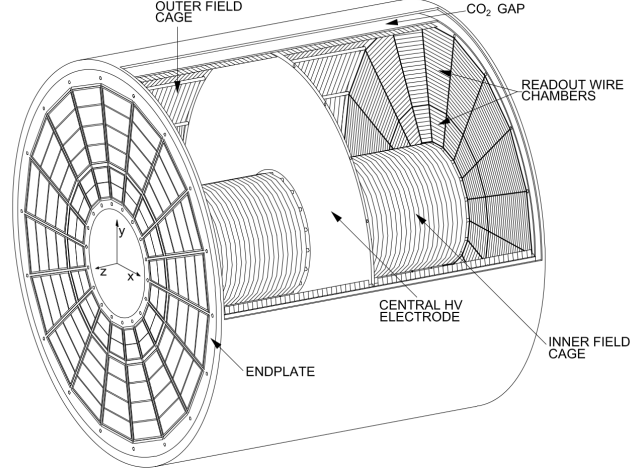


Figure 5.3: The TPC field cage in 3D view [Alm+10].

TPC ionize the gas and the ionization electrons drift, due to the influence of the electric field, towards the endplates of the cylinder where the arrival point is measured. Together with a determination of the arrival time the full trajectory of the traversing charged particles can be determined. The maximum interaction rate for the TPC is 8 kHz for Pb-Pb collisions. After the Long shutdown 2 (LS2) the expected LHC luminosity will increase to about 50 kHz. To cope with this increase in interaction rate an upgrade of the TPC is necessary e.g. to prevent ions from drifting back into the TPC drift volume. This motivates to use for an upgraded version of the TPC GEMs for the new readout chambers [13].

The particle identification in the TPC can be done over a wide momentum range. It is established by measuring simultaneously the specific energy loss (dE/dx), charge, and the momentum of every charged particle which traverse the TPC gas. The energy loss is parametrized by a function [Alm+10]:

$$f(\beta\gamma) = \frac{P_1}{\beta^{P_4}} \left(P_2 - \beta^{P_4} - \ln\left(P_3 + \frac{1}{(\beta\gamma)^{P_5}}\right) \right), \quad (5.2)$$

where β is the velocity of the particle, γ the Lorentz factor and P_{1-5} are fit parameters. A performance plot showing the specific energy loss of charged particles vs its momentum is displayed in Fig. 5.4 for pp collisions at 7 TeV. One can see that the largest separation between the particles is achieved for momenta below $p \approx 1$ GeV/c. Then the different

bands start to overlap and an additional PID information is necessary to distinguish between the individual particle species.

To include the resolution in the PID description one defines the deviation from the measured specific energy loss value from the expected value in steps of the width of the curve:

$$n\sigma_{dE/dx} = \frac{(dE/dx)_{\text{measured}} - (dE/dx)_{\text{expected}}}{\sigma_{dE/dx}}. \quad (5.3)$$

This allows to use always the same resolution for PID selections.

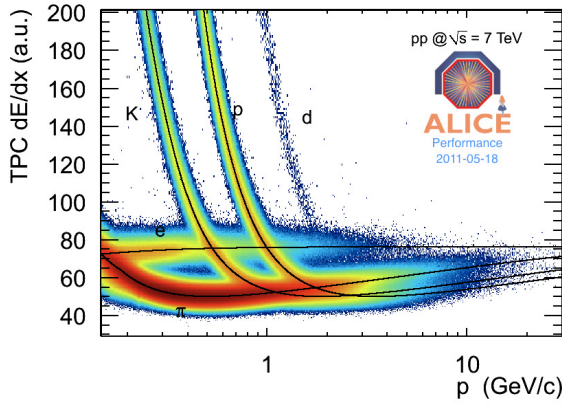


Figure 5.4: The specific energy loss of charged particles versus the particle momentum. One can see a separation for particles for momenta up to 1 GeV/c.

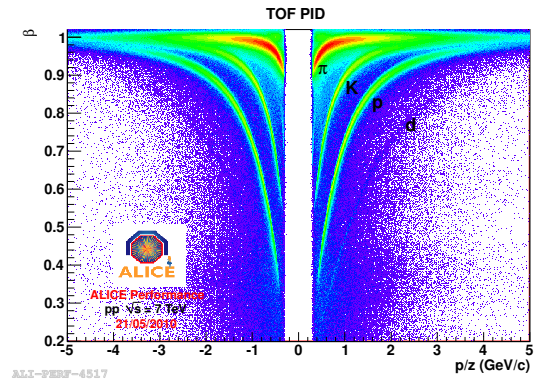


Figure 5.5: The velocity of particles versus their momenta. Different bands develop for the different particle species.

5.0.5 The Time-Of-Flight detector - TOF

The Time-Of-Flight (TOF) detector consists of Multigap Resistive Plate Chambers (MRPC) starting at a radius of 370 cm and ending at a radius of 399 cm. It covers the full azimuthal angle range and a pseudo-rapidity region of $|\eta| < 0.9$. The time resolution was determined for pions in a momentum region around 1 GeV/c for 0 – 70 % Pb-Pb collisions to 80 ps [Abe+14b]. With the TOF the PID can be improved for particles in the intermediate momentum region which can reach up to 2.5 GeV/c for pions and up to 4 GeV/c for kaons and protons. The start time for the TOF is provided by the T0 detectors. The PID in TOF can be established by measuring the particles velocity β . The velocity is related to the momentum of the particle:

$$\beta = \frac{\mathbf{p}^2}{E(\mathbf{p})} = \frac{\mathbf{p}^2}{\sqrt{\mathbf{p}^2 + m^2}}. \quad (5.4)$$

By plotting the velocity β as a function of the momentum (measured by an independent detector) of a charged particle, a mass ordering of bands should be established according to Eq. (5.4). An example plot is shown in Fig. 5.4 for pp collisions at 7 TeV, where the velocity is provided by the TOF detector and the momentum by the TPC. One can clearly see different bands corresponding to the different particle species.

6

Data analysis

In this chapter the femtoscopic analysis performed for the ALICE experiment and the methods used to obtain and correct the correlation functions are presented. Minimum bias events of pp collisions at a center-of-mass energy of 7 TeV are analyzed. The minimum bias trigger MBand and MBor were used for all pp data taking, where the MBor required signals in V0 and SPD, and MBand signals in V0A and V0C [Abe+14b]. In the data taking period 2010 around $825 \cdot 10^6$ pp events at this energy were recorded [Abe+14b]. A summary of the analyzed system and data sample is given in Tab. 6.1. The analysis is performed over Analysed Object Data (AOD). The newest production is AOD147. However, according to PID experts no tender (additional offline PID cali-

| Property | Value |
|-------------------------------------|---|
| Collision system | pp |
| Center-of-mass-energy | 7 TeV |
| Data taking period | 2010 |
| Trigger | Minimum bias |
| Analyzed periods | AOD137 for LHC10b and LHC10c, AOD135 for LHC10d and LHC10e |
| Reconstruction pass | pass2 |
| Number of events passing selections | 245 M |

Table 6.1: Summary about the analyzed collision system.

bration) was used for this period and should not be used for any PID related analysis¹. For this reason the production AOD135/137 where the PID calibration was applied is analyzed.

6.1 Event selection

Events have to fulfill certain quality properties. First of all, events are selected close to the central collision point by requiring that the z position of the primary vertex deviates maximally by 10 cm from this point. To reject pile-up events methods developed by experts² are used. They are checking e.g. if in an event several primary vertices exist. Summarizing all employed event selections:

- Trigger: selection of minimum bias events (kMB).
- Magnetic field and primary vertex: $B > 1$ mT and check if primary vertex is available in event.
- Primary vertex contributors: at least two tracks should contribute to the primary vertex $N_{\text{contributors}} > 1$.
- Primary vertex z coordinate: events should lie close around the central collision point $|z| < 10$ cm.
- Number of tracklets (in central barrel): >0 for a pseudo-rapidity range $|\eta| < 0.8$, at least one tracklet should be available since it is used for multiplicity estimation³.
- Reject pile-up: method from experts which checks e.g. for multiple vertices.⁴

6.2 Track selection

6.2.1 Proton candidates

After the events pass the quality selection criteria listed above the tracks contained in the events are checked for several criteria. After passing a dedicated track selection procedure they are used for the femtoscopy analysis. In the Pb-Pb analysis it was seen that two tracks close together in angle space $((\Delta\eta, \Delta\varphi))$ can share the same cluster in the SPD. This leads to biases if one uses tracks from the global tracking scheme (ITS+TPC)

¹<https://twiki.cern.ch/twiki/bin/viewauth/ALICE/PWGPPAODTrackCuts>

²<http://alroot-docs.web.cern.ch/alroot-docs/AliAnalysisUtils.html>

³The number of SPD tracklets is calculated in every event. Not the reference multiplicity is used.

⁴<http://alroot-docs.web.cern.ch/alroot-docs/AliAnalysisUtils.html>. The minimum contributors to the pile-up SPD vertices was set to three.

[BB15]. This problem can be overcome by using TPC-only tracks avoiding the ITS information in the track reconstruction. For this reason also in the pp analysis TPC-only tracks are used as standard tracking scheme. They are classified by the Filterbit 7 or 128 ($2^7 = 128$). In femtoscopy one is interested in a sample containing dominantly primary tracks that stem from the point of last interaction and carry the source information. This can be achieved by selecting tracks close to the primary vertex both in the xy -plane and z -direction. The fraction of primary particles with the chosen selection criteria will be shown later. Since the analysis is done with TPC-only tracks, one expects that the momentum resolution is worse since the ITS is not included in the Kalman filter employed for the track reconstruction. However, by selecting TPC-only tracks constrained to the primary vertex the resolution is comparable to (ITS+TPC) fitted tracks, as it is shown in the performance paper of ALICE [Abe+14b]. A drawback of TPC-only tracks is that they don't contain any PID information anymore. For this reason one has to find for the TPC-only track the corresponding global track. This can be achieved by a mapping of the track Ids by using the relation: $ID_{\text{global}} = -ID_{\text{TPC}} - 1$. A powerful mapping routine was developed in the PhD thesis of H. Beck for the p - Λ analysis in Pb-Pb collisions at $\sqrt{s_{\text{NN}}}=2.76$ TeV. It avoids to have an additional loop in the track loop to find the corresponding global track. This mapping is also adopted for the pp analysis. For a detailed discussion of the method we refer to [BB15].

In the AOD137/AOD135 data files some pre-defined track cuts are already employed¹. At the physics level, the pre-defined selections constrain the tracks loosely to the primary vertex with values for the distance of closest approach to the primary vertex chosen as $DCA_{xy} < 2.4$ cm and $DCA_z < 3.2$ cm. On the tracking level, the minimum number of TPC cluster is set to 70 and the maximally allowed χ^2 per cluster is set to 4. Kink daughter tracks are also rejected.

According to TPC experts², for TPC related analyses one can achieve a good p_T resolution at large momenta with a selection criteria on the number of crossed rows and on the ratio of number of crossed rows over findable clusters. This selection is employed in this analysis. Additionally, primary tracks are rejected which share cluster in the TPC.

A lower p_T threshold is chosen for protons since in the low region p_T ($p_T \approx 0.5$ GeV/ c) the fraction of protons knocked out from detector material grows [Ada+16]. A large p_T ($p_T \approx 4.05$ GeV/ c) cutoff is necessary since there the purity of protons drops below 80%, which will be shown later in this thesis. This high-momentum region is not that important since the majority of the protons are produced around 1 GeV/ c . For the PID information the $n\sigma$ prescription introduced in the previous Section is used. For momenta below $p_{\text{TPC}} < 0.75$ GeV/ c only the PID selection from the TPC is applied. For momenta $p_{\text{TPC}} > 0.75$ GeV/ c the signals from TPC and TOF are combined since the TPC has not enough separation power to distinguish between protons and other species

¹[https://twiki.cern.ch/twiki/bin/view/ALICE/AddTaskInfoAOD135\(7\)](https://twiki.cern.ch/twiki/bin/view/ALICE/AddTaskInfoAOD135(7))

²<http://svn.cern.ch/guest/AliRoot/trunk/TPC/doc/Definitions/Definitions.pdf>

any more. The combination of TPC and TOF signals is done by employing a circular selection criteria $n\sigma_{\text{combined}} \equiv \sqrt{(n\sigma_{\text{TPC}})^2 + (n\sigma_{\text{TOF}})^2}$. The two selection criteria are displayed in Fig. 6.1. This selection method was introduced and approved for the

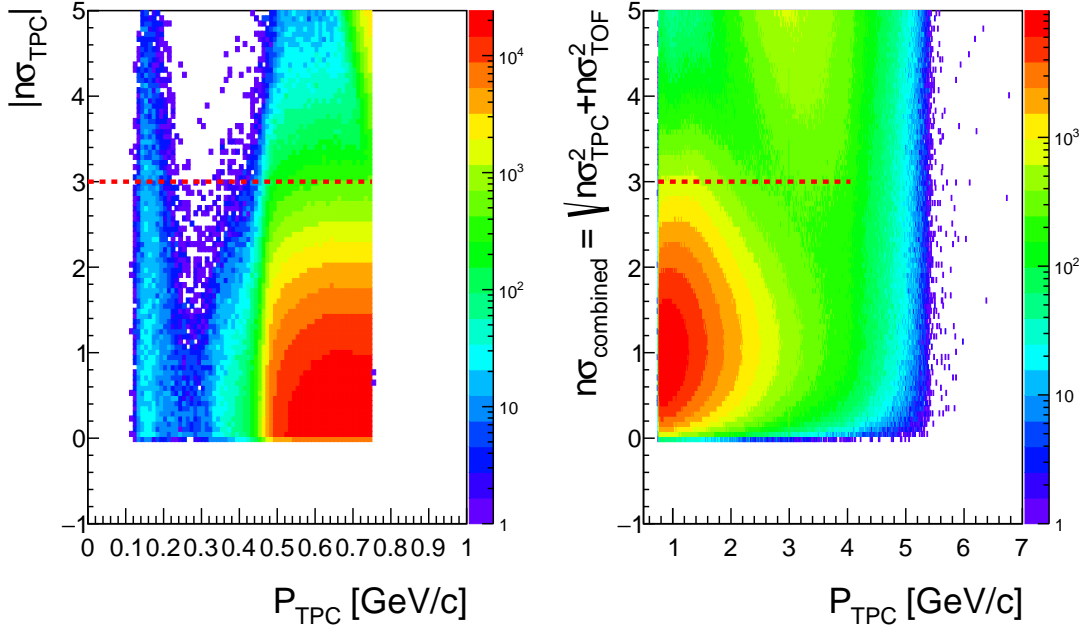


Figure 6.1: Proton selection criteria. Below 0.75 GeV/c only the TPC is used. For momenta above this threshold the TPC signal is combined with the one from the TOF.

$p - p$ correlation function obtained in Pb-Pb collisions at $\sqrt{s_{\text{NN}}}=2.76$ TeV [Ada+15b]. Additionally, if the proton fulfills the $n\sigma$ selection criteria it is compared to the $n\sigma$ value of kaons, electrons and pions. If the $n\sigma$ value of one of the other candidates is smaller the proton hypothesis and thus the track is rejected. In summary, all track cuts used for the (primary) proton selection are the following:

- Filterbit selection 128: TPC-only tracks constrained to primary vertex.
- Minimum number of TPC cluster >80: Ensure good track quality.
- Minimum number of crossed rows >70: good p_{T} resolution at large momenta ¹.
- Minimum number of crossed rows over findable cluster >0.83: remove fake tracks ¹.

¹Described by experts in <http://svn.cern.ch/guest/AliRoot/trunk/TPC/doc/Definitions/Definitions.pdf>

¹Described by experts in <http://svn.cern.ch/guest/AliRoot/trunk/TPC/doc/Definitions/Definitions.pdf>

- Rejection of tracks which share TPC cluster.
- Distance of closest approach to primary vertex $|DCA_{xy}| < 0.1$ cm, $|DCA_z| < 0.2$ cm: to enhance the selection of primary protons emitted from collision point (motivated from [Abb+13]).
- Minimum transverse momentum $p_T > 0.5$ GeV/c: to enlarge the fraction of directly produced protons and reduce protons coming from material.
- Maximum transverse momentum $p_T < 4.05$ GeV/c: since at this point the purity of the protons starts to drop below 80%.
- PID for lower momenta, $p_{TPC} < 0.75$ GeV/c: because in this region the TPC has a large separation power to distinguish between protons and other species, $|n\sigma_{TPC}| < 3$.
- PID for larger momenta, $p_{TPC} > 0.75$ GeV/c: in this region the TPC signal is combined with the TOF signal since the specific-energy loss bands of the TPC start to overlap with other species, $n\sigma_{combined} \equiv \sqrt{(n\sigma_{TPC})^2 + (n\sigma_{TOF})^2} < 3$.
- $n\sigma$ comparison: the $n\sigma$ values of the identified proton is checked for the $n\sigma$ hypothesis of being a kaon, pion, electron. If the $n\sigma$ value of being another candidate is smaller than the track is rejected.

6.2.2 V0 candidates

Λ and K_S^0 are charge neutral particles that decay into a pair of oppositely charged particles. The latter share the momentum of the mother particle. Since the decay topology has often a V-type shape they are called V0s. The method of ALICE to find V0s is described in [Cor+06] and will be shortly explained here. In a first step all secondary tracks are selected. Secondary tracks are defined as tracks which have a minimum impact parameter with respect to the primary vertex (separate values for the positive and negative track). Then all the positively charged secondary tracks are combined with a negatively charged partner. Pair combinations are rejected if the distance of closest approach between such a pair exceeds a certain value. The point of the closest approach of a secondary pair defines the secondary vertex and only such vertices are kept that lie inside a pre-defined fiducial volume. In a last step the V0 momentum is calculated. To get this information the daughter tracks are extrapolated to the point of closest approach and then the sum of the two daughter momenta defines the V0 mother momentum. This momentum vector should be aligned with the vector pointing from the primary vertex to the secondary V0 vertex if the V0 was produced at the primary collision vertex. Taking the cosine of the angle between the two vectors allows to introduce another selection criteria and reduce combinatorial background. A sketch showing the finding procedure of V0s is displayed in Fig. 6.2. In the analyzed data sample some topological pre-selections on the impact parameter and the distance of closest approach are already present. These are listed below. Additionally, a selection criteria on the minimal flight distance in the xy -plane is employed as a pre-selection. In this analysis, a cut on the maximum flight distance in the

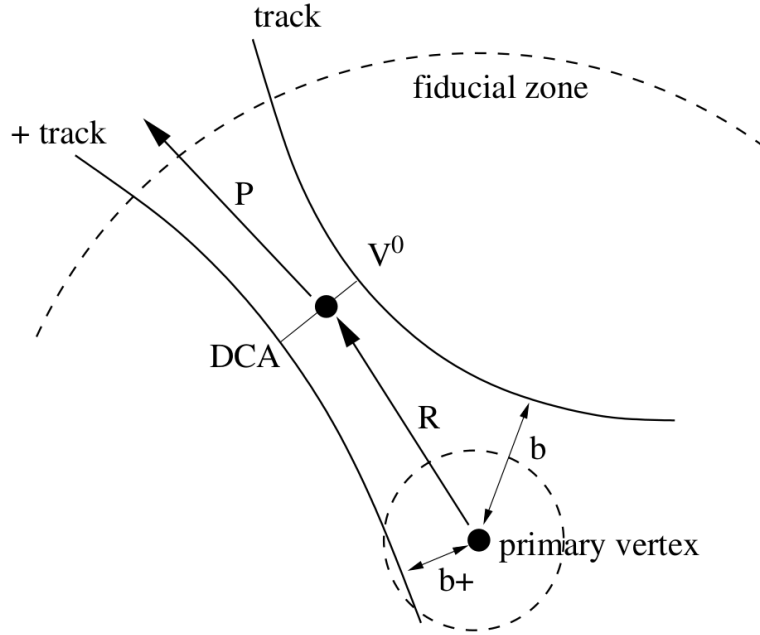


Figure 6.2: Sketch of a V^0 decay and its vertex selection taken from [Cor+06]. Only V^0 vertices inside a fiducial volume are kept and the daughter tracks have to have some minimum impact parameter to the primary vertex. The distance of closest approach of the daughter tracks should not exceed a maximum value.

xy -plane and a selection on the V^0 decay vertex is introduced. The values of the cuts are checked with Monte Carlo samples which show that in the rejected region nearly only background is present. In summary, the following selections are done for the V^0 topology:

- V^0 decay vertex $|x_i| < 100$ cm, $i=x,y,z$: tracks that cannot be reconstructed to the V^0 decay vertex are basically background.
- Impact parameter of daughter tracks to primary vertex: $DCA(|p/\pi^-, PV|) > 0.05$ cm.
- Distance of closest approach of daughter tracks at V^0 decay point: $DCA(|p, \pi^-|) < 1.5$ cm.
- Cosine of pointing angle: $\cos(\alpha) > 0.99$, $\alpha = \angle(PV\vec{SV}, \vec{P}_\Lambda)$.

The PID of the daughter tracks is obtained only with the specific energy loss of the TPC to not decrease the efficiency by requiring an additional detector signal. The daughter tracks are selected by a broad $n\sigma_{\text{TPC}} < 5$ cut. With this pre-selection there is also a finite probability to identify positive pions, stemming from K_S^0 decays instead of protons.

For this reason the hypothesis that the proton could also be positive pion is checked. If the $\pi^+\pi^-$ invariant mass lies inside the K_S^0 region the V0 candidate is rejected. The $p - K_0^S$ correlation function was measured at AGS energies and is in agreement with unity within the error bars [Chu+02]. In pp collisions at LHC energies it can be strongly affected by non-femtoscopic mini-jet background. This is hinted in [BF14], where the $p - K_0^S$ correlation function is obtained in p-Pb collisions at $\sqrt{s_{NN}}=5.02$ TeV. Even if the relative momentum variable is improperly calculated for a non-identical pair, the correlation function shows non-flat or even dip structures. There exist a possibility that this broad mini-jet correlation signal survives a transformation into the p - Λ system, where only the mass hypothesis is changed. This effect is studied by means of a Toy Monte Carlo study and shown in Fig. 6.3. In this simulation the initial momenta follow a Gaus-

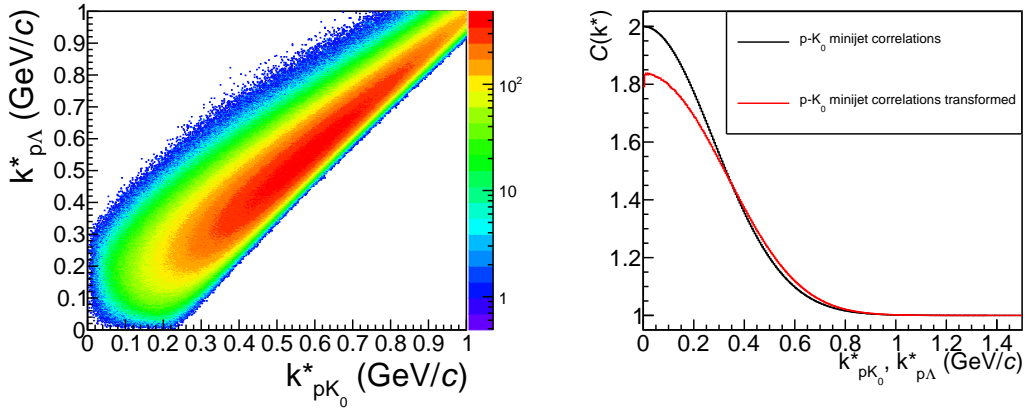


Figure 6.3: Results from a Toy Monte Carlo study. Left: Matrix presenting the correlation between k^* of an initial momentum $p - K_0^S$ transformed to p - Λ . Right: A broad simulated mini-jet background present in $p - K_0^S$ survives the transformation to the p - Λ momentum basis.

sian distribution with a spread of 0.5 GeV/ c for each particle. A correlation matrix of the k^* momenta is obtained by calculating the relative momentum for $p - K_0^S$ pairs and p - Λ (by using the momenta of the K^0 but the mass of the Λ). The correlation matrix is displayed on the left side of Fig. 6.3. The simulated broad mini-jet background included for $p - K_0^S$ pairs survives also the transformation from the $p - K_0^S$ momentum basis to p - Λ because of its broadness. In principle, it can be used as a method to describe the mini-jet background in a certain channel by determining it with an independent pair and transforming it to the pair of interest. Thus the mini-jet background would be fixed and the femtoscopia signal can be measured on top of it. An exploratory study of this kind was performed by the ATLAS collaboration with pion pairs [col15]. Finally, the

full list of V0 kinematic and track cuts is listed below:

- V0 finder/reconstruction: offline
- V0 must have two daughter tracks
- V0 charge must be zero
- V0 transverse radius: $0.2 \text{ cm} < r_{xy} < 100 \text{ cm}$
- Minimum number of TPC cluster for daughter tracks > 70
- Minimum transverse momentum of V0: $p_T > 0.3 \text{ GeV}/c$
- Maximal pseudo-rapidity range of daughter tracks $|\eta| < 0.8$
- K0s rejection: $0.48 \text{ GeV}/c^2 < m_{\pi^+\pi^-} < 0.515 \text{ GeV}/c^2$
- PID of daughter tracks: $|n\sigma_{\text{TPC}}| < 5$
- Selection window of Λ candidates: $|m_{p\pi^-} - m_{\Lambda, \text{PDG}}| < 4 \text{ MeV}/c^2$

The integrated Λ and $\bar{\Lambda}$ signal together with the invariant mass selection cuts are shown in Fig. 6.4. To obtain the Λ purity the Λ invariant mass peaks are fitted as a function of

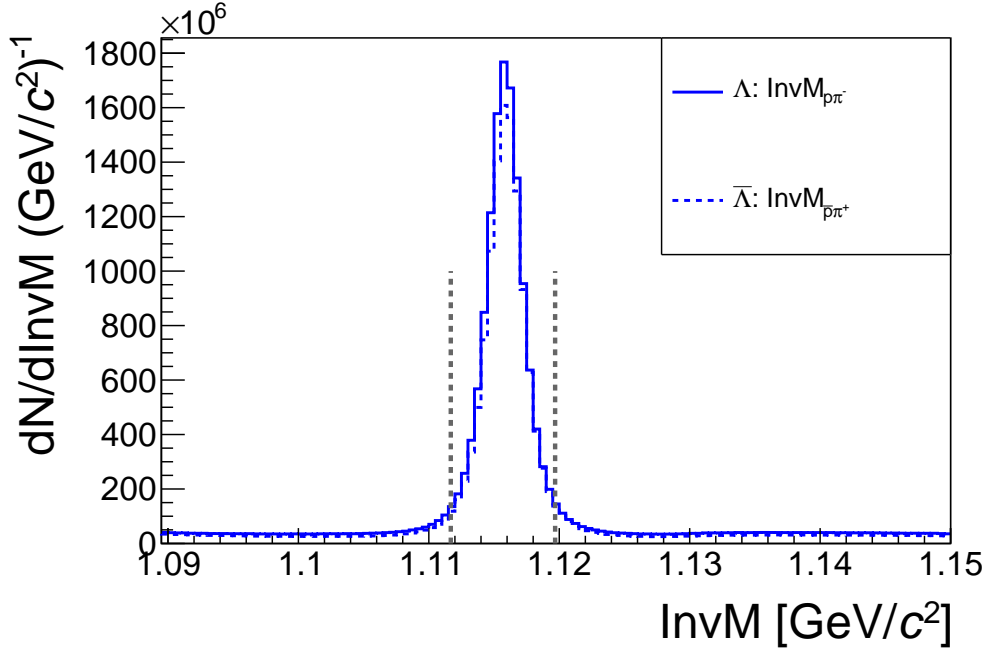


Figure 6.4: Invariant mass distribution of $p\pi^-$ ($\bar{p}\pi^+$) to obtain the Λ ($\bar{\Lambda}$) signal and the selection width used in the analysis.

p_T . The fitfunction is chosen as a sum of two Gaussian functions for the signal region

and a second order polynomial for the combinatorial background. The two Gaussian functions are combined in the form:

$$f(x) = A(\alpha \text{Gauss1}(x) + (1 - \alpha) \text{Gauss2}(x)) , \quad (6.1)$$

where $\text{Gauss}(x)$ are the Gaussian functions, A an amplitude to be scaled to the peak position and $\alpha \in [0, 1]$ the relative contribution of the two Gaussians. The two variances and means of the Gaussians are combined in the following way:

$$\sigma_{\text{combined}} = \alpha\sigma_1 + (1 - \alpha)\sigma_2 , \mu_{\text{combined}} = \frac{\mu_1 + \mu_2}{2} , \quad (6.2)$$

where σ_i, μ_i is the variance, mean of the Gauss i . The resulting means and variances are displayed in Fig. 6.5. One can see that the width reflects the momentum resolution of

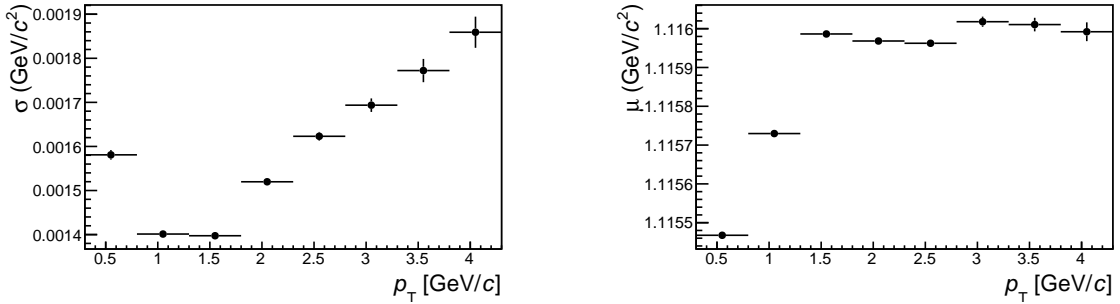


Figure 6.5: The resulting mean and variance of the Λ signal as a function of p_T .

ALICE. At intermediate p_T of ~ 1 GeV/c it is best and grows for very low and high p_T . With the chosen selection criteria around 6M Λ are left for analysis.

6.3 Correlation functions

To obtain the correlation functions the event mixing technique is employed for establishing an uncorrelated pair yield which is given by Eq. (2.50). Only events with similar z vertex positions and multiplicity are mixed, which ensures similar acceptance effects and underlying event activities. The binwidth for the z vertex position is 2 cm. The multiplicity is estimated by counting the number of SPD tracklets in the central barrel in a pseudo-rapidity region of $|\eta| < 0.8$. The event multiplicity is grouped in classes of $[1-4]$, $[5-8]$, $[9-12]$, $[13-16]$, $[17-20]$, $[21-24]$, $[25-28]$, $[29-32]$, $[33-36]$, $[37-40]$, $[41-60]$, $[61-80]$, $[> 80]$. The corresponding distributions for the z vertex and multiplicity are displayed in Fig. 6.6. To avoid any contribution of auto-correlations, all V0 candidates are checked for shared daughter tracks. If V0s share daughter tracks the

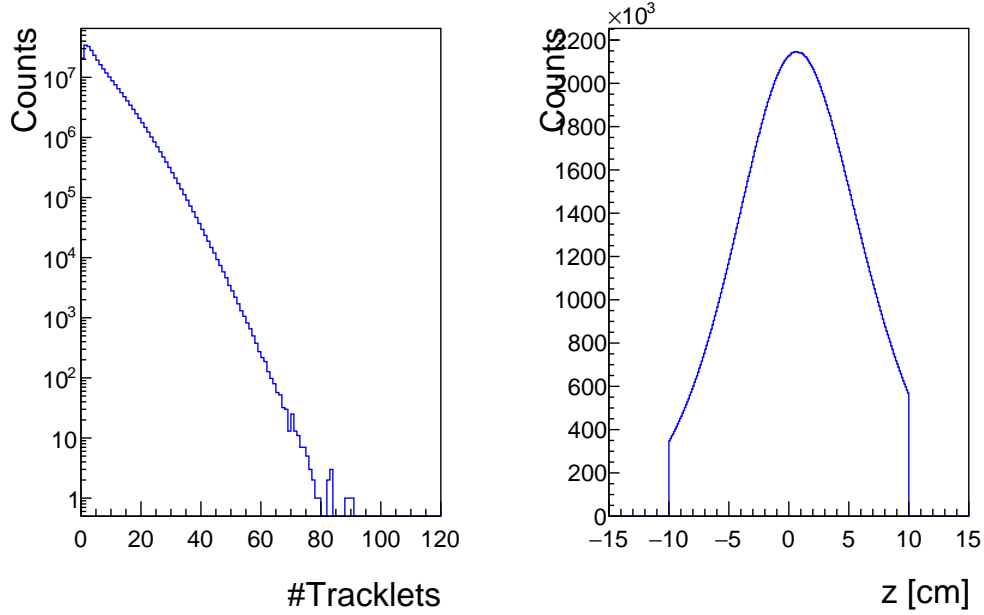


Figure 6.6: Left: Number of SPD tracklets in $|\eta| < 0.8$ used for determining the multiplicity of pp events. Right: z vertex distribution for pp collisions. Both observables are used for event mixing.

V0 with the larger cosine pointing angle is kept and the other one is rejected from the sample. If a primary proton and a V0 daughter share the same track the V0 candidate is rejected. In the next sections the results of raw and uncorrected correlation functions are displayed. Since the correlation functions for (Anti)baryon-(Anti)baryon and Antibaryon-Baryon pairs show very different behaviours they are discussed separately.

6.3.1 Baryon-Antibaryon correlations

In this section results for Baryon-Antibaryon correlation functions are presented. All of them are normalized in the interval $k^* \in [1, 1.5] \text{ GeV}/c$. Before showing the correlation functions a method is introduced with which correlation functions are added in this analysis. The sum is done on the level of the correlation functions itself using the least squares method. If one wants to combine a number of measurements, where all measured values y_i will scatter around a true value λ , the solution for the least squares estimator is [Cow98]:

$$\hat{\lambda} = \frac{\sum_i y_i / \sigma_i^2}{\sum_i 1 / \sigma_i^2}, V[\hat{\lambda}] = \frac{1}{\sum_i 1 / \sigma_i^2}, \quad (6.3)$$

where $V[\hat{\lambda}]$ is the variance of $\hat{\lambda}$. Thus, the measurements are combined by weighting them with the statistical errors. This prescription is also applied to combine the correlation functions of particle and antiparticle pairs.

First pairs containing baryons without strangeness are presented beginning with the $\bar{p}-p$ correlation function shown in Fig. 6.7. For the $\bar{p}-p$ correlation function a mini-jet in-

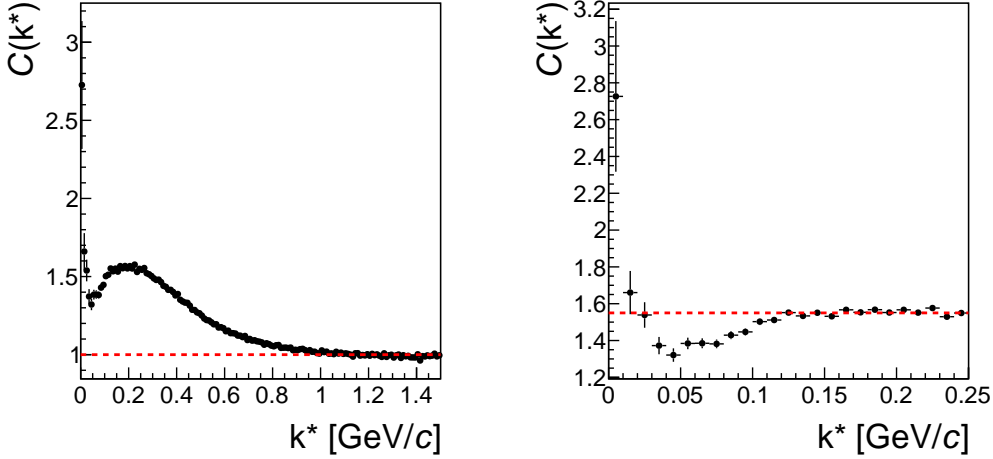


Figure 6.7: Left: Correlation function of $\bar{p}-p$ pairs. A strong contribution from mini-jets is visible, showing up as a broad correlation signal starting at $k^* \sim 1$ GeV/c. Right: Same correlation function zoomed to small relative momenta. One can see a correlation signal having femtoscopic signatures on top of the mini-jet background.

duced background is visible as a broad correlation signal starting already at $k^* \sim 1$ GeV/c. This seems to be typical for pairs of Antibaryon-Baryon pairs, which will be seen later. By going to lower values of k^* there is an indication of an additional signal visible at around 200 MeV/c having its origin in a femtoscopic source sitting on top of the mini-jet background. To make it more visible a new baseline is introduced in the zoomed version shown on the right of Fig. 6.7. Assuming that the shape of the mini-jet contribution below $k^* = 200$ MeV/c stays roughly constant one can see a depletion of pairs and a minimum of the correlation function at a k^* value of about 50 MeV/c. This is an indication for an onset of inelastic scattering processes with the possible reactions $p\bar{p} \rightarrow \pi^+\pi^-$, $\pi^0\pi^0$. The rising of the correlation function for $k^* \rightarrow 0$ is an indication for the Coulomb attraction of the oppositely charged pair.

The contribution of the mini-jet background is investigated also for other pair combinations including strangeness. The result for the sum of $\bar{p}-\Lambda$ and $p-\bar{\Lambda}$ is shown in Fig. 6.8 (the pairs have opposite strangeness but since it is exactly the total antiparticle pair they are summed up). Also for this pair the mini-jet contribution is very obvi-

ous. A zoomed version of the plot is given on the right of Fig. 6.8. Again a loss of pairs is visible, pointing to a process of inelastic scattering. Possible reactions which lead to pair losses are $\bar{p}\Lambda \rightarrow \pi^0 K^-$, $p\bar{\Lambda} \rightarrow \pi^0 K^+$. The last pair which studied is a

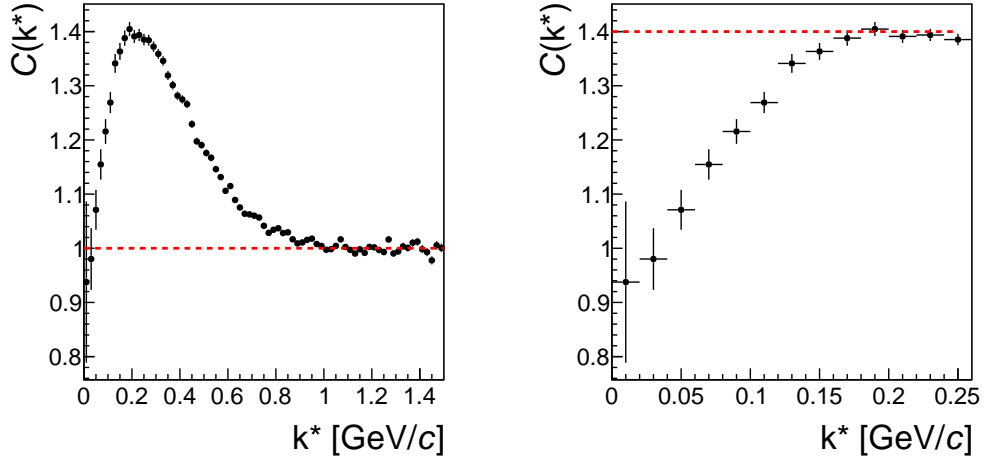


Figure 6.8: Left: Correlation function of the sum of $\bar{p} - \Lambda$ and $p - \bar{\Lambda}$ pairs. Also for this pair a strong contribution from mini-jets is visible, showing up as a broad correlation signal starting at $k^* \sim 1$ GeV/c. Right: Same correlation function zoomed to small relative momenta. One can see a correlation signal having femtoscopic signatures on top of the mini-jet background.

strangeness neutral pair composite of particles carrying strangeness, the $\bar{\Lambda} - \Lambda$ correlation function shown in Fig. 6.9. This pair shows no exception and is not free of the mini-jet background. Having also total baryon number zero in the entrance channel it can easily decay into meson pairs or for this case also in a pair of $\bar{p} - p$. Thus, there is a coupling to the channel presented in Fig. 6.7. This additional channel might introduce an additional loss of pairs. Comparing the relative $p - \bar{\Lambda}$ suppression to the new baseline at the lowest k^* value $\Delta(C(k^* \rightarrow 0))_{\bar{p}\Lambda} \approx 1.4 - 0.9 = 0.5$ with the one of $\Delta(C(k^* \rightarrow 0))_{\bar{\Lambda}\Lambda} \approx 1.8 - 0.2 = 1.6$, one can see that the suppression is stronger for the $\bar{\Lambda} - \Lambda$ channel. This is just a hint and would need much further detailed investigations. A further uncertainty is the unknown shape of the mini-jet background in this momentum region, which could behave differently in both channels.

The question which remains is what is the origin of the strong mini-jet contribution that shows up in the Antibaryon-Baryon correlations in pp collisions. There are basically two different possible scenarios that are schematically depicted Fig. 6.10. In the first scenario one parton hadronizes into a bunch of hadrons and they carry a strong kinematic correlation like a pair stemming from a resonance decay. In the second scenario

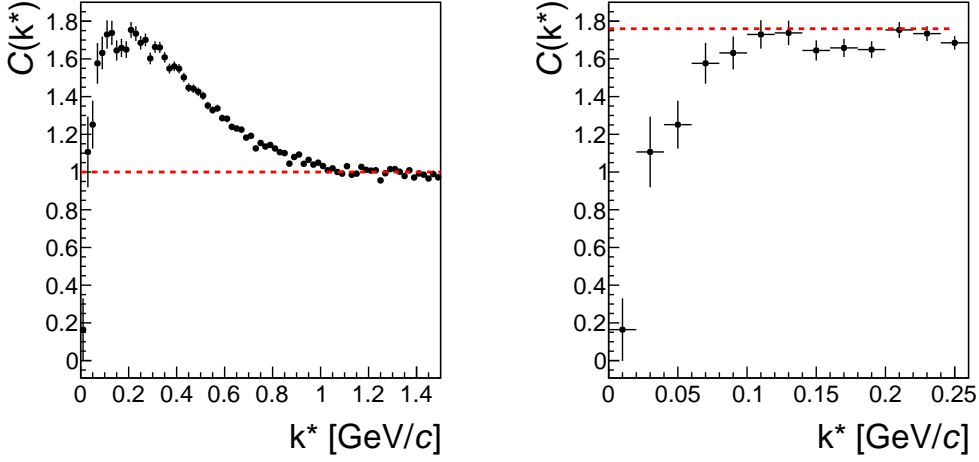


Figure 6.9: Left: The $\bar{\Lambda} - \Lambda$ correlation function. Also for this pair a strong contribution from mini-jets is visible, showing up as a broad correlation signal starting at $k^* \sim 1$ GeV/c. Right: Same correlation function zoomed to small relative momenta. One can see a correlation signal having femtoscopic signatures on top of the mini-jet background.

the pair is produced from different partons which carry a residual correlation from the underlying event. The influence of the hadronization process is tested with Pythia simulations for $\bar{p} - p$ pairs, where one can check the particle history. The hadron production path in the collision history is followed until the first parton of the collision is reached. It is excluded that the proton and antiproton in the pair stem from this parton and the correlation function for this case is calculated. The result is displayed in Fig. 6.11. On the left hand side the transverse momentum of the first parton of the collision is shown. This parton is responsible for the (anti)proton production after some possible intermediate steps. One can see that the transverse momentum, thus the energy can be quite large >50 GeV/c which would be sufficiently large to produce many baryons in a jet. On the right of Fig. 6.11 two different correlation functions are shown. The black dots represent the raw $\bar{p} - p$ correlation function from Pythia simulations. The red squares represent the correlation function with the exclusion that the pair shares in its collision history the same parton as mother. One can see that this has a dramatic influence on the correlation function. It becomes more or less flat and a bit tilted. It seems that the left scenario in Fig. 6.10 is responsible for the mini-jet background that a single parton fragments into a bunch of baryons including a pair of $\bar{p} - p$. From statistics point of view around 50% of $\bar{p} - p$ pairs have the same parton as mother whereas for $p - p$ pairs only 10% have this history. This could maybe be linked to baryon number conservation because for $\bar{p} - p$ pairs the total baryon number is zero but for $p - p$ pairs one has to

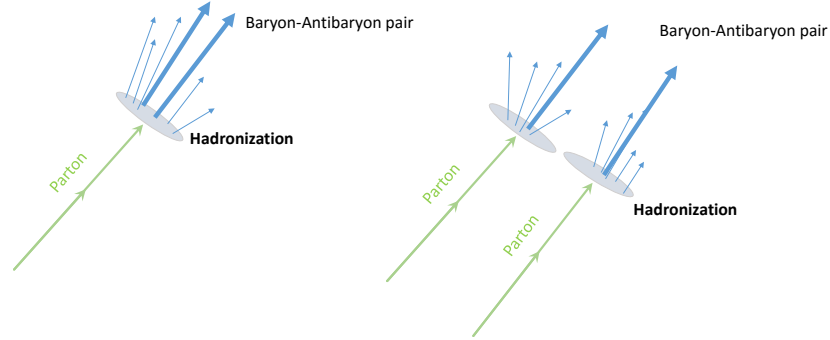


Figure 6.10: Two different scenarios which can lead to a mini-jet contribution in the correlation function. Left: The parton fragments into bunch of hadrons containing the Baryon-Antibaryon pair. Such a process shows a strong kinematic correlation like a pair coming from a resonance decay. Right: The pair stems from two different partons after hadronization.

produce additionally two antibaryons to counterbalance the baryon number. This is just a preliminary study and much more work is needed to have a better understanding of the processes involved. In the end, such correlations may help to better understand the underlying particle productions of baryons and their corresponding antiparticle.

6.3.2 Baryon-Baryon correlations

In this section results for Baryon-Baryon correlation functions are presented. All of them are normalized in the interval $k^* \in [0.4, 0.6]$ GeV/c. The pair combinations from above are taken and the antibaryon replaced with a baryon. These pairs are later also used to compare them to models to extract physical quantities. For this reason they are investigated more in detail. The correlation functions of $p-p$, $p-\Lambda$ and $\Lambda-\Lambda$ are displayed on the top in Fig. 6.12 separately for the Baryon-Baryon and Antibaryon-Antibaryon case. On the bottom of the plot the ratio between Baryon-Baryon and Antibaryon-Antibaryon pairs are shown to explore if they show any difference. One can see that the ratios are equal to unity within the error bars, as expected. It is remarkable that these pairs show no sign of any mini-jet contribution. There is just the femtoscopy signal at low relative momentum visible but not the broad background as in the case with pairs involving one antibaryon. This hints to the fact that baryon number conservation indeed prevents the possibility that two baryons are located in a jet like structure.

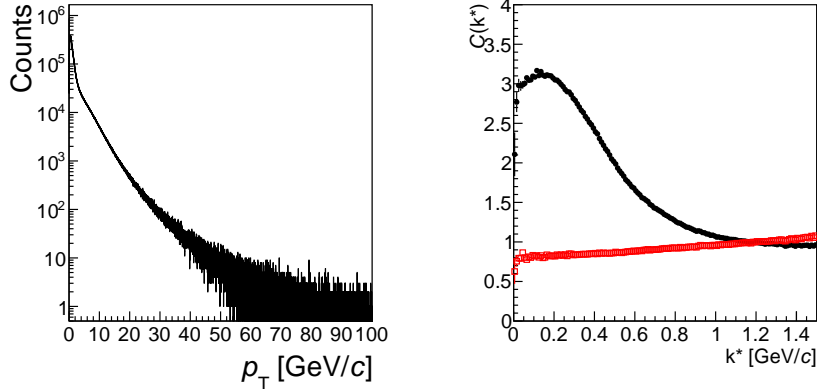


Figure 6.11: Left: Parton transverse momentum in Pythia. Right: Black dots represent the full $\bar{p} - p$ correlation function from Pythia. The red squares show the correlation function obtained by requiring that the $\bar{p} - p$ pair stem from different partons.

For $p - p$ and $p - \Lambda$ pairs the femtoscopic signal looks like expected. The interplay of Coulomb and the attractive strong interaction together with Fermi-Dirac statistics leads to the complex shape of the $p - p$ correlation function. For the $p - \Lambda$ case the attractive interaction implies a positive correlation signal. The strength of the $\Lambda - \Lambda$ interaction is not well established. A femtoscopic correlation function was measured by the STAR collaboration [Ada+15c] in Au+Au collisions at $\sqrt{s_{NN}}=200$ GeV. They extracted values for the scattering parameters by comparing it to a femtoscopic model which includes also the strong interaction. Their measured scattering length is slightly negative $a_0 = -1.10 \pm 0.37^{+2.09}_{-0.08}$ fm [Ada+15c]. Many models on the star STAR $\Lambda - \Lambda$ correlation function were tested by an independent group [MFO15]. It was shown there that the interaction is still far from being understood by the measurement of the correlation function. An additional study of the ALICE collaboration in Pb-Pb collisions will contribute with more data [SH17] to clarify the situation. Also the measured correlation function in pp collisions of this and future analyses will help to better constrain the interaction.

6.4 Linear decomposition of correlation functions

A correlation function is in the very ideal case just the measure of a correlation between a pair of interest, for example of a primary proton p and another baryon e.g. Λ . However, basically two mechanism can distort the measurement. First, with the experimental techniques and the experimental setup one is not able to measure with a 100% probability the particles of interest due to particle misidentifications. A proton might be misidentified as a pion, which means on top of the wanted $p - \Lambda$ one adds $\pi^- - \Lambda$ correlations. If this

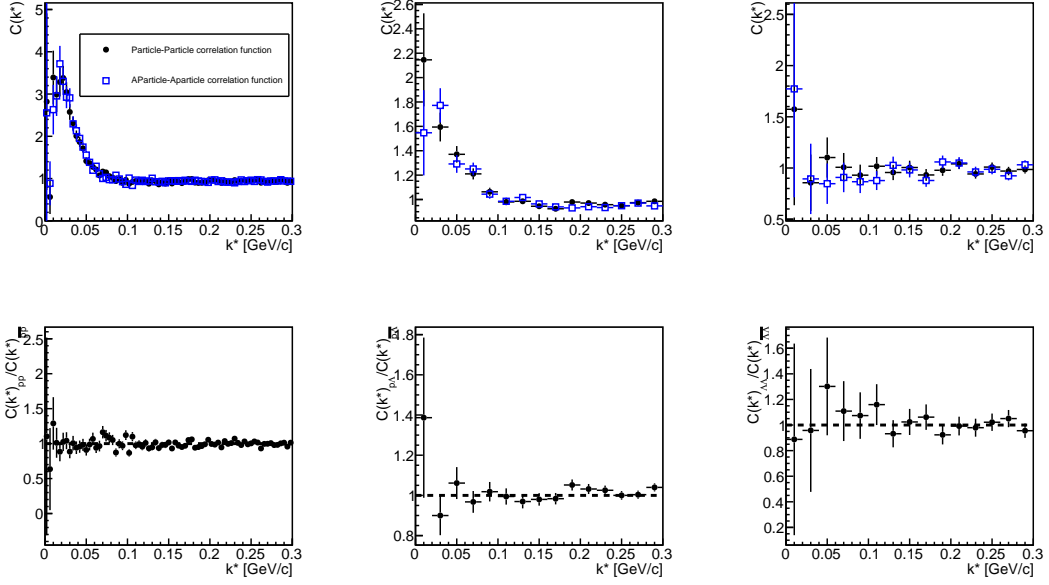


Figure 6.12: Baryon-Baryon and Antibaryon-Antibaryon correlation functions on the top and the corresponding ratios on the bottom. Left: (Anti)proton-(Anti)proton, Middle: (Anti)proton-(Anti)Lambda, Right: (Anti)Lambda-(Anti)Lambda.

happens seldomly, the primary pair will dominate over such small impurities. A second distortion can be introduced by weakly decaying resonances. An example would be a Λ originating from a decay of $\Xi \rightarrow \Lambda\pi$. The primary $p - \Xi$ correlation is then partly transformed to the resulting $p - \Lambda$ pair contributing to the primary $p - \Lambda$ signal.

The question is how one can cook up a model which is able to separate all the individual components contributing to a measured correlation signal. Lets start with an easy example to clarify the method. One might be interested in the correlation function of $p - A$ pairs but due to some experimental limitations also pairs of $p - B$ are included in the sample, where B is a “background” particle and A the baryon of interest. In this example protons are not affected by distortions. Both pairs enter in the following way the experimental correlation function (for simplicity we drop the normalization constant and the k^* dependence):

$$C(pA + pB) = \frac{N(pA + pB)}{N_{mix}(pA + pB)}. \quad (6.4)$$

If all selection criterias are optimized then experimentally one cannot do more. But theoretically nothing prevents one to decompose the individual contributions $N(pA + pB) = N(pA) + N(pB)$ further. Thus the experimental correlation function is a sum

of two individual correlation functions:

$$C(pA+pB) = \underbrace{\left(1 + \frac{N_{mix}(pB)}{N_{mix}(pA)}\right)^{-1}}_{\lambda_1} \underbrace{\frac{N(pA)}{N_{mix}(pA)}}_{C(pA)} + \underbrace{\left(1 + \frac{N_{mix}(pA)}{N_{mix}(pB)}\right)^{-1}}_{\lambda_2} \underbrace{\frac{N(pB)}{N_{mix}(pB)}}_{C(pB)}. \quad (6.5)$$

One can see from this equation that the separation works in the way that the corresponding correlation functions $C(pA)$, $C(pB)$ are weighted with λ parameters and these parameters are completely determined by the involved mixed event samples. The working principle is visualized with p - Λ correlations from Pythia simulations, where also impurities are present. If one identifies Λ hyperons, usually a small fraction of combinatorial background consisting of $p\pi^-$ pairs not originating from Λ decays remains. This is displayed on panel a) of Fig. 6.13. The $A = \Lambda$ baryons are shown by the blue shaded area and the combinatorial background baryons $B = p\pi^-$ are highlighted as black area. In this example $p - A = p - \Lambda$ is the pair of interest and the background pair is the correlation with the combinatorial background $p - B = p - p\pi^-$. Since Pythia simulations are usually free from femtoscopy signals the following functions are used to parametrize the pair correlations:

$$\begin{aligned} C(pA) &= 1 + \exp(-(r_0 Q_{inv})^2), \\ C(pB) &= 1 + \exp(-r_0 Q_{inv}). \end{aligned} \quad (6.6)$$

Additionally, for the background correlation function a rectangular “resonance peak” in the region $k^* \in [0.4, 0.6]$ GeV/ c is included to have a clear reference for the contribution by the background pair to the total correlation function. The individual correlation functions for the signal and background pairs are displayed in panel b) and c) of Fig. 6.13. Panel d) in the same Figure shows the two λ parameters, where λ_1 (black dots) dominates and λ_2 (red squares) is just a small perturbation. This is the expected behavior since the signal dominates over the combinatorial background in the simulation. Panel e) of Fig. 6.13 shows the total correlation function. The black dots represent the correlation function using directly the total sample of the two pairs like it is done in the experimental correlation function of Eq. 6.4. The red squares show the correlation function from the weighting prescription of Eq. 6.5 by constructing first the individual correlation functions $C(pA)$, $C(pB)$, weighting them with the λ parameters and summing them up. The two results agree exactly, which shows that the method works. It is not limited to only two pairs and can be generalized straightforwardly. Before doing so, attention is paid on how a correlation function with impurities would look like, since in most if not all analyses they are neglected as a source of residual correlations. All

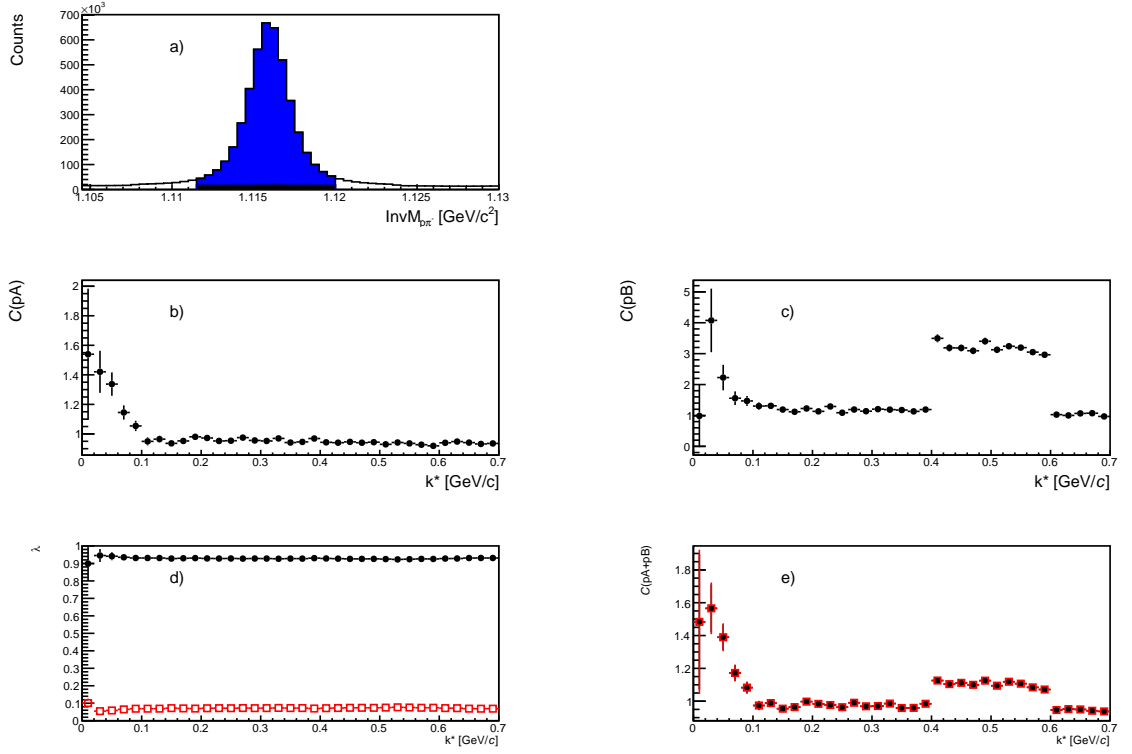


Figure 6.13: Decomposition of the individual correlation signals. The Λ signal is divided in signal (blue shaded) and background (black shaded) contributions. The signal correlation function is denoted as $p - A$ and the background function as $p - B$. With the summation of the individual correlation functions weighted with the λ parameter one gets back the red squares of $C(pA + pB)$. The black dots of $C(pA + pB)$ represent the total correlation function like it would be obtained in the experiment.

possible combinations in case of an identical particle pair including the contributions by impurities are:

$$\begin{aligned}
 C(\text{total}) &= \lambda_{\text{primary,primary}} C(\text{primary} - \text{primary}) \\
 &+ \lambda_{\text{primary,impurity}} C(\text{primary} - \text{impurity}) \\
 &+ \lambda_{\text{impurity,impurity}} C(\text{impurity} - \text{impurity}) .
 \end{aligned} \tag{6.7}$$

From this equation one can see that impurities can lead to two additional correlation functions. An example would be the analysis of $K^+ K^+$ pairs where one charged Kaon can

easily be misidentified as a π^+ . The $K^+\pi^+$ pair is strongly influenced by the Coulomb interaction and can be a source of residual correlations. If such residual correlations are present and a purity correction of the measured total correlation is performed by converting Eq. 6.7 (assuming $impurity - impurity$ is negligible):

$$\begin{aligned} C(\text{purity corrected}) &= \frac{C(\text{total}) - 1}{\lambda_{\text{primary,primary}}} + 1 = \\ &= C(\text{primary, primary}) + \frac{\lambda_{\text{primary,impurity}}}{\lambda_{\text{primary,primary}}} (C(\text{primary} - \text{impurity}) - 1), \end{aligned} \quad (6.8)$$

then the correlation function is corrected for primary pair impurities but also the residual correlation component gets enhanced. For the simplification of the equation the steps which results in Eq. 6.11 were used, which will be explained in a moment. Comparing the experimental measurement at this point to a model not including this source of residual correlations might result in a distortion of the extracted values. This is visualized in a Toy Monte Carlo study, which shows the influence of such residual correlations and thus the importance of having high particle purities. In this Monte Carlo simulation particles are produced with a Gaussian momentum source of variance 0.5 GeV/c. With a large probability these particles are identified as pions and with a small probability misidentified as kaons. The primary correlation signal of the pions are modeled as Bose-Einstein correlations (with chaoticity parameter $\lambda = 1$, which means $C(k^* = 0) = 2$. The Coulomb interaction is neglected) with a Gaussian source size of $r_0=3$ fm. For the impurity correlations the Gamov factor is used to introduce (residual) Coulomb correlations like they are present between charged particles. In Fig. 6.14 the primary correlation function and the purity corrected correlation function of Eq. (6.8) are displayed in case of high pion purities (Purity=0.99). One can see that for high purities the prescription of Eq. (6.14) works very well because residual correlations are negligible. For lower purities (Purity=0.93) the residual correlation terms in Eq. (6.7) start to play a significant role. This is displayed in Fig. 6.15, where the purity corrected correlation function does not recover the primary correlation function anymore. Not only the height but also the shape changes compared to the primary correlation function. This is because the residual component of the total correlation function introduces a non-flat structure. Comparing the data at this stage with a model one need a proper inclusion of the residual correlations. The remaining question is, how one can calculate the λ parameters, which weight the individual contributions. Up to now they were known since only simulations were considered. But in the experiment they are apriori unknown and one has to find a way to calculate them. Is it just the product of the single particle purities assumed in many analysis e.g. [Ada+15b; Ada+15c; Abe+06]? Or is it the product of the pair purity and the fraction of primary pairs, in case one has to deal with impurities and feed-down contributions at the same time assumed e.g. in [Ada+06; Ant+11] (and applied in the

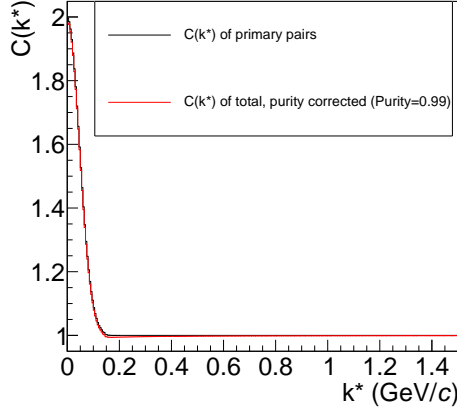


Figure 6.14: The black curve is the correlation function in which one is interested. For high purities (Purity=0.99) the residual correlations are small and one retrieves the correlation function of interest.

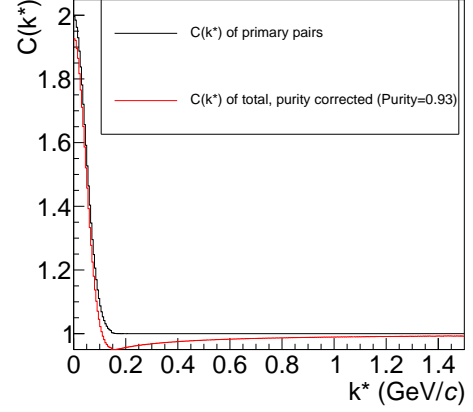


Figure 6.15: For lower purities (Purity=0.93) residual correlations from impurities start to play a role. The two correlation functions do not coincide anymore.

first part of the thesis in the HADES analysis)? Especially important is the question if such receipts are valid for all λ parameters of the correlation function or only for the one involving primary pairs? To answer these questions the formalism for two pairs in Eq. (6.5) is generalized. If one wants to measure the correlation function of $A - B$ pairs, which are part of a total sample of many other contributing pairs $X - Y$, then the total experimental correlation function for the pair $A - B$ has the form:

$$C(AB) = \frac{\sum_{XY} N(XY)}{\sum_{XY} N_{mix}(XY)} = \sum_{XY} \lambda_{XY} C(XY), \quad (6.9)$$

where the sum runs over all pairs $X - Y$ including $A - B$. The individual correlation functions $C(\alpha\beta)$ are weighted with the λ parameter:

$$\lambda_{\alpha\beta} = \frac{N_{mix}(\alpha\beta)}{\sum_{XY} N_{mix}(XY)}. \quad (6.10)$$

The λ parameter fulfill a unitarity relation $\sum_{XY} \lambda_{XY} = 1$. With this relation the superposition of the correlation function in Eq. (6.9) can be rewritten by adding just zero $0 = \sum_{XY} (\lambda_{XY} - \lambda_{XY})$ to it:

$$C(AB) = 1 + \sum_{XY} \lambda_{XY} (C(XY) - 1). \quad (6.11)$$

From this equation one can immediately see that an uncorrelated pair $C(XY) = 1$ does not contribute to the total correlation function, as expected. At this point one could use a Monte Carlo simulation and determine from its output the mixed event samples for all relevant species. This would automatically include a k^* dependency in the λ parameter. To not rely fully on a chosen event generator a different method is chosen. In the experiment one has a handle over single-particle quantities like the purity of a certain particle species. Since the tracks are selected by this single-particle quantities they must also control the properties of the pair sample. Thus, the goal is to link measurable single-particle quantities directly to the λ parameter. Since the λ parameters are determined by ratios of mixed event samples, the event mixing procedure is studied in more details. In a femtoscopy code one is analyzing pairs in a currently open event e.g. event number ten. Afterwards this event is mixed with a number of previous events, lets say with four events. This leads to event combinations 10-9, 10-8, 10-7, 10-6. Thus if one is analyzing $p - A$ correlations the resulting mixed event pair combinatorics reads (dropping the k^* dependence):

$$N_p^{10} \sum_{i=6}^9 N_A^i, \quad (6.12)$$

where N_p^{10} is the number of protons in event number 10 and N_A^i the number of A baryons in the (previous) event number i . The generalization is the following: if $A - B$ pairs are analyzed at event position j and the mixing pool has a depth m (number of previous events), then the total number of $A - B$ pairs is obtained by summing over all events:

$$\sum_{j=1}^{N_{evts}} N_A^j \sum_{i=j-m}^{j-1} N_B^i, \quad (6.13)$$

where N_{evts} is the total number of analyzed events. The arithmetic mean of the number of baryons B averaged over m events at event position j is:

$$\langle N_B^j \rangle = \frac{1}{m} \sum_{i=j-m}^{j-1} N_B^i. \quad (6.14)$$

Thus Eq. (6.13) simplifies to:

$$m \sum_{j=1}^{N_{evts}} N_A^j \langle N_B^j \rangle. \quad (6.15)$$

If the mixing depth m is large enough and nothing special happens during the time of data taking (e.g. that at some point baryons A or B are not produced/detected anymore) then the average over the B baryons should not depend on the event index j and one can

write $\langle N_B^j \rangle \approx \langle N_B \rangle$ (independent of event position one has to perform the average). Then the sum of Eq. (6.15) can be further simplified:

$$m \sum_{j=1}^{N_{evts}} N_A^j \langle N_B^j \rangle \approx m \langle N_B \rangle \sum_{j=1}^{N_{evts}} N_A^j = m N_{evts} \langle N_A \rangle \langle N_B \rangle, \quad (6.16)$$

where the average number of A baryons calculated over the whole statistics $\langle N_A \rangle = 1/N_{evts} \sum_i^{N_{evts}} N_A^i$ is introduced. Thus a mixed event sample can be written as:

$$N_{mix}(AB) = m N_{evts} \langle N_A \rangle \langle N_B \rangle. \quad (6.17)$$

This matches also nicely with the definition of the correlation function as a ratio of a event pair average over the product of single-particle averages:

$$C(AB) = \frac{N(AB)}{N_{mix}(AB)} = \frac{\sum_{i=1}^{N_{evts}} N_A^i N_B^i}{m N_{evts} \langle N_A \rangle \langle N_B \rangle} = \frac{1}{m} \frac{\langle N_A N_B \rangle}{\langle N_A \rangle \langle N_B \rangle}. \quad (6.18)$$

One can realize at this point also an approximation made implicitly when using event mixing. The definition of the experimental correlation function is actually a measure over event averaged yields. But with the event mixing technique only two out of three quantities in Eq. (6.18) are averaged over all events. At this point one has an expression for an event mixing distribution. Now they have to be related to single-particle quantities. To see how this works it is easier to go back to the specific example above of having only two pairs in the analysis, which is shown in Eq. (6.5). The λ parameter of pair $p - A$ reads:

$$\lambda_{pA} = \frac{N_{mix}(pA)}{N_{mix}(pA) + N_{mix}(pB)} = \left(1 + \frac{N_{mix}(pB)}{N_{mix}(pA)} \right)^{-1} = \left(1 + \frac{\langle B \rangle}{\langle A \rangle} \right)^{-1} \quad (6.19)$$

where the relation of Eq. (6.17) was used. One can see that in the λ parameter only ratios of mixed event samples enter, thus the constants in Eq. (6.17) drop out and a ratio of two single-particle averages remain. The result of this ratio depends on the nature of the “background” baryon B . If it is a baryon \tilde{A} that was wrongly identified as baryon A , then the ratio is related to the purity \mathcal{P} :

$$\frac{\langle B \rangle}{\langle A \rangle} = \frac{\langle \tilde{A} \rangle}{\langle A \rangle} = \mathcal{P}^{-1} - 1. \quad (6.20)$$

If B is a baryon A_X which means it is a daughter baryon from a higher lying resonance X , then one can write:

$$\frac{\langle B \rangle}{\langle A \rangle} = \frac{\langle A_X \rangle / \langle N_{tot} \rangle}{\langle A \rangle / \langle N_{tot} \rangle} \approx \frac{f_X}{f_A}, \quad (6.21)$$

where the total number of baryons $N_{tot} = N_A + N_B$ is introduced. $f_{X,A}$ are the fractions of baryons A_X and of directly produced baryons A , where A_X means A is a daughter of a resonance X . Since $f_X + f_A = 1$ one can see that Eq. (6.20) and Eq. (6.21) are symmetric, just the interpretation is different.

A visualization of the decomposition of the correlation function given in Eq. (6.7) is displayed in Fig. 6.16. It shows that the number of primary pairs decreases constantly as

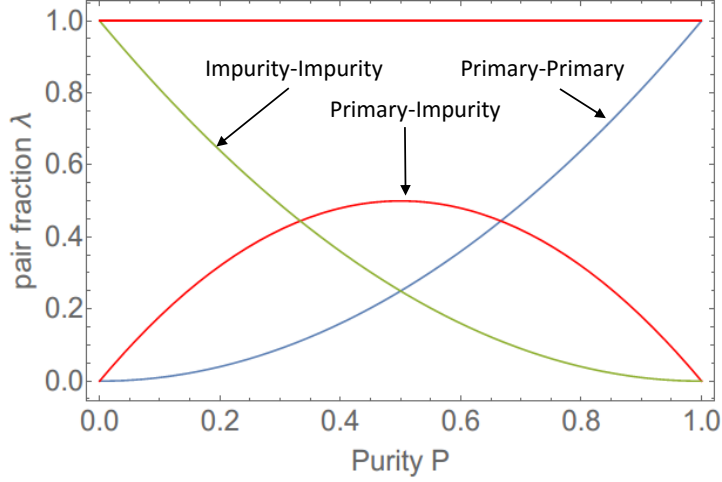


Figure 6.16: Decomposition of the correlation function given in Eq. (6.7) as a function of the single-particle Purity.

\mathcal{P}^2 and the number of impurity pairs builds up such that all contributions sum up to unity. For large purities $\mathcal{P} > 0.8$ the correlation function with both particles misidentified does not play any role. At purities around $\mathcal{P} = 0.7$ the fraction of pairs where one particle is misidentified starts to become larger than the fraction of primary pairs. Latest at this point one should stop to do femtoscopy. In this plot one can see the importance of the single-particle purity to suppress correlations from other sources.

In a last step a Toy Monte Carlo study is performed to calculate the λ parameters of the correlation function given in Eq. (6.7). The λ parameter from the simulation are compared with the method discussed above using the input purity and Eq. (6.19,6.20). To have for all three λ parameter sizeable values an input purity of $\mathcal{P} = 0.8$ is chosen. The comparison is presented in Fig. 6.17.

One can see that the results agree quite well and that there exists a relationship between λ parameter and single-particle purity/fraction.

At this stage it is useful to look at the most general form of the λ parameter in case of different pair combinations. For simplicity the brackets for event averages are dropped. Eq. (6.10) can be divided into terms dealing with purity and terms including feed-down:

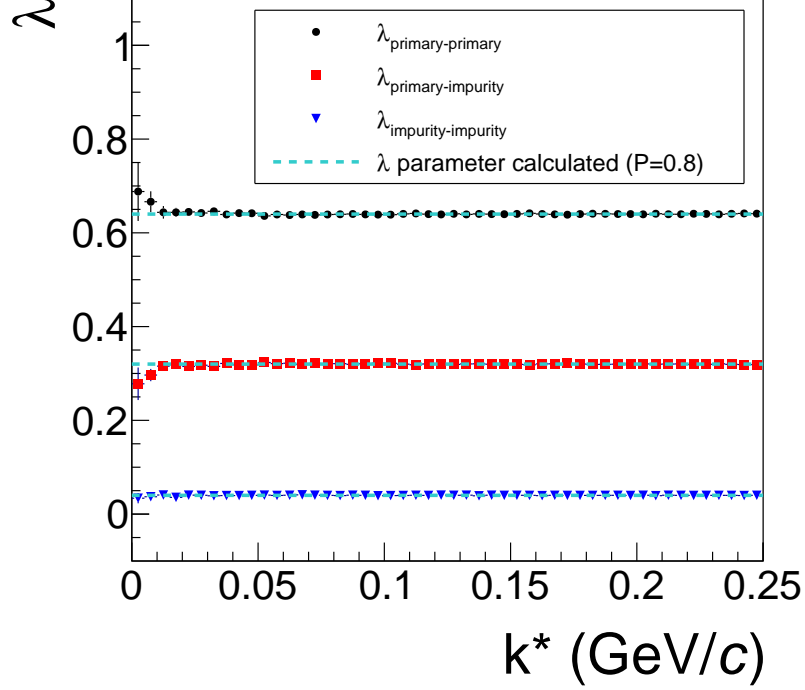


Figure 6.17: Comparison of the two methods to evaluate the λ parameter. The λ parameters presented as marker are the parameter using directly their definition. The dotted line shows the parameter by relating them to the single-particle purity $\mathcal{P} = 0.8$.

$$\lambda_{\alpha\beta} = \left(\frac{\tilde{\alpha}\beta + \alpha\tilde{\beta} + \tilde{\alpha}\tilde{\beta}}{\alpha\beta} + \frac{\sum_{XY} XY}{\alpha\beta} \right)^{-1} = \left(\frac{\tilde{\alpha}\beta + \alpha\tilde{\beta} + \tilde{\alpha}\tilde{\beta}}{\alpha\beta} + (f_\alpha f_\beta)^{-1} \right)^{-1}, \quad (6.22)$$

where the fractions f_α, f_β of α, β particles in the sample are introduced. In principle five different cases of λ parameter are possible. Defining $\bar{P}_X \equiv \mathcal{P}_X^{-1} - 1$, they read:

- Both particles are direct particles, $\alpha = A, \beta = B$:

$$\lambda_{AB} = ((\mathcal{P}_A \mathcal{P}_B)^{-1} + (f_A f_B)^{-1} - 1)^{-1}. \quad (6.23)$$

- Particle A is from resonance X, B direct: $\alpha = A_X, \beta = B$:

$$\lambda_{A_x B} = \left(\frac{f_A}{f_{Ax}} ((\mathcal{P}_A \mathcal{P}_B)^{-1} - 1) + (f_{Ax} f_B)^{-1} \right)^{-1}. \quad (6.24)$$

- Particle A is from resonance X, B from resonancy Y: $\alpha = A_X, \beta = B_Y$:

$$\lambda_{A_x B_Y} = \left(\frac{f_A f_B}{f_{Ax} f_{Ay}} ((\mathcal{P}_A \mathcal{P}_B)^{-1} - 1) + (f_{Ax} f_{By})^{-1} \right)^{-1}. \quad (6.25)$$

- Particle A is misidentified, B direct: $\alpha = \tilde{A}, \beta = B$:

$$\lambda_{\tilde{A} B} = \left(1 + \bar{P}_A^{-1} \bar{P}_B + \bar{P}_B + (\bar{P}_A f_A f_B)^{-1} \right)^{-1}. \quad (6.26)$$

- Both particles are misidentified: $\alpha = \tilde{A}, \beta = \tilde{B}$:

$$\lambda_{\tilde{A} \tilde{B}} = \left(1 + \bar{P}_A^{-1} + \bar{P}_B^{-1} + (\bar{P}_A \bar{P}_B f_A f_B)^{-1} \right)^{-1}. \quad (6.27)$$

One can nicely see in case of vanishing feed-down fractions $f_X = 0$ that the λ parameter for direct pairs scales with the purity of the sample $\lambda_{AB} = \mathcal{P}^2$. This is often used in femtoscopy to correct for purity and recovered here. Since there is a symmetry between f and \mathcal{P} the λ parameter scales also with the fraction of directly produced particles $\lambda = f^2$ for perfect purity $\mathcal{P} = 1$. For combinations of both contributions, thus with finite purity and feed-down the parameter does not factorize as often assumed. If one analyses identical pairs then one has contributions $A_X A$ but also AA_X . Since there is no difference between the two terms ($A_X A = AA_X$), such λ parameter must be multiplied by two. The great advantage of the method is its simplicity. One has just to determine a couple of parameter and they fix all individual contributions at the same time.

As a final word, the presented method can be applied whenever a separation is necessary. It is in principle also applicable in case of having jet-like structures in a two-particle correlation function. The correlation function for this case reads:

$$\begin{aligned} C(k^*)_{\text{exp}} &= 1 + \lambda_{\text{nJet}, \text{nJet}} (C(\text{nJet}, \text{nJet}) - 1) \\ &+ \lambda_{\text{nJet}, \text{Jet}} (C(\text{nJet}, \text{Jet}) - 1) \\ &+ \lambda_{\text{Jet}, \text{Jet}} (C(\text{Jet}, \text{Jet}) - 1), \end{aligned} \quad (6.28)$$

where (n)Jet denotes that a particle is (not) part of a jet. The assumption of a factorization is actually also in this case not justified. If jet-like structures are visible e.g. [Abe+13] it is often compared to a simulation model which does not include femtosopic effects but can model these jet correlations (assuming nJet-Jet is negligible):

$$C(k^*)_{\text{sim}} = 1 + \lambda_{\text{Jet}, \text{Jet}} (C(\text{Jet}, \text{Jet}) - 1). \quad (6.29)$$

Instead of a factorization it might be better to use this prediction and fit it additive to Eq. (6.28).

6.4.1 Decomposition of the proton-proton correlation function

In this section the previously discussed decomposition method is applied to the $p - p$ correlation function. A proton from misidentification is labeled as \tilde{p} and a proton from a resonance decay as p_X . The following pair contributions are taken into account:

$$\{pp\} = pp + p_\Lambda p + p_\Lambda p_\Lambda + p_{\Sigma^+} p + p_{\Sigma^+} p_{\Sigma^+} + p_\Lambda p_{\Sigma^+} + \tilde{p}p + \tilde{p}\tilde{p}. \quad (6.30)$$

Any two step resonance decays e.g. $\Xi \rightarrow \Lambda\pi \rightarrow p\pi\pi$ are not included. They are explicitly considered in the feed-down contribution of the p - Λ equation and would otherwise lead to a double counting of the residual correlations.

To calculate the λ parameter the purity of protons and the fraction of primary protons and their feed-down fractions must be determined. These information are obtained as a function of the transverse momentum p_T . The p_T averages are calculated by weighting them with the production probability dN/dp_T of the particles, where the weight is taken from the dN/dp_T spectrum:

$$\langle A \rangle = \frac{\sum_i w_i A_i}{\sum_i w_i}, w_i \in \{dN/dp_T\}. \quad (6.31)$$

With this method the region where most of the particles are produced is stronger weighted. The fraction of primaries could be directly obtained from a Monte Carlo generator. However, the common generators underestimate the fraction of contaminations [Cho12]. For this reason a more data driven method is employed. The strategy is to divide the Monte Carlo predictions into templates of three parts of proton sources: protons directly produced from the reaction, from weakly decaying resonances and from detector material. A good discrimination of all three contributions is achieved by using the DCA_{xy} impact parameter. Since primary protons are produced at the collision point their distance to the primary vertex is rather small and thus tends to peak around zero in this observable. Secondary protons have a broader distribution due to their origin of a decayed resonance and material protons are distributed more or less flat over all DCA_{xy} values. All three templates are adjusted with help of the ROOT routine *TFractionFitter*¹. The fit range was chosen to be $|DCA_{xy}| < 2.4$ cm. The template fits over the full range of p_T is shown in Fig. 6.18. Since the different contributions are hardly visible an example plot of a fit performed in the second lowest p_T bin ($0.68 < p_T < 0.86$ GeV/c) is shown in Fig. 6.19. The material budget plays a role for small p_T values but decreases with increasing p_T . Due to this reason it is taken out for higher p_T bins to increase the stability of the fit. The resulting number of primary protons averaged over p_T is 87% and the other 13% is addressed to weakly decaying resonances. The contribution of protons from material is negligible. The 13% feed-down component must be decomposed in the contributing

¹<https://root.cern.ch/doc/master/classTFractionFitter.html>

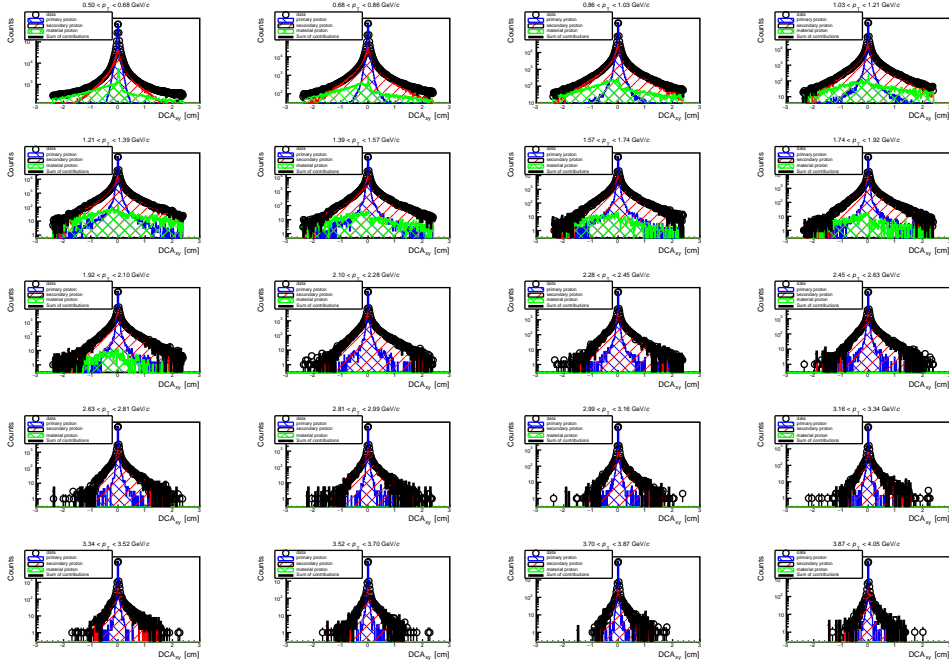


Figure 6.18: Adjusted Monte Carlo Templates from Pythia to the experimental data in the full p_T range.

resonances, which was done with help of Pythia. According to this model there are two sources of feed-down resonances the Σ^+ (30%) and Λ (70%). Their contributions stay constant over the whole p_T range. This is displayed in Fig. 6.20. With this information the values for the feed-down fractions to protons is given by:

$$\begin{aligned} f_{\Sigma^+} &= 13\% \times 30\% = 3.9\% \\ f_{\Lambda} &= 13\% \times 70\% = 9.1\% . \end{aligned} \tag{6.32}$$

All fractions sum to unity $\sum_i f_i = 1$ as needed. The purity of the sample is obtained also from Pythia simulations by calculating $\mathcal{P} = S/(S + B)$. Due to the fact that most protons are produced in a region where the TPC has enough separation power the purity is expected to be rather large. This can be seen in Fig. 6.21. The purity at large p_T drops below 80% but this region is not strongly weighted since in this region not many protons are produced. The summary of the p_T averaged quantities are shown in Fig. 6.21. With all needed values known the individual contributions to the total correlation function are presented in Tab. 6.2.

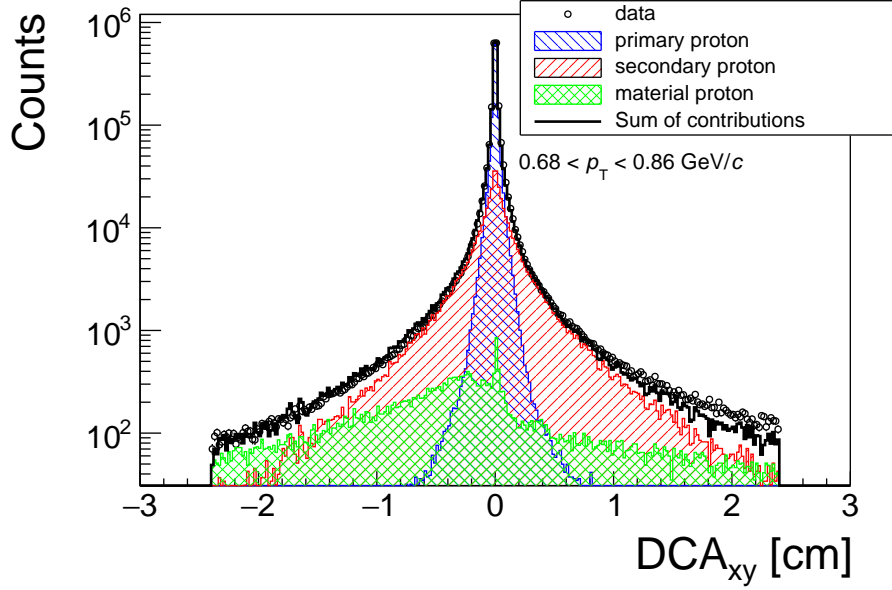


Figure 6.19: Adjusted Monte Carlo Templates from Pythia to the experimental data. Due to the shape of the templates one has a good discrimination of the origin of the protons.

6.4.2 Decomposition of the proton-Lambda correlation function

The method for the decomposition of the p - Λ correlation function is very similar to the one of the p - p pair except that one has to introduce more quantities since one is dealing with a non-identical particle pair and both particles can have different purities and feed-down fractions. Like in the p - p case \tilde{X} labels mis-identified X particles. The following pair combinations are taken into account:

$$\begin{aligned}
 \{p\Lambda\} = & p\Lambda + p\Lambda_{\Xi^-} + p\Lambda_{\Xi^0} + p\Lambda_{\Sigma^0} + p_{\Lambda}\Lambda + p_{\Lambda}\Lambda_{\Xi^-} \\
 & + p_{\Lambda}\Lambda_{\Xi^0} + p_{\Lambda}\Lambda_{\Sigma^0} + p_{\Sigma^+}\Lambda + p_{\Sigma^+}\Lambda_{\Xi^-} + p_{\Sigma^+}\Lambda_{\Xi^0} + p_{\Sigma^+}\Lambda_{\Sigma^0} \\
 & + \tilde{p}\Lambda + p\tilde{\Lambda} + \tilde{p}\tilde{\Lambda}
 \end{aligned} \tag{6.33}$$

The purity is calculated with the relation $\mathcal{P}_{\Lambda} = S/(S+B)$ from fits of the invariant mass spectra. For the fraction of feed-down also a template fit is performed with the cosine pointing angle for separation. The templates are divided in direct, feed-down, material and combinatorial background Λ contributions. The results of the fits are shown in Fig. 6.22. An example template fit is shown in Fig. 6.23. To obtain p_T average values, the

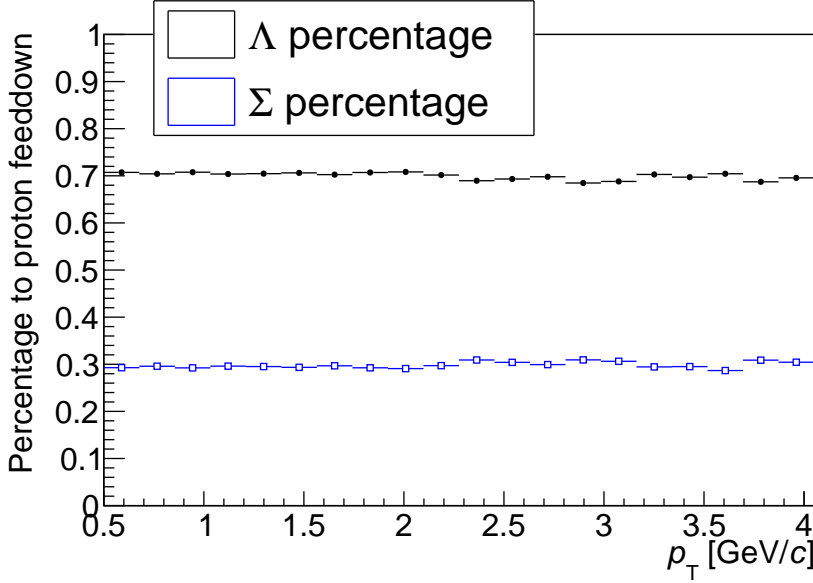


Figure 6.20: Percentage of feed-down to protons from Σ^+ and Λ as a function of p_T .

production probability dN/dp_T is again employed to weight p_T regions stronger where more Λ are produced. The results for the purity and feed-down fractions is shown in Fig. 6.24. The Σ^0 hyperon decays electromagnetically almost exclusively into $\Lambda\gamma$ [Oli+14]. Thus it has a very short lifetime and cannot be rejected from the sample. Another source of feed-down are long living weakly decaying resonances. All sources have to be determined. According to the template fit method around 73% of the Λ are directly produced in the collision and 23% originate from weakly decaying resonances. Similar values are extracted in [Abb+13]. The rest is addressed to combinatorial background and material Λ . The impurity and material budget have to be subtracted from the sample, thus the fraction of primary and secondary Λ is rescaled by $1 - f_{\Lambda,\text{background}} - f_{\Lambda,\text{material}}$. The corrected values are then $f_{\Lambda,\text{primary}} = 77\%$ and $f_{\Lambda,\text{secondary}} = 23\%$. Like in the proton case the relative feed-down composition of this 23% has to be calculated. Again Pythia simulations are used to extract them. The main feed-down contributions are originating from Ξ^0 (48%) and Ξ^- (49%) resonances. The rest is addressed to Σ^0 . It makes sense that the Ξ contributions are equal since there is no special mechanism preferring one of the two Ξ . The Σ^0 fraction is just on the percent level, thus it will be addressed separately. The contribution of Ξ is set to 50%, thus its fractions are:

$$f_{\Xi^{0,-}} = 23\% \times 50\% \approx 12\% . \quad (6.34)$$

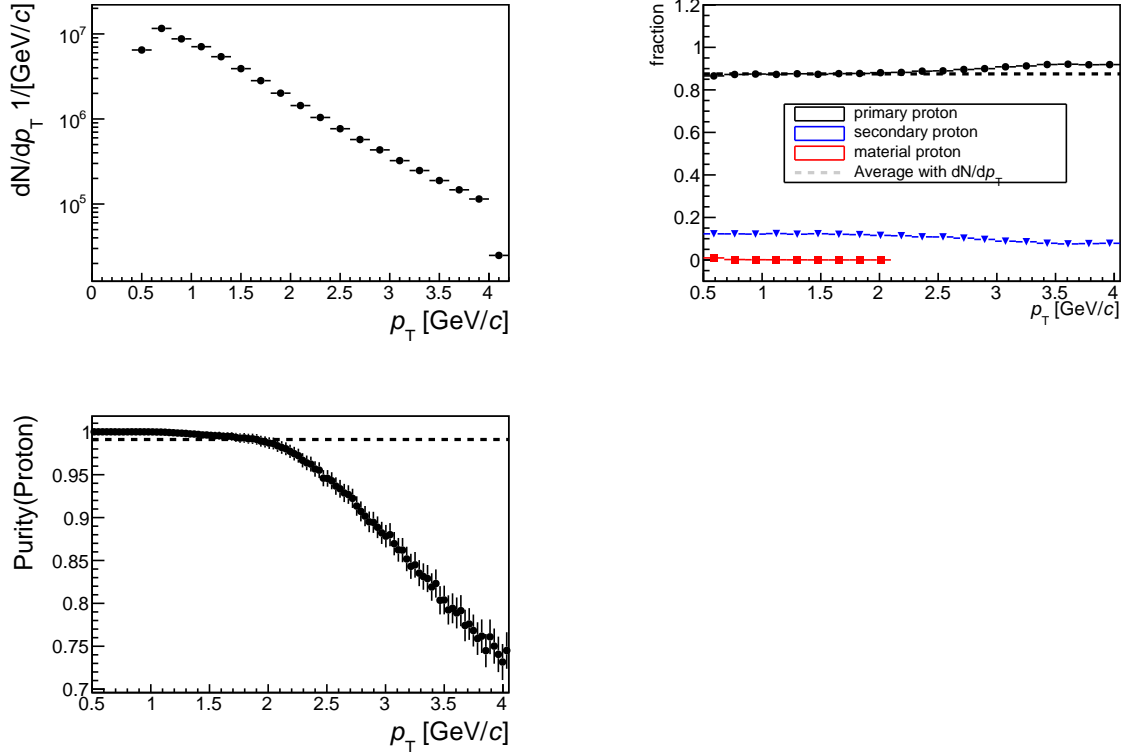


Figure 6.21: The fractions of protons as a function of p_T obtained from the template fitting method. The purity is extracted from Pythia. The averages of the quantities are obtained by using the production probability dN/dp_T of protons.

The Σ^0 contribution can be related to isospin symmetry. The Λ is represented in an isospin singlet state, whereas the Σ^0 belongs to an isospin triplet representation. Thus if the energy in the reaction is large enough there exists the possibility to excite three different Σ states but only one Λ state. Thus the cross section ratio of the Σ^0 to Λ is expected to be $R_{\Sigma^0/\Lambda} = \sigma_{\Sigma^0}/\sigma_{\Lambda} = 1/3$ at large energies. This typical 33% effect is summarized in [Van06] of collision energies up to RHIC energies for various colliding systems. In an analysis in pp collisions at 7 TeV the ratio is determined to be $R_{\Sigma^0/\Lambda} = 0.380 \pm 0.098$ ¹, thus consistent with the ratio of 1/3 which will be used in this analysis. The fraction of directly produced Λ and Σ^0 is known from the template fit and since the

¹<https://aliceinfo.cern.ch/Notes/node/562>

| Pair | Percentage % |
|--------------------------------------|--------------|
| pp | 75 |
| $p_{\Lambda}p$ | 16 |
| $p_{\Lambda}p_{\Lambda}$ | 1 |
| $p_{\Sigma^+}p$ | 6 |
| $p_{\Sigma^+}p_{\Sigma^+}$ | 0 |
| $p_{\Sigma^+}p_{\Lambda}$ | 0 |
| $\tilde{p}p$ | 2 |
| $\tilde{\tilde{p}}\tilde{\tilde{p}}$ | 0 |

Table 6.2: The λ values for the individual components of $p - p$ correlation function.

ratio of both contributions is also fixed one can determine the fraction of Σ^0 :

$$\begin{aligned}
 f_{\Lambda} + f_{\Sigma^0} &\equiv F = 73\%, R_{\Sigma^0/\Lambda} = \frac{f_{\Sigma^0}}{f_{\Lambda}} = 0.33 \\
 \simeq f_{\Sigma^0} &= F \frac{R_{\Sigma^0/\Lambda}}{1 + R_{\Sigma^0/\Lambda}} = 19\%, f_{\Lambda} = F - f_{\Sigma^0} = 58\% .
 \end{aligned}
 \tag{6.35}$$

With this calculations all needed information are collected to evaluate the λ parameter for the p - Λ pair. The results are shown in Tab. 6.3.

6.4.3 Decomposition of the Lambda-Lambda correlation function

For the $\Lambda - \Lambda$ correlation function the following pair contributions are taken into account:

$$\begin{aligned}
 \{\Lambda\Lambda\} &= \Lambda\Lambda + \Lambda\Lambda_{\Sigma^0} + \Lambda_{\Sigma^0}\Lambda_{\Sigma^0} + \Lambda\Lambda_{\Xi^0} + \\
 &\Lambda_{\Xi^0}\Lambda_{\Xi^0} + \Lambda\Lambda_{\Xi^-} + \Lambda_{\Xi^-}\Lambda_{\Xi^-} + \Lambda_{\Sigma^0}\Lambda_{\Xi^0} + \\
 &\Lambda_{\Sigma^0}\Lambda_{\Xi^-} + \Lambda_{\Xi^0}\Lambda_{\Xi^-} + \tilde{\Lambda}\Lambda + \tilde{\Lambda}\tilde{\Lambda}
 \end{aligned}
 \tag{6.36}$$

To calculate the individual pair fractions no new information for the fractions are needed. Everything was already determined for the p - Λ correlation function and the feed-down fractions can directly be reused again. The result of the individual pair fractions is shown in Tab. 6.4. One can see in this table that the pair fractions involving Σ^0 and Ξ have a significant contribution.

| Pair | Percentage % |
|----------------------------------|--------------|
| $p\Lambda$ | 49 |
| $p\Lambda_{\Xi^-}$ | 10 |
| $p\Lambda_{\Xi^0}$ | 10 |
| $p\Lambda_{\Sigma^0}$ | 16 |
| $p_{\Lambda}\Lambda$ | 5 |
| $p_{\Lambda}\Lambda_{\Xi^-}$ | 1 |
| $p_{\Lambda}\Lambda_{\Xi^0}$ | 1 |
| $p_{\Lambda}\Lambda_{\Sigma^0}$ | 2 |
| $p_{\Sigma^+}\Lambda$ | 0 |
| $p_{\Sigma^+}\Lambda_{\Xi^-}$ | 0 |
| $p_{\Sigma^+}\Lambda_{\Xi^0}$ | 1 |
| $p_{\Sigma^+}\Lambda_{\Sigma^0}$ | 2 |
| $\tilde{p}\Lambda$ | 1 |
| $p\tilde{\Lambda}$ | 2 |
| $\tilde{p}\tilde{\Lambda}$ | 0 |

Table 6.3: The λ values for the individual components of the proton- Λ correlation function.

| Pair | Percentage % |
|--|--------------|
| $\Lambda\Lambda$ | 32 |
| $\Lambda\Lambda_{\Sigma^0}$ | 21 |
| $\Lambda_{\Sigma^0}\Lambda_{\Sigma^0}$ | 3 |
| $\Lambda\Lambda_{\Xi^0}$ | 13 |
| $\Lambda_{\Xi^0}\Lambda_{\Xi^0}$ | 2 |
| $\Lambda\Lambda_{\Xi^-}$ | 13 |
| $\Lambda_{\Xi^-}\Lambda_{\Xi^-}$ | 2 |
| $\Lambda_{\Sigma^0}\Lambda_{\Xi^0}$ | 4 |
| $\Lambda_{\Sigma^0}\Lambda_{\Xi^-}$ | 4 |
| $\Lambda_{\Xi^0}\Lambda_{\Xi^-}$ | 3 |
| $\tilde{\Lambda}\Lambda$ | 3 |
| $\tilde{\Lambda}\tilde{\Lambda}$ | 0 |

Table 6.4: The λ values for the individual components of the Λ - Λ correlation function.

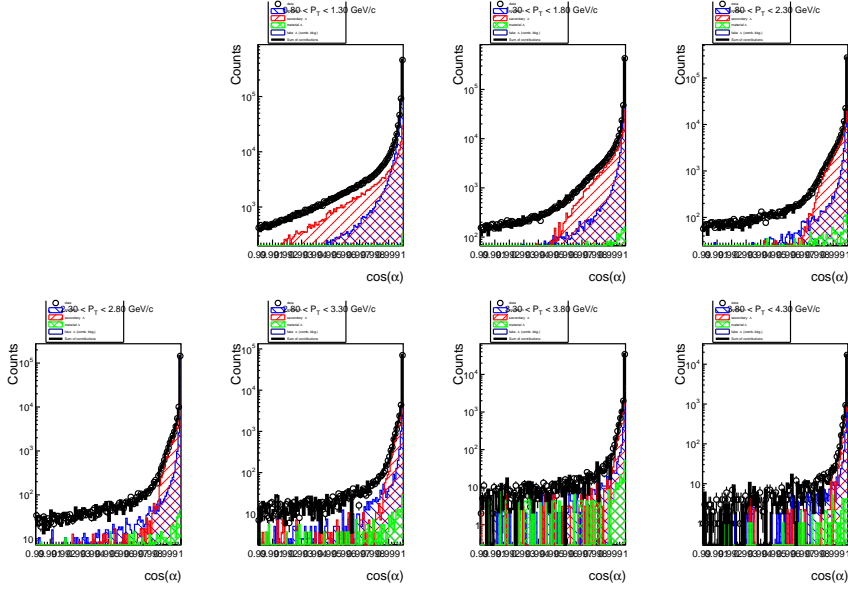


Figure 6.22: Template fit to the cosine pointing angle in the full p_T interval.

6.5 Corrections

In this section all applied corrections are discussed. The main corrections involve the finite momentum resolution of ALICE, the inclusion of residual correlations and the treatment of non-femtoscopic correlations.

6.5.1 Residual Correlations

In case of Baryon-Baryon correlations one or both baryons could stem from a long-lived resonance. An example would be that initially a $p - \Xi$ pair is produced and the $\Xi \rightarrow \Lambda\pi$ decays on the way to the detector. The decay event does only partly deplete the primary $p - \Xi$ femtoscopic signal and part of it is distributed among the resulting $p - \Lambda$ pair. This kind of residual correlations contribute to the total correlation function as was shown in the last Section. A theoretical investigation of this effect was firstly done in [Wan99] for residual correlations from $p - \Lambda$ imposed on $p - p$ pairs. In high energy experiments the effect can be significant since many higher lying resonances are excited. The importance of residual correlations was firstly realized in the STAR $p - \bar{\Lambda}$ analysis [Ada+06], where the resulting source size of $p - \bar{\Lambda}$ was much different compared to the $p - \Lambda$ system. After a re-analysis including residual correlations, the source sizes of both pairs were of similar size [KZS14; Sha+15]. This highlights the influence of including them properly. However, the importance is more pronounced for Antibaryon-Baryon pairs since they tend to have dip structures due to inelastic scattering processes. Such dip structures

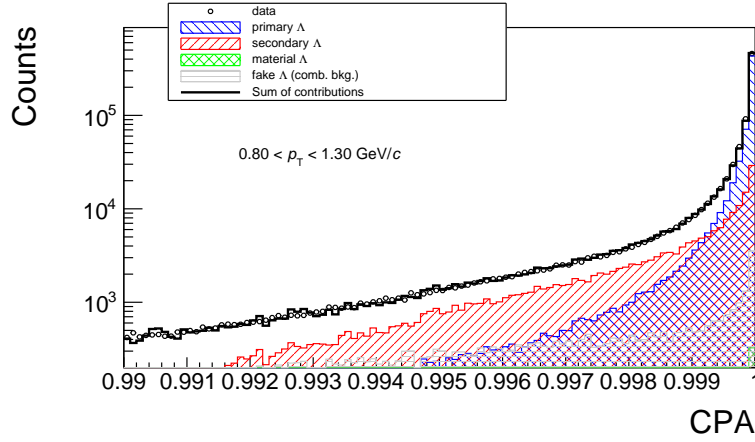


Figure 6.23: Template fit to the cosine pointing angle in a p_T interval.

remain also after the decay. For Baryon-Baryon pairs the initial correlation signals are mostly flattened out due to the decay.

To model residual correlations, the initial correlation function has to be calculated and then transformed to the new momentum basis. This was proposed in [KZS14]. To determine the residual correlation induced by a pair $p - B$ on $p - A$ ($B \rightarrow A_B + \dots$) the equation reads:

$$C(k_{pA}^*)^{pB \rightarrow pA} = \frac{\sum_{k_{pB}^*} C^{pB}(k_{pB}^*) M(k_{pA}^*, k_{pB}^*)}{\sum_{k_{pB}^*} M(k_{pA}^*, k_{pB}^*)}, \quad (6.37)$$

where $M(k_{pA}^*, k_{pB}^*)$ is the matrix which includes the correlation between the momenta k_{pA}^* and k_{pB}^* and $C^{pB}(k_{pB}^*)$ is the correlation function of the pair $p - B$. The matrix $M(k_{pA}^*, k_{pB}^*)$ shows usually a high level of correlation between the momenta since most of the momentum of long living weakly decaying resonances is shared by the daughter baryon. The matrices are calculated using the simple event generator GENBOD¹. It simulates kinematically allowed events according to phase-space distributions and calculates the corresponding probability that such events occur. With this generator one can simulate in a very short time enough statistics for the corresponding transformation matrices. The momenta of the particles are sampled by an uniform distribution in a momentum range $p_{x,y,z} \in [-5, 5]$ GeV/c. With the initial sampled momenta the initial k^* momentum of the pair is calculated. The four-momentum of the pair is then given to GENBOD, which simulates the decay. The resulting matrices from this simulation are displayed in Fig. 6.25 for the decay $p - \Lambda \rightarrow p - p$ and $(p - \Sigma^0, p - \Xi^-) \rightarrow p \Lambda$. One can

¹<https://root.cern.ch/doc/v608/classTGenPhaseSpace.html>

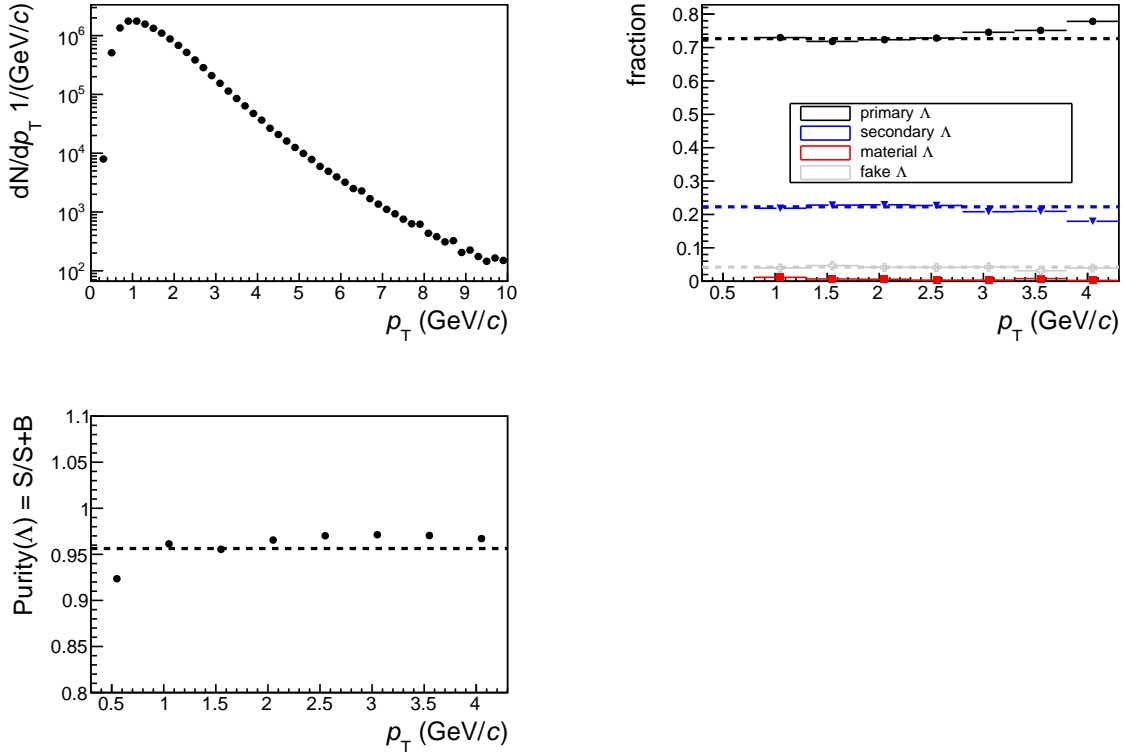


Figure 6.24: The fractions of Λ as a function of p_T obtained from a template fitting method. The purity is extracted by fitting the Λ invariant mass peaks. The averages of the quantities are evaluated by using the production probability dN/dp_T of Λ .

see that the k^* momenta are quite correlated. After the decay only the resulting baryon pair is taken into account for the k^* calculation. Thus the missing meson momentum is responsible for the width of the k^* distribution.

The remaining task is to calculate the initial correlation functions. For the $p - p$ channel only the feed-down from the p - Λ correlation function is considered. It is taken into account by fitting the p - Λ experimental correlation function and then transforming it to the $p - p$ momentum basis. For the p - Λ residual correlations the $p - \Sigma^0$, $p - \Xi^-$ and $\Lambda - \Lambda$ pairs are taken into account. However, since it was presented in Fig. 6.12 that the $\Lambda - \Lambda$ correlation function is quite flat it is also assumed to be consistent with unity and thus uncorrelated. The $p - \Sigma^0$ correlation function is taken from calculations of [Sta+07]. Since Σ hyperons are represented in an isopin triplet configuration the $p - \Sigma^0$ pair can have two isospin configurations. For every $p - \Sigma^0$ isospin state two spin states are possible. Additionally, there exists an inelastic channel $p\Sigma^0 \rightarrow p\Lambda$ such that the scattering length must include also an inelastic part. Above the $p\Sigma^0$ pair the $n\Sigma^+$ pair

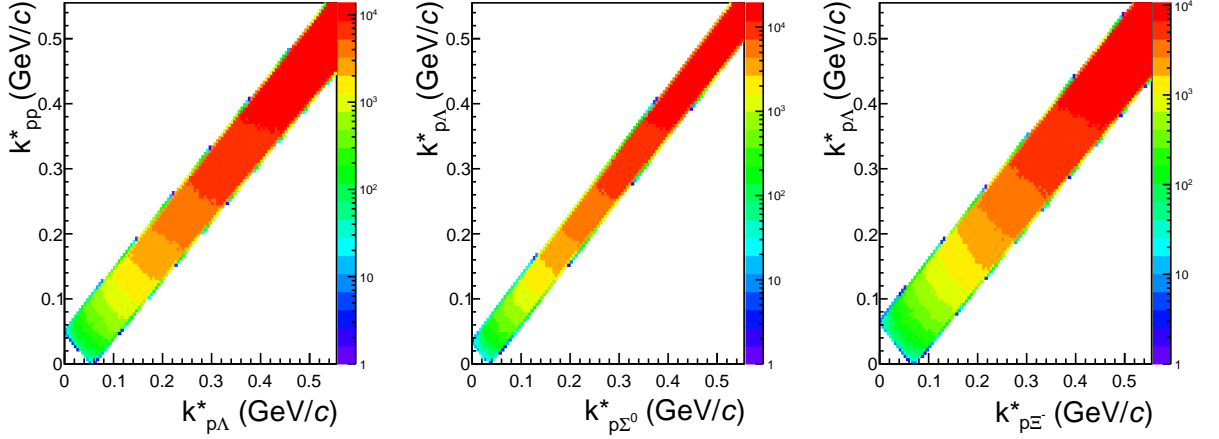


Figure 6.25: Transformation matrix M for p - Λ decaying into pairs of $p-p$ (left) and $p-\Sigma^0$ (middle) $p-\Xi^-$ (right) decaying in pairs of p - Λ .

| Isopin I | $a_I^{S=0}$ [fm] | $a_I^{S=1}$ [fm] | $d_I^{S=0}$ [fm] | $d_I^{S=1}$ [fm] |
|------------|------------------|------------------|------------------|------------------|
| 1/2 | -1.1 | $-1.1+i4.3$ | -1.5 | $-2.2-i2.4$ |
| 3/2 | 2.51 | -0.73 | 4.92 | -1.22 |

Table 6.5: Scattering parameters to model $p\Sigma^0$ correlations. Taken from [Sta+07].

is located in mass, which couples to $p\Sigma^0$ inelastically. All these effects are modeled in [Sta+07]. It is adapted for this analysis. The correlation function is a sum of the two contributions $p\Sigma^0 \rightarrow p\Sigma^0$ and $n\Sigma^+ \rightarrow p\Sigma^0$:

$$C(k^*) = \left\langle |\psi_{-\mathbf{k}^*}^{S, p\Sigma^0 \rightarrow p\Sigma^0}(\mathbf{r}^*)|^2 \right\rangle + \left\langle |\psi_{-\mathbf{k}^*}^{S, n\Sigma^+ \rightarrow p\Sigma^0}(\mathbf{r}^*)|^2 \right\rangle, \quad (6.38)$$

where the brackets $\langle \rangle$ denote the averaging over the space-time configuration with the source function. One can see that the main difference in Eq. (6.38) to p - Λ is the additional inelastic term. The values used for the $p\Sigma^0$ correlation function are given in Tab. 6.5. One can see that the number of parameters is more than doubled compared to the p - Λ case and most of them are unknown. Similar arguments hold for the p - Ξ^- case. Also for this pair inelastic channels are present like $p\Xi^- \rightarrow \Lambda\Lambda$, $n\Xi^0$, $\Sigma^0\Lambda$ and two isospin states with two spin states for each isospin value respectively. A theoretical treatment of the elastic channels can be found in [HMP16]. Additionally, this pair is affected by Coulomb attraction. Thus it is very hard to model. However, the $\Xi^- \rightarrow \Lambda\pi$ decay products in this channel are charged and therefore accessible by ALICE. It is tried to measure

the $p\Xi$ correlation function in pp collisions and parametrize it with a phenomenological function:

$$C(k^*)^{p\Xi^-} = 1 + \frac{\exp(-k^*r_0)}{k^*r_0}. \quad (6.39)$$

This function has some rising for low k^* which mimics a Coulomb attraction. In this case r_0 is just a parameter to scale the function to the data and has no physical meaning. Its value is $r_0 = 3.88$ fm. All initial correlation functions taken into account and their functional shape after the decay are displayed in Fig. 6.26.

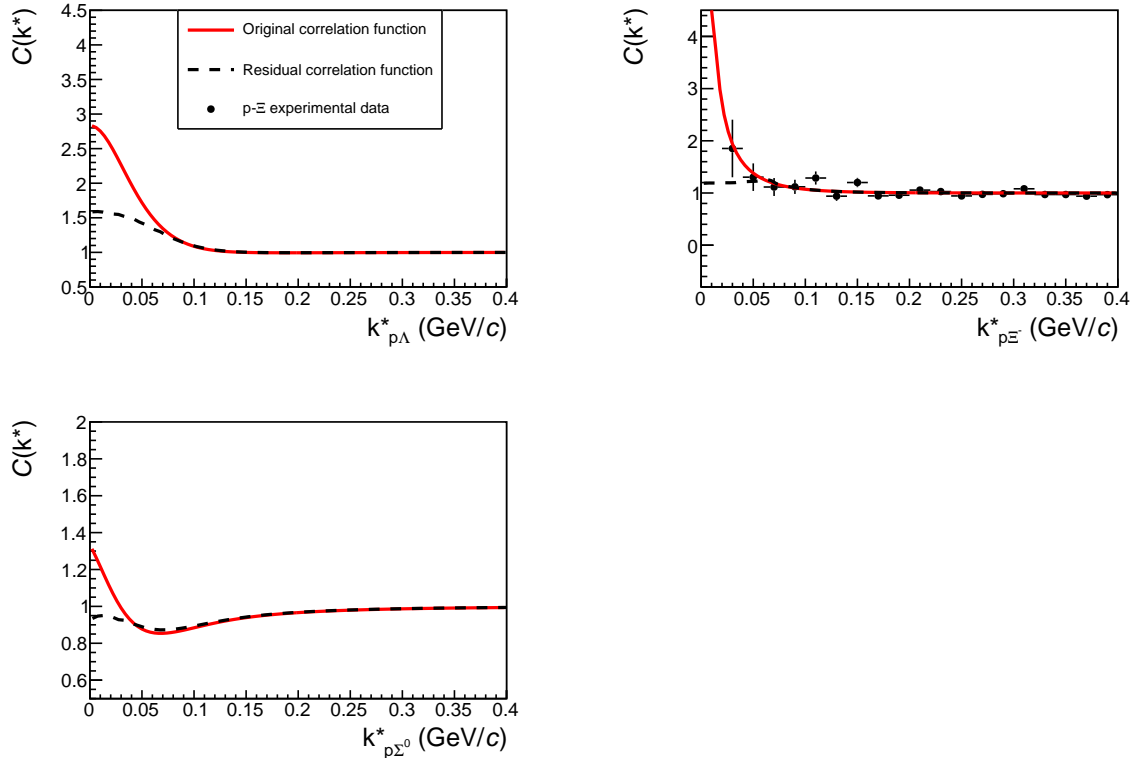


Figure 6.26: Initial correlation functions displayed as red solid lines. The black dashed lines are the residual correlations. Top left: $p-\Lambda \rightarrow p-p$, Top right: $p-\Xi^- \rightarrow p-\Lambda$. Bottom left: $p-\Sigma^0 \rightarrow p-\Lambda$.

6.5.2 Finite momentum resolution

The particles are measured with a finite momentum resolution which has an influence on the measured correlation signal. The single-particle momentum can be written in the

form:

$$p^\mu = \begin{pmatrix} E \\ p_T \cos(\varphi) \\ p_T \sin(\varphi) \\ p_T \sinh(\eta) \end{pmatrix}. \quad (6.40)$$

One can see that the momentum resolution depends on the resolution of the single-particle p_T as well as the resolutions of the angles φ and Θ . Since in femtoscopy the differences of the vectors are contracted $Q_{\text{inv}} = \sqrt{-(p_1 - p_2) \cdot (p_1 - p_2)}$ (for non-identical particles an additional term must be included) all resolutions combine in a non-trivial way to the resolution of the relative momentum. Since one has control over single particle resolutions they are obtained from Pythia simulations in this analysis and compared to published ALICE results, if available. For the inverse p_T resolution, ALICE published their results for the p-Pb system [Abe+14b] at $\sqrt{s_{\text{NN}}}=5.02$ TeV, which is displayed in Fig. 6.27. The default track selection in this thesis corresponds to TPC-

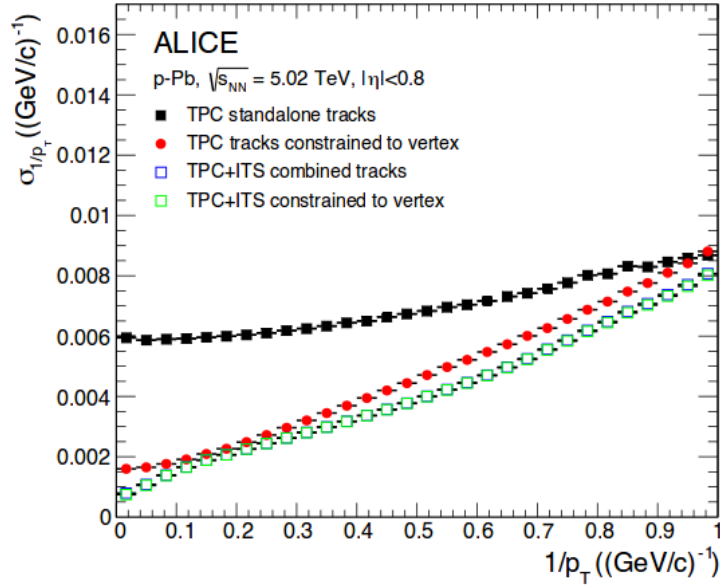


Figure 6.27: Momentum resolution of the p-Pb system at $\sqrt{s_{\text{NN}}}=5.02$ TeV for different track candidates.

only tracks constrained to the primary vertex, which corresponds to the red points in Fig. 6.27. The resolution is a more vivid observable compared to the inverse resolution and both observables are directly linked by the Equation [Abe+14b]:

$$\frac{\sigma_{p_T}}{p_T} = p_T \sigma_{1/p_T}. \quad (6.41)$$

The published results are compared with resolutions obtained from Pythia simulations, where the tracks are propagated to the whole ALICE framework. The resolutions are computed by fitting a Gaussian model to the difference of the generated and reconstructed values in bins of p_T . The result for the p_T , φ and Θ resolutions obtained from these fits are displayed in Fig. 6.28. One can see that the p_T resolution is below 1% at

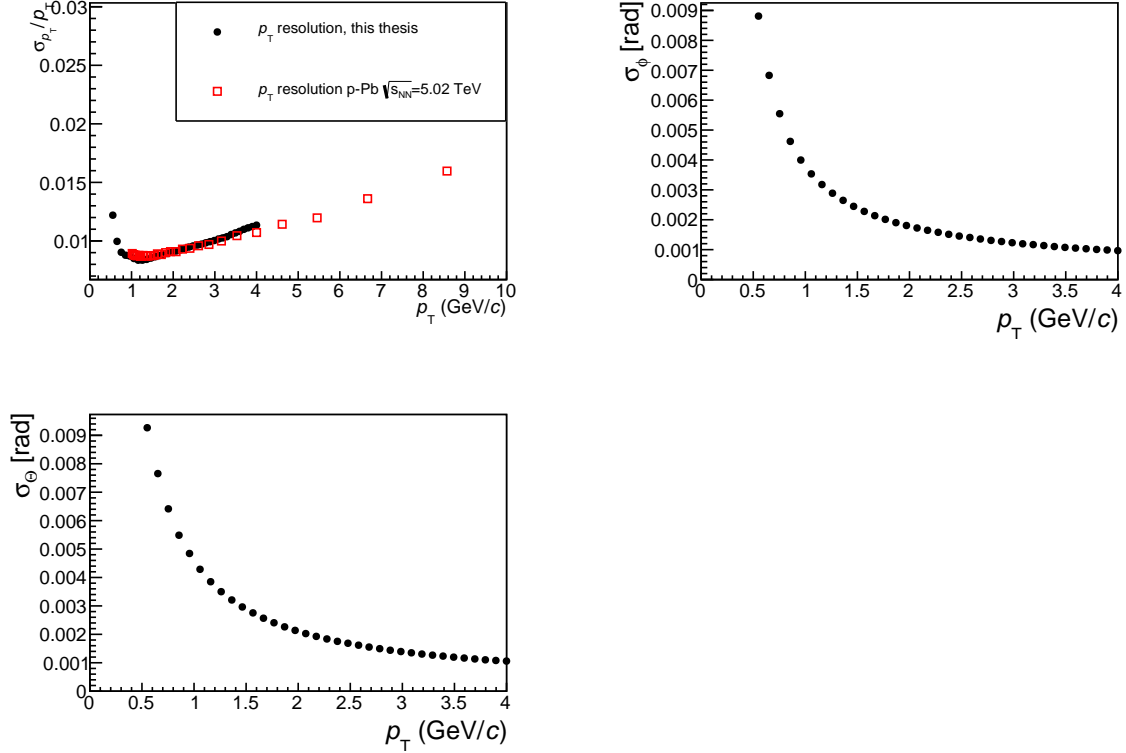


Figure 6.28: Momentum and angle resolutions of the pp system obtained from Pythia simulations.

transverse momenta around 1 GeV/c and stays below 1.5% in the p_T range considered in this analysis. The angle resolution is worse at the lower p_T threshold but decreases with increasing p_T . Since most of the considered particles are produced at around 1 GeV/c, the transverse momentum resolution is at its minimum and one has a medium angle resolution in this range.

Since a total correlation function is separated into feed-down and impurity fractions, theoretically two separate resolution matrices are needed. Since the contribution from impurities can be neglected only the resolution matrix for the feed-down contribution is calculated. It is again extracted from Pythia simulations using event mixing to increase the statistics. For the particles the PDG code is prompted since impurities are separated

as mentioned before. The result of the resolution matrices for the relative momenta k^* of $p - p$ and $p - \Lambda$ pairs is shown in Fig. 6.29. The influence of the finite momentum

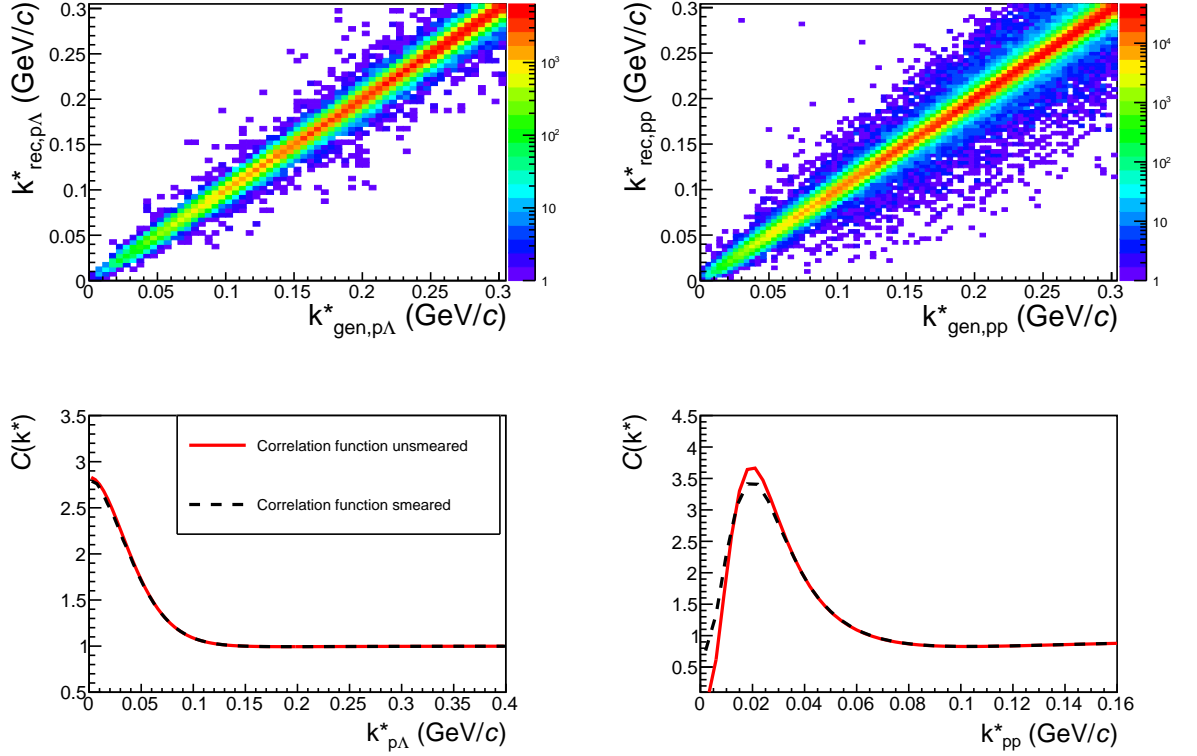


Figure 6.29: Top: Resolution matrices for $p - \Lambda$ and $p - p$. Bottom: Influence of the momentum resolution on the correlation functions.

resolution on the $p - \Lambda$ pair is negligible and has a moderate influence on the $p - p$ correlation function. The resolution effect will be taken into account when the experimental data is compared to model calculations in the fitting procedure by smearing the model with help of Eq. (6.37). The transformation matrix M is then equal to the resolution matrix and the initial unsmeared correlation function is transformed to the reconstructed momentum basis.

6.5.3 Pair selection criteria

Femtoscopy relies on a measurement of the momentum difference of two particles. The correlation signal is visible for small differences. This requires that the tracks of both particles are quite collinear and thus affected by various detector effects. Two of them

are track merging, which means two tracks are reconstructed as one track or track splitting, where one track is reconstructed as two tracks by the detector. Both effects lead to artificial correlations and one has to get rid of them. To check for possible effects of the detector the investigation is done in differences of the angles. Since in ALICE the particles are emitted inside of the magnetic field their differences in φ (and η for non-identical particles) can be different at the collision point and in the TPC where the merging is happening. Since tracks are bended in the magnetic field on a circular trajectory the correction of φ is:

$$\varphi^* = \varphi + \arcsin\left(\frac{0.3RBe}{2p_T} \frac{1}{T_m}\right), \quad (6.42)$$

where B is the strength of the magnetic field, R the radial distance from the collision point, e the charge of the particle and p_T its transverse momentum. The angle differences for $p-p$ pairs from Pythia simulations is shown in Fig. 6.30 for nine different radii in the TPC. The corresponding distributions are divided by its mixed event samples. No clear

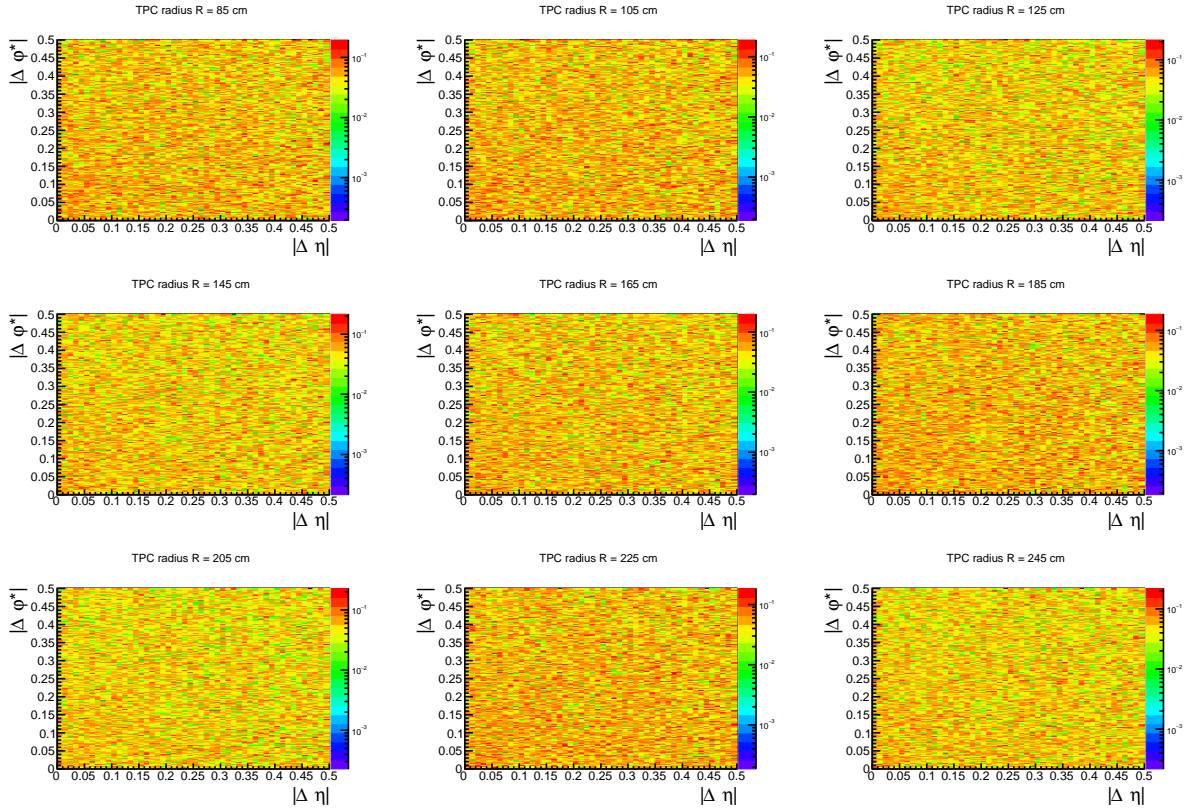


Figure 6.30: Correlation function for $p-p$ in φ^*, η representation for Pythia simulations at different radii of the TPC. Merging or splitting would be visible at the origin (0,0).

sign for merging is visible which would be indicated by a loss of pairs for small angle separations. The angle correlation function looks quite flat. For this reason no explicit selection criteria are introduced.

6.5.4 Non-femtoscopic background

If only the femtoscopic signal is present then it is located in a region $k^* < k_{\text{femto}}^*$, where k_{femto}^* depends on the system size and is of the order of 100 MeV/c. For sufficiently large momentum differences the correlation signal should vanish thus $C(k^* > k_{\text{femto}}^*) \rightarrow 1$. However, in most analysis additional correlation signals are present. They have their origin in energy-momentum-conservation, mini-jets, flow and other sources. The effect of mini-jet induced background was observed for pions in pp [Aam+11] as well as p-Pb collisions [Ada+15a]. However, the same correlation functions were also described in a formalism developed for signals induced solely by energy and momentum conservation [Boc11]. Whatever the reason for the non-femtoscopic effect is, it seems that higher order correlations e.g. a three pion cumulant can suppress such distortions significantly [Abe+14a].

In general such non-femtoscopic structures are more pronounced in small systems, where the multiplicity is low. In this analysis the baseline is also not flat for large k^* and a small tilt of the baseline is visible. To have a better fit performance this tilting is included by describing the baseline with a linear function:

$$C(k^*)_{\text{non-femto}} = ak^* + b, \quad (6.43)$$

where a, b are just fit parameters. The non-femtoscopic structure is taken into account in the total fit function:

$$C(k^*) = C(k^*)_{\text{femto}} \times C(k^*)_{\text{non-femto}}. \quad (6.44)$$

The fit parameters are obtained in the range $k^* \in [0.12, 0.42]$ GeV/c for $p - p$ pairs and $k^* \in [0.2, 0.5]$ GeV/c for the $p - \Lambda$ and $\Lambda - \Lambda$ system. The result of the baseline fits of all three systems with Eq. (6.43) is shown in Fig. 6.31.

6.6 Systematic uncertainties

In this Section the sensitivity of the correlation functions on the chosen selection criteria is explored. First the sensitivity of the correlation functions on the proton selection is tested by varying the proton selection criteria:

- Influence of the primary proton selection with the DCA_{xy} selection
- Influence of the proton PID selection
- Influence of the proton track acceptance

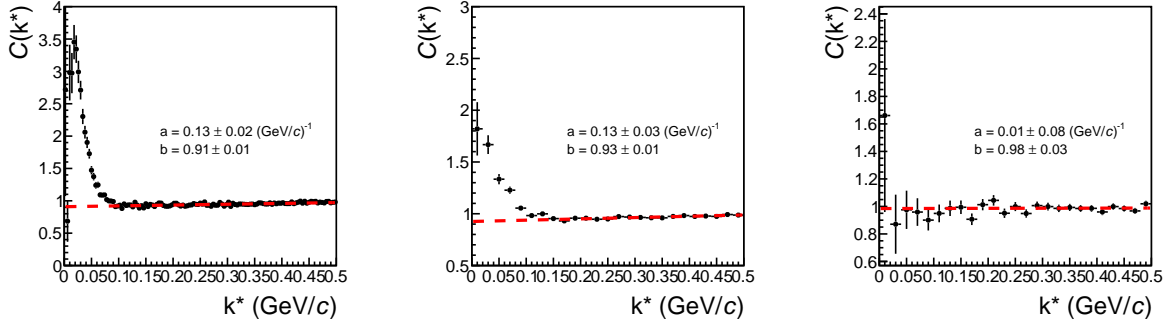


Figure 6.31: Baseline fit (red dashed line) obtained in a non-femtoscopic k^* region with Eq. (6.43).

- Influence of the chosen Filterbit
- Influence of the mixing depth

Then the sensitivity of the V0 selection:

- Influence of the cosine pointing angle
- Influence of the number of TPC cluster of V0 daughter
- Influence of the invariant mass selection width
- Influence of the track acceptance of V0 daughter tracks

A table including all systematic uncertainties can be found in Tab. 6.6. The error on the correlation function is obtained with a *pol2* fit to the ratio of the default correlation function to the one obtained by the cut variation. Whenever a cut variation delivered two systematic uncertainties the larger one is taken into account. In the end all systematic uncertainties from the cut variations are summed up quadratically, assuming they are independent. A change in the DCA_{xy} selection is not taken into account as systematic error. The DCA_{xy} selection has a strong influence on the selection of primary protons. Thus if the value is changed the correlation function is diluted (enhanced) by selecting more secondaries (primaries). This should be recaptured by a change in the λ value. If the result deviates strongly it should be taken into account for the fit results.

6.7 Experimental results

In this Section, the experimental correlation function is compared to femtoscopic models. The goal is to investigate if the theoretical p - Λ correlation function shows some sensitivity on the set of scattering parameters which are plugged in from theory predictions. The theoretical correlation functions are weighted with the λ parameter discussed in the previous Sections. The total fit function is multiplied with the baseline tilting introduced in Sec. 6.5.4 and a total normalization \mathcal{N} of the whole correlation function.

| Variation | p-p | p- Λ | Λ - Λ |
|--------------------------------------|-----|--------------|-----------------------|
| DCA _{xy} , DCA _z | 5% | 2% | - |
| n σ_{proton} | - | - | - |
| $ \eta _{proton}$ | 5% | 1% | - |
| Tracking (Filterbit) | 4% | - | - |
| lower p_T proton | 3% | - | - |
| mixing depth | - | - | - |
| Cosine pointing angle V0 | - | - | 4% |
| # TPC cluster V0 (daughters) | - | - | - |
| InvMass V0 selection width | - | - | - |
| $ \eta _{V0}$ daughter | - | 2% | 1% |
| lower p_T V0 | - | - | - |

Table 6.6: Effect of variations of different selection criteria on the correlation function in percent.

The latter is needed since the baseline is not flat. The $p-p$ and $p-\Lambda$ correlation functions are fitted simultaneously by using a combined χ^2 :

$$\chi_{tot}^2 = \chi_{pp}^2 + \chi_{p\Lambda}^2 . \quad (6.45)$$

In the Appendix B a different Equation for minimization is presented. The fit routine is set up by using the *TMinuit*¹ package of ROOT. The fitrange is $k^* \in [0, 0.12]$ GeV/c for $p-p$ and $k^* \in [0, 0.2]$ GeV/c for $p-\Lambda$. A short remark about a possible transverse mass (m_T) scaling in the pp system, where m_T is the combination of the transverse momentum $k_T = \frac{1}{2}|\mathbf{p}_{T,1} + \mathbf{p}_{T,2}|$ and the rest mass:

$$m_T = \sqrt{k_T^2 + m_0^2} . \quad (6.46)$$

Usually, a scaling of source radii with the transverse mass of the pair, thus a decreasing of the source size with increasing transverse mass indicates the presence of radial flow in the system. Such a collective effect was observed e.g. by ALICE [Ada+15b] in Pb-Pb collisions at $\sqrt{s_{NN}}=2.76$ TeV. There seems to be also a weak m_T scaling present for meson pairs in pp collisions at 7 TeV [Abe+13; Abe+12], at least for large multiplicity events. If the radius of $p-p$ and $p-\Lambda$ are fitted simultaneously the average transverse

¹<https://root.cern.ch/doc/master/classTMinuit.html>

mass should have similar values. The average transverse mass for pairs lying in the femtoscopy region $k^* < 150$ MeV/c for p - Λ pairs is $\langle m_T \rangle = 1.45$ GeV/c² and for p - p pairs $\langle m_T \rangle = 1.27$ GeV/c². One can see that there is a small difference but much smaller than the scales on which m_T scaling happens for meson pairs [Abe+13; Abe+12].

The fitting procedure is the following: The p - p correlation function is fitted with help of the Schrodinger Equation and the p - Λ correlation function with help of the Lednicky model using scattering parameters of the next-to-leading order expansion of a chiral effective field theory at a cutoff scale of $\Lambda = 600$ MeV [Hai+13]. After the fit has converged the leading order values from the same calculation at the same cutoff scale [Hai+13] are also plugged in. Then the difference is explored and checked if one of the two solutions fits better to the data. The result of this investigation is presented in Fig. 6.16. Slightly different λ values for the preliminary ALICE results are used. The reason for this is that the calculation framework of the λ parameter was updated and also the determination of the single-particle fractions slightly changed. For the λ parameter calculation the general framework was not developed and not all combinations of residual correlations could be taken into account. With the new framework all different contributions were summed up. The old values for the preliminary result were:

- $\lambda_{pp} = 0.76, \lambda_{pp\Lambda} = 0.16$
- $\lambda_{p\Lambda} = 0.53, \lambda_{p\Lambda\Xi^-} = 0.10, \lambda_{p\Lambda\Sigma^0} = 0.17$

The new and updated values are:

- $\lambda_{pp} = 0.75, \lambda_{pp\Lambda} = 0.16$
- $\lambda_{p\Lambda} = 0.49, \lambda_{p\Lambda\Xi^-} = 0.10, \lambda_{p\Lambda\Sigma^0} = 0.16$

A fit performed with the updated λ values does not change the result dramatically. This is shown in Fig. 6.33. One can see in Fig. 6.32 that the theoretical correlation function shows a sensitivity towards the input parameter. Especially for $k^* \rightarrow 0$, both solutions differ quite significantly. This is expected since the scattering length for both solutions also differ strongly and they dominate the scattering amplitude for very low momenta. The limiting factor to distinguish both predictions is the available pair statistics in the p - Λ channel. With much more statistics it would be possible to have more k^* bins and the statistical uncertainty for every k^* bin decreased. For an estimation of the amount of the additional statistics needed the first k^* bin of the p - Λ correlation function is taken into account. This bin shows the largest separation and if this bin accumulates enough pairs than all the other bins as well. The separation between LO and NLO in the first k^* bin in the correlation function is $\Delta C(k^*)_1 = 0.2$. One would need in the current measurement at least half of the error bar that the error bar is of the order of the separation. To achieve this roughly 6-7 times the current pair statistics is needed. Then one could in principle distinguish the shape of the correlation function as well as the value, e.g. by doing a P-value evaluation. At the moment the statistics of the RUN1 dataset is too scarce to rule out any parameters. However, it shows the applicability of the method. Especially in the low momentum region femtoscopy is able to perform measurements, where no

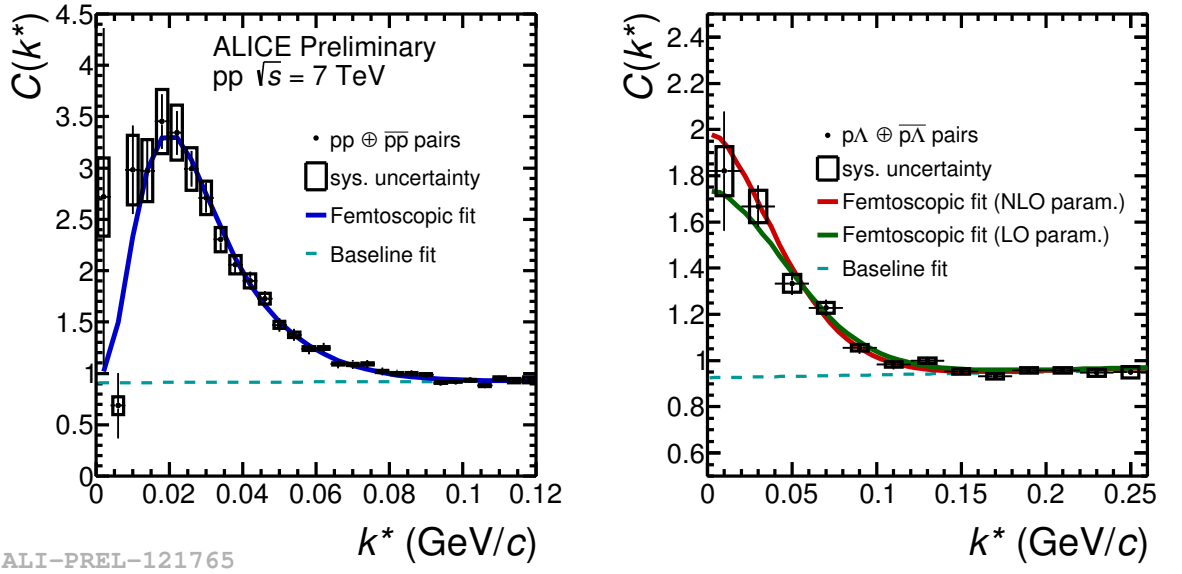


Figure 6.32: Simultaneous fit of the $p - p$ and $p - \Lambda$ pair, where the NLO expansion (red line) is used for the scattering parameter. After the fit is performed the LO parameter set (green line) is plugged in.

data points for the total cross section of $p - \Lambda$ pairs are available.

Finally the comparison to other ALICE result of pp collisions at 7 TeV is done. This measurement is the first measurement with Baryon pairs. The other femtoscopic analysis were done with neutral [Abe+12] and charged [Abe+13] kaon pairs. Also a pion analysis was performed [Aam+11]. Since mesons are quite abundantly produced at LHC energies for them a differential binning in transverse mass and multiplicity was possible. The radii are shown in Fig. 6.34 together with the radius of this analysis (with statistical errors only). From this Figure it is seen that the radius of the baryon pairs is larger than the radius of the meson pairs at the same transverse mass. Contrary to Pb-Pb collisions the underlying source distribution of pp collisions is not well established. In Pb-Pb one produces one fireball which emits the particles. All hadrons stop interacting roughly at the same freeze-out scale. Thus, the radii follow a scaling with transverse mass and are the same withing the errors [Ada+15b]. For pp collisions one might be much more sensitive to the underlying production mechanisms which lead to different radii for all the pairs. Additionally, the charged kaon pairs in the lowest multiplicity class 1-11 also don't coincide with the pairs of pions in the same multiplicity bin. This supports the argument that the pp collision system is much harder to interpret in terms of a scaling of transverse mass and a description with only one source value.

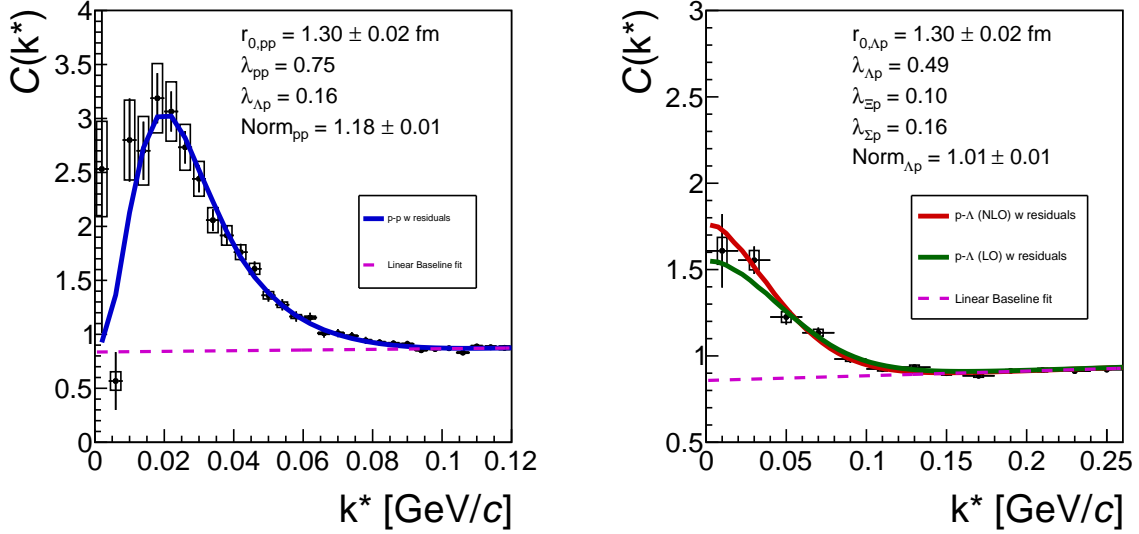


Figure 6.33: Simultaneous fit of the $p - p$ and $p - \Lambda$ pair with updated λ parameter, where the NLO expansion (red line) is used for the scattering parameter. After the fit is performed the LO parameter set (green line) is plugged in.

6.7.1 The Lambda-Lambda correlation function and the relation to bound states

The strength and even the type (repulsive or attractive) of the $\Lambda - \Lambda$ interaction is not settled when models are compared to the correlation function. Discussions about this topic are presented in [MFO15; Ada+15c]. In a next-to-leading order calculation in chiral effective field theory the scattering length is slightly attractive with a value of $a = -0.66$ fm at a cutoff scale $\Lambda = 600$ MeV [HMP16]. As a reminder, a negative scattering length is in the femtoscopy framework positive $f_0 = -a$. First a model calculation with the Lednicky model taking into account the effect of quantum statistics is performed to investigate the shape of the correlation function in pp collisions, where we deal with source sizes of the order of 1.3 fm. For comparison also the correlation function for a larger source size $r_0 = 3$ fm is plotted as achieved in Au-Au/Pb-Pb collisions. For the strong interaction parameter the mean values from the STAR analysis are used [Ada+15c] ($f_0 = -0.11$ fm). The λ parameter is taken from Tab. 6.4. The results are displayed in Fig. 6.35. One can see in this Figure that the larger source size leads to a depletion of pairs at very small k^* . The smaller source size as achieved in pp collisions leads to an even stronger suppression of the correlation function. For the smaller source size also the effect of taking only quantum statistics into account is shown. In the ex-

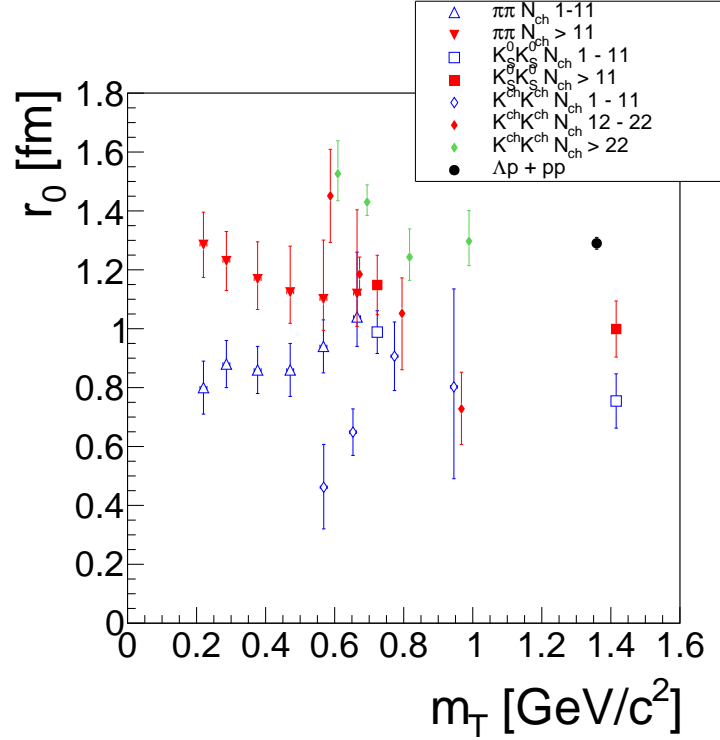


Figure 6.34: Comparison of radii obtained in the pp collision system at 7 TeV. The black point is the radius obtained in this analysis from $p - p$ and $p - \Lambda$ pairs.

perimental correlation function in pp collisions a more flat structure is observed, which is not in agreement with the theoretical prediction of Fig. 6.35. But one may have to take into account several significant contributions from feed-down contributions which are not included in the calculation of Fig. 6.35. They might change the shape of the correlation function. A deeper analysis of the $\Lambda - \Lambda$ correlation function is needed and might lead to insights of the nature of the strong interaction between this pair.

Certain models predict positive scattering length a , which would allow bound states of $\Lambda - \Lambda$. In this section it is explored how a bound state would characterize itself in the correlation function. A summary of $\Lambda - \Lambda$ interaction parameters predicted from model calculations is given in [MFO15]. There are basically four models which provide positive scattering length: ND46, ND48, NF42, NF44. The values of these models and the corresponding binding energies are presented in Tab. 6.7. The binding energies are calculated with the formula:

$$E_B = \frac{(\hbar c)^2}{m_\Lambda} \kappa^2, \kappa = \frac{1}{d_0} \left(1 - \sqrt{1 - \frac{2d_0}{a}} \right). \quad (6.47)$$

From Tab. 6.7 it is seen that two models (ND42, NF42) predict a rather strongly bound

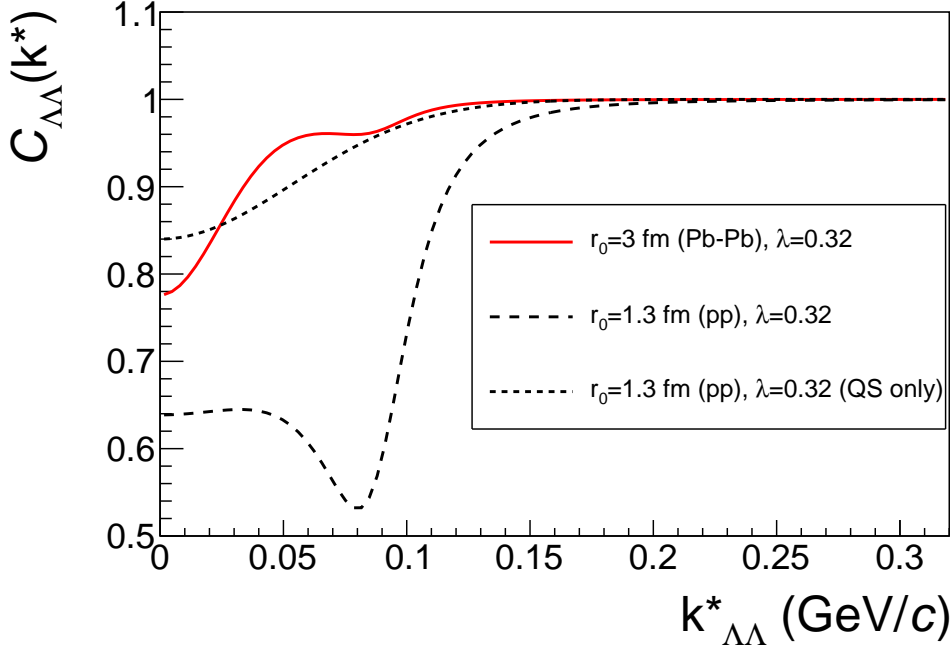


Figure 6.35: The $\Lambda - \Lambda$ correlation function for two different source sizes. For the smaller source size the quantum statistics only correlation function is plotted only for comparison.

state, even stronger than the binding energy of the deuteron ($E_B = 2.2$ MeV). Two models (ND48, NF44) prefer a rather shallow binding. The question is how this large differences are reflected if they are plugged in to a model for the correlation function. To clarify this, the Lednicky model is used including the term for quantum statistics for the identical fermions and assuming a source size of $r_0 = 1.3$ fm, similar to the source sizes of $p-p$ and $p-\Lambda$. A correction for momentum resolution and residual correlations is not included, which would act with the same strength on all four models. The λ parameter is taken from Tab. 6.4. The result for all four models of Tab. 6.7 is presented in Fig. 6.36. In Fig. 6.36 it is seen that the models which predict shallow bound states peak at low k^* , whereas models allowing strongly bound states develop a more flat correlation signal. Thus it seems to be the case that if $\Lambda - \Lambda$ develops a bound state it must be strongly bound to be in agreement with the experimental data. The physics behind the two scenarios can be understood as follows. One has two single-particle sources which emit Λ hyperons. On the way to the detector there are two competing effects, elastic scattering and the formation of bound states. If a model allows strongly bound states the formation of bound states dominates the elastic scattering and no separate $\Lambda - \Lambda$

| Model | Scattering length a [fm] | effective range r_{eff} [fm] | Binding energy E_B [MeV] |
|-------|-------------------------------|--|-------------------------------|
| ND46 | 4.621 | 1.300 | 2.37 |
| ND48 | 14.394 | 1.633 | 0.19 |
| NF42 | 3.659 | 0.957 | 3.68 |
| NF44 | 23.956 | 1.258 | 0.06 |

Table 6.7: Scattering length and effective ranges and the corresponding binding energies of models that predict bound states. The values for the scattering parameters are taken from [MFO15].

pairs are detected anymore. The correlation signal decreases. For shallow bound states the formation of a $\Lambda - \Lambda$ bound state is less probable and the elastic scattering is more pronounced. The correlation signal is stronger.

6.7.2 EPOS predictions for the source function

In this thesis only Gaussian source functions are used. It would be interesting to see what kind of source comes out from a dynamical model for pp collisions at 7 TeV. For this purpose the EPOS model is used [Pie+15]. It is a Monte Carlo generator especially designed for minimum bias hadronic interactions, applicable to small systems like pp but also heavy-ion collisions can be simulated.

The EPOS generator delivers freeze-out coordinates of the produced particles. It is either the point of the freeze-out surface if it comes from the fluid or the last interaction point if the particle rescatters [Wer]. EPOS simulates in some reference frame and all coordinates have to be boosted to the pair rest frame. In the same reference frame where EPOS produces the particles additionally Gaussian and Cauchy freeze-out coordinates with source sizes of $r_{0,G} = 1.5$ fm and $r_{0,C} = 0.5$ fm are sampled with a freeze-out time set to zero. This helps to compare the freeze-out coordinates of EPOS to a perfect Gaussian and Cauchy source and interpret the produced source values of the EPOS model. Only the $p - p$ coordinates are shown but $p - \Lambda$ pairs behaves rather similar. The source is investigated in the out-side-long pair rest frame in cartesian as well as spherical coordinates in the femtoscopic momentum region $k^* < 0.1$ GeV/c. The result for the cartesian coordinates is displayed in Fig. 6.37. One can see that the EPOS coordinates (black dots) tend to peak around the origin. This is also slightly captured by the Cauchy source with a width of $r_{0,C} = 0.5$ fm, but this source even peaks stronger. The Gaussian source coordinates are wider in space. If one would use the EPOS model for the calculation of the correlation function it would pronounce the region of small pair separations. In $p - p$ correlations this is the region of the repulsive hard-core.

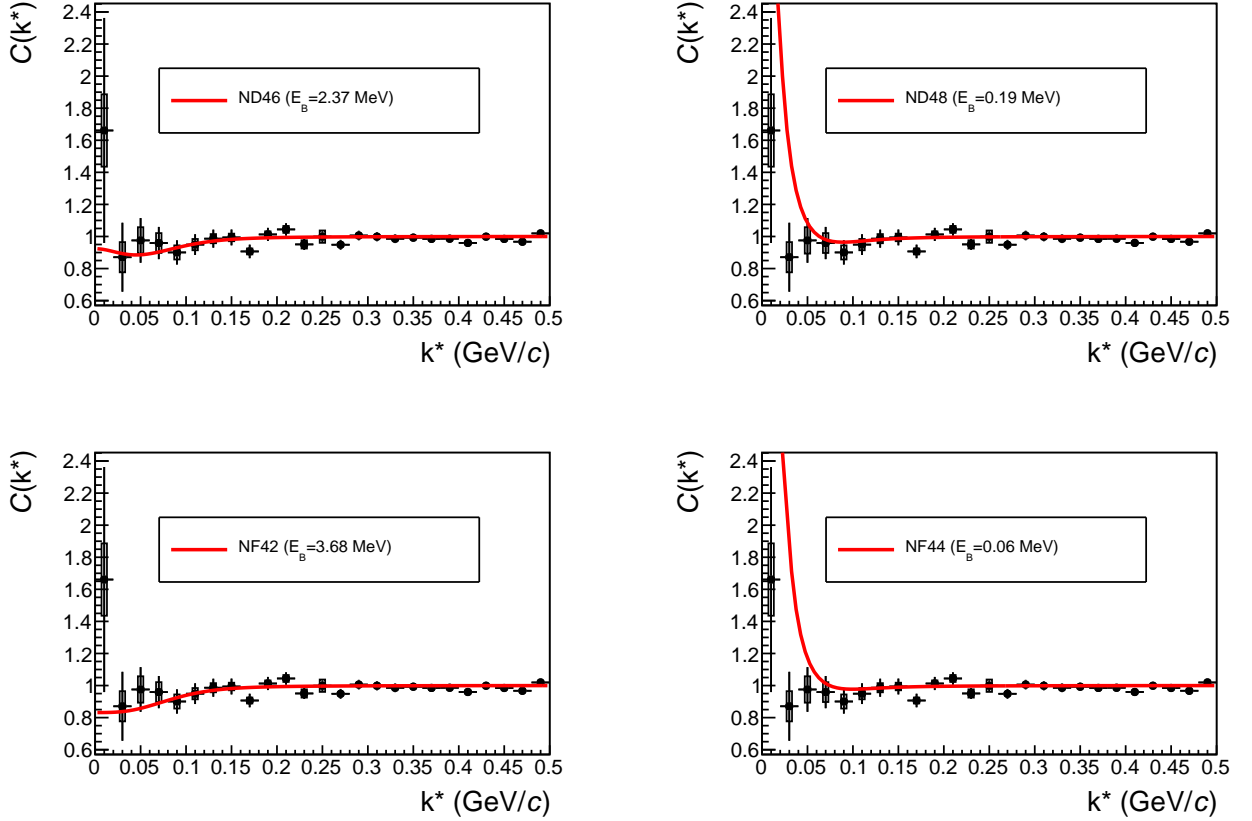


Figure 6.36: Comparison of the influence of the scattering parameters of Tab. 6.7 on the theoretical $\Lambda - \Lambda$ correlation function.

The differences between the source types is better visible in spherical coordinates. Since one boosts from the reference frame where EPOS simulates the coordinates to the pair rest frame the boost might influence the observables. This is especially true for the φ angle. An initial flat distribution can show structures after the boost is performed. The Θ and r^* distributions do only slightly change. How strong the influence of the boost is depends on the width of the momenta, which define the β values. Thus, for source comparisons only the Θ and r^* distributions are considered and φ is shown for completeness. The result is shown in Fig. 6.38. One can see that the peak structures of Fig. 6.37 is transformed to a narrow r^* structure, which is also partly captured by the Cauchy source. The Gaussian source function predicts a broader structure. A characteristics of the Cauchy source is the clustering of pairs around $\pi/2$ in the Θ projection. The Gaussian source shows only the trivial correlation $\sin(\Theta)$ originating from the Jacobian and EPOS follows this distribution too. This shows that EPOS does not produce a Cauchy

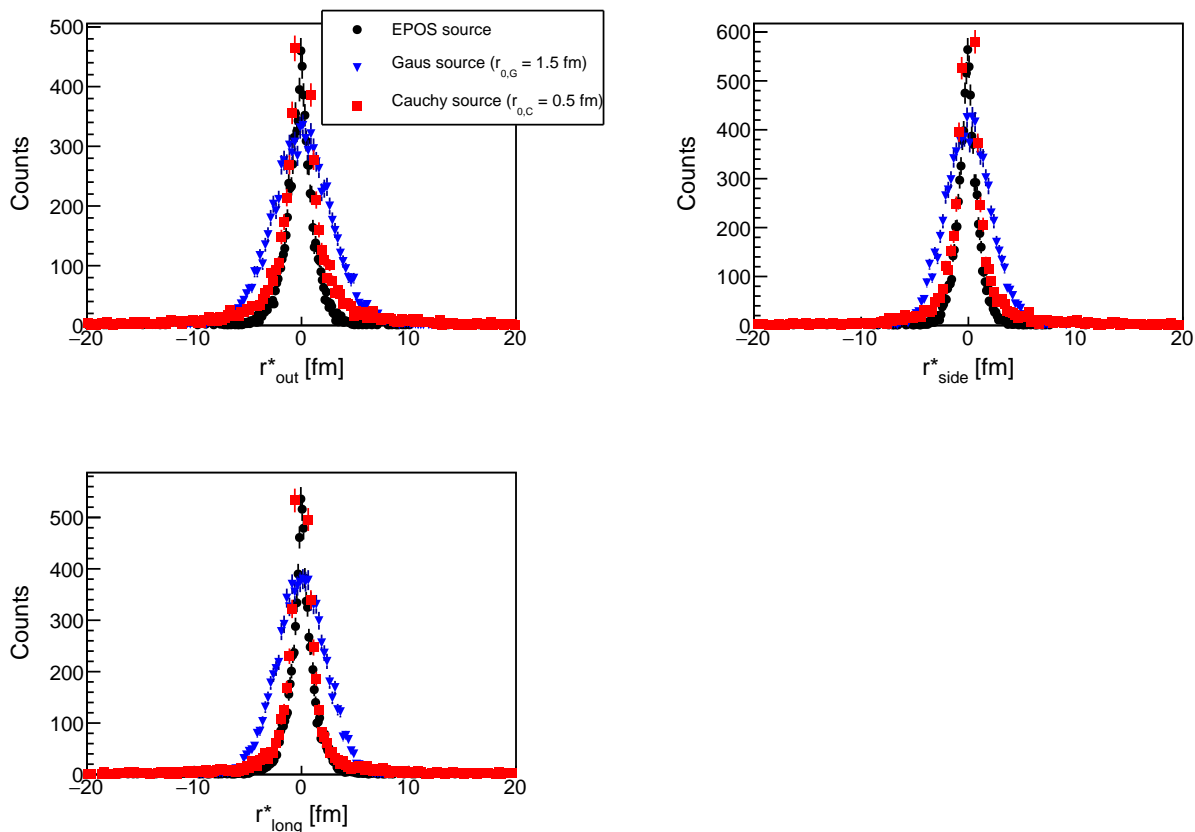


Figure 6.37: Comparison of freeze-out coordinates for $p - p$ pairs predicted by the EPOS model compared to coordinates sampled from a Gaussian and Cauchy p.d.f. The coordinates are shown in cartesian coordinates.

like source even if it looks like the case in the r^* projection or in $r^*_{o,s,l}$ coordinates. The φ distribution is the same for all three sources but strongly influenced by the boost as mentioned already.

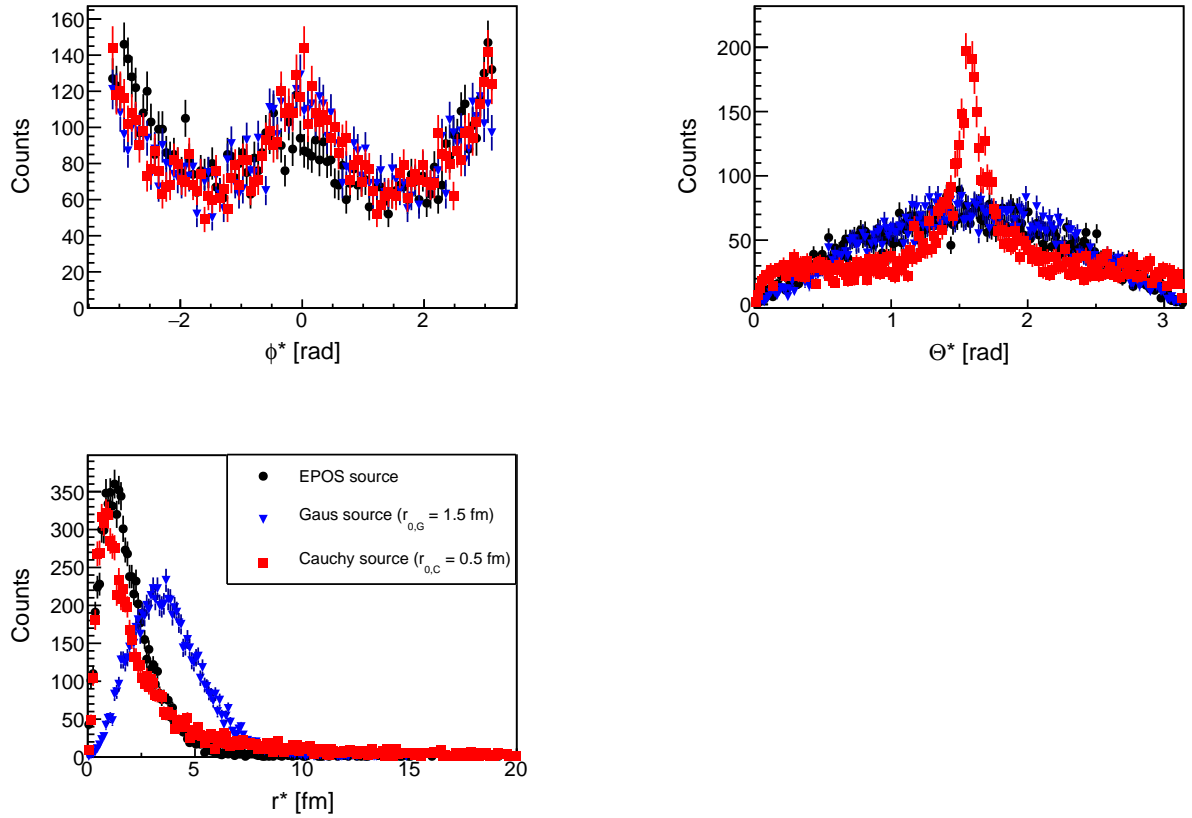


Figure 6.38: Comparison of freeze-out coordinates for $p - p$ pairs predicted by the EPOS model compared to coordinates sampled from a Gaussian and Cauchy p.d.f. The coordinates are shown in spherical coordinates.

7

Outlook

7.1 Imaging - Fixing the source

Femtoscscopy is mainly considered for the extraction of the size of a system at freeze-out. However, in most of the cases a Gaussian source shape is assumed, which introduces automatically some model dependence on the extracted parameter values. Thus, if the source is not of Gaussian shape but the Gaussian shape is assumed in the fitting step the extracted scattering parameter are wrong. An example of how much a Gaussian source can deviate from the “true“ source is shown in Fig. 7.1 for $p - p$ correlations, which is taken from [Ver+02]. The ”true“ source is in this case the source which is obtained from an imaging technique and the Gaussian source is obtained by fitting the correlation function with a Gaussian source shape. One can see that both source shapes disagree quite significantly. The imaging technique is applicable whenever the interaction is known, which is the case for $p - p$ pairs. The femtoscopy equation is inverted to get back from the experimental measurement the source function. A short explanation of the imaging technique is given here to clarify its working principle. It is based on arguments from [BD01]. Since the source function is normalized to unity the femtoscopy equation can be written as (for an angle independent source):

$$R(q) = 4\pi \int dr r^2 K(q, r) S(r) , \quad (7.1)$$

where $K(q, r) = \frac{1}{2} \int_{-1}^1 d(\cos(\Theta)) K(\mathbf{q}, \mathbf{r})$ is the angle averaged kernel and $S(r)$ is the source function. Actually, Eq. (7.1) includes also an approximation, namely that $S(\mathbf{r})$ is

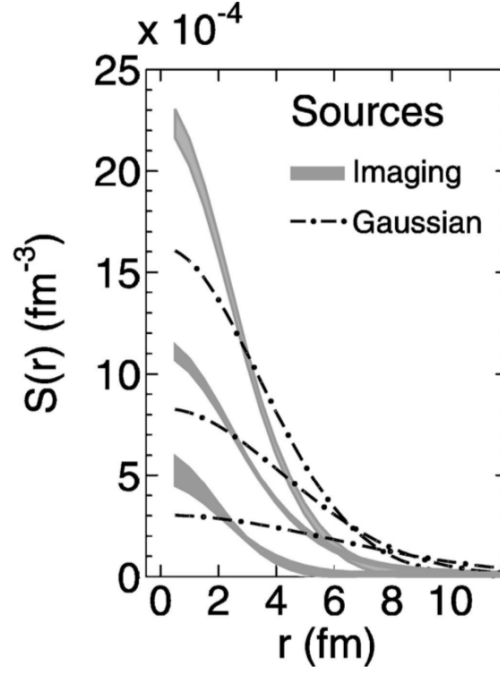


Figure 7.1: The Gaussian source which was fitted to the experimental data is compared to the source extracted from Imaging. Taken from [Ver+02].

angle independent and the whole angle dependence is included in the wave function. As it was shown in this thesis this is actually true for a Gaussian but not for a Cauchy source function. One can discretize Eq. (7.1) in q - and r -space (e.g. having a finite binning):

$$R_i = \sum_j K_{ij} S_j \quad (7.2)$$

where i is the index in q -space (q bins) and j in r -space (r bins). If the source is expanded in basis functions $B_j(r)$:

$$S(r) = \sum_j c_j B_j(r), \quad (7.3)$$

where c_j are free parameters, then Eq. 7.2 can be rewritten as:

$$R_i = \tilde{K}_{ij} c_j, \quad (7.4)$$

where the basis functions were put into a new kernel matrix \tilde{K} . Thus formally Eq. (7.4) is nothing else then a matrix multiplication:

$$\mathbf{R} = \tilde{K} \cdot \mathbf{c}. \quad (7.5)$$

Thus for this Equation one can calculate the χ^2 :

$$\chi^2 = (\mathbf{R} - \tilde{K} \cdot \mathbf{c})^T (\Delta^2 R)^{-1} (\mathbf{R} - \tilde{K} \cdot \mathbf{c}), \quad (7.6)$$

where $\Delta^2 R$ is the error of the experimental correlation function. Formally, the solution for the parameter vector \mathbf{c} , which minimizes the χ^2 is given by:

$$\mathbf{c} = \Delta^2 S \cdot \tilde{K}^T (\Delta^2 R)^{-1} \cdot \mathbf{R}, \quad (7.7)$$

where $\Delta^2 S$ is the error of the extracted source. Besides using this equation one can also perform an explicit numerical minimization. The whole problem breaks actually down to an matrix inversion. The inversion problem is quite challenging since e.g. the Kernel can be singular [Bro98]. Progress has been made in selecting proper basis functions [BD01] with B-Splines. Imaging was also started in this thesis with a very similar strategy like in [BD01], but the framework is far away from being established. Only the usage of such a framework will be explained. One could in principle use a pair of baryons where the interaction is well established to extract the source function. A pair which provides such properties would be again $p-p$. In pp collisions the source functions might be roughly the same for the baryon pairs, just the weighting with the λ parameter is different. Thus it might be possible to use the extracted $p-p$ source function directly in the femtoscopy equation of $p-\Lambda$. Actually, then there would be no free parameter left regarding the source size. One could then solely concentrate on the pair interaction and plug in scattering parameters and test them. If the source function is known, one might also try to find out the Kernel function directly from the femtoscopy equation. This would provide the Kernel of the interaction, thus the square of the pair wave function. This would deliver the interaction in a least model independent way.

Source images were extracted for $p-p$, $p-\Lambda$ and $\pi^-\pi^-$ correlations in Au-Au collisions at $\sqrt{s_{NN}}=6$ GeV [Chu+03]. The correlation functions and the corresponding source functions from the imaging equations are displayed in Fig. 7.2. One can see that for all pairs the size and shape of the source function is different. The source is in this case strongly influenced by secondary decays. For pp collisions at the TeV scale no such study was performed and it would be interesting to see how it evolves. One could image the sources of the $p-p$ and $p-\Lambda$ pair and compare them to investigate if they differ much. If not then a fixing of the $p-\Lambda$ source function with the extracted $p-p$ one is justified.

7.2 Femtoscopy in two spatial dimensions

It might be also interesting to perform a femtoscopy measurement in only two spatial dimensions. To do this one has to select particles e.g. pions which fly in a very narrow pseudo-rapidity range e.g. defined with respect to the reaction plane. This would ensure that both particles are confined to the φ -plane. Then one might be selecting only a

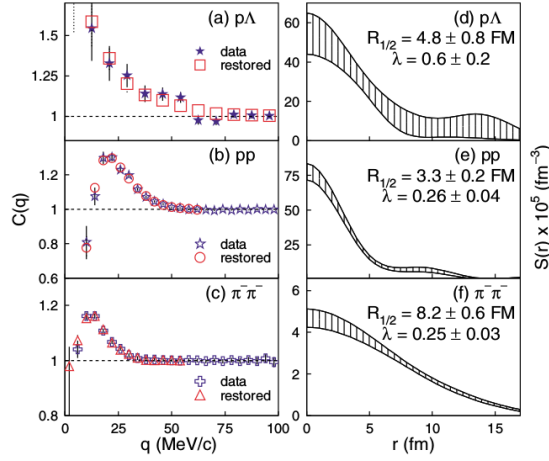


Figure 7.2: Correlation functions for $p-p$, $p-\Lambda$ and $\pi^-\pi^-$ and the corresponding source images. Taken from [Chu+03].

”matter slice“ from a heavy-ion collisions which might help to constrain transport coefficients further. If only the Bose-Einstein enhancement is taken into account as correlation source (for Coulomb in two dimensions the potential changes to a logarithmic form) then the two particles can be described by plane waves and the squared wave function reads:

$$|\psi(\mathbf{q})|^2 = 1 + \cos(\mathbf{q} \cdot \mathbf{r}^*) . \quad (7.8)$$

A Gaussian source function in two dimensions reads:

$$S(r^*) = \frac{\exp(-\frac{r^{*2}}{4r_0^2})}{4\pi r_0^2} . \quad (7.9)$$

This leads finally to the Bose-Einstein correlation function:

$$C(q) = 1 + \int d\varphi dr^* r^* \cos(\mathbf{q} \cdot \mathbf{r}^*) S(r^*) = 1 + \exp(-r_0^2 q^2) \quad (7.10)$$

Thus it is actually the same form like in 3D. The parameter r_0 is now a measure of the width of the source in two dimensions.

Part III

Appendix

A

Solution of the Schrodinger Equation

The Schrodinger Equation in three dimensions can be separated in a radial and angular part. The radial Schrodinger equation reads [Daw78]:

$$\left(\frac{d^2}{dr^2} - \frac{l(l+1)}{r^2} + k^2 \right) R_l(r) = \frac{2\mu V(r)}{\hbar^2} R_l(r), \quad (\text{A.1})$$

where l is the angular momentum, μ the reduced mass and $R_l(r)$ the radial wave function connected to the wave function via:

$$\psi(r) = (kr)^{-1} \sum_l (2l+1) i^l R_l(r) P_l(\cos(\Theta)). \quad (\text{A.2})$$

For convenience we introduced the dimensionless parameter $\rho \equiv kr$ with which the Schrodinger equation can be rewritten:

$$\left(\frac{d^2}{d\rho^2} - \frac{2\mu}{\hbar^2 k^2} V(\rho/k) - \frac{l(l+1)}{\rho^2} + 1 \right) R_l(\rho) = 0. \quad (\text{A.3})$$

The solution of Eq. (A.3) for the free case ($V(r) = 0$) is given in terms of spherical Bessel functions, substituting $R_l(\rho) \rightarrow \rho j_l(\rho)$ in Eq. (A.2). The expansion of the spherical Bessel function for $\rho \gg l$ reads:

$$\rho_l(\rho) \equiv \rho j_l(\rho) \approx \sin\left(\rho - \frac{l\pi}{2}\right) = \frac{i}{2} \left(\exp\left(-i\left(\rho - \frac{l\pi}{2}\right)\right) - \exp\left(i\left(\rho - \frac{l\pi}{2}\right)\right) \right). \quad (\text{A.4})$$

One can see that the free wave is described by an undistorted incoming wave and an undistorted outgoing wave. The scattering process can only change the outgoing wave, thus one can write in the asymptotic region for the radial wave function:

$$R_l(\rho) = \frac{i}{2} \left(\exp\left(-i\left(\rho - \frac{l\pi}{2}\right)\right) - S_l \exp\left(i\left(\rho - \frac{l\pi}{2}\right)\right) \right), \rho \gg l, \quad (\text{A.5})$$

where the diagonal elements of the scattering matrix S_l are introduced. For elastic scattering it can be written as:

$$S_l = \exp(2i\delta_l). \quad (\text{A.6})$$

If one plugs Eq. (A.5) in Eq. (A.2) one retrieves the representation of an undistorted plane wave and a scattered spherical symmetric wave:

$$\psi(\rho) = \exp(ikz) + f(\Theta) \frac{\exp(i\rho)}{r}, \quad (\text{A.7})$$

with the scattering amplitude:

$$f(\Theta) = \frac{i}{2k} \sum_l (2l+1)(1-S_l)P_l(\cos(\Theta)). \quad (\text{A.8})$$

At this point we collected the necessary knowledge to calculate the wave function from the Schrodinger equation. Since the correlation function deviates usually at the threshold $k^* \rightarrow 0$ from unity, s-wave scattering dominates, thus only $l = 0$ waves contribute to the scattering amplitude. Since a free wave converges quite slowly to the exact solution, many waves have to be summed up. To overcome this problem we project out only the scattered wave from the total wave function in Eq. (A.7).

$$\phi(\rho) \equiv f(\Theta) \frac{\exp(i\rho)}{r} = \psi(\rho) - \exp(ikz). \quad (\text{A.9})$$

In the correlation function the full wave function square enters $|\psi|^2$, where we integrate out the plane wave part. Defining $u(\rho) = \rho\phi(\rho)$ the remaining equation for the correlation function reads:

$$C(k) = 4\pi \sum_S \rho_S \int_0^\infty \frac{d\rho}{k^3} S(\rho/k) (\rho^2 + 2\Re u(\rho) \sin(\rho) + |u(\rho)|^2), \quad (\text{A.10})$$

where $S(r)$ is the source function.

At this point one can solve the whole problem on the computer. We define a numerical derivative as the difference quotient between a point i and a point $i + 1$ which are separated by a distance Δ :

$$\frac{dy}{d\Delta} \approx \frac{y(i+1) - y(i)}{\Delta}. \quad (\text{A.11})$$

With this prescription one can also determine the second derivative:

$$\frac{d^2y}{d\Delta^2} \approx \frac{y(i+1) + y(i-1) - 2y(i)}{\Delta^2} \rightarrow y(i+1) = \frac{d^2y}{d\Delta^2} \Delta^2 - y(i-1) + 2y(i). \quad (\text{A.12})$$

Thus by knowing the solution of two past points $y(i)$ and $y(i-1)$ one can calculate the next point $y(i+1)$ do some update and calculate the next point etc. We solved the Schrodinger Equation in the following way:

- Start with an incoming plane wave in the asymptotic region
- Propagate this wave towards $\rho \rightarrow 0$ with the potential switched on and off at the same time
- At $\rho \rightarrow 0$ extract the phaseshift by comparing the free and the scattered wave
- Start again in the asymptotic region with the full wave function
- Calculate at every point ρ the scattered part of the wave function and thus the correlation integral

B

Probability density function for two-particle correlation functions

In this Section the underlying p.d.f. for two-particle correlation functions will be shown. The correlation function is defined as a ration of same event to mixed event samples $C(q) = \frac{A(q)}{B(q)}$. The ratio is done for every q-bin separately. The p.d.f. in the individual q-bins is distributed according to a Poisson distribution in the samples $A(q), B(q)$ with two different means μ, ν :

$$\begin{aligned} P(A) &= \frac{\mu^A}{A!} \exp(-\mu) , \\ P(B) &= \frac{\nu^B}{B!} \exp(-\nu) , \end{aligned} \tag{B.1}$$

where A, B are the counts in the q-bins of the samples $A(q), B(q)$. Since the two samples are statistically independent, the joint p.d.f. can be written as:

$$P(A, B) = P(A) \cdot P(B) = \frac{\mu^A}{A!} \exp(-\mu) \frac{\nu^B}{B!} \exp(-\nu) . \tag{B.2}$$

From this p.d.f. we want to project out the p.d.f. for the ratio μ/ν . This can be done by introducing new variables a_1, a_2 :

$$\begin{aligned} a_1 \cdot a_2 &\equiv \mu, \\ a_2 &\equiv \nu. \end{aligned} \tag{B.3}$$

The Jacobian matrix for this new variables reads:

$$J = \begin{pmatrix} \frac{\partial A}{\partial a_1} & \frac{\partial A}{\partial a_2} \\ \frac{\partial B}{\partial a_1} & \frac{\partial B}{\partial a_2} \end{pmatrix} = \begin{pmatrix} a_2 & a_1 \\ 0 & 1 \end{pmatrix}. \tag{B.4}$$

The p.d.f. of the new observables is then (using the transformation described in [Cow98]):

$$g(a_1, a_2) = |J| = P(A(a_1, a_2), B(a_1, a_2)) = a_2 \frac{(a_1 \cdot a_2)^A}{A!} \frac{a_2^B}{B!} \exp(-a_1 \cdot (1 + a_2)). \tag{B.5}$$

Since we are interested in the variable $C \equiv \mu/\nu = a_1$ the variable a_2 has to be integrated out:

$$g(a_1) = \int_0^\infty da_2 g(a_1, a_2) = \frac{a_1^A \Gamma(A + B + 2)}{A! B! (a_1 + 1)^{A+B+2}}. \tag{B.6}$$

This result was actually for the first time obtained in [Ahl+02]. However, the integral in this reference looks different and would give a different result than stated in the publication. This was a motivation for reevaluating it. The Gamma function can be replaced by the recursive relation $\Gamma(n + 1) = n\Gamma(n)$. With the p.d.f. for the correlation function C its mean and variance can be calculated:

- Mean: $E[C] = \int_0^\infty dC C P(C|A, B) = \frac{A+1}{B}$.
- Variance: $V[C] = \int_0^\infty dC (C - E[C])^2 P(C|A, b) = \frac{(A+1)(A+B+1)}{B^2(B-1)}$.

It is interesting to see that the mean is shifted by one count. Thus it would be perhaps more precise to do the ratio $A + 1/B$ for the construction of the experimental correlation function.

Since the p.d.f. for the correlation function is known, the likelihood can be defined:

$$\mathcal{L} \equiv P(C|A, B). \tag{B.7}$$

Taking twice the negative logarithm of this equation and minimizing it gives the parameter estimates for the correlation function:

$$L\mathcal{L} \equiv -2 \log(\mathcal{L}) \tag{B.8}$$

This can be used for finding the parameters for the correlation function.

C

How to obtain projections in out-side-long coordinate system

The projections in out-side-long-coordinates is done by filling a TH3 histogram, where each dimension represents a direction in q-space. It is filled for same event and mixed event separately. The TH3 object allows to project onto a certain 1D axis in a given interval. This is done for mixed and same event on the out, side and long axis. After the projection the ratio is build to get the correlation function in the specific direction. It is important to perform first the projection and then the ratio.

Danksagung

Dieses Projekt, bzw. die beiden Projekte wurden erfolgreich abgeschlossen da viele helfende Hände dazu beitrugen. Als erstes ist natürlich Prof. Dr. Laura Fabbietti zu nennen. Du hast mich in diese Gruppe geholt und meine Fähigkeiten stets gefördert. Durch dieses unermüdliche Engagement und den Glauben daran, dass ich zwei Projekte auch erfolgreich stemmen kann haben wir zusammen viel erreicht. Zudem lernte ich eigenständiges Arbeiten und wie man seine Ergebnisse mit einer klaren Struktur präsentiert. Danke für deine bedingungslose Förderung, und dass ich meine Ergebnisse auf internationalen Konferenzen vorstellen konnte. Zudem brachte mich der lösungsorientierte Ansatz immer weiter in meinem Fortschritt.

Ich danke Prof. Dr. Marcus Bleicher für die vielen nützlichen Diskussionen zu meiner Arbeit, die immer zu neuen Einblicken führten. Auch möchte ich Prof. Dr. Raimond Snellings danken, dass er als Mentor fungierte.

Für viele hilfreiche Diskussionen zum Thema “Femtoscopy” möchte ich Dr. Dariusz Miskowiec danken. Durch seine Hilfe wurde mir der Einstieg in dieses breite Forschungsgebiet massiv erleichtert. Dr. Roland Kotte danke ich dafür, dass er mir den “Koonin Code” überlassen hat. Dadurch wurde erst die physikalische Interpretation der Daten möglich. Der HADES Kollaboration danke ich für die Inputs auf diversen Kollaborationsmeetings. Selbstverständlich ist hier auch die ALICE Kollaboration zu nennen. Durch die regelmäßigen Femto Meetings bekam ich immer wieder nützliches Feedback. HGS-HIRE möchte ich für die finanzielle Unterstützung danken und ihrem breiten Programmangebot, wie den Soft-Skill Kursen.

Desweiteren danke ich aus der “ersten Generation” von Lauras Gruppe Dr. Johannes Siebenson. Er hat mir den Einstieg in die Analyse wesentlich erleichtert. Dazu ist auch Dr. Kirill Lapidus zu nennen, der immer wieder kritische Fragen stellte. Seine “secret projects” sind legendär. Dr. Eliane Epple hatte auch immer wieder ein offenes Ohr und Vorschläge für Verbesserungen. Dr. Rafal Lalik half mir gerade zu Beginn immer wieder mit seinem tiefen Verständnis für C++ und für seine vielen Lösungsvorschläge bin ich dankbar. Meinen Bürokollegen Ante und Dimitar danke ich für die entspannte Zeit im Büro. Die Gespräche über Physik aber gerade auch über viele nicht-physikalische Themengebiete waren immer eine willkommene Abwechslung. Es ist auch an ihren Arbeiten zu erkennen wie sich die Femtoscopy Methode mittlerweile in Lauras Gruppe etabliert hat. Den “Newcomern” Bernhard und Andi wünsche ich auch eine erfolgreiche Zeit auf

diesem Gebiet.

Der Einstieg in die ALICE Analyse und das Erlernen des Frameworks war nur möglich durch die Hilfe von Dr. Alessandro Grelli, der sich einen Monat Zeit nahm um mir alles wichtige zu zeigen. Hier ist auch Dr. Michael Weber zu nennen, der sich immer wieder für meine Fragen interessierte und immer eine Antwort parat hatte. Sein breiter Überblick über ALICE Ergebnisse waren sehr nützlich. Dr. Torsten Dahms hatte auch immer ein offenes Ohr für meine Fragen.

Zuletzt danke ich meiner besseren Hälfte Moni für ihre unermüdliche Unterstützung. Ohne sie hätte ich das alles so nicht geschafft.

List of Figures

| | | |
|------|---|----|
| 1.1 | Running coupling from QCD compared to measurements. Taken from [Bet07]. | 3 |
| 1.2 | Comparison of predictions from lattice QCD (points) to experimental results (horizontal lines). Taken from [Lus03]. | 4 |
| 1.3 | Phase diagram of QCD in terms of the temperature T and chemical potential μ_B . Taken from [FH11]. | 5 |
| 1.4 | Neutron star properties for the EoS of Eq. (1.6) with $\gamma = 5/3$. The energy density $\epsilon(r)$ is calculated for the stiffest version of the EoS and the largest reachable neutron star mass. | 8 |
| 1.5 | Results of a mass radius relation calculated on the basis of a Quantum Monte Carlo simulation [Lon+15]. The red curve shows only the inclusion of two-body forces whereas the other two curves include two different versions of three-body ΛNN interactions. | 9 |
| 1.6 | Single-particle potential $U_\Lambda(p_\Lambda = 0, \rho)$ for (a) nuclear matter and (b) neutron matter. The dashed dotted curve (green band) shows the result from NLO calculations and the red band includes also effects from a density dependent three-body ΛNN force. Taken from [Hai+17]. | 10 |
| 1.7 | Phaseshift of the $\Lambda p \ ^3S_1$ state for the NLO model as well as Jülich '04 (blue dashed) and NSC97f (black dashed). Taken from [Hai+17]. | 11 |
| 1.8 | A film containing an elastic Λp scattering event. Taken from [Sec+68]. | 13 |
| 1.9 | A comparison of the measurement of the elastic Λp cross section to calculations from an chiral effective field theory prediction. The green band is for the leading order expansion whereas the red band represents the next-to-leading-order expansion. Taken from [Hai+13]. | 14 |
| 1.10 | Phaseshift calculations from the effective field theory. No data points are available for elastic Λp scattering. Taken from [Hai+13]. | 14 |
| 1.11 | Feynman diagrams to describe the ΛN interaction. Taken from [GHM16]. | 14 |
| 1.12 | Phaseshift of Usmani potential of the form given in Eq. (1.10) | 15 |

| | | |
|------|--|----|
| 2.1 | Projections of the source functions on r^*, Θ and φ . The red distribution corresponds to a Gaussian and the black to a Cauchy source choice. See text for more details. | 22 |
| 2.2 | Bose-Einstein correlation function for a source size of $r_0=1.5$ fm calculated for single-particle emitters having a Gaussian and Cauchy shape. The influence on the correlation function is significant. For comparison also the correlation function obtained neglecting the typical angular behavior included in a Cauchy source function is displayed. | 23 |
| 2.3 | Kernel for two identical bosons. | 24 |
| 2.4 | Correlation function for two identical bosons. The blue line is the quantum statistics correlation function for a Gaussian source size of $r_0 = 1.5$ fm and the red one for a source size of $r_0 = 3$ fm. | 24 |
| 2.5 | Kernel of the Coulomb interaction. | 25 |
| 2.6 | Coulomb correlation function. The green dashed line shows just the Gamov factor. The blue line is the Coulomb correlation function for a Gaussian source size of $r_0 = 1.5$ fm and the red one for a source size of $r_0 = 3$ fm. | 25 |
| 2.7 | Kernel of the strong interaction. | 27 |
| 2.8 | Strong interaction correlation function. The blue line is the strong interaction correlation function for a Gaussian source size of $r_0 = 1.5$ fm and the red one for a source size of $r_0 = 3$ fm. They were calculated using $f_0 = 1.5$ fm, $d_0 = 2$ fm. | 27 |
| 2.9 | The black function represents a typical short range nuclear potential and the red function corresponds to a pair distribution according to Eq. (2.29) for $r_0 = 1.5$ fm. A fraction of pairs is produced within the range of the potential and the rest in a region where it vanishes. This plot demonstrates that at some point the assumption of the asymptotic form of the wave function breaks down if the potential strength becomes non-negligible. | 28 |
| 2.10 | Comparison of the Lednicky model and the full solution of the Schrodinger Equation for a source radius of $r_0 = 3$ fm. | 32 |
| 2.11 | Comparison of the Lednicky model and the full solution of the Schrodinger Equation for a source radius of $r_0 = 1.5$ fm. | 32 |
| 2.12 | Two example plots of proton-proton correlation functions for source sizes of $r_0 = 1.5$ fm (blue) and $r_0 = 3$ fm (red). The proton-proton correlation function includes Fermi-Dirac statistics and Coulomb repulsion, which lead to a suppression of the correlation signal below unity for $q \approx 0$ as well as strong interaction which shows up as a bump structure at $q \approx 20$ MeV/c. | 35 |

| | | |
|------|---|----|
| 2.13 | Definition of the longitudinally-comoving-system. The “long” component is aligned with the beam direction, “out” is parallel to the pair transverse momentum and “side” perpendicular to the other two directions. | 37 |
| 2.14 | Number of proton pairs in the femtoscopy region $k^* < 150$ MeV/ c as a function of the Gaussian momentum production width of the protons. The pair statistics in the femtoscopic range is highly non-linear. | 39 |
| 3.1 | Setup of the HADES detector. The green line indicates the beam. | 44 |
| 3.2 | Side view of the HADES detector system and its detector components. | 45 |
| 3.3 | Schematic layout of the RICH detector. The Cherenkov light of the positron is reflected at the mirror and focused to a ring on the readout pads. | 46 |
| 3.4 | Schematic view of the drift chambers oriented at $\pm 0^\circ, \pm 20^\circ, \pm 40^\circ$ | 47 |
| 3.5 | Specific energy loss distributions for MDC, TOF and TOFINO as a function of the particles momentum. One can clearly see the different bands corresponding to different particle species. | 51 |
| 4.1 | Sketch of a Λ decay and the explanation of topological selection criteria. | 55 |
| 4.2 | Purity as a function of the remaining signal for different topological cut selections. The black circles show the selected cuts. | 56 |
| 4.3 | $p - \pi^-$ invariant mass spectrum for combination 1 of topological cuts. | 56 |
| 4.4 | $p - \pi^-$ invariant mass spectrum for combination 2 of topological cuts. | 56 |
| 4.5 | $p - \pi^-$ invariant mass spectrum for combination 3 of topological cuts. | 56 |
| 4.6 | Angle correlations of $(\Delta\phi, \Delta\Theta)$ for $p - p$ pairs. The left plot shows $p - p$ pairs after GEANT which filters the pairs for acceptance. The right plot includes also the tracking which introduces a hole in the distribution. | 58 |
| 4.7 | Experimental correlation function in $(\Delta\phi, \Delta\Theta)$ for $p - p$ pairs. | 59 |
| 4.8 | Experimental correlation function in $(\Delta\phi, \Delta\Theta)$ for $\pi^- - \pi^-$ pairs. | 60 |
| 4.9 | Experimental correlation function in $(\Delta\phi, \Delta\Theta)$ for $\pi^+ - \pi^+$ pairs. | 60 |
| 4.10 | Experimental correlation function in $(\Delta\phi, \Delta\Theta)$ for $\pi^- - \pi^+$ pairs. | 60 |
| 4.11 | Experimental correlation $p - p$ function with different cut selections on $(\Delta\phi, \Delta\Theta)$ to reject close pairs. | 61 |
| 4.12 | Comparison of the $p - p$ correlation function in the k and $q_{o,s,l}$ representation. The reduction of the merging effect is clearly visible. | 62 |
| 4.13 | Correlation functions for $p - p$ (top) and $p - \Lambda$ (bottom) obtained from UrQMD and GiBUU (see text). One can see that a minimal cut on angles between the particles cures the track merging. | 64 |
| 4.14 | Effects of LRC on the correlation function. Top: $p - p$ pairs where UrQMD is used to describe the baseline. Bottom: $p - \Lambda$ pairs where Eq. 4.3 is used to describe LRC. The experimental (dashed) as well as the simulation (solid) correlation function is fitted in $k \in [250, 600]$ MeV/ c to check for any differences at low k | 65 |

| | | |
|------|---|----|
| 4.15 | Resolution matrix of $p - p$ for the momentum differences k . The x-axis shows the input momenta and the y-axis the reconstructed momenta. . . | 66 |
| 4.16 | Right: Correlation function from simulation for $p - p$. The open circles show the unsmeared correlation function and the blue triangles the effect of the momentum resolution. | 66 |
| 4.17 | Effect of the momentum resolution for $k_{o,s,l}$ projections. | 67 |
| 4.18 | Resolution matrix of $p-\Lambda$ for the momentum differences k . The x-axis shows the input momenta and the y-axis the reconstructed momenta. . . | 68 |
| 4.19 | Right: Correlation function from simulation for $p-\Lambda$. The open circles show the unsmeared correlation function and the blue triangles the effect of the momentum resolution. | 68 |
| 4.20 | Effect of the correction for momentum resolution the measured experimental correlation functions of $p - p$ (top) and $p-\Lambda$ (bottom). | 69 |
| 4.21 | Cross section for $p-\Lambda$ scattering. The AQM is part of the standard UrQMD model. The LO and NLO expansions are motivated by [Hai+13]. | 72 |
| 4.22 | Freeze-out coordinates in the out-side-long basis for $p - p$ pairs from UrQMD. | 76 |
| 4.23 | Freeze-out coordinates in the out-side-long basis for $p-\Lambda$ pairs from UrQMD. | 76 |
| 4.24 | The projections in out-side-long direction in the PRF for $p - p$ (open circles) and $p-\Lambda$ (blue triangles) pairs from UrQMD. The $p-\Lambda$ values are scaled to fit on the same plot. The width in every direction is obtained by fitting to it a Gaussian function (solid $p - p$, dashed $p-\Lambda$). | 77 |
| 4.25 | Comparison of fully corrected experimental $p - p$ correlations (open circles) to predictions of CRAB (red lines) which use UrQMD as input. The plot at the top is the one-dimensional correlation function. The other three are projections of the 3D correlation function in the LCMS. | 78 |
| 4.26 | Model comparison of the $p - p$ correlation function (top) and $p-\Lambda$ (bottom) to extract the source size. | 79 |
| 4.27 | The $p - p$ source size as a function of the total transverse momentum k_T . | 79 |
| 4.28 | Comparison of cross sections of NN scattering and $p-\Lambda$ | 79 |
| 4.29 | Comparison of the extracted source radius to measurements of other radii from p+A collisions. | 80 |
| 4.30 | Influence of different sets of scattering parameter on the correlation function. The LO and NLO scattering length at a cutoff value of 600 MeV are taken from [Hai+13]. A small bug entered this figure, which is explained in the text. | 81 |
| 4.31 | Influence of different sets of scattering parameter on the correlation function. The LO and NLO scattering length at a cutoff value of 600 MeV are taken from [Hai+13]. This figure includes the fully correct Lednický model. See text for details. | 82 |

| | | |
|-----|--|-----|
| 5.1 | The ALICE detector with its individual components [Aam+08]. | 86 |
| 5.2 | The structure of the Inner Tracking System (ITS) with its six layers SPD (two innermost), SDD (two intermediate), SDD (two outermost) [Aam+10]. | 87 |
| 5.3 | The TPC field cage in 3D view [Alm+10]. | 88 |
| 5.4 | The specific energy loss of charged particles versus the particle momen- tum. One can see a separation for particles for momenta up to 1 GeV/c. | 89 |
| 5.5 | The velocity of particles versus their momenta. Different bands develop for the different particle species. | 89 |
| 6.1 | Proton selection criteria. Below 0.75 GeV/c only the TPC is used. For momenta above this threshold the TPC signal is combined with the one from the TOF. | 94 |
| 6.2 | Sketch of a V0 decay and its vertex selection taken from [Cor+06]. Only V0 vertices inside a fiducial volume are kept and the daughter tracks have to have some minimum impact parameter to the primary vertex. The distance of closest approach of the daughter tracks should not exceed a maximum value. | 96 |
| 6.3 | Results from a Toy Monte Carlo study. Left: Matrix presenting the cor- relation between k^* of an initial momentum $p - K_0^S$ transformed to $p-\Lambda$. Right: A broad simulated mini-jet background present in $p - K_0^S$ sur- vives the transformation to the $p-\Lambda$ momentum basis. | 97 |
| 6.4 | Invariant mass distribution of $p\pi^-$ ($\bar{p}\pi^+$) to obtain the Λ ($\bar{\Lambda}$) signal and the selection width used in the analysis. | 98 |
| 6.5 | The resulting mean and variance of the Λ signal as a function of p_T | 99 |
| 6.6 | Left: Number of SPD tracklets in $ \eta < 0.8$ used for determining the multiplicity of pp events. Right: z vertex distribution for pp collisions. Both observables are used for event mixing. | 100 |
| 6.7 | Left: Correlation function of $\bar{p} - p$ pairs. A strong contribution from mini-jets is visible, showing up as a broad correlation signal starting at k^* ~ 1 GeV/c. Right: Same correlation function zoomed to small relative momenta. One can see a correlation signal having femtoscopic signa- tures on top of the mini-jet background. | 101 |
| 6.8 | Left: Correlation function of the sum of $\bar{p} - \Lambda$ and $p - \bar{\Lambda}$ pairs. Also for this pair a strong contribution from mini-jets is visible, showing up as a broad correlation signal starting at $k^* \sim 1$ GeV/c. Right: Same correlation function zoomed to small relative momenta. One can see a correlation signal having femtoscopic signatures on top of the mini-jet background. | 102 |

| | | |
|------|--|-----|
| 6.9 | Left: The $\bar{\Lambda} - \Lambda$ correlation function. Also for this pair a strong contribution from mini-jets is visible, showing up as a broad correlation signal starting at $k^* \sim 1$ GeV/c. Right: Same correlation function zoomed to small relative momenta. One can see a correlation signal having femtoscopic signatures on top of the mini-jet background. | 103 |
| 6.10 | Two different scenarios which can lead to a mini-jet contribution in the correlation function. Left: The parton fragments into bunch of hadrons containing the Baryon-Antibaryon pair. Such a process shows a strong kinematic correlation like a pair coming from a resonance decay. Right: The pair stems from two different partons after hadronization. | 104 |
| 6.11 | Left: Parton transverse momentum in Pythia. Right: Black dots represent the full $\bar{p} - p$ correlation function from Pythia. The red squares show the correlation function obtained by requiring that the $\bar{p} - p$ pair stem from different partons. | 105 |
| 6.12 | Baryon-Baryon and Antibaryon-Antibaryon correlation functions on the top and the corresponding ratios on the bottom. Left: (Anti)proton-(Anti)proton, Middle: (Anti)proton-(Anti)Lambda, Right: (Anti)Lambda-(Anti)Lambda. | 106 |
| 6.13 | Decomposition of the individual correlation signals. The Λ signal is divided in signal (blue shaded) and background (black shaded) contributions. The signal correlation function is denoted as $p - A$ and the background function as $p - B$. With the summation of the individual correlation functions weighted with the λ parameter one gets back the red squares of $C(pA + pB)$. The black dots of $C(pA + pB)$ represent the total correlation function like it would be obtained in the experiment. | 108 |
| 6.14 | The black curve is the correlation function in which one is interested. For high purities (Purity=0.99) the residual correlations are small and one retrieves the correlation function of interest. | 110 |
| 6.15 | For lower purities (Purity=0.93) residual correlations from impurities start to play a role. The two correlation functions do not coincide anymore. | 110 |
| 6.16 | Decomposition of the correlation function given in Eq. (6.7) as a function of the single-particle Purity. | 113 |
| 6.17 | Comparison of the two methods to evaluate the λ parameter. The λ parameters presented as marker are the parameter using directly their definition. The dotted line shows the parameter by relating them to the single-particle purity $\mathcal{P} = 0.8$ | 114 |
| 6.18 | Adjusted Monte Carlo Templates from Pythia to the experimental data in the full p_T range. | 117 |

| | | |
|------|--|-----|
| 6.19 | Adjusted Monte Carlo Templates from Pythia to the experimental data. Due to the shape of the templates one has a good discrimination of the origin of the protons. | 118 |
| 6.20 | Percentage of feed-down to protons from Σ^+ and Λ as a function of p_T | 119 |
| 6.21 | The fractions of protons as a function of p_T obtained from the template fitting method. The purity is extracted from Pythia. The averages of the quantities are obtained by using the production probability dN/dp_T of protons. | 120 |
| 6.22 | Template fit to the cosine pointing angle in the full p_T interval. | 123 |
| 6.23 | Template fit to the cosine pointing angle in a p_T interval. | 124 |
| 6.24 | The fractions of Λ as a function of p_T obtained from a template fitting method. The purity is extracted by fitting the Λ invariant mass peaks. The averages of the quantities are evaluated by using the production probability dN/dp_T of Λ | 125 |
| 6.25 | Transformation matrix M for p - Λ decaying into pairs of p - p (left) and p - Σ^0 (middle) p - Ξ^- (right) decaying in pairs of p - Λ | 126 |
| 6.26 | Initial correlation functions displayed as red solid lines. The black dashed lines are the residual correlations. Top left: p - $\Lambda \rightarrow p$ - p , Top right: p - $\Xi^- \rightarrow p$ - Λ . Bottom left: p - $\Sigma^0 \rightarrow p$ - Λ | 127 |
| 6.27 | Momentum resolution of the p-Pb system at $\sqrt{s_{NN}}=5.02$ TeV for different track candidates. | 128 |
| 6.28 | Momentum and angle resolutions of the pp system obtained from Pythia simulations. | 129 |
| 6.29 | Top: Resolution matrices for p - Λ and p - p . Bottom: Influence of the momentum resolution on the correlation functions. | 130 |
| 6.30 | Correlation function for p - p in φ^*, η representation for Pythia simulations at different radii of the TPC. Merging or splitting would be visible at the origin (0,0). | 131 |
| 6.31 | Baseline fit (red dashed line) obtained in a non-femtoscopic k^* region with Eq. (6.43). | 133 |
| 6.32 | Simultaneous fit of the p - p and p - Λ pair, where the NLO expansion (red line) is used for the scattering parameter. After the fit is performed the LO parameter set (green line) is plugged in. | 136 |
| 6.33 | Simultaneous fit of the p - p and p - Λ pair with updated λ parameter, where the NLO expansion (red line) is used for the scattering parameter. After the fit is performed the LO parameter set (green line) is plugged in. | 137 |
| 6.34 | Comparison of radii obtained in the pp collision system at 7 TeV. The black point is the radius obtained in this analysis from p - p and p - Λ pairs. | 138 |

| | | |
|------|--|-----|
| 6.35 | The $\Lambda - \Lambda$ correlation function for two different source sizes. For the smaller source size the quantum statistics only correlation function is plotted only for comparison. | 139 |
| 6.36 | Comparison of the influence of the scattering parameters of Tab. 6.7 on the theoretical $\Lambda - \Lambda$ correlation function. | 141 |
| 6.37 | Comparison of freeze-out coordinates for $p - p$ pairs predicted by the EPOS model compared to coordinates sampled from a Gaussian and Cauchy p.d.f. The coordinates are shown in cartesian coordinates. . . . | 142 |
| 6.38 | Comparison of freeze-out coordinates for $p - p$ pairs predicted by the EPOS model compared to coordinates sampled from a Gaussian and Cauchy p.d.f. The coordinates are shown in spherical coordinates. . . . | 143 |
| 7.1 | The Gaussian source which was fitted to the experimental data is compared to the source extracted from Imaging. Taken from [Ver+02]. . . . | 146 |
| 7.2 | Correlation functions for $p - p$, p - Λ and $\pi^- \pi^-$ and the corresponding source images. Taken from [Chu+03]. | 148 |

List of Tables

| | | |
|-----|--|-----|
| 4.1 | Summary pN_b | 53 |
| 4.2 | Topological cut selections for the Λ hyperon to reduce combinatorial background. The corresponding purities are also listed. | 55 |
| 4.3 | Channels in GiBUU that are responsible for the Λ production. The corresponding (scaled) cross section factor is displayed. | 63 |
| 4.4 | Purity parameter used to correct the correlation functions for purity. . . | 69 |
| 6.1 | Summary | 91 |
| 6.2 | lambda values for proton-proton | 121 |
| 6.3 | lambda values | 122 |
| 6.4 | lambda values | 122 |
| 6.5 | Scattering parameters to model $p\Sigma^0$ correlations. Taken from [Sta+07]. | 126 |
| 6.6 | Systematic uncertainties | 134 |
| 6.7 | Summary | 140 |

Bibliography

- [13] *Upgrade of the ALICE Time Projection Chamber*. Tech. rep. CERN-LHCC-2013-020. ALICE-TDR-016. 2013-10 (cit. on p. 88).
- [Aad+12] Georges Aad et al. “Observation of a new particle in the search for the Standard Model Higgs boson with the ATLAS detector at the LHC”. *Phys. Lett. B* 716 (2012), pp. 1–29. doi: 10.1016/j.physletb.2012.08.020 (cit. on p. 1).
- [Aai+15] Roel Aaij et al. “Observation of $J/\psi p$ Resonances Consistent with Pentaquark States in $\Lambda_b^0 \rightarrow J/\psi K^- p$ Decays”. *Phys. Rev. Lett.* 115 (2015), p. 072001. doi: 10.1103/PhysRevLett.115.072001 (cit. on p. 2).
- [Aam+08] K. Aamodt et al. “The ALICE experiment at the CERN LHC”. *JINST* 3 (2008), S08002. doi: 10.1088/1748-0221/3/08/S08002 (cit. on pp. 85, 86).
- [Aam+10] K Aamodt et al. “Alignment of the ALICE Inner Tracking System with cosmic-ray tracks”. *JINST* 5 (2010), P03003. doi: 10.1088/1748-0221/5/03/P03003 (cit. on p. 87).
- [Aam+11] K. Aamodt et al. “Femtoscopy of pp collisions at $\sqrt{s} = 0.9$ and 7 TeV at the LHC with two-pion Bose-Einstein correlations”. *Phys. Rev. D* 84 (2011), p. 112004. doi: 10.1103/PhysRevD.84.112004 (cit. on pp. 74, 132, 136).
- [Aba+16] V. M. Abazov et al. “Evidence for a $B_s^0 \pi^\pm$ state”. *Phys. Rev. Lett.* 117.2 (2016), p. 022003. doi: 10.1103/PhysRevLett.117.022003 (cit. on p. 2).
- [Abb+13] E. Abbas et al. “Mid-rapidity anti-baryon to baryon ratios in pp collisions at $\sqrt{s} = 0.9, 2.76$ and 7 TeV measured by ALICE”. *Eur. Phys. J. C* 73 (2013), p. 2496. doi: 10.1140/epjc/s10052-013-2496-5 (cit. on pp. 95, 119).
- [Abb+16] B. P. Abbott et al. “Observation of Gravitational Waves from a Binary Black Hole Merger”. *Phys. Rev. Lett.* 116.6 (2016), p. 061102. doi: 10.1103/PhysRevLett.116.061102 (cit. on p. 11).

- [Abd+10] M. Abdel-Bary et al. “Production of Λ and Σ^0 hyperons in proton-proton collisions”. *Eur. Phys. J. A*46 (2010). [Erratum: *Eur. Phys. J. A*46,435(2010)], pp. 27–44. doi: 10.1140/epja/i2010-11023-0,10.1140/epja/i2010-11062-5 (cit. on p. 68).
- [Abe+06] B. I. Abelev et al. “Neutral kaon interferometry in Au+Au collisions at $\sqrt{s_{NN}} = 200$ -GeV”. *Phys. Rev. C*74 (2006), p. 054902. doi: 10.1103/PhysRevC.74.054902 (cit. on pp. 62, 109).
- [Abe+12] Betty Abelev et al. “ $K_s^0 - K_s^0$ correlations in pp collisions at $\sqrt{s} = 7$ TeV from the LHC ALICE experiment”. *Phys. Lett. B*717 (2012), pp. 151–161. doi: 10.1016/j.physletb.2012.09.013 (cit. on pp. 74, 134–136).
- [Abe+13] B. Abelev et al. “Charged kaon femtoscopic correlations in pp collisions at $\sqrt{s} = 7$ TeV”. *Phys. Rev. D*87.5 (2013), p. 052016. doi: 10.1103/PhysRevD.87.052016 (cit. on pp. 74, 115, 134–136).
- [Abe+14a] Betty Bezverkhny Abelev et al. “Freeze-out radii extracted from three-pion cumulants in pp , p -Pb and Pb-Pb collisions at the LHC”. *Phys. Lett. B*739 (2014), pp. 139–151. doi: 10.1016/j.physletb.2014.10.034 (cit. on p. 132).
- [Abe+14b] Betty Bezverkhny Abelev et al. “Performance of the ALICE Experiment at the CERN LHC”. *Int. J. Mod. Phys. A*29 (2014), p. 1430044. doi: 10.1142/S0217751X14300440 (cit. on pp. 85, 89, 91, 93, 128).
- [Ada+05] J. Adams et al. “Pion interferometry in Au+Au collisions at $\sqrt{s_{NN}} = 200$ -GeV”. *Phys. Rev. C*71 (2005), p. 044906. doi: 10.1103/PhysRevC.71.044906 (cit. on p. 63).
- [Ada+06] J. Adams et al. “Proton - lambda correlations in central Au+Au collisions at $\sqrt{s_{NN}} = 200$ -GeV”. *Phys. Rev. C*74 (2006), p. 064906. doi: 10.1103/PhysRevC.74.064906 (cit. on pp. 67, 109, 123).
- [Ada+15a] J. Adam et al. “Two-pion femtoscopy in p -Pb collisions at $\sqrt{s_{NN}} = 5.02$ TeV”. *Phys. Rev. C*91 (2015), p. 034906. doi: 10.1103/PhysRevC.91.034906 (cit. on p. 132).
- [Ada+15b] Jaroslav Adam et al. “One-dimensional pion, kaon, and proton femtoscopy in Pb-Pb collisions at $\sqrt{s_{NN}} = 2.76$ TeV”. *Phys. Rev. C*92.5 (2015), p. 054908. doi: 10.1103/PhysRevC.92.054908 (cit. on pp. 94, 109, 134, 136).
- [Ada+15c] L. Adamczyk et al. “ $\Lambda\Lambda$ Correlation Function in Au+Au collisions at $\sqrt{s_{NN}} = 200$ GeV”. *Phys. Rev. Lett.* 114.2 (2015), p. 022301. doi: 10.1103/PhysRevLett.114.022301 (cit. on pp. 105, 109, 137).
- [Ada+16] Jaroslav Adam et al. “Insight into particle production mechanisms via angular correlations of identified particles in pp collisions at $\sqrt{s} = 7$ TeV” (2016) (cit. on p. 93).

- [Aga+09] G. Agakishiev et al. “The High-Acceptance Dielectron Spectrometer HADES”. *Eur. Phys. J. A*41 (2009), pp. 243–277. doi: 10.1140/epja/i2009-10807-5 (cit. on p. 43).
- [Aga+10] G. Agakishiev et al. “Lambda-p femtoscopy in collisions of Ar+KCl at 1.76 AGeV”. *Phys. Rev. C*82 (2010), p. 021901. doi: 10.1103/PhysRevC.82.021901 (cit. on pp. 60, 67, 74).
- [Aga+11] G. Agakishiev et al. “p p and pi pi intensity interferometry in collisions of Ar + KCl at 1.76A-GeV”. *Eur. Phys. J. A*47 (2011), p. 63. doi: 10.1140/epja/i2011-11063-x (cit. on p. 67).
- [Aga+14a] G. Agakishiev et al. “Lambda hyperon production and polarization in collisions of p(3.5 GeV)+Nb”. *Eur. Phys. J. A*50 (2014), p. 81. doi: 10.1140/epja/i2014-14081-2 (cit. on p. 61).
- [Aga+14b] G. Agakishiev et al. “Medium effects in proton-induced K^0 production at 3.5 GeV”. *Phys. Rev. C*90 (2014), p. 054906. doi: 10.1103/PhysRevC.90.054906 (cit. on p. 59).
- [Aga+16] G. Agakishiev et al. “Statistical model analysis of hadron yields in proton-nucleus and heavy-ion collisions at SIS 18 energiesStatistical hadronization model analysis of hadron yields in p + Nb and Ar + KCl at SIS18 energies”. *Eur. Phys. J. A*52.6 (2016), p. 178. doi: 10.1140/epja/i2016-16178-x (cit. on p. 68).
- [Ahl+02] L. Ahle et al. “System, centrality, and transverse mass dependence of two pion correlation radii in heavy ion collisions at 11.6-A-GeV and 14.6-A-GeV”. *Phys. Rev. C*66 (2002), p. 054906. doi: 10.1103/PhysRevC.66.054906 (cit. on p. 156).
- [Ale+68] G. Alexander et al. “Study of the lambda-n system in low-energy lambda-p elastic scattering”. *Phys. Rev.* 173 (1968), pp. 1452–1460. doi: 10.1103/PhysRev.173.1452 (cit. on pp. 12, 71).
- [Alm+10] J. Alme et al. “The ALICE TPC, a large 3-dimensional tracking device with fast readout for ultra-high multiplicity events”. *Nucl. Instrum. Meth. A*622 (2010), pp. 316–367. doi: 10.1016/j.nima.2010.04.042 (cit. on pp. 87, 88).
- [Ant+11] T. Anticic et al. “Proton - Lambda Correlations in Central Pb+Pb Collisions at $\sqrt{s_{NN}} = 17.3$ GeV”. *Phys. Rev. C*83 (2011), p. 054906. doi: 10.1103/PhysRevC.83.054906 (cit. on pp. 67, 109).
- [Ant+13] John Antoniadis et al. “A Massive Pulsar in a Compact Relativistic Binary”. *Science* 340 (2013), p. 6131. doi: 10.1126/science.1233232 (cit. on p. 6).

- [Awe+95] T. Awe et al. “Two-proton correlations in the target fragmentation region of nuclear collisions at 200 A GeV”. *Zeitschrift für Physik C65* (1995), pp. 207–213 (cit. on p. 74).
- [Azi+84] S. A. Azimov et al. “STUDY OF CORRELATIONS BETWEEN SECONDARY PROTONS PRODUCED IN PROTON NEON INTERACTIONS AT 300-GEV/C”. *Phys. Rev. D29* (1984), pp. 1304–1308. doi: 10.1103/PhysRevD.29.1304 (cit. on p. 74).
- [Bas+98] S. A. Bass et al. “Microscopic models for ultrarelativistic heavy ion collisions”. *Prog. Part. Nucl. Phys.* 41 (1998). [Prog. Part. Nucl. Phys.41,225(1998)], pp. 255–369. doi: 10.1016/S0146-6410(98)00058-1 (cit. on p. 59).
- [BB15] Hans Beck and Christoph Blume. “Femtoscopic $p\Lambda$ and $\gamma\gamma$ Correlations in Pb-Pb Collisions at $\sqrt{s_{NN}}=2.76$ TeV with ALICE”. Presented 07 Sep 2015. PhD thesis. Goethe U., Frankfurt (main), 2015-06 (cit. on p. 93).
- [BD01] D. A. Brown and P. Danielewicz. “Observing nongaussian sources in heavy ion reactions”. *Phys. Rev. C64* (2001), p. 014902. doi: 10.1103/PhysRevC.64.014902 (cit. on pp. 24, 145, 147).
- [BD98] David A. Brown and Pawel Danielewicz. “Optimized discretization of sources imaged in heavy ion reactions”. *Phys. Rev. C57* (1998), pp. 2474–2483. doi: 10.1103/PhysRevC.57.2474 (cit. on p. 24).
- [BDZ08] I. Bloch, J. Dalibard, and W. Zwerger. “Many-body physics with ultracold gases”. *Reviews of Modern Physics* 80 (2008-07), pp. 885–964. doi: 10.1103/RevModPhys.80.885 (cit. on p. 36).
- [Bet07] Siegfried Bethke. “Experimental tests of asymptotic freedom”. *Prog. Part. Nucl. Phys.* 58 (2007), pp. 351–386. doi: 10.1016/j.ppnp.2006.06.001 (cit. on pp. 2, 3).
- [Bet30] H. Bethe. “Theory of the Passage of Fast Corpuscular Rays Through Matter”. *Annalen Phys.* 5 (1930). [Annalen Phys.397,325(1930)], pp. 325–400. doi: 10.1002/andp.19303970303 (cit. on p. 50).
- [Bet49] H. A. Bethe. “Theory of the Effective Range in Nuclear Scattering”. *Phys. Rev.* 76 (1949), pp. 38–50. doi: 10.1103/PhysRev.76.38 (cit. on p. 29).
- [BF14] Remco de Boer and Laura Fabbietti. “ K_0^S -p correlations in $\sqrt{s_{NN}}=5.02$ TeV p-Pb collisions at ALICE”. Utrecht University, 2014-01 (cit. on p. 97).
- [BFZ15] Andrzej Bialas, Wojciech Florkowski, and Kacper Zalewski. “Finite size of hadrons and Bose–Einstein correlations in pp collisions at 7 TeV”. *Phys. Lett. B748* (2015), pp. 9–12. doi: 10.1016/j.physletb.2015.06.053 (cit. on p. 30).

- [BGJ90] D. H. Boal, C. K. Gelbke, and B. K. Jennings. “Intensity interferometry in subatomic physics”. *Rev. Mod. Phys.* 62 (1990), pp. 553–602. doi: 10.1103/RevModPhys.62.553 (cit. on p. 29).
- [Ble+99] M. Bleicher et al. “Relativistic hadron hadron collisions in the ultrarelativistic quantum molecular dynamics model”. *J. Phys.* G25 (1999), pp. 1859–1896. doi: 10.1088/0954-3899/25/9/308 (cit. on p. 59).
- [Boc11] Nicolas Bock. “Femtoscopy of proton-proton collisions in the ALICE experiment”. PhD thesis. Ohio State University, 2011 (cit. on pp. 61, 132).
- [Bog+99] H. Boggild et al. “Two proton correlations near mid-rapidity in p + Pb and S + Pb collisions at the CERN SPS”. *Phys. Lett.* B458 (1999), pp. 181–189. doi: 10.1016/S0370-2693(99)00614-0 (cit. on p. 74).
- [Bro] David Brown. “private communication” () (cit. on p. 71).
- [Bro98] David Alan Brown. “Accessing the space-time development of heavy-ion collisions with theory and experiment”. PhD thesis. Michigan State University, 1998 (cit. on p. 147).
- [BT56] R. Hanbury Brown and R. Q. Twiss. “Correlation between Photons in two Coherent Beams of Light”. *Nature* 177 (1956), pp. 27–29. doi: 10.1038/177027a0 (cit. on p. 17).
- [BU88] A. R. Bodmer and Q. N. Usmani. “Binding Energies of the S Shell Hypernuclei and the Λ Well Depth”. *Nucl. Phys.* A477 (1988), pp. 621–651. doi: 10.1016/0375-9474(88)90410-1 (cit. on pp. 15, 31).
- [Bus+12] O. Buss et al. “Transport-theoretical Description of Nuclear Reactions”. *Phys. Rept.* 512 (2012), pp. 1–124. doi: 10.1016/j.physrep.2011.12.001 (cit. on p. 59).
- [Cha+12] Serguei Chatrchyan et al. “Observation of a new boson at a mass of 125 GeV with the CMS experiment at the LHC”. *Phys. Lett.* B716 (2012), pp. 30–61. doi: 10.1016/j.physletb.2012.08.021 (cit. on p. 1).
- [Cha+13] N. Chamel et al. “On the Maximum Mass of Neutron Stars”. *Int. J. Mod. Phys.* E22 (2013), p. 1330018. doi: 10.1142/S021830131330018X (cit. on pp. 8, 10).
- [Cha09] Zbigniew Chajecki. “Global Conservation Laws and Femtoscopy at RHIC”. PhD thesis. Ohio State University, 2009 (cit. on p. 61).
- [Cho12] Marek Chojnacki. “Measurement of pions, kaons and protons with the ALICE detector in pp collisions at the LHC”. PhD thesis. Utrecht U., 2012 (cit. on p. 116).

- [Chu+02] P. Chung et al. “Neutral strange particle dynamics in Au + Au collisions at AGS energies”. *J. Phys.* G28 (2002), pp. 1567–1574. doi: 10.1088/0954-3899/28/7/307 (cit. on p. 97).
- [Chu+03] P. Chung et al. “Comparison of source images for protons, pi-’s and Lambda’s in 6-AGeV Au+Au collisions”. *Phys. Rev. Lett.* 91 (2003), p. 162301. doi: 10.1103/PhysRevLett.91.162301 (cit. on pp. 147, 148).
- [CL08] Zbigniew Chajecki and Mike Lisa. “Global Conservation Laws and Femtoscopy of Small Systems”. *Phys. Rev.* C78 (2008), p. 064903. doi: 10.1103/PhysRevC.78.064903 (cit. on pp. 33, 61).
- [col15] The ATLAS collaboration. “Femtoscopy with identified charged pions in proton-lead collisions at $\sqrt{s_{NN}} = 5.02$ TeV with ATLAS” (2015) (cit. on p. 97).
- [Cor+06] P Cortese et al. “ALICE: Physics performance report, volume II”. *J. Phys.* G32 (2006). Ed. by B Alessandro et al., pp. 1295–2040. doi: 10.1088/0954-3899/32/10/001 (cit. on pp. 95, 96).
- [Cow98] Glen Cowan. *Statistical Data Analysis*. Oxford Science publications, 1998 (cit. on pp. 21, 100, 156).
- [Daw78] A.S. Dawydow. *Quantenmechanik*. VEB Deutscher Verlag der Wissenschaften, 1978 (cit. on pp. 25, 70, 151).
- [Day81] B. D. Day. “Three-body correlations in nuclear matter”. *Phys. Rev. C* 24 (3 1981-09), pp. 1203–1271. doi: 10.1103/PhysRevC.24.1203 (cit. on p. 34).
- [Dem+10] Paul Demorest et al. “Shapiro Delay Measurement of A Two Solar Mass Neutron Star”. *Nature* 467 (2010), pp. 1081–1083. doi: 10.1038/nature09466 (cit. on p. 6).
- [DLP14] Alessandro Drago, Andrea Lavagno, and Giuseppe Pagliara. “Can very compact and very massive neutron stars both exist?” *Phys. Rev.* D89.4 (2014), p. 043014. doi: 10.1103/PhysRevD.89.043014 (cit. on p. 11).
- [EB08] Lyndon Evans and Philip Bryant. “LHC Machine”. *JINST* 3 (2008), S08001. doi: 10.1088/1748-0221/3/08/S08001 (cit. on p. 85).
- [FH11] Kenji Fukushima and Tetsuo Hatsuda. “The phase diagram of dense QCD”. *Rept. Prog. Phys.* 74 (2011), p. 014001. doi: 10.1088/0034-4885/74/1/014001 (cit. on p. 5).
- [GHM16] A. Gal, E. V. Hungerford, and D. J. Millener. “Strangeness in nuclear physics”. *Rev. Mod. Phys.* 88.3 (2016), p. 035004. doi: 10.1103/RevModPhys.88.035004 (cit. on pp. 12, 14).

- [Gil+07] A. Gil et al. “Front-end electronics development for the new resistive plate chamber detector of HADES”. *JINST* 2 (2007), T11001. doi: 10.1088/1748-0221/2/11/T11001 (cit. on p. 48).
- [Gmi+86] M. Gmitro et al. “On the Sensitivity of Nucleon-nucleon Correlations to the Form of Short Range Potential”. *Czech. J. Phys.* B36 (1986), p. 1281. doi: 10.1007/BF01598029 (cit. on p. 29).
- [Gol+60] Gerson Goldhaber et al. “Influence of Bose-Einstein statistics on the anti-proton proton annihilation process”. *Phys. Rev.* 120 (1960), pp. 300–312. doi: 10.1103/PhysRev.120.300 (cit. on p. 17).
- [Gou83] Konstantin A. Goulianos. “Diffractive Interactions of Hadrons at High-Energies”. *Phys. Rept.* 101 (1983), p. 169. doi: 10.1016/0370-1573(83)90010-8 (cit. on p. 70).
- [Hai+13] J. Haidenbauer et al. “Hyperon-nucleon interaction at next-to-leading order in chiral effective field theory”. *Nucl. Phys.* A915 (2013), pp. 24–58. doi: 10.1016/j.nuclphysa.2013.06.008 (cit. on pp. 9, 13, 14, 71, 72, 75, 81, 82, 135).
- [Hai+17] J. Haidenbauer et al. “Lambda-nuclear interactions and hyperon puzzle in neutron stars”. *Eur. Phys. J.* A53.6 (2017), p. 121. doi: 10.1140/epja/i2017-12316-4 (cit. on pp. 9–11).
- [Hig64] Peter W. Higgs. “Broken Symmetries and the Masses of Gauge Bosons”. *Phys. Rev. Lett.* 13 (1964), pp. 508–509. doi: 10.1103/PhysRevLett.13.508 (cit. on p. 1).
- [HJ99] Ulrich W. Heinz and Barbara V. Jacak. “Two particle correlations in relativistic heavy ion collisions”. *Ann. Rev. Nucl. Part. Sci.* 49 (1999), pp. 529–579. doi: 10.1146/annurev.nucl.49.1.529 (cit. on pp. 18, 24).
- [HMP16] J. Haidenbauer, Ulf-G. Meißner, and S. Petschauer. “Strangeness $S = -2$ baryon–baryon interaction at next-to-leading order in chiral effective field theory”. *Nucl. Phys.* A954 (2016), pp. 273–293. doi: 10.1016/j.nuclphysa.2016.01.006 (cit. on pp. 126, 137).
- [HT56] R. Hanbury Brown and R. Q. Twiss. “A Test of a new type of stellar interferometer on Sirius”. *Nature* 178 (1956), pp. 1046–1048. doi: 10.1038/1781046a0 (cit. on p. 17).
- [HW14] Thomas Hell and Wolfram Weise. “Dense baryonic matter: constraints from recent neutron star observations”. *Phys. Rev.* C90.4 (2014), p. 045801. doi: 10.1103/PhysRevC.90.045801 (cit. on p. 7).

- [Kad+71] J. A. Kadyk et al. “Lambda p interactions in momentum range 300 to 1500 meV/c”. *Nucl. Phys.* B27 (1971), pp. 13–22. doi: 10.1016/0550-3213(71)90076-9 (cit. on p. 12).
- [Kis10] Adam Kisiel. “Non-identical particle femtoscopy at $\sqrt{s(NN)}^{1/2} = 200$ -AGeV in hydrodynamics with statistical hadronization”. *Phys. Rev.* C81 (2010), p. 064906. doi: 10.1103/PhysRevC.81.064906 (cit. on p. 72).
- [Koo77] S. E. Koonin. “Proton Pictures of High-Energy Nuclear Collisions”. *Phys. Lett.* B70 (1977), pp. 43–47. doi: 10.1016/0370-2693(77)90340-9 (cit. on p. 34).
- [Kop74] G. I. Kopylov. “Like particle correlations as a tool to study the multiple production mechanism”. *Phys. Lett.* B50 (1974), pp. 472–474. doi: 10.1016/0370-2693(74)90263-9 (cit. on p. 36).
- [Kot+99] R. Kotte et al. “On the space-time difference of proton and composite particle emission in central heavy ion reactions at 400-A/MeV”. *Eur. Phys. J.* A6 (1999), pp. 185–195. doi: 10.1007/s100500050333 (cit. on p. 73).
- [Krü+13] T. Krüger et al. “Neutron matter from chiral effective field theory interactions”. *Phys. Rev.* C88 (2013), p. 025802. doi: 10.1103/PhysRevC.88.025802 (cit. on p. 7).
- [KZS14] Adam Kisiel, Hanna Zbroszczyk, and Maciej Szymański. “Extracting baryon-antibaryon strong interaction potentials from $p\bar{\Lambda}$ femtoscopic correlation functions”. *Phys. Rev.* C89.5 (2014), p. 054916. doi: 10.1103/PhysRevC.89.054916 (cit. on pp. 123, 124).
- [Lap+09] K. Lapidus et al. “Dielectron production in pp and dp collisions at 1.25-GeV/u with HADES”. *19th International Baldin Seminar on High Energy Physics Problems: Relativistic Nuclear Physics and Quantum Chromodynamics (ISHEPP 2008) Dubna, Russia, September 29-October 4, 2008*. 2009 (cit. on p. 49).
- [Led] Richard Lednicky. “private communication” () (cit. on p. 71).
- [Led09] Richard Lednicky. “Finite-size effects on two-particle production in continuous and discrete spectrum”. *Phys. Part. Nucl.* 40 (2009), pp. 307–352. doi: 10.1134/S1063779609030034 (cit. on p. 18).
- [Lis+05] Michael Annan Lisa et al. “Femtoscopy in relativistic heavy ion collisions”. *Ann. Rev. Nucl. Part. Sci.* 55 (2005), pp. 357–402. doi: 10.1146/annurev.nucl.55.090704.151533 (cit. on pp. 18, 24, 38, 66).
- [LL79] L.D. Landau and E.M. Lifschitz. *Lehrbuch der theoretischen Physik. Quantenmechanik*. Akademie Verlag Berlin, 1979 (cit. on pp. 26, 35).

- [LL82] R. Lednicky and V. L. Lyuboshits. “Final State Interaction Effect on Pairing Correlations Between Particles with Small Relative Momenta”. *Sov. J. Nucl. Phys.* 35 (1982). [*Yad. Fiz.*35,1316(1981)], p. 770 (cit. on pp. 26, 29, 34).
- [Lon+15] Diego Lonaroni et al. “Hyperon Puzzle: Hints from Quantum Monte Carlo Calculations”. *Phys. Rev. Lett.* 114.9 (2015), p. 092301. doi: 10.1103/PhysRevLett.114.092301 (cit. on pp. 8, 9).
- [Lor12] Manuel Lorenz. “Vector meson production in p+*Nb* reactions and statistical particle production in Ar+KCl collisions”. PhD thesis. Johann Wolfgang Goethe-Universität, 2012 (cit. on p. 53).
- [Lus03] Martin Luscher. “Lattice QCD: From quark confinement to asymptotic freedom”. *Annales Henri Poincare* 4 (2003), S197–S210. doi: 10.1007/s00023-003-0916-z (cit. on p. 4).
- [ME11] R. Machleidt and D. R. Entem. “Chiral effective field theory and nuclear forces”. *Phys. Rept.* 503 (2011), pp. 1–75. doi: 10.1016/j.physrep.2011.02.001 (cit. on p. 4).
- [MFO15] Kenji Morita, Takenori Furumoto, and Akira Ohnishi. “ $\Lambda\Lambda$ interaction from relativistic heavy-ion collisions”. *Phys. Rev. C*91.2 (2015), p. 024916. doi: 10.1103/PhysRevC.91.024916 (cit. on pp. 105, 137, 138, 140).
- [Mih] Dimitar Mihaylov. “private communication” () (cit. on p. 70).
- [MM09] Radoslaw Maj and Stanislaw Mrowczynski. “Coulomb Effects in Femtoscopy”. *Phys. Rev. C*80 (2009), p. 034907. doi: 10.1103/PhysRevC.80.034907 (cit. on pp. 24, 25).
- [Nig+16] G. A. Nigmatkulov et al. “The Transverse Momentum Dependence of Charged Kaon Bose–Einstein Correlations in the SELEX Experiment”. *Phys. Lett. B*753 (2016), pp. 458–464. doi: 10.1016/j.physletb.2015.12.041 (cit. on p. 74).
- [Oli+14] K. A. Olive et al. “Review of Particle Physics”. *Chin. Phys.* C38 (2014), p. 090001. doi: 10.1088/1674-1137/38/9/090001 (cit. on pp. 54, 74, 119).
- [OV39] J. R. Oppenheimer and G. M. Volkoff. “On Massive neutron cores”. *Phys. Rev.* 55 (1939), pp. 374–381. doi: 10.1103/PhysRev.55.374 (cit. on p. 6).
- [Pae14] H. Paetz gen. Schieck. *Nuclear reactions. An introduction*. Springer, 2014 (cit. on p. 16).
- [Pie+15] T. Pierog et al. “EPOS LHC: Test of collective hadronization with data measured at the CERN Large Hadron Collider”. *Phys. Rev. C*92.3 (2015), p. 034906. doi: 10.1103/PhysRevC.92.034906 (cit. on p. 140).

- [Pra17] Scott Pratt. *CRAB, Correlation After Burner*. <http://www.pa.msu.edu/~pratts/freecodes/crab/home.html>. [Online; accessed 2015]. 2017 (cit. on p. 70).
- [Pra84] S. Pratt. “Pion Interferometry for Exploding Sources”. *Phys. Rev. Lett.* 53 (1984), pp. 1219–1221. doi: 10.1103/PhysRevLett.53.1219 (cit. on p. 18).
- [PSH13] Christopher J. Plumberg, Chun Shen, and Ulrich W Heinz. “Hanbury-Brown–Twiss interferometry relative to the triangular flow plane in heavy-ion collisions”. *Phys. Rev. C* 88 (2013). [Erratum: *Phys. Rev. C* 88, no. 6, 069901 (2013)], p. 044914. doi: 10.1103/PhysRevC.88.069901, 10.1103/PhysRevC.88.044914 (cit. on p. 36).
- [Rad+16] David Radice et al. “Probing Extreme-Density Matter with Gravitational Wave Observations of Binary Neutron Star Merger Remnants” (2016) (cit. on p. 11).
- [Rei68] Roderick V. Reid Jr. “Local phenomenological nucleon-nucleon potentials”. *Annals Phys.* 50 (1968), pp. 411–448. doi: 10.1016/0003-4916(68)90126-7 (cit. on p. 34).
- [Sak94] J.J. Sakurai. *Modern quantum mechanics*. Addison-Wesley, 1994 (cit. on p. 50).
- [Sec+68] B. Sechi-Zorn et al. “Low-energy lambda-proton elastic scattering”. *Phys. Rev.* 175 (1968), pp. 1735–1740. doi: 10.1103/PhysRev.175.1735 (cit. on pp. 12, 13, 71).
- [Sek+11] Yuichiro Sekiguchi et al. “Effects of hyperons in binary neutron star mergers”. *Phys. Rev. Lett.* 107 (2011), p. 211101. doi: 10.1103/PhysRevLett.107.211101 (cit. on p. 11).
- [SH17] Jai Salzwedel and Thomas Humanic. “Lambda femtoscopy in $\sqrt{s_{NN}} = 2.76$ TeV Pb-Pb collisions at ALICE”. Presented 15 Dec 2016. PhD thesis. Ohio State U., 2017-01 (cit. on p. 105).
- [Sha+15] V. M. Shapoval et al. “Extracting $p\Lambda$ scattering lengths from heavy ion collisions”. *Phys. Rev. C* 92.3 (2015), p. 034910. doi: 10.1103/PhysRevC.92.034910 (cit. on pp. 72, 123).
- [Sta+04] A. V. Stavinsky et al. “Proton source size measurements in the eA \rightarrow e-prime ppX reaction”. *Phys. Rev. Lett.* 93 (2004), p. 192301. doi: 10.1103/PhysRevLett.93.192301 (cit. on pp. 29, 74).
- [Sta+07] A. Stavinskiy et al. “Residual correlations between decay products of π^0 and p Σ^0 systems” (2007) (cit. on pp. 68, 125, 126).

- [Tol39] Richard C. Tolman. “Static solutions of Einstein’s field equations for spheres of fluid”. *Phys. Rev.* 55 (1939), pp. 364–373. doi: 10.1103/PhysRev.55.364 (cit. on p. 6).
- [Tsu+99] Kazuo Tsushima et al. “Resonance model study of kaon production in baryon baryon reactions for heavy ion collisions”. *Phys. Rev.* C59 (1999). [Erratum: *Phys. Rev.* C61,029903(2000)], pp. 369–387. doi: 10.1103/PhysRevC.61.029903,10.1103/PhysRevC.59.369 (cit. on p. 59).
- [Van06] G. Van Buren. “The Ratio Σ_0 / Λ at RHIC”. *Rom. Rep. Phys.* 58 (2006), pp. 069–074 (cit. on p. 120).
- [Ver+02] G. Verde et al. “Imaging sources with fast and slow emission components”. *Phys. Rev.* C65 (2002), p. 054609. doi: 10.1103/PhysRevC.65.054609 (cit. on pp. 145, 146).
- [Wan99] Fu-Qiang Wang. “Residual correlation in two proton interferometry from Λ proton strong interactions”. *Phys. Rev.* C60 (1999), p. 067901. doi: 10.1103/PhysRevC.60.067901 (cit. on p. 123).
- [WCS12] Simon Weissenborn, Debarati Chatterjee, and Juergen Schaffner-Bielich. “Hyperons and massive neutron stars: vector repulsion and SU(3) symmetry”. *Phys. Rev.* C85.6 (2012). [Erratum: *Phys. Rev.* C90,no.1,019904(2014)], p. 065802. doi: 10.1103/PhysRevC.85.065802, 10.1103/PhysRevC.90.019904 (cit. on p. 7).
- [Web11] Michael Weber. “Dielektronen Spektroskopie in kalter Kernmaterie”. PhD thesis. Technische Universität München, 2011 (cit. on p. 53).
- [Wei79] Steven Weinberg. “Phenomenological Lagrangians”. *Physica* A96 (1979), pp. 327–340. doi: 10.1016/0378-4371(79)90223-1 (cit. on p. 3).
- [Wer] Klaus Werner. “private communication” () (cit. on p. 140).
- [WFH99] Urs Achim Wiedemann, Daniel Ferenc, and Ulrich W. Heinz. “Coulomb final state interactions for Gaussian wave packets”. *Phys. Lett.* B449 (1999), pp. 347–353. doi: 10.1016/S0370-2693(99)00087-8 (cit. on p. 30).
- [WP99] Fu-qiang Wang and Scott Pratt. “ Λ proton correlations in relativistic heavy ion collisions”. *Phys. Rev. Lett.* 83 (1999), pp. 3138–3141. doi: 10.1103/PhysRevLett.83.3138 (cit. on pp. 16, 31, 36).
- [WSS95] Robert B. Wiringa, V. G. J. Stoks, and R. Schiavilla. “An Accurate nucleon-nucleon potential with charge independence breaking”. *Phys. Rev.* C51 (1995), pp. 38–51. doi: 10.1103/PhysRevC.51.38 (cit. on p. 30).